Hydrodynamic Study of Stereociliary Tuft Motion in Hair Cell Organs

Dennis M. Freeman

Technical Report 523

March 1987

Massachusetts Institute of Technology
Research Laboratory of Electronics
Cambridge, Massachusetts 02139

HYDRODYNAMIC STUDY OF STEREOCILIARY TUFT MOTION IN HAIR CELL ORGANS

Dennis M. Freeman

Technical Report 523

March 1987

Massachusetts Institute of Technology
Research Laboratory of Electronics
Cambridge, Massachusetts 02139

This document is a corrected version of the thesis document of May 1986.

This work was supported in part by grants from the National Institutes of Health (Grant 5 R01 NS20322-03) and from the Sherman Fairchild Foundation.

HYDRODYNAMIC STUDY OF STEREOCILIARY TUFT MOTION IN HAIR CELL ORGANS

by

Dennis M. Freeman

B.S., The Pennsylvania State University (1973)
M.S., Massachusetts Institute of Technology (1976)
E.E., Massachusetts Institute of Technology (1976)

SUBMITTED IN PARTIAL FULFILLMENT
OF THE REQUIREMENTS FOR THE
DEGREE OF

DOCTOR OF PHILOSOPHY

at the

MASSACHUSETTS INSTITUTE OF TECHNOLOGY
June 1986

Signature of Author 
Department of Electrical Engineering and Computer Science
May 16, 1986

Certified by _____
Thomas F. Weiss
Thesis Supervisor

Accepted by _____
Arthur C. Smith
Chairman, Departmental Committee on Graduate Students

HYDRODYNAMIC STUDY OF STEREOCILIARY TUFT MOTION IN HAIR CELL ORGANS

by

DENNIS MELVIN FREEMAN

Submitted to the Department of Electrical Engineering and Computer Science,
M. I. T., on May 16, 1986 in partial fulfillment of the
requirements for the degree of Doctor of Philosophy.

ABSTRACT

In auditory, vestibular, and lateral-line systems, environmental stimuli act through a variety of mechanical linkages to displace the stereociliary tufts of hair cells, the sensory receptor cells that transduce motion into electrical signals. We investigate the theory of hydrodynamics to determine the effect of fluid on stereociliary tuft motion, and to isolate the features of receptor organ morphology that most directly affect the fluid forces that act on tufts. We conclude that for physiological stimuli: fluid compressibility is negligible; convective non-linear inertial forces are small; and both viscous and linear inertial forces are appreciable. We examine the frequency dependence of viscous and inertial fluid forces that act on isolated, vibrating bodies of regular geometry in viscous, incompressible, Newtonian fluids, and show that the mechanical admittance of a system in which such a body is supported by springs shows a geometry-dependent resonance.

To assess the effect of nearby structures on the motions of stereociliary tufts, we study the motion of a rigid body (representing a tuft) that is: immersed in a Newtonian fluid (representing endolymph); connected by a spring-loaded hinge to a vibrating "basal" plate (representing the reticular lamina); and surmounted by a parallel, independently vibrating "tectorial" plate (representing the tectorial membrane). We characterize the motion of the body for both asymptotically high and low frequencies of excitation. We conclude that three limiting tuft morphologies, free-standing (where no tectorial structure surmounts the tuft), tectorial-unattached (where a tuft is closely surmounted by but not attached to a tectorial structure), and tectorial-attached (where tufts are attached to a tectorial structure), give rise to different frequency dependence of tuft motion at low frequency and similar frequency dependence at high frequency.

We show by numerical analysis that the motion of a massless, rectangular flap that is attached to a rigid plate with a spring-loaded hinge (a special case of the previous class of models) exhibits a passive mechanical resonance that results from the fluid inertia and the hinge compliance. This resonance can play a critical role in the frequency selective properties of hair cells.

Thesis Supervisor: Thomas F. Weiss
Title: Professor of Electrical Engineering and Computer Science

Acknowledgement

I am most indebted to Professor Thomas F. Weiss, whose ability to express ideas clearly has contributed not only to the research but also to my personal development. Professors A. Grodzinsky and A. Patera served as readers for this thesis. I appreciate their efforts, and their suggestions. I also thank R. A. Eatock, L. S. Frishkopf, K. Gabriel, W. T. Peake, P. M. Peterson, W. M. Rabinowitz, C. Rose, J. J. Rosowski, and C. L. Searle for many helpful discussions. I thank the Communications Biophysics Group for the use of their computer facility. I acknowledge the financial support of the National Institutes of Health and of the Fairchild Foundation.

I wish to thank Professor L. D. Braida for the opportunity to work with the Communications Biophysics Group during the six years that followed my masters program. Without his help, I would not have entered the doctoral program. I thank Professor A. Drake, who gave me an opportunity to teach, and thereby prodded my interest in a doctoral program. I am deeply indebted to Professor C. L. Searle for his constant support during the past ten years, for developing my interest in auditory perception, and for generating my initial interest in my doctoral project. I especially thank P. M. Peterson for his help and encouragement during my time as an engineer.

TABLE OF CONTENTS

1 STRUCTURE AND MECHANICAL FUNCTION OF HAIR CELL SYSTEMS . . 6
1.1 Sensory Transduction of Mechanical Stimuli 6
1.2 Functional Significance of Micromechanics 11
1.3 Previous Models of Stereociliary Mechanics 15
1.4 Summary 21

2 ON THE ROLE OF FLUID INERTIA AND VISCOSITY IN STEREOCILIARY TUFT MOTION: ANALYSIS OF ISOLATED BODIES OF REGULAR GEOMETRY 22
2.1 Equations of Motion for Cochlear Fluids 22
2.2 Fluid Forces on Isolated Bodies of Regular Geometry 25
2.3 Discussion 31

3 ISOLATED THE KINEMATICALLY IMPORTANT FEATURES OF MICROMECHANICAL MORPHOLOGY 32
3.1 Simplifying the Geometry 32
3.2 Isolating Key Features of Micromechanical System 36
3.3 Models Studied in this Thesis 39

4 EQUATIONS OF MOTION FOR A RIGID BODY THAT IS ATTACHED TO A VIBRATING PLATE WITH A SPRING LOADED HINGE 40
4.1 Formulation of the Equations of Motion 42
4.2 Equations of Motion for Small Excitations 46
4.3 Superposition of Hydrodynamic Component Solutions 51

5 LOW FREQUENCY ANALYSIS OF A RIGID BODY THAT IS ATTACHED TO A VIBRATING PLATE WITH A SPRING LOADED HINGE 55
5.1 Solution by Series Expansion in Frequency 58
5.2 Characterization of the Series 63
5.3 Low-Frequency Relationships for Free-Standing Models 70
5.4 Low-Frequency Relationships for Tectorial Models. 75
5.5 Low-Frequency Relationships for Tectorial Models when G>>L 80
5.6 Conclusions 82

6 HIGH FREQUENCY ANALYSIS OF A RIGID BODY THAT IS ATTACHED TO A VIBRATING PLATE WITH A SPRING LOADED HINGE 84
6.1 Inviscid Approx. to the Equations of Motion for High Frequency Excitation . . . 84
6.2 Properties of Inviscid Fluids 88
6.3 High Frequency Expressions for the Motion of a Hinged Body. 90

7 ASYMPTOTIC ANALYSIS OF THE MOTION OF A FREE-STANDING FLAP . 94
7.1 The Equations of Motion for the Hinged Flap 96
7.2 Low Frequency Asymptotic Motion of a Free-Standing Flap 105
7.3 High Frequency Asymptotic Motion for a Free-Standing Flap 109
7.4 Conclusions 116

8 NUMERICAL ANALYSIS OF THE MOTION OF A FREE-STANDING FLAP . 117
8.1 Difference Approximation of the Equations of Motion 118
8.2 Computational Method 129
8.3 Numerical Results 133
8.4 Summary 155

9 RESULTS AND CONCLUSIONS 156
9.1 Summary of Results 156
9.2 Conclusions 165

References 169

CHAPTER 1
STRUCTURE AND MECHANICAL FUNCTION OF HAIR CELL SYSTEMS

In auditory, vestibular, and lateral-line systems, environmental stimuli act through a variety of mechanical linkages to displace the stereociliary tufts of hair cells. Hair cells are sensory receptor cells that transduce those tuft displacements into electrical signals that ultimately produce discharges of action potentials in nerve fibers. In section 1.1, we briefly outline the structure and function of hair cell systems with the purpose of isolating the features of hair cell systems that most directly impact the motion of stereociliary tufts. In section 1.2, we trace ideas about the functional significance of the mechanical excitation of stereociliary tufts. We review evidence that the hydrodynamics of stereociliary tuft motion plays an important role in the processing of environmental stimuli in hair cell systems. In section 1.3, we review specific models of the mechanical and hydrodynamical excitation of hair cells. In the last section of this chapter, we propose that since experiments evidence the signal processing role of hydrodynamics in stereociliary tuft motion, and since current understanding of hydrodynamical theory is limited, a more thoroughstudy of hydrodynamics is needed.

1.1 SENSORY TRANSDUCTION OF MECHANICAL STIMULI

In this section, we review how mechanical stimuli are transferred to hair cells. After a brief morphological description of stereociliary tufts, the mechanically receptive portion of a hair cell, we review experimental evidence that isolates the mode of mechanical excitation that elicits electrical responses from hair cells. We close this section with a brief overview of structures in different hair cell systems that transfer mechanical excitations to hair cells and a discussion about the aspects of these structures that are most important to exciting hair cell responses.

1.1.1 HAIR CELL MORPHOLOGY

Hair cells are specialized epithelial cells that cluster in patches among non-sensory cells to form a continuous epithelial sheet. A tuft of mechanically sensitive stereocilia protrudes from the apical surface of a hair cell into the fluid filled environment that faces the epithelial sheet (Figure 1.1). From 30 to 150 individual, cylindrically-shaped stereocilia of different lengths form the tuft of a single hair cell. Although various arrangements of stereocilia in a tuft occur in different organs, the tuft always contains an axis of symmetry that defines a morphological polarity.

1.1.2 MECHANICAL EXCITATION OF HAIR CELLS

The structure of stereocilia suggests how stereociliary tufts might move in response to mechanical stimulation. Stereocilia contain cross-linked actin filaments whose arrangement suggests that stereocilia are stiff (Flock and Cheung, 1977; Tilney et al., 1980; DeRosier et al., 1980; Flock et al., 1981). The diameter of a stereocilium narrows near its point of attachment to the hair cell (Figure 1.1), suggesting that mechanical forces would result in very localized bending near the point of attachment.

Measurements of tuft motion are consistent with this conjecture based on structure. When a stereociliary tuft is displaced by micromanipulation with a glass fiber, by a jet of water, or by sound, the entire tuft of stereocilia pivots about the base of the tuft (Flock et al., 1977; Flock and Orman, 1983; Flock and Strelioff, 1984; Frishkopf and DeRosier; 1983; Holton and Hudspeth, 1983). If after deflecting a stereociliary tuft, the external stimulus is removed, the tuft tends to return to its initial position, suggesting that the attachment of stereocilia to the epithelial surface is compliant (Orman and Flock, 1981; Ashmore and Russell, 1983; Strelioff and Flock, 1984).

By observing the intracellular potential of a hair cell while manipulating its tuft with a glass micropipette (Hudspeth and Jacobs, 1979), it has been shown experimentally that stereociliary tuft displacement electrically excites a hair cell. Greater electrical responses are elicited by motions that are parallel to the the axis of morphological polarization than by motions in any other direction (Shotwell, Jacobs, and Hudspeth, 1981).

1.1.3 MECHANICAL EXCITATION OF STEREOCILIARY TUFTS

In vertebrate acoustico-lateralis systems, mechanical linkages, specific to the particular system, transform diverse environmental stimuli into motion of the stereociliary tufts of hair cells. In the lateral line organs of fishes and aquatic amphibians, the tufts of hair cells project into a gelatinous cupula. Local water currents deflect the cupula and thereby deflect stereocilia. In semi-circular canal organs, tufts of hair cells also project into a cupula, but the hydrodynamical forces arise from rotational accelerations of the head that act on the fluids that fill ring-shaped canals. In otolith organs, linear acceleration generates motion of an otolithic membrane that contacts the stereociliary tufts of hair cells and induces their motion. In auditory systems, sound is transmitted

---

Figure 1.1 (on next page): Stereociliary tufts in the auditory organ of alligator lizard. This figure is a scanning electron micrograph of a portion of the surface of the auditory receptor organ of the alligator lizard. The length of the bar indicates a distance of 1 μm. Most prominent in the center of the micrograph are two stereociliary tufts. Each tuft consists of many stereocilia (about 60 are visible in each of these tufts) with lengths that vary from roughly 1 to 18 μm. Each stereocilium is nearly cylindrical in shape and tapers near its attachment to the surface of the organ. Stereocilia from many neighboring hair cells can be seen in the background. [This figure was provided by R. A. Eatock.]

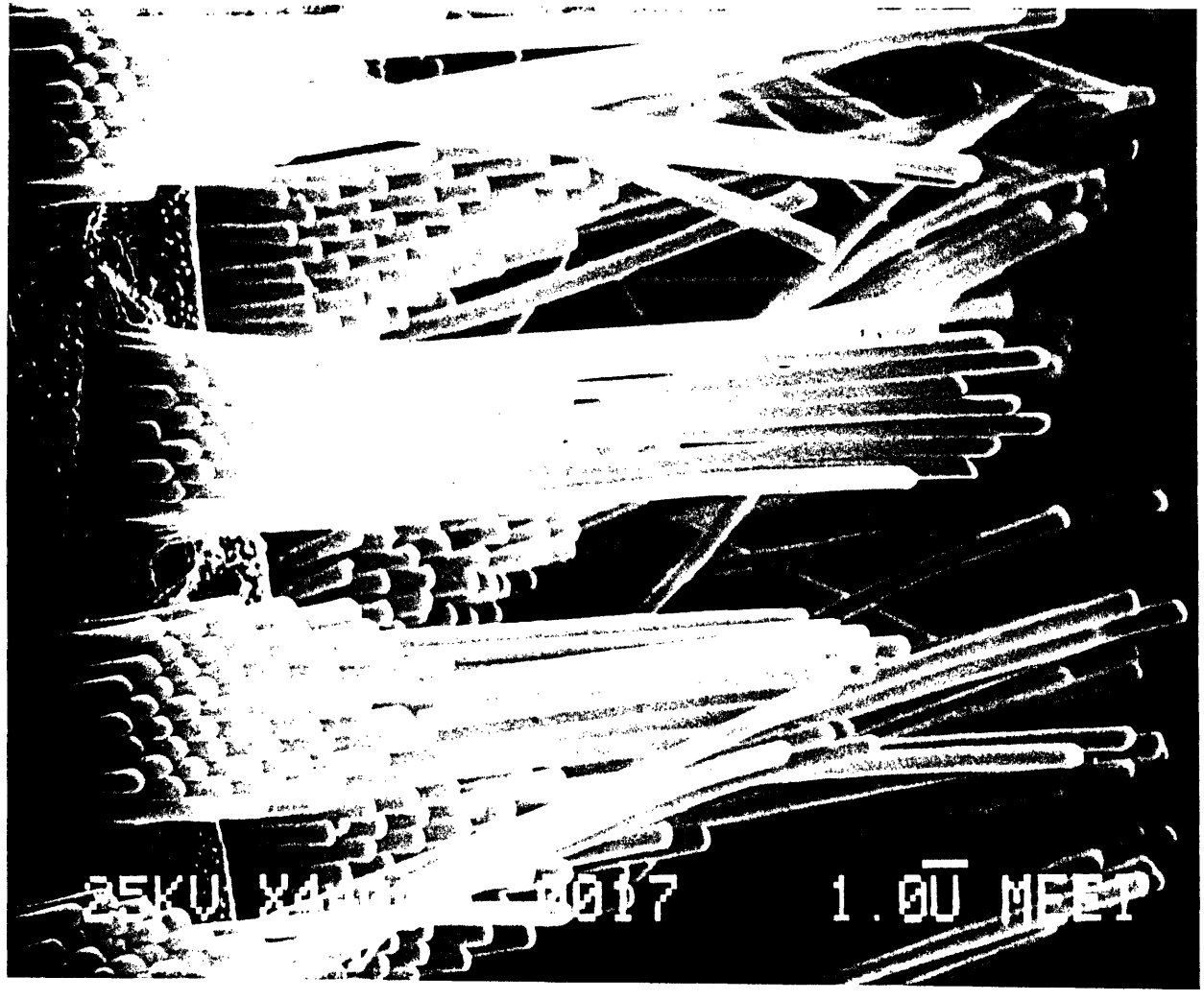
1.0U MEP

through a chain of vibrating structures whose details differ across species. Auditory hair cells in reptiles, birds, and mammals lie on a vibrating basilar membrane. Except for the lizards, the tufts of auditory hair cells are invariably in close proximity with other vibrating structures which we refer to as tectorial structures. In the lizards, patches of hair cells are found whose stereociliary tufts are not in close proximity to a tectorial structure, but are free-standing in endolymph (Figure 1.2).

1.1.4 DEFINITION AND CHARACTERIZATION OF THE MICROMECHANICAL SYSTEM

Diverse mechanical linkages generate forces on and thereby deflect stereociliary tufts. Motions of tufts in particular directions stimulate electrical responses of hair cells. Using the knowledge that it is shearing motion of the tuft that is functionally relevant, we can define several classes of "micromechanical systems" and group the anatomically complex systems that excite stereociliary motion into functional categories.

The simplest class of micromechanical systems is motivated by lizards, whose free-standing stereociliary tufts are presumably deflected by hydrodynamical forces alone. We refer to this class as free-standing.

In other systems, a tectorial structure is present and is in contact with the stereociliary tufts. In these tectorial-attached systems, stereociliary tufts are deflected by mechanical forces that are conveyed both through the tectorial structure and through the fluid.

In mammals, a tectorial membrane overlies both outer and inner hair cells and is clearly in contact with the outer hair cell stereocilia (Lim, 1980). However, the relation of the tectorial membrane to the stereocilia of inner hair cells has been a matter of some controversy. The possibility that inner hair cells are surmounted by but not in contact with the tectorial membrane suggests a third class of micro-mechanical systems in which nearby, but unattached, tectorial structures influence the motion of stereociliary tufts. We refer to this third possibility as tectorial-unattached.

Figure 1.2 (on next page): Illustration of the surface of the auditory organ of the alligator lizard (drawn by Anne Greene). The insets are cross sectional views of the patch taken from spots marked by the arrows. The auditory receptor organ consists of a patch of about 150 hair cells whose stereociliary tufts are aligned in rows. The hair cells in the upper portion of this drawing are free-standing in cochlear fluid. A tectorial membrane overlies hair cells in the tectorial region of the organ (nearest the bottom of the drawing). The receptor organ is on the basilar membrane (see insets); the organ and membrane form a portion of an epithelium that separates two fluid filled chambers. The organ is surrounded by a ring of connective tissue. The lines in the lower left corners of the insets and those to the left of the organ indicate schematically the nerve fibers that project to the sensory organ.

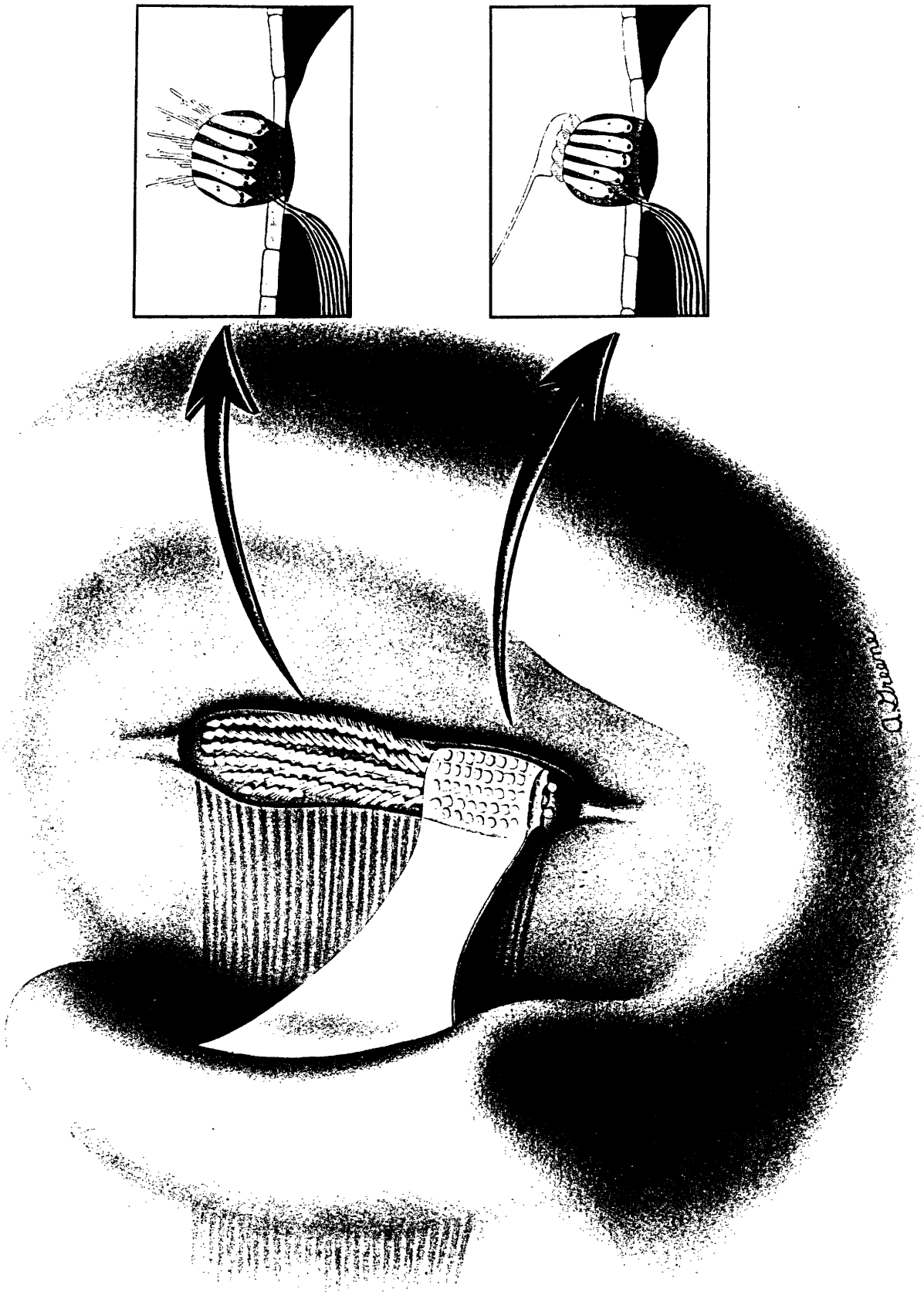

1.2 FUNCTIONAL SIGNIFICANCE OF MICROMECHANICS

In the previous section, we suggested that a variety of linkages generate forces on stereociliary tufts and thereby excite electrical responses from hair cells. In this section we describe ideas about the functional significance of these linkages.

1.2.1 EARLY IDEAS ABOUT MICROMECHANICS IN THE AUDITORY SYSTEM

The inner ear in mammals (Figure 1.3) is anatomically complex, and there are few direct observations of mechanical events within the inner ear. Based on functional interpretations of the structures, the observations of von Bekesy (1960) on cadaver ears, and a variety of indirect physiological studies, some concepts of the mechanism by which stereocilia are mechanically stimulated arose.

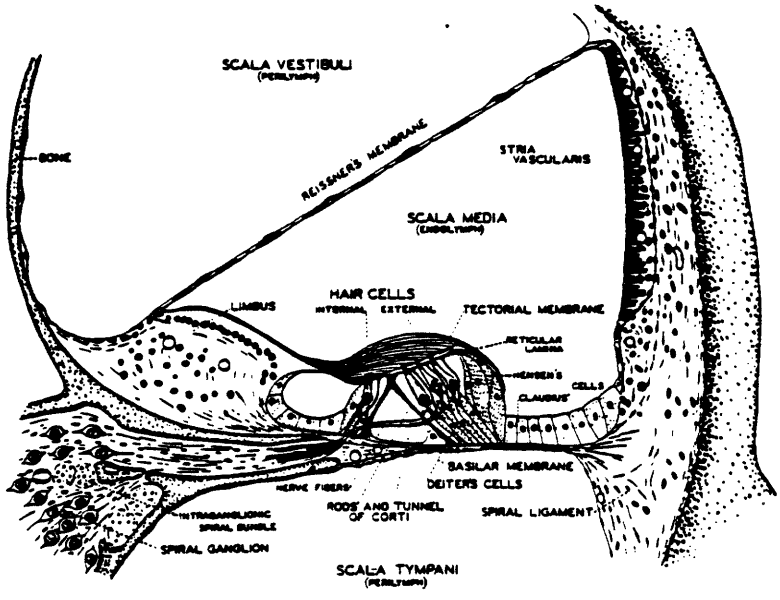

Figure 1.3: Schematized representation of a cross section through the inner ear of mammals (Davis, 1953). The inner ear (cochlea) is partitioned into three fluid filled chambers. Pressures are induced in the fluid of scala vestibuli by vibrations of structures in the middle ear (not shown) and cause motion of the basilar membrane. Auditory hair cells (marked internal and external hair cells) rest on the basilar membrane. The tectorial membrane comes in close contact with the tufts of auditory hair cells in mammals.

1.2.1.1 LEVER MODEL

In early models of cochlear function, the inner ear structures were thought to act as a lever system, so that motion of the basilar membrane would produce a shearing motion between the tectorial membrane and the surface of the hair cells (Figure 1.4). Stereocilia, presumably attached to opposing points on these two structures, were therefore bent. The mechanical properties of stereociliary tufts played no important role in such models (Johnstone and Johnstone, 1966; Rhode and Geisler, 1967).

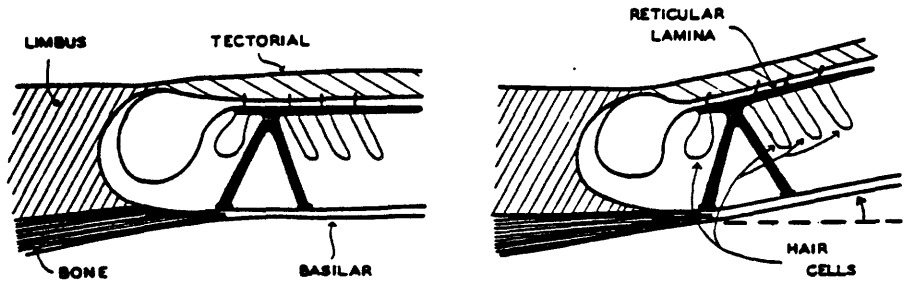

Figure 1.4: Illustration of the lever model of stereociliary tuft excitation (Davis, 1956). The left and right panels of this figure illustrate the changes in the positions of inner ear structures that were presumed to acompany deflection of the basilar membrane (labeled in left panel) if the inner ear structures moved as a lever system. The resulting shearing motion between the tectorial membrane and reticular lamina would deflect the tufts of hair cells, which were assumed to be attached to opposing points on these two structures.

1.2.1.2 VELOCITY SENSITIVE INNER HAIR CELLS AND DISPLACEMENT SENSITIVE OUTER HAIR CELLS

Electron microscopic studies of the tectorial membrane suggested that the longer stereocilia of outer hair cells contact the surface of the tectorial membrane while such contact does not occur for stereocilia of inner hair cells (Lim, 1971). This led to the conception that tufts of inner and outer hair cells move differently in response to motion of the basilar membrane (Dallos, Billone, Durrant, Wang, and Raynor, 1972). To explain briefly, since the stereocilia of outer hair cells are attached to the tectorial membrane, their deflection should be directly proportional to the relative displacement between the tectorial membrane and the surface of the hair cells. Since this relative displacement was taken to result from the action of a lever system of which both the tectorial membrane and the patch of sensory cells were a part, it followed that the response of outer hair cells would be linearly proportional to basilar membrane displacement. In contrast, if the stereocilia of inner hair cells are free-standing in cochlear fluid and do not come in contact with the tectorial membrane, their stimulation will result from viscous fluid drag. Since viscous drag is proportional to the difference between the velocity of the surface of the cells and the velocity of the tectorial membrane, it follows that the response of inner hair cells should be proportional to basilar membrane velocity.

This conception of the mechanism by which hair cells are mechanically stimulated was supported by a theoretical study of tuft motion (Billone and Raynor, 1973), to be described later, and by indirect measurements of the electrical activity of populations of hair cells (Dallos and Harris, 1978). These hypothesized mechanical modes of excitation have not been studied directly, and the evidence of tectorial attachment to stereocilia of inner and outer hair cells remains controversial.

1.2.2 OBSERVATIONS OF THE AUDITORY SYSTEM IN ALLIGATOR LIZARD

Studies of the auditory system of the alligator lizard demonstrate that stereocilia and their tectorial structures can play a more important role in the stimulation of hair cells than is implied by simple extensions of the lever model of Figure 1.4 (Weiss, Peake, Ling, and Holton, 1978). We briefly outline experimental evidence from the free-standing region of the auditory receptor organ of alligator lizard (Figure 1.2) that suggests that stereociliary tuft motion may contribute to a frequency selective function of that organ.

Discharges from nerve fibers that project to the auditory hair cells are most vigorous for a narrow range of acoustical frequencies. Nerve fibers that project to hair cells with free-standing stereocilia have tonotopically organized frequency selectivity (Holton and Weiss, 1983) -- i.e. fibers that project to the part of the free-standing region that is closest to the tectorial membrane respond most vigorously to acoustical frequencies near 1 kHz while fibers that project to the part of the free-standing region that is most distant from the tectorial membrane respond most vigorously to acoustical frequencies near 4 kHz.

Physiological observations of the receptor organ indicate that acoustical stimulation causes the receptor organ to move as a rigid body with a rocking motion about its long axis (Weiss, Peake, Ling, and Holton, 1978; Peake and Ling, 1980; Frishkopf and DeRosier, 1983). If all of the free-standing tufts responded to basilar membrane velocity, then their responses would be identical. Since a range of best frequencies is seen within the free-standing region, it is clear that frequency selective mechanisms operate at levels more microscopic than basilar membrane motion.

Microscopic observations of stereociliary tuft motion demonstrate that the displacements of stereociliary tufts that result from acoustical excitation are tonotopically organized (Frishkopf and DeRosier, 1983; Holton and Hudspeth, 1983). The lengths of the tallest stereocilia in a tuft also change systematically along the long axis of the patch of free-standing hair cells. The free-standing tufts nearest the tectorial region respond best to frequencies near 1 kHz and have tallest stereocilia on the order of 30 μm long. The free-standing tufts most distant from the tectorial membrane respond best to frequencies near 4 kHz and have tallest stereocilia on the order of 12 μm in length. These observations suggest that the frequency selective properties of cochlear neurons could in fact result from mechanical resonances of stereociliary tufts.

1.2.3 CONCLUSIONS

Sound stimuli from the external environment induces motion of the fluid filled inner ear structures and thereby excites sterociliary tufts of auditory hair cells. Indirect experimental evidence suggests that two different populations of hair cells in the mammalian auditory system respond differently to sound stimulation even though they are excited by the same basilar membrane motion. A simple theory has been proposed to account for these differences in terms of the way that relative motion of the tectorial membrane stimulates mechanical deflections of stereociliary tufts. Direct observations of free-standing tufts in the auditory organ of alligator lizard shows that tufts in that organ move most for a small range of frequencies and that the most sensitive frequencies correlate with stereociliary lengths. Thus there is a variety of experimental evidence that dynamical relationships, at the level of stereociliary tufts, play roles of functional significance.

In the next section, we review quantitative models of the mechanical excitation of hair cells.

1.3 PREVIOUS MODELS OF STEREOCILIARY MECHANICS

1.3.1 MODELS OF STEREOCILIARY MECHANICS IN MAMMALS

The idea that stereociliary tuft mechanics differ in inner and outer hair cells was quantified in a model that is illustrated in Figure 1.5 (Billone and Raynor (1973)).

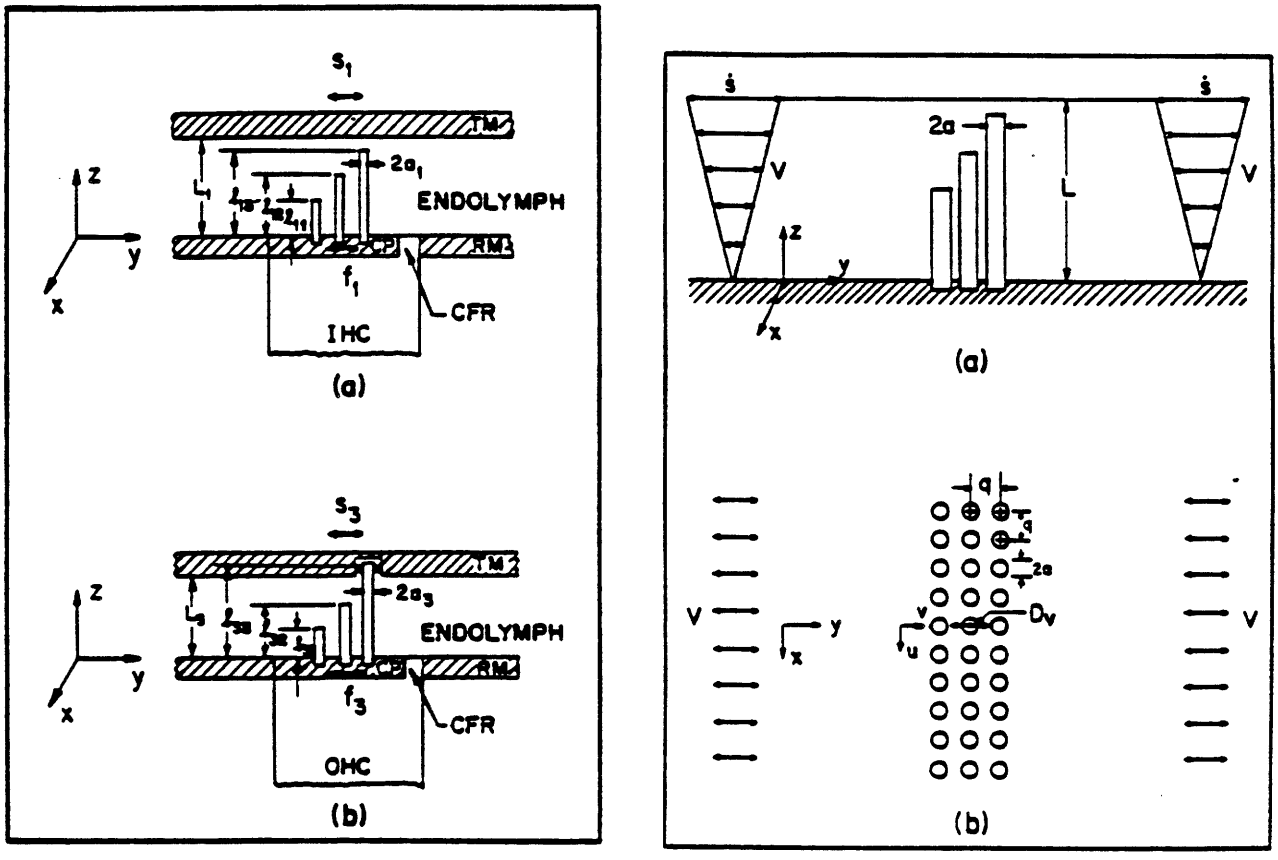

Figure 1.5: Model for mechanical excitation of inner and outer hair cells (Billone and Raynor, 1973). The left panels show cross sections through the tufts of an inner hair cell (IHC in (a)) and an outer hair cell (OHC in (b)). The crosshatched regions are plates representing the tectorial membrane (TM) and the reticular membrane (RM). The three vertical bars in each of (a) and (b) represent stereocilia of different lengths. Notice that the longest stereocilia in the outer hair cell model (b) penetrate the surface of the plate that represents the tectorial membrane. The top figure in the right panel illustrates that the model is excited by a velocity that is imposed on the tectorial plate ($\dot{s}$) that generates a linearly increasing velocity profile in the fluid that is very distant from the model stereocilia (V). The lower figure in the right panel illustrates (in a view from the tectorial plate) that the model consists of a rectangular array of cylinders that represent stereocilia. The radius of each cylinder is "a" and the centers of the cylinders are located on a rectangular grid separated by nearest neighbors by a distance "q". The double headed arrows illustrate the direction of fluid velocity (V).

1.3.1.1 DESCRIPTION OF THE MODEL

The surface of the sensory patch is modeled as a rigid flat plate (referred to here as the "basal" plate). Stereocilia are modeled as elastic cantilevered beams of circular cross section that are rigidly attached to a small portion of the basal plate, called the "cuticular plate". The tectorial membrane is modeled as a second rigid flat plate (referred to as the "tectorial" plate) whose plane is parallel to that of the basal plate. The longest cylinders in the outer hair cell model penetrate small openings in the tectorial plate. None of the cylinders in the inner hair cell model come into contact with the tectorial plate. The space between the two plates is filled by incompressible Newtonian fluid taken to model the cochlear fluid that surrounds stereociliary tufts.

Motion of the model is excited by a velocity that is imposed on the tectorial plate. Motion of the tectorial plate shears the fluid and generates a force on the cantilevered cylinders. The response of the model is taken as the force exerted on the cuticular plate.

The fluid motion was taken to be laminar so that increments of the model (in planes taken parallel to the x-y plane of Figure 1.5) could be analyzed as though they were cross sections through a uniform geometry. The force on each increment of the model was approximated by the force that is generated by steady fluid motion through a rectangular array of infinitely long cylinders (Miyagi, 1958). Forces dues to fluid inertia were ignored.

1.3.1.2 RESULTS FROM THE MODEL

The authors conclude from analysis of the model in Figure 1.5 that "inner hair cells are stimulated by a viscous force which is linearly proportional to, and in phase with, basilar membrane velocity. The outer hair cells are stimulated by a shear force which is linearly proprtional to, and in phase, with, basilar membrane displacement at low frequencies" (Billone and Raynor, 1973). Thus analysis of the model in Figure 1.5 suggests that mechanics at the level of stereociliary tufts have functional significance in the mammalian auditory system.

Analysis of the model in Figure 1.5 also suggests that particular features of stereociliary tuft morphology impact the motion of tufts that is generated by motion of the basilar membrane and tectorial membrane. Foremost is whether stereocilia contact the tectorial membrane, but other features were also identified as important. The response of the model in Figure 1.5 is a force that is due primarily to viscous drag in the narrow gaps between adjacent cylinders. For parameters chosen to model stereocilia in the guinea pig, the force that is imposed on a particular cylinder in a row of cylinders that is oriented perpendicular to the direction of fluid motion has a magnitude that is fifty times that which would be imposed on a single cylinder that is not a member of an array. Thus the presence of other stereocilia in a row causes a large increase in the drag experienced by a single stereocilium in the row.

While the existence of many cylinders in a row has a significant effect on the cylinder drag, the presence of more than one row has only a small effect. The average drag per cylinder decreases roughly 5% when the number of rows is changed from one to two. The average drag per cylinder decreases roughly 7% when the number of rows is changed from one to three. Thus analysis of the model in Figure 1.5 suggests that the motion of stereocilia is very sensitive to the detailed structure of "rows" of stereocilia that are perpendicular to the direction of fluid motion and less sensitive to the detailed organization of stereocilia parallel to the direction of fluid motion.

1.3.1.3 CONCLUSIONS

Recent experimental results suggests that a number of the assumptions of the model in Figure 1.5 are not reasonable. Stereocilia, for example, are represented as cantilevered beams with uniform elasticity. Direct microscopic observation of stereociliary motion however shows that stereocilia are stiff and pivot about their insertion (Flock, Flock, and Murray, 1977; Flock and Orman, 1983). Second, the response of the model was taken to be the shearing force on the cuticular plate. Measurements of the intracellular potentials that accompany direct micromanipulation of tufts suggest that the angular deflection of stereocilia is the important mechanical input to a hair cell (Hudspeth and Jacobs, 1979). These details of the model are however not likely to impact the conclusion that inner and outer hair cells respond differently to similar motions of the basilar and tectorial membranes.

More important to the conclusion that inner and outer hair cells respond differently to similar motions of the basilar and tectorial membranes is the method of analysis. The effect of the mass of the fluid was estimated by comparing the magnitudes of the viscous and inertial terms of the equations of motion for an incompressible viscous fluid. It was found that in the gaps between adjacent stereocilia, the magnitudes of viscous forces were likely to exceed the magnitudes of inertial forces by at least a factor of 10 over the interesting range of frequencies ($\omega < 10^5$ rad/sec). Based on this argument, the forces that result from the mass of the fluid were ignored, and the response of the model was estimated from a drag formulation of the hydrodynamical problem.

Bounding the magnitudes of inertial forces of fluid origin in the gaps between adjacent stereocilia does not bound the magnitudes of inertial contributions to the force on the cuticular plate however. Stereocilia are clustered in tufts and the spacing between tufts is significantly greater than the spacing between stereocilia. To estimate the magnitude of the inertial force of fluid origin that acts on a tuft, one must use dimensions that are characteristic of tufts. Estimates of the inertial contributions to the total force on a tuft suggests that inertial and viscous forces may in fact be comparable in magnitude. Thus the "conclusion" that inner hair cells (whose stereocilia do not come into contact with the tectorial membrane) are stimulated by a viscous force that is proportional to the velocity of the membrane should more correctly be called an "assumption".

1.3.2 MODELS OF STEREOCILIARY MECHANICS IN ALLIGATOR LIZARD

A model of auditory function in the free-standing region of the auditory organ of alligator lizard has been formulated (Weiss, Peake, and Rosowski, 1985; Rosowski, Peake, Lynch, Leong, and Weiss, 1985; Weiss and Leong, 1985a,b, 1986; Leong and Weiss, 1985), and the behavior of the model has been compared to physiological observations of:

1) motion of middle ear structures (Rosowski, Peake, Lynch, Leong, and Weiss, 1985),
2) basilar membrane motion (Peake and Ling, 1980),
3) stereociliary motion (Frishkopf and DeRosier, 1983; Holton and Hudspeth, 1983),
4) hair cell receptor potentials (Holton and Weiss, 1983a,b), and
5) discharges from cochlear neurons (Weiss, Mulroy, Turner, and Pike, 1976; Weiss, Peake, Ling, and Holton, 1978; Holton and Weiss, 1983b).

Stereociliary mechanics plays an important signal processing role in this model. Figure 1.6 illustrates the model of stereociliary tuft motion developed by Weiss and Leong (1985a).

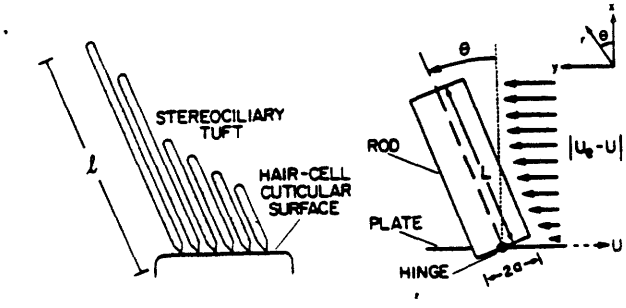

Figure 1.6: Model of stereociliary tuft motion in the free-standing region of the auditory organ of alligator lizard (taken from Weiss and Leong, 1985a). The left panel shows a schematized representation of a stereociliary tuft. The length of the tallest stereocilium in the tuft is "l". The right panel illustrates elements of the mechanical system that are used to model the motion of the stereociliary tuft in the left panel. A rod of length "L" and radius "a" is attached by a spring-loaded hinge to a flat plate. The entire structure is surrounded by fluid. The velocity of the fluid relative to the velocity of the plate depends on distance from the plate, and is indicated by the family of arrows whose lengths are proportional to the magnitude of the relative velocity. θ represents the angular displacement of the rod about its attachment at the hinge.

1.3.2.1 DESCRIPTION OF THE MODEL

The surface of the sensory patch is modeled as a rigid flat plate. The motion of a stereociliary tuft and a volume of cochlear fluid that is entrained to move with the tuft is approximated by that of a rod that is connected by a spring-loaded hinge to the plate. Motion of the model is excited by sinusoidal translation of the plate in its plane. The

vibration of the plate induces motion in the surrounding fluid. Torques on the rod, generated by the motion of the fluid that surrounds the rod (which exerts both viscous and inertial forces on the rod), by the spring, and by the moment of inertia of the rod cause an angular displacement of the rod about its hinged attachment to the plate.

Motion of the rod will entrain fluid in the neighborhood of the rod to move with the rod. The effect of this boundary layer of fluid on the motion of the rod is approximated by increasing the radius of the rod to encompass not only the space occupied by the tuft, but also that occupied by the boundary layer of fluid. The hydrodynamical torque on the rod is computed in an approximate manner. The fluid motion is approximated as laminar, in planes taken parallel to the plane of the plate. Very distant from the rod, the fluid velocity in each layer is presumed to be unaffected by the rod, so that its magnitude depends exponentially on the distance from the plate. The viscous torque that is generated on the rod by a particular layer of fluid is approximated by that which would be generated by steady motion of fluid past an increment of an infinitely long cylinder. The inertial torque that is generated on the rod is approximated by that which would be generated by an inviscid fluid on an increment of an infinitely long cylinder.

1.3.2.2 RESULTS FROM THE MODEL

The equation of motion that results from the analysis indicated above can be represented by a series resonant mechanical network. The compliance in the network results from the spring in the hinge. The mass in the network has contributions from both the mass of the rod and the mass of entrained fluid. The damping in the network results from the viscosity of the fluid. The frequency for which the angular displacement of the rod is greatest and the quality of tuning (Q_{3dB}) for the angular displacement of the rod depend on mechanical parameters of the tuft model. For parameters chosen to model free-standing tufts in alligator lizard, the frequency selectivity of the model for stereociliary tuft motion dominates that of the other components of the peripheral auditory model. Figure 1.7 shows results from the analysis of the peripheral auditory model along with measurements of neural spike activity taken from a physiological experiment.

The compliance of the spring that is required so that the frequency selectivity of the model approximates that of cochlear nerve fibers is within an order of magnitude of the static compliance that has been experimentally measured by a number of researchers (Orman and Flock, 1981; Strelioff and Flock, 1982; Ashmore and Russell, 1983). The damping that is required is consistent with a drag formulation of viscous loss (Johnson and Brokaw, 1979). The mass that is required however exceeds the mass of a tuft by more than an order of magnitude. The additional mass is consistent with the notion that a boundary layer of fluid will be entrained to move with the fluid -- so that the rod must occupy a volume that includes not only that of the tuft, but also that of the entrained fluid.

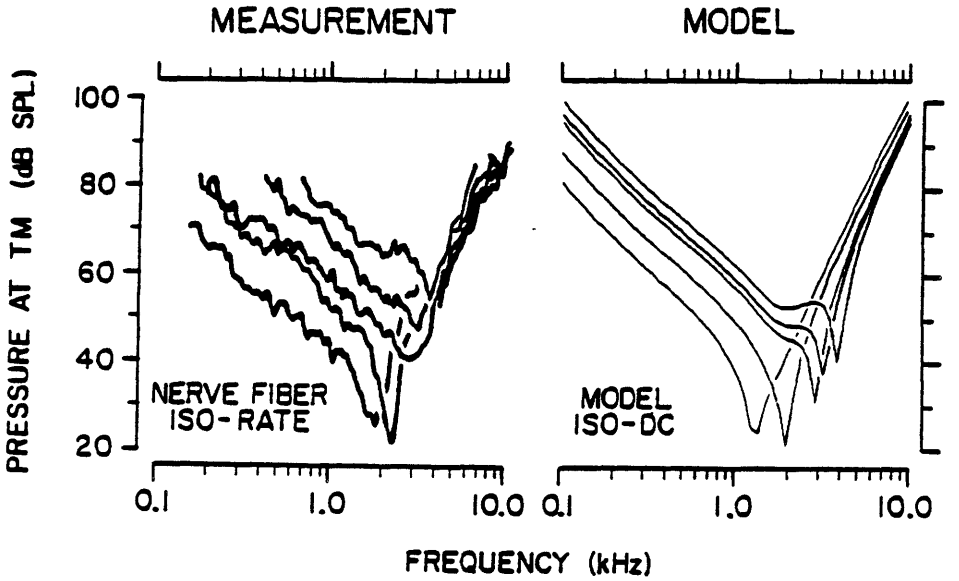

Figure 1.7: Comparison of the behavior of the peripheral auditory model with physiological observations (Weiss and Leong, 1985a). The left side of this figure plots nerve fiber iso-rate contours as a function of acoustical frequency for five different cochlear nerve fibers (Holton and Weiss, 1983). For each curve, the ordinate plots the magnitude of the pressure that is required at the tympanic membrane (in dB re 0.002 dynes/cm^2) to elicit a criterion discharge rate of action potentials on a single nerve fiber. Nerve fibers are most sensitive to acoustical excitations at a particular frequency. Fibers shown here are most responsive to roughly 1.9, 2.3, 3.0, 3.2, and 3.8 kHz. The right panel shows the response of the peripheral auditory model displayed in a fashion similar to the left panel. The different curves in the right panel illustrate the effect of varying the length of the rod in the micromechanical part of the model. The values of L used in the computation were (from left most curve to right most curve) 24, 18, 15, 13, and 12 μm.

1.2.2.3 CONCLUSIONS

The approximations that were made to simplify the analysis complicates interpretation of the results of the model in Figure 1.6. The laminar approximation to fluid motion is likely to be increasingly valid as the amplitude of the imposed velocity of the plate is decreased (see chapter 5). Within each laminate, the analysis is basically a boundary layer technique (Yih, 1979). No attempt is made to estimate the magnitude of the errors that result because the boundary layer thickness is large relative to the dimensions of the structure. To the extent that the radius of the rod includes the thickness of the boundary layer of fluid that is entrained to move with the rod, "a" should be a function of frequency. The model results in Figure 1.7 do not reflect this dependence.

1.4 SUMMARY

Indirect experimental evidence in the mammalian auditory system suggests that the hydrodynamical coupling between the tectorial membrane and stereociliary tufts is important in determining the response of hair cells to accoustical stimulation. This idea has been central to the interpretation of many physiological observations. Direct experimental observation of the motion of free-standing stereociliary tufts in the auditory system of the alligator lizard shows that stereociliary tuft dynamics play an important frequency selective role.

Theoretical understanding of hydrodynamics at the level of stereociliary tufts is limited. Analyses to date have dealt with the interaction between model tufts and fluid in only approximate fashions. Important theoretical questions about the hydrodynamics of tuft motion have not been addressed. For example, do hydrodynamics impose fundamental limits on the sharpness of mechancal resonances that are possible for free-standing tufts? Which morphological features of hair cell organs contribute most to hydrodynamical coupling between the motion of the tectorial membrane and stereociliary tuft motion?

In this thesis, we propose a series of studies to clarify the role of hydrodynamics in exciting stereociliary tuft motion and we carry out the first few of the studies.

CHAPTER 2
ON THE ROLE OF FLUID INERTIA AND VISCOSITY IN STEREOCILIARY TUFT MOTION: ANALYSIS OF ISOLATED BODIES OF REGULAR GEOMETRY

Stereociliary tuft displacement is the mechanical input to hair cells in the acoustico-lateralis system. In a system where we have extensive observations, the alligator lizard cochlea, stereociliary tuft motion is frequency selective and clearly contributes to the frequency selectivity and tonotopic organization observed in cochlear hair-cell and nerve-fiber responses (Weiss and Leong, 1985).

In this chapter, we examine the forces of fluid origin that act on stereociliary tufts. We assume that cochlear fluids are Newtonian and show that for physiological stimuli: fluid compressibility is negligible; convective non-linear inertial forces are small; and both viscous and linear inertial forces are appreciable.

To determine hydrodynamical limitations on frequency selectivity, we examine the frequency dependence of viscous and inertial fluid forces that act on isolated vibrating bodies of regular geometry in viscous, incompressible, Newtonian fluids (Stokes, 1851). The mechanical admittance of a system in which such a body is supported by springs shows a geometry-dependent resonance. This resonance has a quality (Q_{3dB}) that is less than 1 for an infinitesimally thin plate vibrating in its plane, but can be arbitrarily large both for a sphere and for a circular cylinder oscillating in a direction perpendicular to its long axis. From considerations of hair cells with free-standing stereocilia in alligator lizard cochlea we conclude that stereociliary tufts in the cochlea could exhibit a passive, mechancial resonance.

2.1 EQUATIONS OF MOTION FOR COCHLEAR FLUIDS

2.1.1 CONTINUUM HYPOTHESIS

Stereocilia are small structures. For example, the small stereocilia on mammalian outer hair cells have a length of 0.5 μm and a diameter of 0.1 μm (Saunders and Garfinkle, 1985). Nevertheless, stereocilia are large compared to water molecules: 1.3×10^8 molecules of water would fit in the volume occupied by one such outer hair cell stereocilium. We will therefore ignore the underlying molecular nature of the fluid and use continuum macroscopic hydrodynamic variables to characterize fluids.

2.1.2 NEWTONIAN FLUID

A Newtonian fluid has a uniform density and a viscosity that is both uniform and independent of direction. The motions of many fluids are adequately modeled by a Newtonian model, especially at low velocities. A Newtonian model accounts for the behavior of water, for example, except when the velocities approach the speed of sound (Batchelor, 1967, p. 146). Endolymph contains molecules other than water, however, including ions and proteins (Rauch and Rauch, 1974). Liquids composed primarily of elaborately chained molecules can have viscosities that depend on velocity, direction, and

even past history. Hydrodynamical modeling of even dilute solutions of such molecules has had limited success. Results are sensitive to the detailed molecular description of the fluid and are not easily generalized. Since knowledge of the material properties of endolymph is limited, and since the theoretical treatment of non-Newtonian fluids is difficult, we will represent cochlear fluids as Newtonian. The equation of motion of such fluids can be described in terms of the variables listed below.

$\bar{u}$	particle velocity	cm/sec	x	distance	cm
P	pressure	dynes/cm^2	t	time	sec
ρ	density	gm/cm^3	c	speed of sound	cm/sec
μ	viscosity	gm/cm-sec	f	frequency	Hz
$\nu=\mu/\rho$	kinematic viscosity	cm^2/sec	$\omega=2\pi f$	angular velocity	rad/sec

2.1.3 FLUID COMPRESSIBILITY IS NEGLIGIBLE

Fluid compression is one of several factors that can contribute to spatial variations of fluid velocity. If the gradient in velocity resulting from compression is small compared to the total gradient in velocity, the flow is approximately incompressible, and the analysis is simplified. Let U_c represent a characteristic particle-velocity difference between two points separated by L_c. The magnitude of the ratio of the compression-generated velocity gradient to total velocity gradient is less than the larger of U_c^2/c^2 and $\omega^2 L_c^2/c^2$ (Batchelor, 1967; p. 167). The length of the entire sensory epithelium in alligator lizard (4×10^{-2}cm) can be used as a conservative value for L_c. The velocity of the basilar membrane with high intensity acoustic stimulation (100 dB SPL) is roughly 1 cm/sec (Peake and Ling, 1980) which provides a value for U_c. The physiological range of excitation frequencies extends to $\omega\approx10^5$ rad/sec. We assume the velocity of sound in endolymph equals that in water, $c\approx1.5\times10^5$cm/sec. Thus $U_c^2/c^2 \approx 4\times10^{-11}$ and $\omega^2L^2/c^2 \approx 7\times10^{-4}$. Therefore, the compression-generated velocity gradient is likely to be less than 1/1000 of the total and cochlear fluids can be assumed incompressible.

2.1.4 VISCOUS FORCES AND LINEAR INERTIAL FORCES ARE IMPORTANT

The equations of motion for an incompressible, Newtonian fluid are:

$$\frac{D\bar{u}}{Dt} \equiv \frac{\partial\bar{u}}{\partial t} + \bar{u}\cdot\nabla\bar{u} = -\frac{1}{\rho}\nabla P + \nu\nabla^2\bar{u} \quad ; \quad \nabla\cdot\bar{u} = 0 \, . \tag{2.1}$$

The expansion of the material derivative, D/Dt, includes a nonlinear term that derives from the movement of fluid particles relative to a frame of reference that is fixed in space. Since such motion convects momentum, $(\bar{u}\cdot\nabla\bar{u})$ is often called the "convective nonlinearity".

The relative magnitudes of the terms in Equation (2.1) can be evaluated by expressing this equation in dimensionless variables. Let U represent the peak velocity magnitude, and L represent the smallest distance over which the velocity changes

significantly (e.g. by a factor of e). Scaling all velocities by U, all distances by L, and time by $1/\omega$, we define

$$\hat{u} = \bar{u}/U \; ; \quad \hat{x} = x/L \; ; \quad \hat{t} = \omega t \; . \tag{2.2}$$

Equation (2.1) becomes

$$\frac{L^2\omega}{\nu} \frac{\partial \hat{u}}{\partial \hat{t}} + \frac{UL}{\nu} (\hat{u} \cdot \hat{\nabla}\hat{u}) = - \frac{L}{\rho \nu U} \hat{\nabla} P + \hat{\nabla}^2 \hat{u} \; , \tag{2.3}$$

where $\hat{\nabla}$ denotes derivatives with respect to the new spatial scale. Equation (2.3) defines three dimensionless parameters,

$$R_l = L^2\omega/\nu \; ; \quad R_{nl} = UL/\nu \; ; \quad P_{ref} = \rho \nu U/L \; , \tag{2.4}$$

where P_{ref}, a scale factor for pressure, is a consequence of the choice of scale factors in Equation (2.2), and the two Reynold's numbers, R_{nl} and R_l, characterize the relative importance of inertia to viscosity for the nonlinear and the linear inertial terms, respectively.

When the boundary conditions are oscillatory, a spatial scale is also defined by the Stokes' boundary layer thickness

$$\delta = \sqrt{2\nu/\omega} \; , \tag{2.5}$$

whose significance is discussed below. We express R_l in terms of δ as follows:

$$R_l = 2 (L/\delta)^2 \; . \tag{2.6}$$

The velocity gradients that result from oscillation of an isolated body in an infinite fluid typically extend over distances (L) that are comparable to δ. For such isolated bodies, R_l is neither very large nor very small and neither viscous nor linear inertial terms can be ignored. To evaluate R_{nl}, let X represent the peak fluid-particle displacement, i.e. $X=U/\omega$. For $L=\delta$,

$$R_{nl} = 2 (X/\delta) \; . \tag{2.7}$$

Thus, for motions of isolated bodies, the magnitude of the nonlinearity in Equation (2.1) is proportional to the ratio of peak body displacement to boundary layer thickness. In the alligator lizard cochlea, displacements of free-standing stereocilia are estimated to be about 0.2 μm at 1 kHz for levels of about 80 dB SPL (Frishkopf and DeRosier, 1983; Holton and Hudspeth, 1983). At this frequency and level, δ is roughly 20 μm and R_{nl} is approximately 0.02. Thus there is a physiologically important range of levels for which R_{nl} is less than 0.02.

In summary, fluid compression is negligible, the convective nonlinearity is negligible except perhaps at high sound-pressure levels, and both viscous and linear inertial forces of fluid orgin are appreciable. Therefore, in subsequent analyses, we have used Equation (2.1) and omitted the convective nonlinear term.

2.2 FLUID FORCES ON ISOLATED BODIES OF REGULAR GEOMETRY

The mechanisms by which fluids generate both inertial and viscous forces on moving bodies can be understood by considering bodies of regular geometry. We assume that the bodies are supported by massless springs as shown in Figure 2.1a. First imagine the bodies in a perfect vacuum. If the bodies are perturbed, they will oscillate forever at a natural frequency determined by their mass and the compliance of the springs. The differences in geometry of these bodies play no role in determining their motion. Next imagine the bodies immersed in a fluid that is both incompressible and inviscid. To the extent that the plate is infinitesimally thin -- the plate's motion, which is parallel to its surface, displaces no fluid. Since the fluid is inviscid, the is no frictional force on the plate. Hence, the motion of the plate is the same as in a vacuum. The cylinder however, in order to move at all, must push some fluid out of its path (Figure 2.1b). In contrast to the plate, the cylinder experiences an inertial force due to the mass of the fluid. That is, the springs must accelerate an effective mass that consists of the mass of the cylinder plus the mass of some fluid. Motion of the sphere similarly displaces fluid, however the resulting pattern of fluid motion is different, and therefore the mass of fluid that is effectively coupled to the sphere differs from that coupled to a cylinder. Because there is no frictional force, the cylinder and sphere will oscillate forever if perturbed, but at frequencies that are lower than their resonant frequencies in a vacuum. In summary, immersing these bodies in an inviscid fluid generates a geometry dependent inertial load on the bodies.

Now consider how a viscous fluid affects the motion. When the plate is displaced (Figure 2.1c), the fluid in its neighborhood is dragged along -- but this fluid also has inertia. Thus, while an inviscid fluid has no effect on the motion of the plate, a viscous fluid produces both viscous and inertial forces. These forces give rise to a layer of fluid, the boundary layer, that is sheared by the relative motion of the plate and the distant, motionless fluid. Thus, the boundary layer increases the effective mass of the plate, but as we shall see, the inertial and viscous forces on the plate are equal. Thus the system is highly damped so that a transient displacement of the plate is quickly damped out and a high quality resonance does not occur. With the cylinder (Figure 2.1d) and the sphere, the boundary-layer effect is combined with the inertial effect that occurs in an inviscid fluid. Fluid near the cylinder is entrained by the viscous forces to move with the cylinder, and the motion of the resulting somewhat larger effective cylinder pushes fluid out of its path. We shall see that unlike the plate, the sharpness of the resonance for the cylinder and the sphere is not limited and is determined by their dimensions as well as by the boundary layer thickness.

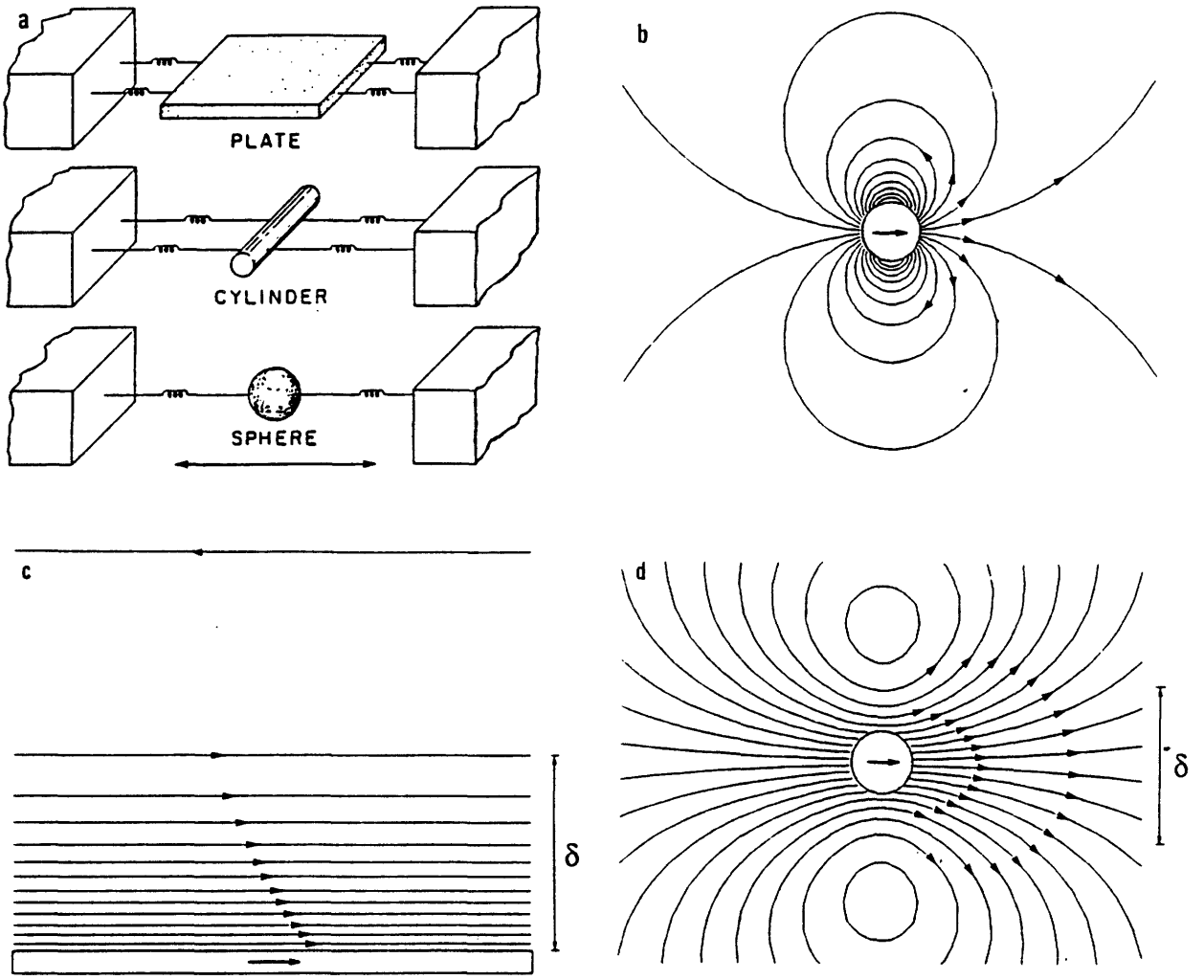

Figure 2.1: (a) Bodies of regular geometry -- a flat plate, a circular cylinder, and a sphere -- are connected by springs to rigid supports. Motion of these bodies in the direction of the arrow is considered when the bodies are immersed in various fluids. Streamlines (lines drawn parallel to the direction of fluid motion with a density proportional to the magnitude of the fluid velocity) depict the fluid motion that results from sinusoidal oscillation of: a cylinder in an inviscid fluid (b), a plate in a viscous fluid (c), and a cylinder in a viscous fluid (d). For clarity, the springs and supports have been omitted in (b), (c), and (d). The streamlines are obtained from exact solutions of the equations of motion for the fluid (Stokes, 1851). These streamlines change with time. The arrow on each streamline in (b), (c), and (d) indicates the direction of fluid particle motion at the time of maximum body velocity in the direction indicated by the arrow on the body. The vertical arrows in (c) and (d) indicate the thickness of the boundary layer δ.

2.2.1 IMPEDANCE OF FLUID LOAD ON ISOLATED BODIES OF REGULAR GEOMETRY

The forces of fluid origin that act on each of the bodies of Figure 2.1 can be characterized quantitatively by an impedance. For the plate, the impedance is defined as the ratio of the force exerted by the fluid on a unit area of the plate to the plate velocity, and is

$$Z_p = \mu\sqrt{\pi f/\nu}\,(1+j)\ , \tag{2.8}$$

where $j=\sqrt{-1}$. For a sphere of radius a, the impedance is defined as the ratio of the force exerted by the fluid on the sphere to the sphere velocity. Let $f_a=\nu/\pi a^2$, then (Stokes, 1851)

$$Z_s = 6\pi a\mu\left[\,(1+\sqrt{f/f_a}) + j\sqrt{f/f_a}\,(1+2/9\sqrt{f/f_a})\right]\ . \tag{2.9}$$

For a cylinder of radius a, the impedance is defined as the ratio of the force exerted by the fluid per unit length of cylinder to the cylinder velocity. No simple mathematical expression is available for Z_c, but it can be evaluated by series approximations (Stokes, 1851).

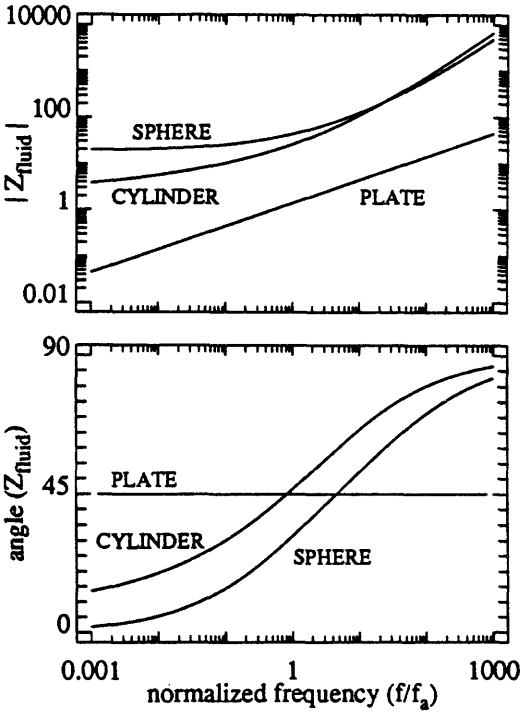

Figure 2.2: Normalized impedance of the fluid load on a plate, a cylinder, and a sphere as a function of normalized frequency f/f_a. Since $f/f_a=(a/\delta)^2$, these plots also show the dependence of the impedance on the ratio of the radius (of the cylinder and sphere) to the boundary layer thickness. The upper panel shows the magnitude of the impedance and the lower panel shows the angle of the impedance in degrees. In order to plot the impedance of the plate in the same coordinates as the other bodies we note that Equation (2.8) can be written as $(a/\mu)Z_p=\sqrt{f/f_a}\,(1+j)$. The curves labelled PLATE describe $(a/\mu)Z_p$. The curves labelled CYLINDER describe $(1/\mu)Z_c$. The curves labelled SPHERE describe $(1/(a\mu))Z_s$.

Z_p, Z_c, and Z_s have magnitudes that increase with frequency and angles that vary between 0^o and 90^o (Figure 2.2). Although these impedances have both viscous (resistance) and inertial (mass) components, none of the three is the impedance of a constant resistance in series with a constant mass. The impedance of the plate has a magnitude that increases at 10 dB/decade and an angle that is 45^o for all frequencies, i.e. the viscous and inertial components of the impedance have the same magnitude at each frequency and both have a magnitude that increases as $\sqrt{f}$. Therefore, as frequency increases the resistance increases while the mass decreases. The mass decreases because the boundary layer thickness decreases with increasing frequency (Equation (2.5)) and hence the mass of fluid entrained to move with the plate decreases. In contrast to the plate, both the cylinder and sphere behave as constant resistances at low frequency and as constant masses at high frequencies. Consider the impedance of the sphere. At low frequencies, Z_s approaches the constant resistance $6\pi a\mu$; a result known as "Stokes' law". As frequency increases, Z_s approaches $j2\pi f(2/3\pi a^3\rho)$ which is the impedance of a mass equivalent to half the mass of fluid that has the volume of the sphere. The impedance has an angle of 45^o at a normalized frequency that equals 4.5, i.e. at a frequency for which the boundary layer thickness equals about twice $(3/\sqrt{2})$ the radius of the sphere. The impedance of the cylinder has some similarities to that of the sphere. As frequency increases, Z_c approaches $j2\pi f(\pi a^2\rho)$ (Stokes, 1851), the impedance of a mass that equals the mass of fluid whose volume equals that of the cylinder. For the low frequencies shown, the impedance approaches that of a resistance. The impedance has an angle of 45^o at a normalized frequency of 1, i.e. at a frequency for which the boundary layer thickness just equals the radius of the cylinder. To summarize, when the dimensions of the cylinder or sphere are much larger than the boundary layer thickness, the fluid exerts a predominantly inertial force on the body. When the boundary layer thickness exceeds these dimensions, the fluid exerts a predominantly viscous force.

2.2.2 FREQUENCY-SELECTIVE MOTION OF ISOLATED BODIES OF REGULAR GEOMETRY

Motion of the bodies in Figure 2.1 is determined by the body masses, by forces of fluid origin, by forces from the spring attachments, and by externally applied forces. These systems can resonate. Figure 2.3 shows the ratio of body velocity to externally applied force (a mechanical admittance). Each of the admittances displayed in Figure 2.3 shows frequency selectivity. At sufficiently low frequencies in all cases, the admittance has a magnitude that increases with frequency at a rate of 20 dB/decade and an angle that approaches 90^o, i.e. the admittance approaches the admittance of the spring. As frequency increases, the magnitude of the impedance of the spring decreases and the magnitude of the impedance of both the body mass and fluid load (Figure 2.2) increases. Hence, at high frequencies, the admittance of the plate system has a magnitude that decreases at 10 dB/decade of frequency and an angle that approaches -45^o. This is the

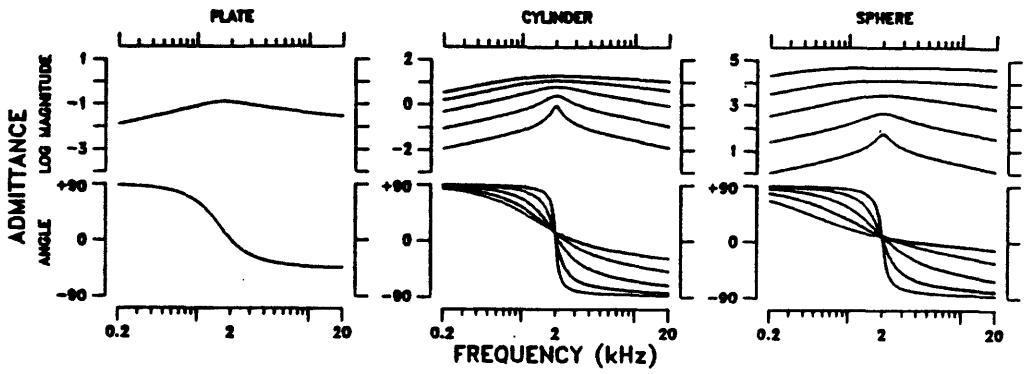

Figure 2.3: Frequency selectivity of spring-loaded bodies in fluid. Magnitude and angle of the: plate velocity that results from applying one unit of force per unit area of the plate; cylinder velocity that results from applying one unit of force per unit length of the cylinder; sphere velocity that results from applying one unit of force to the sphere. The different curves shown for the cylinder and sphere correspond to different radii -- 1, 3.16, 10, 31.6, and 100 μm. The smaller radii correspond to magnitudes and angles that have more broadly tuned frequency responses. The density of both the cylinder and sphere is equal to the density of the fluid. The spring constants were chosen so that the response magnitudes had peaks at 2 kHz. The spring constants were: for the plate -- 10^5 dynes/cm^3; for the cylinder (in order of increasing radius) -- 3.6×10^2, 7.9×10^2, 2.6×10^3, 1.4×10^4, and 1.1×10^5 dynes/cm^2; for the sphere (in order of increasing radius -- 5.6×10^{-2}, 0.39, 3.6, 52, 1.2×10^3 dynes/cm.

admittance of the fluid load. The situation is more complex for the cylinder and sphere. As frequency increases, there is a frequency at which the magnitude of the admittance of the spring equals that of the combined body mass and fluid load. If at that frequency, the combined (body mass and fluid load) impedance is predominantly resistive, then the system admittance is broadly tuned as occurs for the smaller bodies. Alternatively, if at that frequency the combined impedance is predominately inertial, then the system admittance shows sharp tuning as occurs for the larger bodies. The sharpness of tuning increases with increasing radius for both the cylinder and sphere (Figure 2.4). Q_{3dB} is less than 1 for the plate but exceeds 1 for cylinders with radii greater than 10 μm and for spheres with radii exceeding 18 μm.

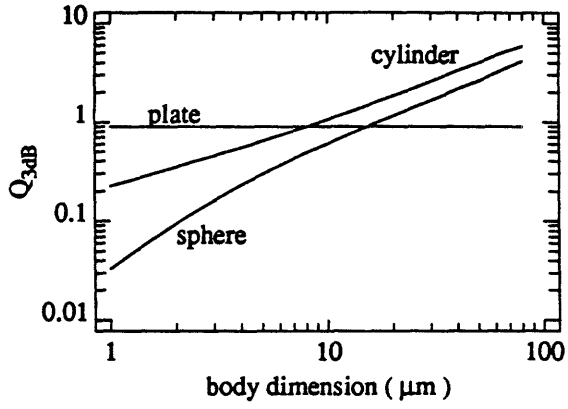

Figure 2.4: Quality of tuning as a function of radius. The curved lines show the dependence of Q_{3dB} on radius for the responses shown in Figure 2.3 for the cylinder and sphere. Q_{3dB} for the plate is 0.9. Q_{3dB} is defined as the ratio of the frequency of maximal response divided by the bandwidth 3 dB below the maximum admittance magnitude.

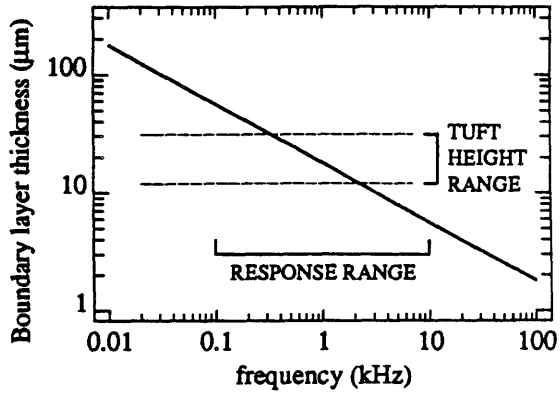

Figure 2.5: Boundary layer thickness δ in water as a function of frequency. Indicated are both the range of tuft heights (the length of the longest stereocilium in the tuft) for hair cells that have free-standing stereocilia in the alligator lizard cochlea (Mulroy, 1974) and the frequency range of physiological responses obtained from hair cells and cochlear neurons projecting to these hair cells (Holton and Weiss, 1983).

2.3 DISCUSSION

Newtonian fluids impose both viscous and inertial forces on isolated bodies. The magnitude of the inertial force exceeds that of the viscous force if the boundary layer thickness is smaller than the dimensions of the body (Figure 2.2). The potential for a high quality resonance of an isolated, spring-loaded body of arbitrary geometry can be assessed qualitatively by comparing its dimensions to the boundary layer thickness. Since tuft heights are comparable to boundary layer thickness (Figure 2.5), appreciable viscous and inertial fluid forces will act on stereociliary tufts. Furthermore, isolated bodies with dimensions comparable to these tufts can resonate (Fgure 2.4) with frequency selectivities comparable to the frueqency selectivity observed in responses from alligator lizard cochlear neurons (Holton and Weiss, 1983). Thus it appears possible that stereociliary tufts are mechanically resonant systems. However, the sharpness of frequency selectivity depends on geometry, and tufts differ appreciably from the isolated bodies of regular geometry that we have considered. First, tufts are not solid bodies but are composed of tens of stereocilia spaced about 1 μm apart. However, the inter-stereociliary distance is much smaller than the boundary layer thickness indicated in Figure 2.5. We therefore expect that viscous forces alone will tend to couple stereocilia so that they will move in unison, i.e. on fluid dynamic grounds we expect that the tuft will act as a rigid body. Second, tufts are not isolated bodies. They protrude from the receptor surface which has considerable spatial extent. The effect of this surface on the motion of the tufts has not been considered here. Also the distance between tufts of neighboring hair cells is of the order of 10 μm and is thus comparable to the boundary layer thickness. Therefore, it is likely that appreciable mechanical coupling through the intervening fluid exists between neighboring tufts. If we are to further understand the mechanics of even the relatively simple free-standing stereociliary tufts, we will need to better understand both the effects of the receptor surface and of neighboring tufts on the motion of a stereociliary tuft.

CHAPTER 3
ISOLATING THE KINEMATICALLY IMPORTANT FEATURES OF MICROMECHANICAL MORPHOLOGY

The morphology of hair cell organs is complex from the perspective of hydrodynamical analysis. We exploit the knowledge that hair cells are physiologically responsive to shearing motion of their stereociliary tufts to simplify the geometry that we analyze. A number of key features of micromechanical systems become clear in the process of simplification that constitutes the first part of this chapter. In the second part of this chapter, we define a sequence of geometries that isolate these key features in very simple hydrodynamical contexts.

3.1 SIMPLIFYING THE GEOMETRY

In this section, we illustrate a sequence of simplifications of hair cell morphology that leads to a geometry for which hydrodynamical analysis is possible. The goal is to generate a model whose relationship to hair cell morphology is clear, and whose hydrodynamical behavior can be fully determined.

3.1.1 EXCITATION OF TUFT MOTION BY FLUID SHEAR

Experimental observations show that hair cells are mechanically sensitive to shearing motions of their stereociliary tufts (Hudspeth and Jacobs, 1979). Both mechanical connections with tectorial structures and motion of nearby fluids generate shearing forces on stereociliary tufts. In this section we suggest simple models for the shearing forces on tufts that result from their hydrodynamical coupling to moving structures.

3.1.1.1 MODELS OF FREE-STANDING STEREOCILIARY TUFTS

The simplest class of micromechanical models is motivated by lizards, whose free-standing stereociliary tufts are presumably deflected by hydrodynamical forces alone. Physiological observations (Weiss, Peake, Ling, and Holton 1978; Peake and Ling, 1980; Frishkopf and DeRosier, 1983) indicate that acoustical excitation induces the auditory receptor organ of alligator lizard to move as a rigid body in a rocking fashion about its long axis. The rocking motion of the receptor organ drags free-standing stereociliary tufts of hair cells through the surrounding fluid and thereby deflects the tufts (Figures 1.2 and 3.1). It is thus the shearing motion of the nearby fluid that tends to deflect free-standing stereociliary tufts. The geometry can be simplified and this shearing motion preserved if we consider a group of tufts attached to a plate that is vibrated in pure translation (Figure 3.2).

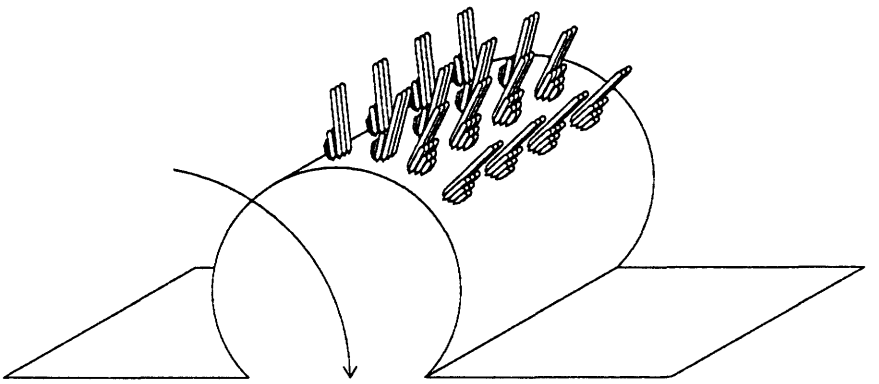

Figure 3.1: Rocking motion of the receptor organ that results from deflection of the basilar membrane. This figure is a schematic representation of a cross sectional portion of the sensory patch illustrated in Figure 1.2. The flat margins represent the basilar membrane. The curved arrow illustrates the motion of the patch that is induced by deflection of the basilar membrane. Each of the 16 bodies represents a single stereociliary tuft.

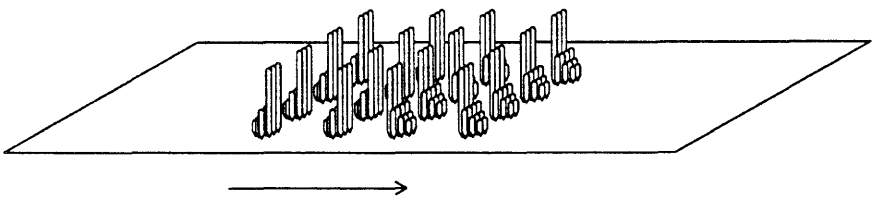

Figure 3.2: Translational approximation of the motion of the receptor organ that results from deflection of the basilar membrane. The plate in this figure represents a planar approximation of the surface of the receptor organ schematized in Figure 3.1. The straight arrow indicates translation of the plate.

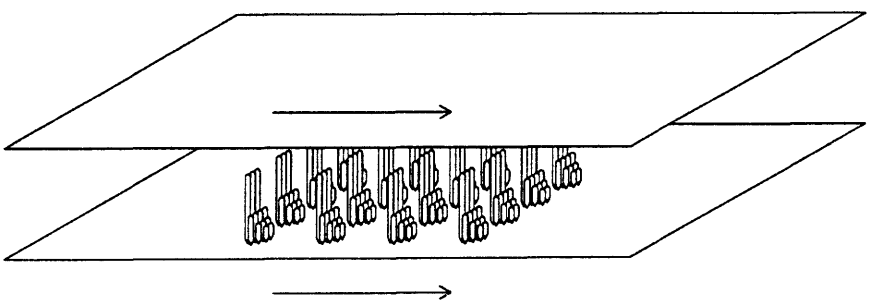

Figure 3.3: Two plate model for the excitation of stereociliary tuft motion. The model of Figure 3.2 is combined in this figure with a rigid plate that overlies but does not directly contact the stereociliary tufts. The external excitation of stereociliary motion is represented in this model by the velocities that are imposed on the two plates.

3.1.1.2 MODELS OF TUFTS WITH UNATTACHED TECTORIAL MEMBRANES

A second class of micromechanical models is motivated by the hypothesis that the inner hair cells of mammals do not come into contact with the tectorial membrane with which they are in close proximity. The shearing motion of the fluid in the model of Figure 3.3 is excited by velocities imposed on two plates. We will usually refer to the velocity that is imposed by the external stimulus on the plate to which the bodies are attached as the "basal velocity" (with reference to the basilar membrane) and the velocity that is imposed by the external stimulus on the overlying plate as the "tectorial velocity".

3.1.2 MECHANICAL MODELS OF STEREOCILIARY TUFTS

When a stereociliary tuft is displaced by micromanipulation with a glass fiber or by a jet of water, the entire tuft which consists of many stereocilia moves as a unit, pivoting about the base of the tuft (Flock et al., 1977; Flock and Orman, 1983; Flock and Strelioff, 1984). This suggests that one might approximate the motion of an entire tuft by that of a single rigid body. The argument for such an approximation is made even stronger by considering the effect of viscous coupling through the fluid. Neighboring stereocilia within a tuft are closely spaced -- with inter-stereociliary distances that are very small fractions of a micrometer. Boundary layer thicknesses (chapter 2) are larger than a micrometer in water for all frequencies of excitation less than about 100 kHz (a very high frequency relative to the frequencies for which hair cell systems generally respond). Thus viscous mechanisms alone will tend to entrain individual stereocilia within a tuft to move as a unit. The rigid body approximation to the motion of entire stereociliary tufts is illustrated in Figure 3.4.

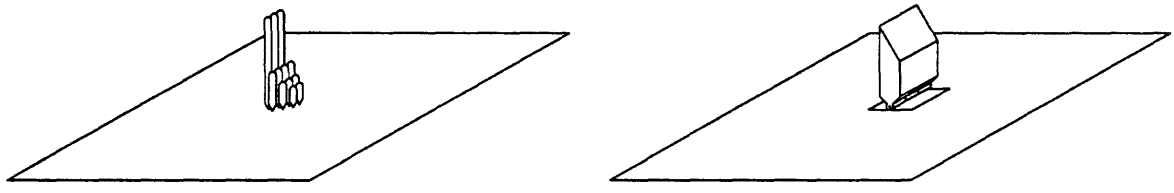

Figure 3.4: Rigid body approximation to a stereociliary tuft. The left panel schematically depicts a single stereociliary tuft which is composed of many (in this case 12) individual stereocilia. The right panel illustrates a rigid body that is attached to a flat plate by a hinge. The mechanical system on the right is used as a model of an entire tuft for the purpose of analyzing tuft motion.

If after deflecting a stereociliary tuft by micromanipulation or with a jet of water the external stimulus is removed, the tuft tends to return to its initial position (Orman and Flock, 1981; Ashmore and Russell, 1983; Strelioff and Flock; 1984). This indicates that the attachment of stereocilia to the surface of the patch is compliant. We model this compliance by loading the hinge in Figure 3.4 with a torsional spring.

3.1.3 SUMMARY

In this section we have proposed several simplifications of the morphology of hair cell systems for the purpose of studying the hydrodynamical effects of the fluid that surrounds stereociliary tufts. The receptor surface is treated as a a flat plate. The entire tuft of a hair cell is treated as a single rigid body that is attached to the basal plate with a spring-loaded hinge. We propose to study the role of the tectorial membrane in inducing fluid forces on tufts by surmounting the basal plate with a parallel tectorial plate.

We characterize the stimulus of the model by specifying the velocities imposed on the basal and tectorial plates. We characterize the response of the model by the angular displacement of the rigid body that represents a particular tuft.

The class of models that result from the simplifications in this section are still complex from the perspective of hydrodynamical analysis. All of the parameters -- the size and shape of each body, the number of bodies, the spatial organization of the bodies, and the distance between the plates -- will conceivably impact the angular displacements of all of the rigid bodies. In the next section we isolate key features of the models for closer study.

3.2 ISOLATING KEY FEATURES OF MICROMECHANICAL SYSTEMS

The previous sections suggest that it would be helpful to understand some canonical micromechanical models in order to develop an understanding of stereociliary tuft mechanics. These canonical models are described in this section.

3.2.1 ISOLATED RIGID BODIES VIBRATING IN A NEWTONIAN FLUID

In chapter 2, we investigated the motion of isolated bodies of regular geometry immersed in a Newtonian fluid. This illustrated the role of fluid inertia and viscosity in a particularly simple context. Stereociliary tufts are not isolated bodies however. The models in the next few sections isolate key geometric features of micromechanical systems.

3.2.2 RIGID BODIES ATTACHED TO A VIBRATING PLATE

The surface of the receptor organ from which stereociliary tufts protrude has considerable spatial extent (relative to the tuft) and is therefore likely to play an important role in determining the motion of a tuft. The next class of models include a plate that represents that receptor surface (Figure 3.2).

3.2.2.1 SINGLE RIGID BODY ATTACHED TO A PLATE BY A SPRING-LOADED HINGE

Figure 3.5 defines a simple class of models for exploring the effect of the basal plate. A single rigid body is attached to the basal plate with a spring-loaded hinge. Motion of the model is stimulated by translation of the plate in its plane. The response of the model is the angular displacement of the body about its hinged attachment to the plate. The body in Figure 3.5 might represent an isolated stereociliary tuft.

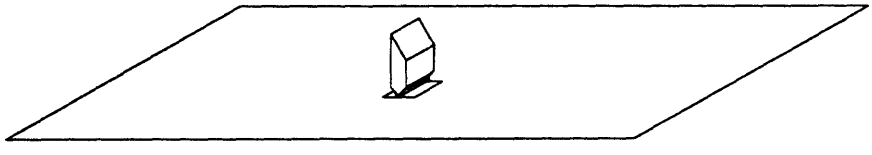

Figure 3.5: Single rigid body attached to a plate by a spring loaded hinge. The plate has infinite spatial extent and the entire structure is surrounded by fluid.

3.2.2.2 RIGID FLAP ATTACHED TO A PLATE BY A SPRING-LOADED HINGE

Hydrodynamical analysis of structures that are essentially two dimensional is considerably easier than analysis of three dimensional structures. Figure 3.6 illustrates an infinitely long rigid flap that is induced to rotate about its hinged attachment to the basal plate by hydrodynamical forces induced in the fluid by vibration of the basal plate. The drawing in Figure 1.2 correctly represents the organization of the free-standing stereociliary tufts in alligator lizard in long rows along the long axis of the receptor organ. The flap model might therefore represent an single row of stereociliary tufts.

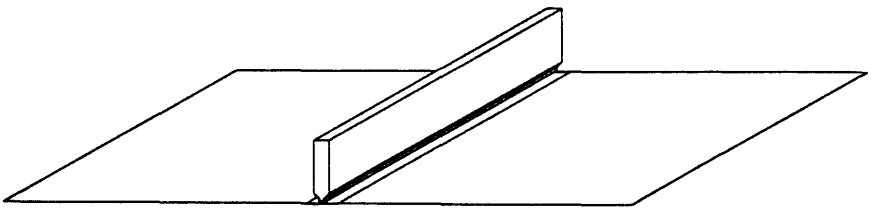

Figure 3.6: Single rigid flap attached to a plate by a spring loaded hinge. This figure illustrates a section of an infinitely long flap that is attached by a hinge (with infinite length) to an infinite flat plate. The entire structure is surrounded by fluid.

3.2.2.3 MULTIPLE RIGID BODIES ATTACHED TO A PLATE BY SPRING-LOADED HINGES

Stereociliary tufts generally occur in clusters. Figure 3.7 illustrates a class of models in which many rigid bodies are each attached to a plate by a spring-loaded hinge. Each of the bodies represents a single tuft. The motion of a particular body in the "multiple body" model is determined not only by its mechanical properties but also by the properties of the other bodies. Analysis of the multiple body model can thus address interactions between tufts.

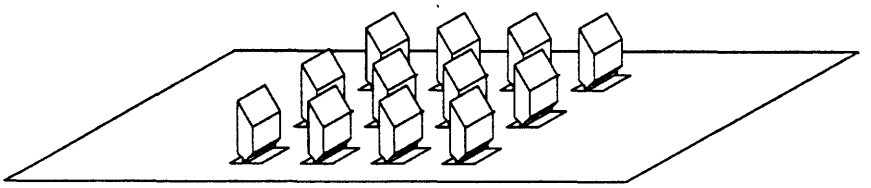

Figure 3.7: Multiple rigid bodies attached to a plate with spring-loaded hinges. Each of the 12 bodies in this figure represent one stereociliary tuft. Each body is attached to the plate by a spring-loaded hinge. The entire structure is surrounded by fluid.

3.2.3 MODELS WITH NEARBY BUT UNATTACHED TECTORIAL PLATES

Including a tectorial plate (Figure 3.3) in each of the preceding models results in structures that are illustrated in Figures 3.8-3.10.

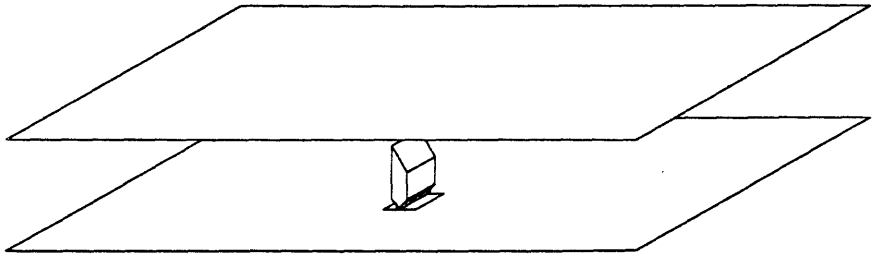

Figure 3.8: Single rigid body attached to a basal plate with a spring loaded hinge and in close proximity with but not attached to an overlying tectorial plate. The space between the plates is filled by fluid.

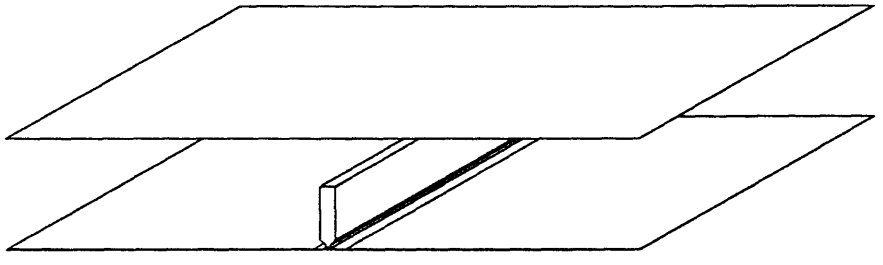

Figure 3.9: Single rigid flap attached to a basal plate with a spring loaded hinge and in close proximity with but not attached to an overlying tectorial plate. This figure illustrates a section of in infinitely long flap connected by an infinitely long hinge to a flat plate of infinite extent. The space between the plates is filled by fluid.

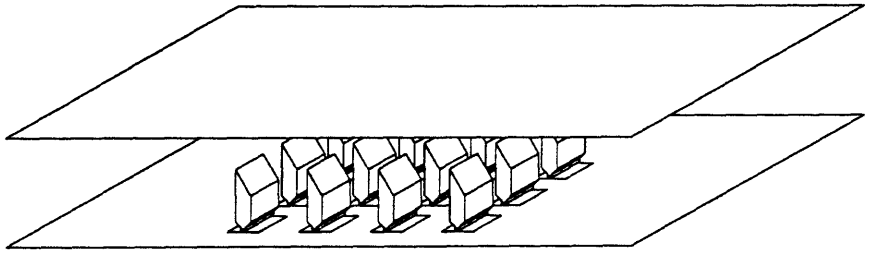

Figure 3.10: Multiple bodies attached to a basal plate with spring-loaded hinges and in close proximity with but not attached to an overlying tectorial plate. The space between the plates is filled by fluid.

3.3 MODELS STUDIED IN THIS THESIS

A thorough understanding of the canonic micromechanical models of section 3.2 is essential if we are to understand the micromechanics of hair cell organs. In this thesis we analyze the first few of these canonic models.

In chapter 2, we used the results of Stokes to characterize the motion of isolated, spring-loaded bodies of regular geometry (Figure 2.1). Because of the simplicity of this model, we were able to completely characterize the range of behaviors that are possible for this model.

In chapters 4, 5, and 6, we study the motion of the hinged body model of Figure 3.8. In chapter 4, we develop equations of motion for that model, and show that the solution to those equations can be understood in terms of a lumped parameter model (circuit model) for motion. In chapters 5 and 6, we determine expressions for the angular displacement of the body that is induced by asymptotically low and asymptotically high frequencies of plate vibrations. We show that the asymptotic frequency dependence of the angular displacement of the body is insensitive to the shape of the rigid body. The results of chapters 4, 5, and 6 qualitatively describe the hydrodynamics of the hinged body model of Figure 3.8 for all possible body shapes.

In chapters 7 and 8, we study the motion of the free-standing hinged flap in Figure 3.6. In chapter 7, we show special properties of the equations of motion for that essentially two-dimensional structure that simplify analysis. In chapter 8, we use a numerical method to completely characterize the angular displacement of the free-standing flap that is induced by translation of the plate. The results of chapters 7 and 8 quantitatively characterize the motion of the free-standing hinged flap in Figure 3.6.

CHAPTER 4
EQUATIONS OF MOTION FOR A RIGID BODY THAT IS ATTACHED TO A VIBRATING PLATE WITH A SPRING LOADED HINGE

Newtonian fluids impose both viscous and inertial forces on vibrating bodies. The hydrodynamical impedance imposed on spring-loaded bodies of regular geometry that are isolated in an infinite fluid can produce a mechanical resonance with a sharpness of frequency selectivity that depends on the geometry of the body (chapter 2). We seek to characterize the effect of nearby fluid on the motion of stereociliary tufts however, and stereociliary tufts are not isolated bodies. They protrude from a receptor surface which has considerable spatial extent and are often in close proximity to tectorial structures. In the remaining parts of this thesis, we investigate simple models that include not only bodies that represent tufts but also plates that represent nearby surfaces (chapter 3).

In the remaining chapters of this thesis, we analyze the motion of a rigid body that lies in a fluid filled region that is bounded by two parallel plates (Figure 4.1). We take the rigid body as a model for stereociliary structures. It is attached to a "basal" plate, which we take as a model for the surface of the epithelium from which stereociliary structures project, with a hinge. The hinge is spring loaded so that angular displacements of the rigid body are resisted by a torque that grows linearly with angular displacement. The rigid body is surmounted by, but does not come into contact with, a "tectorial" plate, which we take as a model for nearby tectorial accessory structures that are <u>not</u> mechanically attached to stereociliary tufts (chapter 3). The fluid is incompressible and has a viscosity μ, density ρ, and kinematic viscosity $\nu=\mu/\rho$ (chapter 2).

Translation of either of the plates in its plane induces motion of the interposed fluid, generates a hydrodynamic torque on the rigid body, and causes an angular displacement of the rigid body. We seek to find relationships between the velocities imposed on the plates and the resulting angular displacement of the body.

The equations of motion for the hinged body in Figure 4.1 are developed in section 4.1. Although the equations of motion are non-linear, for sufficiently small amplitudes of excitation ($u_b(t)$ and $u_t(t)$), the magnitudes of the non-linear terms are small relative to the magnitudes of the linear terms. The non-linear equations of motion can be approximated by linear equations of motion (developed in section 4.2), for the range of velocities that have been experimentally observed in hair cell systems.

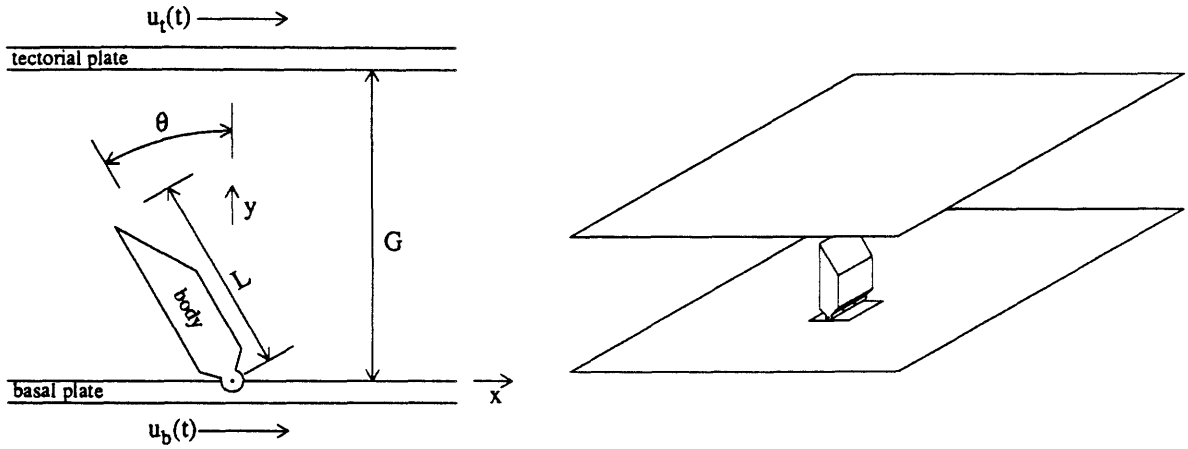

Figure 4.1: Single rigid body attached to a basal plate with a spring-loaded hinge and surmounted by, but not attached to, a tectorial plate. This figure illustrates the hinged-body structure with a three dimensional view in the right panel and a cross sectional view in the left panel. Two parallel flat plates that are of infinite dimension and are separated by a perpendicular distance G bound a fluid filled region. A rigid body is attached by a spring-loaded hinge to the basal plate and does not come in contact with the tectorial plate. x, y, and z are rectangular position coordinates in an inertial frame of reference with origin at the (undisplaced) location of the hinge. $\hat{x}$, $\hat{y}$, and $\hat{z}$ are unit vectors pointing in the x, y, and z directions. The z axis (not labeled in this figure) is perpendicular to the plane of x and y so that $\hat{z} = \hat{x} \times \hat{y}$. The hinge permits rotation about the z-axis only. The dimension of the body L is taken as the distance from the hinge to the point most distant from the hinge. The system is set into motion by vibration of the plates in the x direction. The velocity of the basal plate is $u_b(t)$ and the velocity of the tectorial plate is $u_t(t)$. The imposed vibrations of the plates sets the fluid between the plates into motion and rotates the rigid body through an angle $\theta(t)$.

In section 4.3, we show that the solution to the linear equations of motion can be obtained by: (1) solving three hydrodynamical problems and (2) combining those results in a single torque balance equation. Each of the hydrodynamical problems in (1) characterizes the fluid motion generated by one of three different modes of exciting the structure in Figure 4.1 and none of the hydrodynamical problems in (1) depend on the mechanical parameters of the hinge. Each of the hydrodynamical problems in (1) is thus considerably simpler to solve than the original set of equations. Furthermore, the solutions in (1) completely characterize all possible fluid behaviors, so that, after solving these three hydrodynamical problems, the effect of altering the mechanical characterization of the hinge can be studied without further hydrodynamical work.

4.1 FORMULATION OF THE EQUATIONS OF MOTION

The equations of motion for the system shown in Figure 4.1 are developed in this section. The rigid body -- which can rotate about its hinged attachment -- forms part of the boundary conditions for the equations of motion for the fluid. The boundary conditions for the hydrodynamical problem are thus a mixture of velocity conditions imposed at the plates and a relatively complicated impedance condition imposed at the (moveable) rigid body. Mechanical forces due to the mass of the body and the compliance of the spring combine with forces of fluid origin that act on the surface of the rigid body to generate an angular displacement of the body. The equations of motion thus include the interaction of both hydrodynamical and mechanical elements.

4.1.1 EQUATIONS OF MOTION FOR THE FLUID

Let $\bar{x}$ represent the position vector of a point in the fluid domain that has coordinates (x,y,z). Let $\bar{u}(\bar{x},t)$ and $p(\bar{x},t)$ denote the fluid velocity and pressure at the point $\bar{x}$ and the time t. The equations of motion for an incompressible Newtonian fluid are given in Equations (4.1)-(4.2)

$$\rho\left[\frac{\partial \bar{u}(\bar{x},t)}{\partial t} + \bar{u}(\bar{x},t)\cdot\nabla\bar{u}(\bar{x},t)\right] = -\nabla p(\bar{x},t) + \mu\nabla^2\bar{u}(\bar{x},t) \tag{4.1}$$

$$\nabla\cdot\bar{u}(\bar{x},t) = 0 \tag{4.2}$$

where the notation $\bar{a}\cdot\nabla\bar{b}$ is defined in Equation (4.3).

$$(a_x\hat{x} + a_y\hat{y} + a_z\hat{z})\cdot\nabla\bar{b} = a_x\frac{\partial\bar{b}}{\partial x} + a_y\frac{\partial\bar{b}}{\partial y} + a_z\frac{\partial\bar{b}}{\partial z} \tag{4.3}$$

Equation (4.1) expresses conservation of momentum at each point in the fluid domain and will be refered to as the momentum equation. Equation (4.2) expresses continuity of fluid velocity at every point in the fluid domain -- a consequence of fluid incompressibility and conservation of mass. Equation (4.2) will be refered to as the continuity equation.

4.1.2 BOUNDARY CONDITIONS WITH RIGID SURFACES

The velocity of the fluid that is adjacent to the mechanical boundaries in Figure 4.1 must equal the velocity of the boundaries. This technically incorporates two separate constraints. The continuity equation (4.2) requires that the normal component of the velocity of the fluid near a surface equal that of the surface. The viscosity of the fluid requires that a no-slip condition be imposed on the tangential component of velocity near the rigid surfaces. The fluid velocity near the "basal" plate is therefore constrained to be $u_b(t)\hat{x}$, and the fluid velocity near the "tectorial" plate is constrained to be $u_t(t)\hat{x}$.

$$\bar{u}(\bar{x},t) = u_b(t)\hat{x} \qquad ;\ \bar{x}=(x,y,z)\mid y=0 \tag{4.4}$$

$$\bar{u}(\bar{x},t) = u_t(t)\hat{x} \qquad ;\ \bar{x}=(x,y,z)\mid y=G \tag{4.5}$$

The velocities and positions of points on the surface of the rigid body depend both on the velocity and displacement of the basal plate and on the angular velocity and angular displacement of the rigid body about the hinge. Since the hinge is attached to the basal plate, the y and z components of the position of the hinge are zero. The x component of the position of the hinge is a function of time. Let $x_b(t)\hat{x}$ denote the position of the hinge as a function of time ($u_b(t) = dx_b(t)/dt$). Let $\theta(t)$ denote the angular displacement of the rigid body in Figure 4.1 about the hinge as a function of time. The coordinates of a point on the surface of the rigid body in a relative frame of reference with origin at the hinge, $\bar{r}(\theta)$, have a simple trigonometric dependence on the angular displacement of the hinge $\theta(t)$. The coordinates of a particular point on the rigid body in the absolute frame of reference, $\bar{x}_r(t)$, is then the sum of $x_b(t)\hat{x}$ and $\bar{r}(\theta)$.

$$\bar{x}_r(t) = x_b(t)\hat{x} + \bar{r}(\theta) \tag{4.6}$$

Figure 4.2 illustrates the vectors used to identify points on the surface of the rigid body.

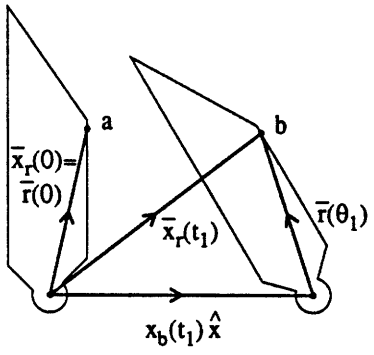

Figure 4.2: Coordinates of points on the surface of the rigid body. The outline on the left of this figure illustrates the position of the rigid body at time t=0, when the position of the hinge, $\bar{x}_b(0)$, is (by definition) equal to $\bar{0}$, and the angular displacement of the body, $\theta(0)$, is (by definition) equal to 0. The outline on the right of this figure illustrates the position of the rigid body at a later time $t=t_1$, when the basal plate has been translated a distance $x_b(t_1)$ in the $\hat{x}$ direction and the body has rotated through an angular displacement $\theta(t_1)$ of roughly 30°. The dot labeled "a" marks a particular point on the rigid body at time t=0. The absolute coordinates of that point are represented by the vector $\bar{x}_r(0)$. The coordinates of that point relative to the hinge are represented by the vector $\bar{r}(0)$. The dot labeled "b" marks the position of this same point at the time $t=t_1$. The absolute coordinates of the point at time t_1 are represented by the vector $\bar{x}_r(t_1)$. The coordinates of the point at time t_1 (when $\theta(t_1)=\theta_1$) relative to the hinge are represented by the vector $\bar{r}(\theta_1)$.

Let $\{R(\theta)\}$ denote the set of all points that lie on the surface of the rigid body ($\{R(\theta)\}$ is a function of $\theta(t)$). The fluid velocity at points $\bar{x}_r(t)$ in $\{R(\theta)\}$ must equal the velocity of the rigid body at $\bar{x}_r(t)$, which is the derivative of the position of the body (Equation (4.6)) with respect to time.

$$\bar{u}(\bar{x}_r(t), t) \equiv \frac{d}{dt}\left[\bar{x}_r(t)\right] = u_b(t)\hat{x} + \frac{d\bar{r}(\theta)}{dt} \qquad ; \text{ for all } \bar{x}_r(t) \text{ in } \{R(\theta)\} \tag{4.7}$$

4.1.3 DISTANT BOUNDARY CONDITIONS

The fluid domain in Figure 4.1 is bounded in y ($0 \leq y \leq G$) but is infinite in extent in both the x and z directions. At points that are distant from the body, the fluid motion is relatively unaffected by the body. In the limit of increasing distance from the body, the fluid velocity approaches the velocity that would occur between the two plates in the absence of the body. Let $\bar{u}_\delta(\bar{x},t)$ represent the fluid velocity that results in the absence of the body.

$$\lim_{x,z \to \infty} \bar{u}(\bar{x},t) = \bar{u}_\delta(\bar{x},t) \tag{4.8}$$

Since

$$\bar{u}_\delta(\bar{x},t) = u_b(t)\hat{x} \qquad ; \bar{x} = (x,0,z) \tag{4.9}$$

$$\bar{u}_\delta(\bar{x},t) = u_t(t)\hat{x} \qquad ; \bar{x} = (x,G,z) \tag{4.10}$$

Equations (4.4), (4.5), and (4.8) can be combined into a single equation.

$$\bar{u}(\bar{x},t) = \bar{u}_\delta(\bar{x},t) \qquad ; \{y = 0,G\} \text{ or } \{x,z \to \infty\} \tag{4.11}$$

4.1.4 EQUATION OF MOTION FOR THE RIGID BODY

Since the velocity of one point on the rigid body is known (the velocity of the hinge is equal to the velocity of the basal plate ($= u_b(t)\hat{x}$)), the dynamics of the motion of the rigid body can be completely characterized by a torque balance equation about the hinge.

$$\bar{\tau}_{ext} = \frac{d\bar{\alpha}}{dt} + u_b(t)\hat{x} \times \bar{\lambda} \tag{4.12}$$

In Equation (4.12), $\bar{\tau}_{ext}$ denotes the sum of external torques applied to the body about the hinge, $\bar{\alpha}$ denotes the angular momentum of the body, and $\bar{\lambda}$ denotes the linear momentum of the body. The final term in Equations (4.12) reflects the acceleration of the point about which $\bar{\tau}_{ext}$ is measured.

The angular momentum of the body about the hinge is the product of the moment of inertia of the body about the hinge (I) and the angular velocity of the body ($\dot{\theta}(t)\hat{z} = \hat{z}\,d\theta(t)/dt$).

$$\bar{\alpha} = I\dot{\theta}(t)\,\hat{z} \tag{4.13}$$

The linear momentum of the body is the product of the mass of the body (M) and velocity of the center of mass of the body. Let $\bar{r}_c(\theta)$ denote the position of the center of mass of the body relative to the position of the hinge.

$$\bar{\lambda} = M\left(u_b(t)\hat{x} + \frac{d\bar{r}_c(\theta)}{dt} \right) \tag{4.14}$$

A component of $\bar{\lambda}$ is in the same direction as the velocity of the hinge, and the cross product in Equation (4.12) can be simplified as in Equation (4.15).

$$u_b(t)\hat{x} \times \bar{\lambda} = Mu_b(t)\,\hat{x} \times \frac{d\bar{r}_c(\theta)}{dt} \tag{4.15}$$

External torques are generated on the body by three mechanisms. First, the spring exerts a torque $\bar{\tau}_{spring}$ on the rigid body.

$$\bar{\tau}_{spring} = -K\theta(t)\,\hat{z} \tag{4.16}$$

Second, the fluid exerts hydrodynamical forces on the surfaces of the body and thereby generates a torque on the body. Let $\overline{dR}(\theta)$ denote a differential element of the surface of the rigid body. $\overline{dR}(\theta)$ is a vector whose magnitude is equal to the area of the surface element and whose direction $\hat{dR}(\theta)$ is normal to the plane of the surface element. The notation $\overline{dR}(\theta)$ is intended to make clear that the orientation of the differential element depends on $\theta(t)$. The increment of force $\overline{dF}$ that is exerted on $\overline{dR}(\theta)$ has both inertial and viscous components.

$$\overline{dF} = -p(\bar{x},t)\overline{dR}(\theta) + \mu\,\overline{dR}(\theta)\cdot\nabla\bar{u}(\bar{x},t) \tag{4.17}$$

The total hydrodynamical torque $\bar{\tau}$ is the integral of the incremental torques.

$$\bar{\tau} = \int_{R(\theta)}(\bar{r}(\theta)\times\overline{dF}). \tag{4.18}$$

The third mechanism that generates torque on the body is due to the hinge. Since the hinge in Figure 4.1 has a single degree of rotational freedom, it will exert sufficient torque about the x and y axes to preclude angular displacements of the body about those axes. Both the x and y components of $\bar{\alpha}$ are therefore equal to zero, and only the z component of Equation (4.12) need be considered to fully characterize the motion of the rigid body. Substitute Equations (4.17), (4.18), (4.16), (4.15), and (4.13) into the z component of Equation (4.12).

$$\hat{z}\cdot\left[\int_{R(\theta)}\bar{r}(\theta)\times\left[-p(\bar{x},t)\overline{dR}(\theta)+\mu\overline{dR}(\theta)\cdot\nabla\bar{u}(\bar{x},t)\right]\right] - K\theta(t) = I\ddot{\theta}(t) + \hat{z}\cdot\left[Mu_b(t)\hat{x}\times\frac{d\bar{r}_c(t)}{dt}\right] \tag{4.19}$$

$\rho\left[\frac{\partial\bar{u}(\bar{x},t)}{\partial t}+\bar{u}(\bar{x},t)\cdot\nabla\bar{u}(\bar{x},t)\right] = -\nabla p(\bar{x},t)+\mu\nabla^2\bar{u}(\bar{x},t)$	; $\bar{x}$ in the fluid domain	(4.1)
$\nabla\cdot\bar{u}(\bar{x},t) = 0$	; $\bar{x}$ in the fluid domain	(4.2)
$\bar{u}(\bar{x}_r(t),t) = u_b(t)\hat{x}+\frac{d\bar{r}(\theta)}{dt}$	; for all $\bar{x}_r(t)$ in $\{R(\theta)\}$	(4.7)
$\bar{u}(\bar{x},t) = \bar{u}_\delta(\bar{x},t)$	; $\{y=0,G\}$ or $\{x,z\to\infty\}$	(4.11)
$\hat{z}\cdot\left[\int_{R(\theta)}\bar{r}(\theta)\times\left[-p(\bar{x},t)\overline{dR}(\theta)+\mu\overline{dR}(\theta)\cdot\nabla\bar{u}(\bar{x},t)\right]\right] - K\theta(t) = I\ddot{\theta}(t)+\hat{z}\cdot\left[Mu_b(t)\hat{x}\times\frac{d\bar{r}_c(t)}{dt}\right]$		(4.19)

Table 4.1: Summary of equations of motion for the hinged body in Figure 4.1.

4.2 EQUATIONS OF MOTION FOR SMALL EXCITATIONS

Two different mechanisms give rise to nonlinear terms in the equations of motion for the rigid body (listed in Table 4.1). The first of these mechanisms can be understood by considering the velocity field generated by a vibrating sphere immersed in a fluid of infinite spatial extent. If the fluid is inviscid, then the velocity at some particular point in the field is an instantaneous function of the velocity of the sphere and the position of the sphere relative to the point of interest. As the sphere vibrates however, both the velocity of the sphere and the position of the sphere change as a function of time. So long as the amplitude of the vibrations of the sphere are small relative to the distance over which the velocity field induced by the motion of the sphere changes, the magnitude of the velocity at a particular point in the fluid domain will be nearly proportional to the magnitude of the velocity of the sphere. If however the distance over which the sphere moves is large relative to the distance over which the velocity field generated by the sphere changes, the magnitude of the velocity at a particular point in the fluid domain will be a nonlinear function of the magnitude of the velocity of the sphere.

The second mechanism that generates nonlinear terms in the equations of motion for the rigid body involves the nonlinear relationship between the velocity of points on the rigid body and the angular velocity of the rigid body about the hinge. So long as the angular velocity is small enough that the associated angular displacement is less than a few degrees, the translational velocity of points on the rigid body will increase nearly linearly with the magnitude of the angular velocity. For large angular velocities however, not only will the magnitude of the translational velocity change with the magnitude of the angular velocity, but its direction will also change.

The importance of both of these nonlinear mechanisms decreases as the amplitudes of the excitations ($u_b(t)$ and $u_t(t)$) are decreased. In the limit of infinitesimally small excitation, strictly linear relationships exist between the amplitude of the excitations and the resulting fluid and rigid body velocities. The error introduced by neglecting the nonlinear terms can be estimated by comparing the magnitudes of the displacements that occur physiologically with the distances over which the fluid fields change appreciably. Such analysis suggests that the linear equations that are certainly valid for infinitesimal excitations are also likely to be valid except at extremely high intensity stimulation. This argument is more fully described in chapter 2.

Linear approximations to the equations of motion in Table 4.1 are developed in section 4.2.1 and a spectral representation is given in section 4.2.2.

4.2.1 LINEARIZATION OF THE EQUATIONS OF MOTION

As $u_b(t)$ and $u_f(t)$ are decreased in amplitude, the magnitude of the fluid velocity field decreases. For infinitesimally small $u_b(t)$ and $u_f(t)$, the convective non-linear term in Equation (4.1), $\bar{u}(\bar{x}, t) \cdot \nabla\bar{u}(\bar{x}, t)$, is negligible relative to the other terms in Equation 4.1. For small excitations, Equation (4.1) can be approximated by a linear relationship between $\bar{u}(\bar{x}, t)$ and $p(\bar{x}, t)$.

$$\rho \frac{\partial\bar{u}(\bar{x},t)}{\partial t} = -\nabla p(\bar{x},t) + \mu\nabla^2\bar{u}(\bar{x},t) \qquad ; \ \bar{x} \text{ in the fluid domain} \tag{4.20}$$

The velocity of the fluid near the rigid body (Equation 4.7) is a nonlinear function of the angular displacement of the rigid body for two reasons. First, $\bar{r}(\theta)$ is a nonlinear function of θ (that involves trigonometric functions) so that $d\bar{r}(\theta)/dt$ contains nonlinear terms. For small excitations $u_b(t)$ and $u_f(t)$, the angular displacement of the rigid body, $\theta(t)$, is also small, and the dependence of $\bar{r}(\theta)$ on θ is nearly linear.

$$\bar{r}(\theta) \approx \bar{r}(0) + \theta(t)\,\hat{z} \times \bar{r}(0) \tag{4.21}$$

Equation (4.21) states that for small angular displacements $\theta(t)$, the position of a point on the surface of the rigid body varies about its position when $\theta=0$ in a direction that is perpendicular to the projection of $\bar{r}(0)$ into the x-y plane. Points on the surface of the rigid body that lie on the line $x=0$ therefore move horizontally, while points on the rigid body that lie along the line $x=y$ have both a vertical and horizontal component of motion. Equation (4.21) ignores the change in direction that occurs with large deviations from $\theta=0$. Substituting Equation (4.21) into the right hand side of Equation (4.7)

$$\bar{u}(\bar{x}_r(t), t) \approx u_b(t)\hat{x} + \dot{\theta}(t)\,\hat{z} \times \bar{r}(0) \tag{4.22}$$

generates an approximation to the boundary velocity that is a linear function of $u_b(t)$ and $\theta(t)$. Even though the right hand side of Equation (4.22) is linearly dependent on $u_b(t)$ and $\theta(t)$, since the points on the boundary are moving, we show that the velocity at points that are fixed in space is a nonlinear function of $\bar{u}(\cdot,t)$ and $\theta(t)$. Substitute the linearized expression for $\bar{r}(\theta)$ from Equation (4.21) into the expression for $\bar{x}_r(t)$ in Equation (4.6).

$$\bar{x}_r(t) \approx x_b(t)\hat{x} + \bar{r}(0) + \theta(t)\,\hat{z}\times\bar{r}(0) \tag{4.23}$$

Substitute Equation (4.23) into the left hand side of Equation (4.22).

$$\bar{u}(\bar{x}_r(t), t) \approx \bar{u}(x_b(t)\hat{x}+\bar{r}(0)+\theta(t)\,\hat{z}\times\bar{r}(0), t) \tag{4.24}$$

Expanding the fluid velocity field near the moving boundary in a spatial Taylor series (retaining just the constant and linear terms),

$$\bar{u}(x_b(t)\hat{x}+\bar{r}(0)+\theta(t)\hat{z}\times\bar{r}(0), t) \approx \bar{u}(\bar{r}(0), t) + \left[x_b(t)\hat{x}+\theta(t)\hat{z}\times\bar{r}(0)\right] \cdot \nabla\bar{u}(\bar{r}(0), t) \tag{4.25}$$

and equating the right hand sides of Equations (4.22) and (4.25) shows that the fluid velocity at points that are near the boundary but fixed in space is a nonlinear function of $\bar{u}(\cdot,t)$ and $\theta(t)$.

$$\bar{u}(\bar{r}(0), t) \approx u_b(t)\hat{x} + \dot{\theta}(t)\hat{z}\times\bar{r}(0) - \left[x_b(t)\hat{x}+\theta(t)\hat{z}\times\bar{r}(0)\right] \cdot \nabla\bar{u}(\bar{r}(0), t) \qquad (4.26)$$

The last term in Equation (4.26) is nonlinear. The term in square brackets is equal to the displacement of particular points on the rigid body as a function of time. The magnitude of the nonlinear term in Equation (4.26) will therefore be small so long as the distance over which the fluid velocity near the body ($\bar{u}(\bar{r}(0),t)$) varies is much larger than the peak displacements of points on the rigid body. For infinitesimal excitations $u_b(t)$ and $u_t(t)$, both the term in square brackets and $\nabla\bar{u}(\bar{r}(0),t)$ have infinitesimal amplitudes and their product is negligible compared to $u_b(t)$. Therefore, for vanishingly small amplitudes of excitation $u_b(t)$ and $u_t(t)$, the boundary conditions that are imposed near the rigid body can be approximated by a linear function of $u_b(t)$ and $\theta(t)$ at stationary points in the fluid domain.

$$\bar{u}(\bar{r}(0), t) \approx u_b(t)\hat{x} + \dot{\theta}(t)\hat{z} \times \bar{r}(0) \qquad ; \ \bar{r}(0) \text{ in } \{R(0)\} \qquad (4.27)$$

Equation (4.27) is a linearized approximation to Equation (4.7) in Table 4.1.

The hydrodynamic torque $\bar{\tau}$ that is exerted on the rigid body (Equation (4.19)) is the integral of incremental torques on a moving surface. For infinitesimal amplitudes of excitation $u_b(t)$ and $u_t(t)$, the difference between the integral over $R(\theta)$ and $R(0)$ is negligible. For vanishingly small amplitudes of excitation, the hydrodynamic torque $\bar{\tau}$ can be approximated by

$$\bar{\tau} \approx \int_{R(0)}\bar{r}(0)\times\left[-p(x_b(t)\hat{x}+\bar{r}(0), t)\,\overline{dR}(0) + \mu\overline{dR}(0)\cdot\nabla\bar{u}(x_b(t)\hat{x}+\bar{r}(0), t)\right] \qquad (4.28)$$

which is a linear function of $p(\cdot,t)$ and $\bar{u}(\cdot,t)$.

The small angle approximation of $\bar{r}(\theta)$ (Equation (4.21)) can be used to simplify the expression for $u_p(t)\hat{x}\times\bar{\lambda}$ (substitute Equation (4.21) into Equation (4.15)).

$$u_b(t)\hat{x} \times \bar{\lambda} \approx Mu_b(t)\dot{\theta}(t)r_{cx}\hat{z} \qquad (4.29)$$

r_{cx} is the x component of $\bar{r}_c(0)$ -- a constant. Equation (4.29) contains the product of $u_b(t)$ and $\dot{\theta}(t)$ and is thus a nonlinear term. In the limit of vanishingly small excitation amplitude, this product is negligible relative to the other terms in Equation (4.12). Therefore the final term of Equation (4.19) is omitted in the linearized approximation to that equation.

$$K\theta(t) + I\ddot{\theta}(t) = \hat{z}\cdot\int_{R(0)}\bar{r}(0)\times\left[-p(\bar{x},t)\overline{dR}(0)+\mu\overline{dR}(0)\cdot\nabla\bar{u}(\bar{x},t)\right] \qquad (4.30)$$

$\rho \frac{\partial \bar{u}(\bar{x},t)}{\partial t} = -\nabla p(\bar{x},t) + \mu \nabla^2 \bar{u}(\bar{x},t)$	; $\bar{x}$ in the fluid domain	(4.20)
$\nabla \cdot \bar{u}(\bar{x},t) = 0$	; $\bar{x}$ in the fluid domain	(4.2)
$\bar{u}(\bar{r}(0), t) = u_b(t)\hat{x} + \dot{\theta}(t)\hat{z} \times \bar{r}(0)$	; $\bar{r}(0)$ in $\{R(0)\}$	(4.27)
$\bar{u}(\bar{x},t) = \bar{u}_\delta(\bar{x},t)$	; $\{y = 0,G\}$ or $\{x,z \rightarrow \infty\}$	(4.11)
$K\theta(t) + I\ddot{\theta}(t) = \hat{z} \cdot \int_{R(0)} \bar{r}(0) \times \left[-p(\bar{x},t)d\bar{R}(0) + \mu d\bar{R}(0) \cdot \nabla \bar{u}(\bar{x},t) \right]$		(4.30)

Table 4.2: Summary of the equations of motion for infinitesimally small excitations of the hinged body in Figure 4.1.

4.2.2 STEADY-STATE SINUSOIDAL REPRESENTATION

Since the equations of motion in Table 4.2 are linear, their solution for any excitation ($u_b(t)$ and $u_t(t)$) can be expressed as a linear combination of solutions for steady state sinusoidal excitations.

$$u_b(t) = \mathrm{Re}\{U_b e^{j\omega t}\} \tag{4.31}$$
$$u_t(t) = \mathrm{Re}\{U_t e^{j\omega t}\} \tag{4.32}$$

The fluid velocity $\bar{u}(\bar{x}, t)$ that results from the excitations in Equations (4.31) and (4.32) can be represented by a complex-valued vector field $\bar{U}(\bar{x},\omega)$

$$\bar{u}(\bar{x}, t) = \mathrm{Re}\{\bar{U}(\bar{x},\omega)e^{j\omega t}\} \tag{4.33}$$

and the pressure $p(\bar{x}, t)$ can be represented by a complex-valued scalar field $P(\bar{x},\omega)$.

$$p(\bar{x}, t) = \mathrm{Re}\{P(\bar{x},\omega)e^{j\omega t}\} \tag{4.34}$$

The mechanical variables can be represented by complex-valued scalars $\Theta(\omega)$ and $T(\omega)$.

$$\theta(t) = \mathrm{Re}\{\Theta(\omega)e^{j\omega t}\} \tag{4.35}$$
$$\tau(t) = \mathrm{Re}\{T(\omega)e^{j\omega t}\} \tag{4.36}$$

The fluid velocity that results in the absence of the rigid body ($\bar{u}_\delta(\bar{x}, t)$) for sinusoidal steady state excitation can be expressed in closed form.

$$\bar{u}_\delta(\bar{x}, t) = \mathrm{Re}\{\bar{U}_\delta(\bar{x},\omega)e^{j\omega t}\} \tag{4.37}$$
$$\bar{U}_\delta(\bar{x},\omega) = \left[U_b \frac{\sinh((G-y)\sqrt{j\omega/\nu})}{\sinh(G\sqrt{j\omega/\nu})} + U_t \frac{\sinh(y\sqrt{j\omega/\nu})}{\sinh(G\sqrt{j\omega/\nu})} \right] \hat{x} \tag{4.38}$$

The spectral formulation of the equations of motion for the hinged body in Figure 4.1 follows from the substitution of Equations (4.31)-(4.38) into the equations of Table 4.2. The resulting equations are listed in Table 4.3.

$$j\omega\rho\bar{U}(\bar{x},\omega) = -\nabla P(\bar{x},\omega) + \mu\nabla^2\bar{U}(\bar{x},\omega) \quad ; \ \bar{x} \text{ in the fluid domain} \quad (4.40)$$

$$\nabla\cdot\bar{U}(\bar{x},\omega) = 0 \quad ; \ \bar{x} \text{ in the fluid domain} \quad (4.41)$$

$$\bar{U}(\bar{x},\omega) = \left[U_b \frac{\sinh((G-y)\sqrt{j\omega/\nu})}{\sinh(G\sqrt{j\omega/\nu})} + U_t \frac{\sinh(y\sqrt{j\omega/\nu})}{\sinh(G\sqrt{j\omega/\nu})}\right]\hat{x} \quad ; \ \{y=0,G\} \text{ or } \{x,z\to\infty\} \quad (4.42)$$

$$\bar{U}(\bar{x},\omega) = U_b\hat{x} + j\omega\Theta(\omega)\,\hat{z}\times\bar{r} \quad ; \ \bar{x} \text{ in } \{R\} \quad (4.43)$$

$$(K-I\omega^2)\,\Theta(\omega) = \hat{z}\cdot\left[\int_R \bar{r}\times\left[-P(\bar{x},\omega)\overline{dR} + \mu\,\overline{dR}\cdot\nabla\bar{U}(\bar{x},\omega)\right]\right] \quad (4.44)$$

Table 4.3: Spectral representation of the linearized equations of motion for the rigid body in Figure 4.1. In Equations (4.43) and (4.44), $\bar{r}$ denotes the position of a point in the rigid body relative to the position of the hinge when the angular displacement of the body is zero. (The $\bar{r}$ in the equations in Table 4.3 represents the vector that was refered to as $\bar{r}(0)$ in the equations in Table 4.2.) In Equation (4.44), {R} represents the set of points that lie on the surface of the rigid body when the angular displacement of the body is zero. (The {R} in Equation (4.44) represents the same set of points that {R(0)} represents in Equation (4.30).)

4.3 SUPERPOSITION OF HYDRODYNAMIC COMPONENT SOLUTIONS

The equations of motion for the fluid in Table 4.3 have boundary conditions that depend on the angular velocity of the rigid body (Figure 4.1). The equation of motion for the rigid body, however, depends on the hydrodynamical torque on the body. Thus the mechanical and hydrodynamical equations of motion are coupled. In this section, we outline a method whereby the hydrodynamical and mechanical aspects of the equations of motion can be separated.

Fluid motion results from motion of three structures -- translation of the basal plate, translation of the tectorial plate, and rotation of the rigid body. Because the equations of motion in Table 4.3 are linear, we can calculate that "total" fluid motion by superposition of the fluid motions that result from motion of each of the three structures with the others held fixed. Each of the component motions can be completely characterized to within a multiplicative constant without knowledge of the mechanical properties of the hinge. The constants can then be evaluated by solving a single torque balance equation that characterizes both the hydrodynamical solutions to the three component problems and the mechanical properties of the hinge.

We define the three hydrodynamical components in section 4.3.1 and illustrate the superposition method graphically in section 4.3.2.

4.3.1 DEFINITION OF THE HYDRODYNAMIC COMPONENTS

Since Equations (4.42)-(4.43) specify velocity boundary conditions on a fully enclosed region of fluid, Equations (4.40)-(4.43) can be taken to (completely) define $\bar{U}(\bar{x},\omega)$ and $P(\bar{x},\omega)$ in terms of the three complex-valued scalar amplitudes U_b, U_t, and $\Theta(\omega)$. We distinquish three components of the solution. Each component corresponds to setting two of the complex amplitudes to zero and finding the solution when one of the complex amplitudes is non-zero.

Let $\bar{U}_B(\bar{x},\omega)$, $P_B(\bar{x},\omega)$, and $T_B(\omega)$ be defined by Equations (4.45)-(4.49). The solution to Equations (4.45)-(4.49) will be called the B-component (basal component) of the solution to Equations (4.40)-(4.44). Equations (4.45)-(4.49) describe the fluid motion around and the hydrodynamic torque on a rigid body (Figure 4.1) that cannot rotate ($\theta=0$), when the basal plate velocity is U_b and the tectorial plate velocity is zero.

$$j\omega\rho\bar{U}_B(\bar{x},\omega) = -\nabla P_B(\bar{x},\omega) + \mu\nabla^2\bar{U}_B(\bar{x},\omega) \qquad ; \ \bar{x} \text{ in the fluid domain} \qquad (4.45)$$

$$\nabla\cdot\bar{U}_B(\bar{x},\omega) = 0 \qquad ; \ \bar{x} \text{ in the fluid domain} \qquad (4.46)$$

$$\bar{U}_B(\bar{x},\omega) = \bar{V}_B(\bar{x},\omega) = U_b\frac{\sinh((G-y)\sqrt{j\omega/\nu})}{\sinh(G\sqrt{j\omega/\nu})} \qquad ; \ \{y=0,G\} \text{ or } \{x,z\to\pm\infty\} \qquad (4.47)$$

$$\bar{U}_B(\bar{x},\omega) = U_b\hat{x} \qquad ; \ \bar{x} \text{ in } \{R\} \qquad (4.48)$$

$$T_B(\omega) = \hat{z}\cdot\left[\int_R \bar{r}\times\left[-P_B(\bar{x},\omega)\overline{dR} + \mu\overline{dR}\cdot\nabla\bar{U}_B(\bar{x},\omega)\right]\right] \qquad (4.49)$$

Let $\bar{U}_T(\bar{x},\omega)$, $P_T(\bar{x},\omega)$, and $T_T(\omega)$ be defined by Equations (4.50)-(4.54). The solution to Equations (4.50)-(4.54) will be called the T-component (tectorial component) of the solution to Equations (4.40)-(4.44). Equations (4.50)-(4.54) describe the fluid motion around and the hydrodynamic torque on a rigid body whose hinge is fixed ($\theta=0$) when the tectorial plate velocity is U_t and basal plate velocity is zero.

$$j\omega\rho\bar{U}_T(\bar{x},\omega) = -\nabla P_T(\bar{x},\omega) + \mu\nabla^2\bar{U}_T(\bar{x},\omega) \quad ; \bar{x} \text{ in the fluid domain} \quad (4.50)$$

$$\nabla\cdot\bar{U}_T(\bar{x},\omega) = 0 \quad ; \bar{x} \text{ in the fluid domain} \quad (4.51)$$

$$\bar{U}_T(\bar{x},\omega) = \bar{V}_T(\bar{x},\omega) = U_t\frac{\sinh(y\sqrt{j\omega/\nu})}{\sinh(G\sqrt{j\omega/\nu})} \quad ; \{y=0,G\} \text{ or } \{x,z\to\pm\infty\} \quad (4.52)$$

$$\bar{U}_T(\bar{x},\omega) = \bar{0} \quad ; \bar{x} \text{ in } \{R\} \quad (4.53)$$

$$T_T(\omega) = \hat{z}\cdot\left[\int_R \bar{r}\times\left[-P_T(\bar{x},\omega)\overline{dR} + \mu\overline{dR}\cdot\nabla\bar{U}_T(\bar{x},\omega)\right]\right] \quad (4.54)$$

Let $\bar{U}_R(\bar{x},\omega)$, $P_R(\bar{x},\omega)$, and $T_R(\omega)$ be defined by Equations (4.55)-(4.59). The solution to Equations (4.55)-(4.59) will be called the R-component (rotational component) of the solution to Equations (4.40)-(4.44). Equations (4.55)-(4.59) describe the fluid motion and the hydrodynamic torque induced by rotation of the rigid body in Figure 4.1 in the absence of motion of either plate.

$$j\omega\rho\bar{U}_R(\bar{x},\omega) = -\nabla P_R(\bar{x},\omega) + \mu\nabla^2\bar{U}_R(\bar{x},\omega) \quad ; \bar{x} \text{ in the fluid domain} \quad (4.55)$$

$$\nabla\cdot\bar{U}_R(\bar{x},\omega) = 0 \quad ; \bar{x} \text{ in the fluid domain} \quad (4.56)$$

$$\bar{U}_R(\bar{x},\omega) = \bar{0} \quad ; \{y=0,G\} \text{ or } \{x,z\to\pm\infty\} \quad (4.57)$$

$$\bar{U}_R(\bar{x},\omega) = j\omega\Theta(\omega)\,\hat{z}\times\bar{r} \quad ; \bar{x} \text{ in } \{R\} \quad (4.58)$$

$$T_R(\omega) = \hat{z}\cdot\left[\int_R \bar{r}\times\left[-P_R(\bar{x},\omega)\overline{dR} + \mu\overline{dR}\cdot\nabla\bar{U}_R(\bar{x},\omega)\right]\right] \quad (4.59)$$

The solution to Equations (4.40)-(4.44) can be written as a linear combination of the solutions to Equations (4.45)-(4.59).

$$\bar{U}(\bar{x},\omega) = \bar{U}_B(\bar{x},\omega) + \bar{U}_T(\bar{x},\omega) + \bar{U}_R(\bar{x},\omega) \quad (4.60)$$

$$P(\bar{x},\omega) = P_B(\bar{x},\omega) + P_T(\bar{x},\omega) + P_R(\bar{x},\omega) \quad (4.61)$$

$$T(\omega) = T_B(\omega) + T_T(\omega) + T_R(\omega) \quad (4.62)$$

subject also to the constraint that arises from Equation (4.44).

$$T(\omega) = (K - I\omega^2)\,\Theta(\omega) \quad (4.63)$$

Equations (4.40)-(4.44) describe the motion of a system with both rotational mechanical and hydrodynamical components. The boundary conditions in Equations (4.40)-(4.44) are a function of the dependent variable $\Theta(\omega)$. $\Theta(\omega)$ depends on torques that are of hydrodynamic origin as well as on torques generated by the mechanical attachment at the hinge. The decomposition of the solution to Equations (4.40)-(4.44) into B-, T-, and

R- components separates the mechanical and hydrodynamic equations of motion. All three component sets of equations -- (4.45)-(4.49), (4.50)-(4.54), and (4.55)-(4.59) -- can be solved without regard to the mechanical impedance of the hinge. Equation (4.63) alone depends on the mechanical properties of the hinge.

4.3.2 EQUIVALENT CIRCUIT REPRESENTATION

Equations (4.45)-(4.49) define a transformation from U_b to $T_B(\omega)$ that can be characterized explicitly by

$$H_B(\omega) = T_B(\omega)/U_b \ . \tag{4.64}$$

$H_B(\omega)$ is a transfer impedance which is equal to the torque generated by a unit velocity of the basal plate, zero velocity of the tectorial plate, and zero angular velocity of the body. Equations (4.50)-(4.54) define a transformation from U_t to $T_T(\omega)$ that can be characterized explicitly by

$$H_T(\omega) = T_T(\omega)/U_t \ . \tag{4.65}$$

$H_T(\omega)$ is a transfer impedance which is equal to the torque generated by a unit velocity of the tectorial plate, zero velocity of the basal plate, and zero angular velocity of the body. Equations (4.55)-(4.59) define a transformation from $j\omega\Theta(\omega)$ to $T_R(\omega)$ that can be characterized explicitly by

$$Z_R(\omega) = -T_R(\omega)/j\omega\Theta(\omega) \ . \tag{4.66}$$

$Z_R(\omega)$ is a mechanical rotational impedance which is equal to the torque generated by a unit angular velocity of the body and zero velocity of both the basal and tectorial plates. Substitute Equations (4.64)-(4.66) into (4.62)-(4.63) and eliminate T.

$$(K + j\omega Z_R(\omega) - \omega^2 I)\ \Theta(\omega) = H_B(\omega)U_b + H_T(\omega)\,U_t \tag{4.67}$$

Each of the five terms in the torque balance equation (4.67) are represented by one component in a lumped parameter model in Figure 4.3. Three of the components, $Z_R(\omega)$, $H_B(\omega)$, and $H_T(\omega)$, are of hydrodynamic origin, and the other two, I and K, are of mechanical origin.

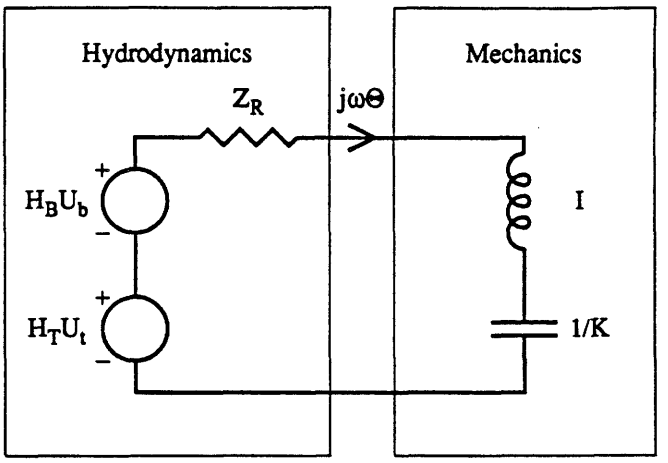

Figure 4.3: Separation of the hydrodynamic and mechanical components of the equations of motion (4.40)-(4.44). This circuit model illustrates the balance of torques that is required at the hinge by Equations (4.62)-(4.63). The torque that is generated on the rigid body by displacement of the basal plate, when the tectorial plate is stationary and the body is not permitted to rotate is represented by the source H_BU_b (which of course has a magnitude that is proportional to U_b). The torque that is generated on the rigid body by displacement of the tectorial plate, when the basal plate is stationary and the body is not permitted to rotate is represented by the source H_TU_t. The angular velocity of the body is $j\omega\Theta$. The torque that is generated on the rigid body by rotation of the body with angular velocity equal to $j\omega\Theta$ is represented by the impedance Z_R. I represents the moment of inertial of the body. K represents the stiffness of the torsional spring in the hinge.

The values the hydrodynamical components are independent of the values of the mechanical components, and completely summarize the effect of the fluid on the motion of the body. Figure 4.3 makes clear that by exploiting superposition, the hydrodynamics of stereociliary tuft motion can be "decoupled" from the mechanics of stereociliary tuft motion. Without knowledge of the mechanical properties of the hinged-attachment of the body, one can "solve" the hydrodynamical problem by computing three functions of frequency, $Z_R(\omega)$, $H_B(\omega)$, and $H_T(\omega)$. One can then study the effect of the mechanical properties of the hinged-attachment without further hydrodynamical calculations.

The lumped parameter representation ($Z_R(\omega)$, $H_B(\omega)$, and $H_T(\omega)$) of the effect of the fluid on the motion of the hinged-body does not depend on any of the assumptions about the mechanical representation of the hinged-attachment that were made in the derivation above. For example, the left part of Figure 4.3 (marked "Hydrodynamics") can be combined with other mechanical models of the attachment to account for losses in the hinge, non-linearities in the hinge, or even coupling between the motion of a tuft and the electrical response of a hair cell (Weiss, 1982).

CHAPTER 5
LOW FREQUENCY ANALYSIS OF A RIGID BODY THAT IS ATTACHED TO A VIBRATING PLATE WITH A SPRING LOADED HINGE

It is increasingly evident that the dynamics of the motion of stereocilia play an important signal processing role in acoustico-lateralis systems. Though a firm theoretical understanding of the mechanics of stereociliary motion is not available, certain aspects of that motion have been presumed. Specifically, many authors have presumed that at low frequencies, the deflection of stereocilia whose excitation is fluid-coupled is proportional to the velocity of the structure that sets the fluid into motion. This "velocity sensor" model of stereociliary motion follows from the presumption that forces of fluid origin are viscosity-dominated at low frequencies. In this report, we analyze the equations of motion for a Newtonian fluid without assumptions about the relative magnitude of viscous and inertial forces -- and thereby test the theoretical plausibility of the "viscous-dominated" presumption. We show that the "velocity sensor" model of stereociliary motion is valid for only a subset of the model morphologies analyzed here, and for that subset, the "velocity sensor" model is valid for only a limited range of low frequencies (that we specify quantitatively). We also show that the "velocity sensor" model of stereociliary motion is not valid for certain model morphologies. We show that for free-standing models, inertial forces of fluid origin are important at all frequencies -- no matter how low.

In this report, we analyze the motion of a rigid body that lies in a fluid filled region that is bounded by two parallel plates (Figure 4.1). We take the rigid body as a model for stereociliary structures. It is attached to a "basal" plate -- which we take as a model for the surface of the epithelium from which stereociliary structures project -- with a hinge. The hinge is spring loaded so that angular displacements of the rigid body are resisted by a torque that grows linearly with angular displacement. In this model, the rigid body does not come into contact with the "tectorial" plate -- which we take as a model for nearby tectorial accessory structures that are not directly attached to stereociliary structures. The fluid is incompressible and has a viscosity μ, density ρ, and kinematic viscosity $\nu=\mu/\rho$.

Translation of either of the plates in its plane induces motion of the interposed fluid, generates a hydrodynamic torque on the rigid body and causes an angular displacement of the rigid body. We seek to find the relationships between the velocities imposed on the plates and the resulting angular displacement of the body.

The fluid motion in the neighborhood of the hinged body, and the torque generated on the hinged body by that fluid motion, generally depend on the shape of the rigid body. The wide variation in stereociliary tuft morphology (both within and across species) makes it difficult to generate a specific rigid body shape that is generally applicable, so one is faced with the prospect of solving the equations of motion for a number of differently shaped bodies. Unfortunately, solving the equations of motion for even a single very simply shaped body is a formidable task and one is therefore driven to seek special circumstances for which robust (i.e. geometry independent) results can be established.

At very low frequencies of excitation, boundary layers of large dimensions are induced in the fluid. These boundary layers preclude complicated patterns of fluid motion in the neighborhood of the body and decrease the sensitivity of the solution of the equations of motion to the details of the body shape. Thus for arbitrarily low frequencies of excitation, some characteristics of the solutions to the equations of motion are independent of the detailed body shape.

We take L as the maximum distance from the hinge to any point on the body. Without specifying any other aspects of the shape of the body (except that the shape permits rotation of the body about the hinge), we derive low frequency asymptotic relationships between the velocity of imposed vibrations of the plates and the resulting angular displacement of the rigid body. Since they do not depend on the detailed shape of the body, the results of this chapter address the motion of a single (isolated) stereocilium, or (lumped models of) entire tufts of stereocilia, or even (lumped models of) entire rows of stereociliary tufts.

We show that, although the response to very low frequency excitation is different from the response to steady excitation, the former can be computed from the latter. This result is established by expanding the hydrodynamical and mechanical variables in the equations of motion in ascending power series of frequency. Substituting these series into the equations of motion and separating terms with equivalent order generates a sequence of simpler, frequency-independent, sets of equations -- each set describing progressively higher order terms of the power series expansions. Low frequency asymptotic relationships between the angular displacement of the body and the velocities of the plates are developed in terms of the solutions to steady equations of motion.

We develop the power series method in section 5.1 and investigate the error that is incurred by truncating the series in section 5.2. In the next three sections, we develop results for three (collectively exhaustive) sub-classes of models of the form given in Figure 4.1.

In section 5.3, we characterize the low frequency response of models of free-standing stereociliary tufts by taking the inter-plate distance G to be very large. We show that, in the limit as $G \rightarrow \infty$, the low frequency ratio of angular displacement of the body to basal plate velocity is proportional to $(j\omega)^{1/2}$, and that the phase of the angular displacement at low frequencies therefore leads the phase of the basal plate velocity by 45 degrees.

In section 5.4, we characterize the low frequency response of models with inter-plate distances G that are comparable to the body dimension L. We show that, the low frequency ratio of angular displacement to basal plate velocity of models with $G \approx L$ approaches a constant, and that the angular displacement at low frequencies is therefore in phase with the velocity of the basal plate.

Since the results for $G \rightarrow \infty$ and for $G \approx L$ are different, we analyze a third case of models with large (but finite) G in section 5.5. For $G >> L$, two distinct low frequency response regimes emerge. In the lowest frequency regime, the angular displacement of the body is proportional to (and in phase with) the imposed plate velocities. This frequency regime corresponds to the "velocity" sensor regime and is limited to frequencies smaller than the frequency for which the boundary layer thickness is equal to the interplate distance G. In the second frequency regime, in which boundary layer thickness is small relative to G but large relative to the size of the body L, the phase of the angular displacement of the body leads that of the imposed plate velocities by 45 degrees. This second frequency regime is increasingly important as the ratio of $G/L \rightarrow \infty$ and corresponds to the low frequency result for free-standing stereocilia.

5.1 SOLUTION BY SERIES EXPANSION IN FREQUENCY

5.1.1 METHOD

The equations of motion for the hinged body (Table 4.3) depend on the frequency at which the plates are vibrated (ω). For asymptotically low frequencies of excitation, some of the terms in the equations of motion have infinitesimal amplitudes. If these are ignored, the resulting simpler set of equations can be solved to yield the asymptotic low frequency relationships between excitation (U_b and U_t) and response ($\Theta(\omega)$).

In this section, we identify the dominant terms of the equations of motion for low frequency excitation by expressing each of the hydrodynamical and mechanical variables in an ascending power series of ω. The series expansions for the hydrodynamical and mechanical variables are then substituted into the equations of motion, and terms in each equation that have equal powers of ω are equated. This process results in a sequence of simpler sets of equations -- each set of equations describing progressively higher order terms in the power series expansions. The low order sets of equations are solved (in sections 5.3, 5.4, and 5.5) and the low frequency asymptotic relationships between the angular displacement of the body ($\Theta(\omega)$) and the velocities of the plates (U_b and U_t) are developed.

We apply the series expansion technique discussed above to solve each of the three sets of component equations of motion (4.45)-(4.59). The expansion technique could equally be applied directly to the composite equations of motion in Table 4.3, however, we have found that the explicit development of asymptotic expressions for each of the components illustrated in Figure 4.3 gives intuition about the equations of motion.

5.1.2 B-COMPONENT

The "distant" boundary condition that excites the B-component of the equations of motion (Equation (4.47)) is a velocity $\bar{V}_B(\bar{x},\omega)$ that depends on both frequency (ω) and distance from the basal plate (y). Expand $\bar{V}_B(\bar{x},\omega)$ in a power series in $(j\omega)^{1/2}$ about $\omega=0$,

$$\bar{V}_B(\bar{x},\omega) = \sum_{n=0}^{\infty} (j\omega)^{n/2} \bar{V}_{Bn}(y) \tag{5.1}$$

so that none of the coefficient fields $\bar{V}_{B0}(y)$, $\bar{V}_{B1}(y)$, $\bar{V}_{B2}(y)$, ... depend on frequency. The low order terms of Equation (5.1) can be used to approximate the solution to Equations (4.45)-(4.49) for sufficiently low frequencies of excitation.

The equations of motion (4.45)-(4.49) explicitly depend on the frequency of excitation (ω in Equation (4.45)). To approximate the solution to Equations (4.45)-(4.49) at low frequencies, expand each of the dependent variables in Equations (4.45)-(4.49) in a power series with a form similar to that of Equation (5.1).

$$\bar{U}_B(\bar{x},\omega) = \bar{U}_{B0}(\bar{x}) + (j\omega)^{1/2} \bar{U}_{B1}(\bar{x}) + (j\omega)^{2/2} \bar{U}_{B2}(\bar{x}) + \cdots \tag{5.2}$$

$$P_B(\bar{x},\omega) = P_{B0}(\bar{x}) + (j\omega)^{1/2} P_{B1}(\bar{x}) + (j\omega)^{2/2} P_{B2}(\bar{x}) + \cdots \tag{5.3}$$

$$T_B(\omega) = T_{B0} + (j\omega)^{1/2} T_{B1} + (j\omega)^{2/2} T_{B2} + \cdots \tag{5.4}$$

where none of the amplitudes ($\bar{U}_{B0}(\bar{x})$, $\bar{U}_{B1}(\bar{x})$, $\bar{U}_{B2}(\bar{x})$, ..., $P_{B0}(\bar{x})$, $P_{B1}(\bar{x})$, $P_{B2}(\bar{x})$, ..., T_{B0}, T_{B1}, T_{B2}, ...) depend on ω. Substituting Equations (5.1)-(5.4) into Equations (4.45)-(4.49) and equating terms in each equation that are of equal order $(j\omega)^{n/2}$ generates a sequence of simpler sets of equations.

$(j\omega)^0$:

$$\bar{0} = -\nabla P_{B0}(\bar{x}) + \mu\nabla^2 \bar{U}_{B0}(\bar{x}) \quad ; \ \bar{x} \text{ in the fluid domain} \tag{5.5}$$

$$\nabla \cdot \bar{U}_{B0}(\bar{x}) = 0 \quad ; \ \bar{x} \text{ in the fluid domain} \tag{5.6}$$

$$\bar{U}_{B0}(\bar{x}) = \bar{V}_{B0}(y) \quad ; \ \{y=0,G\} \text{ or } \{x,z\rightarrow\infty\} \tag{5.7}$$

$$\bar{U}_{B0}(\bar{x}) = U_b\hat{x} \quad ; \ \bar{x} \text{ in } \{R\} \tag{5.8}$$

$$T_{B0} = \hat{z}\cdot\left[\int_R \bar{r}\times\left[-P_{B0}(\bar{x})\overline{dR} + \mu\overline{dR}\cdot\nabla\bar{U}_{B0}(\bar{x})\right]\right] \tag{5.9}$$

$(j\omega)^{1/2}$:

$$\bar{0} = -\nabla P_{B1}(\bar{x}) + \mu\nabla^2 \bar{U}_{B1}(\bar{x}) \quad ; \ \bar{x} \text{ in the fluid domain} \tag{5.10}$$

$$\nabla \cdot \bar{U}_{B1}(\bar{x}) = 0 \quad ; \ \bar{x} \text{ in the fluid domain} \tag{5.11}$$

$$\bar{U}_{B1}(\bar{x}) = \bar{V}_{B1}(y) \quad ; \ \{y=0,G\} \text{ or } \{x,z\rightarrow\infty\} \tag{5.12}$$

$$\bar{U}_{B1}(\bar{x}) = \bar{0} \quad ; \ \bar{x} \text{ in } \{R\} \tag{5.13}$$

$$T_{B1} = \hat{z}\cdot\left[\int_R \bar{r}\times\left[-P_{B1}(\bar{x})\overline{dR} + \mu\overline{dR}\cdot\nabla\bar{U}_{B1}(\bar{x})\right]\right] \tag{5.14}$$

$(j\omega)^{n/2}$: $n>1$

$$\rho\bar{U}_{B(n-2)}(\bar{x}) = -\nabla P_{Bn}(\bar{x}) + \mu\nabla^2 \bar{U}_{Bn}(\bar{x}) \quad ; \ \bar{x} \text{ in the fluid domain} \tag{5.15}$$

$$\nabla \cdot \bar{U}_{Bn}(\bar{x}) = 0 \quad ; \ \bar{x} \text{ in the fluid domain} \tag{5.16}$$

$$\bar{U}_{Bn}(\bar{x}) = \bar{V}_{Bn}(y) \quad ; \ \{y=0,G\} \text{ or } \{x,z\rightarrow\infty\} \tag{5.17}$$

$$\bar{U}_{Bn}(\bar{x}) = \bar{0} \quad ; \ \bar{x} \text{ in } \{R\} \tag{5.18}$$

$$T_{Bn} = \hat{z}\cdot\left[\int_R \bar{r}\times\left[-P_{Bn}(\bar{x})\overline{dR} + \mu\overline{dR}\cdot\nabla\bar{U}_{Bn}(\bar{x})\right]\right] \tag{5.19}$$

5.1.2.1 EACH TERM IN THE POWER SERIES EXPANSIONS IS COMPLETELY DETERMINED BY FREQUENCY-INDEPENDENT EQUATIONS

None of Equations (5.5)-(5.19) depend on frequency (ω). All of Equations (5.5)-(5.19) are thus similar in form to equations that describe the steady motion of fluid.

5.1.2.2 INERTIAL AND VISCOUS TERMS ARE DE-COUPLED

The momentum equation for a Newtonian fluid expresses a balance between forces due to fluid inertia, forces due to fluid viscosity, and forces due to pressure gradients (Equation (4.45)). The role of fluid inertia in Equations (5.5)-(5.19) is different. The first term in Equation (5.15) -- which is proportional to fluid density and derives from the inertial term ($j\omega\rho\bar{U}_B(\bar{x},\omega)$) in Equation (4.45) -- is <u>not</u> a dependent variable. The first term in Equation (5.15) for n=2 is the solution to Equations (5.5)-(5.9). The first term in Equation (5.15) for n=3 is the solution to Equations (5.10)-(5.14). The first term in Equation (5.15) for n=4 is the solution to Equations (5.15)-(5.19) for n=2. The density dependent terms in Equations (5.5)-(5.19) -- $\rho\bar{U}_{B0}(\bar{x})$, $\rho\bar{U}_{B1}(\bar{x})$, $\rho\bar{U}_{B2}(\bar{x})$, ... -- have the form of driving forces that are distributed over the body of the fluid.

5.1.3 T-COMPONENT

Expand each of the variables in the equations that define the T-component (4.50)-(4.54) in series analogous to those defined in Equations (5.1)-(5.4) for the B-component.

$$\bar{V}_T(\bar{x},\omega) = \sum_{n=0}^{\infty} (j\omega)^{n/2}\, \bar{V}_{Tn}(y) \tag{5.20}$$

$$\bar{U}_T(\bar{x},\omega) = \bar{U}_{T0}(\bar{x}) + (j\omega)^{1/2}\bar{U}_{T1}(\bar{x}) + (j\omega)^{2/2}\bar{U}_{T2}(\bar{x}) + \cdots \tag{5.21}$$

$$P_T(\bar{x},\omega) = P_{T0}(\bar{x}) + (j\omega)^{1/2}_{1/2} P_{T1}(\bar{x}) + (j\omega)^{2/2}_{2/2} P_{T2}(\bar{x}) + \cdots \tag{5.22}$$

$$T_T(\omega) = T_{T0} + (j\omega)^{1/2} T_{T1} + (j\omega)^{2/2} T_{T2} + \cdots \tag{5.23}$$

Substituting Equations (5.20)-(5.23) into Equations (4.50)-(4.54) and collecting terms of equal order $(j\omega)^{n/2}$ generates a sequence of simpler sets of equations.

$(j\omega)^0$:

$$\bar{0} = -\nabla P_{T0}(\bar{x}) + \mu\nabla^2 \bar{U}_{T0}(\bar{x}) \quad ; \ \bar{x} \text{ in the fluid domain} \tag{5.24}$$

$$\nabla \cdot \bar{U}_{T0}(\bar{x}) = 0 \quad ; \ \bar{x} \text{ in the fluid domain} \tag{5.25}$$

$$\bar{U}_{T0}(\bar{x}) = \bar{V}_{T0}(y) \quad ; \ \{y=0,G\} \text{ or } \{x,z\to\infty\} \tag{5.26}$$

$$\bar{U}_{T0}(\bar{x}) = \bar{0} \quad ; \ \bar{x} \text{ in } \{R\} \tag{5.27}$$

$$T_{T0} = \hat{z}\cdot\left[\int_R \bar{r}\times\left[-P_{T0}(\bar{x})\overline{dR} + \mu\overline{dR}\cdot\nabla\bar{U}_{T0}(\bar{x})\right]\right] \tag{5.28}$$

$(j\omega)^{1/2}$:

$$\bar{0} = -\nabla P_{T1}(\bar{x}) + \mu\nabla^2 \bar{U}_{T1}(\bar{x}) \quad ; \ \bar{x} \text{ in the fluid domain} \tag{5.29}$$

$$\nabla \cdot \bar{U}_{T1}(\bar{x}) = 0 \quad ; \ \bar{x} \text{ in the fluid domain} \tag{5.30}$$

$$\bar{U}_{T1}(\bar{x}) = \bar{V}_{T1}(y) \quad ; \ \{y=0,G\} \text{ or } \{x,z\to\infty\} \tag{5.31}$$

$$\bar{U}_{T1}(\bar{x}) = \bar{0} \quad ; \ \bar{x} \text{ in } \{R\} \tag{5.32}$$

$$T_{T1} = \hat{z}\cdot\left[\int_R \bar{r}\times\left[-P_{T1}(\bar{x})\overline{dR} + \mu\overline{dR}\cdot\nabla\bar{U}_{T1}(\bar{x})\right]\right] \tag{5.33}$$

$(j\omega)^{n/2}$: $n>1$

$$\rho\bar{U}_{T(n-2)}(\bar{x}) = -\nabla P_{Tn}(\bar{x}) + \mu\nabla^2 \bar{U}_{Tn}(\bar{x}) \quad ; \ \bar{x} \text{ in the fluid domain} \tag{5.34}$$

$$\nabla \cdot \bar{U}_{Tn}(\bar{x}) = 0 \quad ; \ \bar{x} \text{ in the fluid domain} \tag{5.35}$$

$$\bar{U}_{Tn}(\bar{x}) = \bar{V}_{Tn}(y) \quad ; \ \{y=0,G\} \text{ or } \{x,z\to\infty\} \tag{5.36}$$

$$\bar{U}_{Tn}(\bar{x}) = \bar{0} \quad ; \ \bar{x} \text{ in } \{R\} \tag{5.37}$$

$$T_{Tn} = \hat{z}\cdot\left[\int_R \bar{r}\times\left[-P_{Tn}(\bar{x})\overline{dR} + \mu\overline{dR}\cdot\nabla\bar{U}_{Tn}(\bar{x})\right]\right] \tag{5.38}$$

The equations that describe the series expansion of the T-component are very similar to those that describe the B-component. Each of Equations (5.20)-(5.38) are identical in form with the corresponding equation in the set (5.1)-(5.19) with the exception of Equation (5.27). The velocity of the rigid body is equal to that of the basal plate (in the absence of rotation about the hinge) so that the zeroth order boundary conditions for the fluid adjacent to the rigid body are different for the B- and T-components.

5.1.4 R-COMPONENT

Expand each of the variables in the equations that define the R-component (4.55)-(4.59) in series analogous to those defined in Equations (5.1)-(5.4) for the B-component.

$$\bar{U}_R(\bar{x},\omega) = \bar{U}_{R0}(\bar{x}) + (j\omega)^{1/2}_{1/2}\bar{U}_{R1}(\bar{x}) + (j\omega)^{2/2}_{2/2}\bar{U}_{R2}(\bar{x}) + \cdots \quad (5.39)$$

$$P_R(\bar{x},\omega) = P_{R0}(\bar{x}) + (j\omega)^{1/2}_{1/2}P_{R1}(\bar{x}) + (j\omega)^{2/2}_{2/2}P_{R2}(\bar{x}) + \cdots \quad (5.40)$$

$$T_R(\omega) = T_{R0} + (j\omega)^{1/2}T_{R1} + (j\omega)^{2/2}T_{R2} + \cdots \quad (5.41)$$

Substituting Equations (5.39)-(5.41) into Equations (4.55)-(4.59) and collecting terms of equal order $(j\omega)^{n/2}$ generates a sequence of simpler sets of equations.

$(j\omega)^{n/2}$:

$$\bar{0} = -\nabla P_{Rn}(\bar{x}) + \mu\nabla^2\bar{U}_{Rn}(\bar{x}) \quad ; \bar{x} \text{ in the fluid domain} \quad (5.42)$$

n=0,1,

$$\nabla\cdot\bar{U}_{Rn}(\bar{x}) = 0 \quad ; \bar{x} \text{ in the fluid domain} \quad (5.43)$$

3,5,...

$$\bar{U}_{Rn}(\bar{x}) = \bar{0} \quad ; \{y=0,G\} \text{ or } \{x,z\to\infty\} \quad (5.44)$$

$$\bar{U}_{Rn}(\bar{x}) = \bar{0} \quad ; \bar{x} \text{ in } \{R\} \quad (5.45)$$

$$T_{Rn} = \hat{z}\cdot\left[\int_R \bar{r}\times\left[-P_{Rn}(\bar{x})\overline{dR} + \mu\overline{dR}\cdot\nabla\bar{U}_{Rn}(\bar{x})\right]\right] \quad (5.46)$$

$(j\omega)^{2/2}$:

$$\bar{0} = -\nabla P_{R2}(\bar{x}) + \mu\nabla^2\bar{U}_{R2}(\bar{x}) \quad ; \bar{x} \text{ in the fluid domain} \quad (5.47)$$

$$\nabla\cdot\bar{U}_{R2}(\bar{x}) = 0 \quad ; \bar{x} \text{ in the fluid domain} \quad (5.48)$$

$$\bar{U}_{R2}(\bar{x}) = \bar{0} \quad ; \{y=0,G\} \text{ or } \{x,z\to\infty\} \quad (5.49)$$

$$\bar{U}_{R2}(\bar{x}) = \Theta(\omega)\,\hat{z}\times\bar{r} \quad ; \bar{x} \text{ in } \{R\} \quad (5.50)$$

$$T_{R2} = \hat{z}\cdot\left[\int_R \bar{r}\times\left[-P_{R2}(\bar{x})\overline{dR} + \mu\overline{dR}\cdot\nabla\bar{U}_{R2}(\bar{x})\right]\right] \quad (5.51)$$

$(j\omega)^{n/2}$:

$$\rho\bar{U}_{R(n-2)}(\bar{x}) = -\nabla P_{Rn}(\bar{x}) + \mu\nabla^2\bar{U}_{Rn}(\bar{x}) \quad ; \bar{x} \text{ in the fluid domain} \quad (5.52)$$

n=4,6,

$$\nabla\cdot\bar{U}_{Rn}(\bar{x}) = 0 \quad ; \bar{x} \text{ in the fluid domain} \quad (5.53)$$

8,...

$$\bar{U}_{Rn}(\bar{x}) = \bar{0} \quad ; \{y=0,G\} \text{ or } \{x,z\to\infty\} \quad (5.54)$$

$$\bar{U}_{Rn}(\bar{x}) = \bar{0} \quad ; \bar{x} \text{ in } \{R\} \quad (5.55)$$

$$T_{Rn} = \hat{z}\cdot\left[\int_R \bar{r}\times\left[-P_{Rn}(\bar{x})\overline{dR} + \mu\overline{dR}\cdot\nabla\bar{U}_{Rn}(\bar{x})\right]\right] \quad (5.56)$$

Equations (5.42)-(5.46) have homogeneous boundary conditions. The solution to Equations (5.42)-(5.46)

$$\left.\begin{aligned} U_{Rn}(\bar{x}) &= \bar{0} \\ P_{Rn}(\bar{x}) &= P_{Rn} = \text{constant} \\ T_{Rn}(\bar{x}) &= 0 \end{aligned}\right| \quad ; n = 0, 1, 3, 5, 7, \ldots \quad (5.57)$$

plays no role in determining the hydrodynamic torque on the rigid body.

The explicit $(j\omega)$ in the boundary equation (4.58) implies that the first occurance of non-homogeneous boundary conditions for the R-component occurs for the $(j\omega)^{2/2}$ order term (Equation (5.50)).

5.1.5 SUMMARY

In this section, we have shown that the solutions to the B-, T-, and R-component equations of motion can be determined in steps. First, compute the fluid motion that would have occured if the excitation frequency ω had been zero (Equations (5.5)-(5.9) for the B-component). The solution for $\omega=0$ specifies the $(j\omega)^{0/2}$ terms in the series expansions of the hydrodynamical variables (Equations (5.2)-(5.4) for the B-component). Next, compute the solution to a second set of steady equations of motion (Equations (5.10)-(5.14) for the B-component) whose (constant) driving functions differ from those of the $\omega=0$ equations. The solution to this second set of equations specifies the $(j\omega)^{1/2}$ terms in the series expansions of the hydrodynamical variables. Next, compute the solution to a third set of steady equations of motion (Equations (5.15)-(5.19) with n=2, for the B-component) whose driving functions differ from those in either the first or the second set. The solution to this third set of equations specifies the $(j\omega)^{2/2}$ terms in the series expansions of the hydrodynamical variables. This process generates expressions (Equations (5.2)-(5.4) for the B-component) for the solution to the frequency-dependent equations of motion in terms of the solutions to steady equations of motion.

We wish to use the low order terms of the series expansions to derive approximations to the solution of the frequency-dependent equations of motion that are valid for asymptotically low frequencies of excitation. In the next section, we discuss the effect of truncating the infinite series expansions to a finite number of terms.

5.2 CHARACTERIZATION OF THE SERIES

In section 5.1, each of the component equations of motion (e.g. Equations (4.45)-(4.49) for the B-component) were replaced by a sequence of simpler sets of equations (Equations (5.5)-(5.19) for the B-component). The solutions to these simpler equations are meaningful however only if the series expansions for the hydrodynamical and mechanical variables (Equations (5.1)-(5.4)) converge. Further, the extent to which the low frequency asymptotic behavior of the underlying equations of motion (Equations (4.45)-(4.49)) is adequately described by the low order sets of equations (Equations (5.5)-(5.14)) depends on the rate of convergence of the series in Equations (5.1)-(5.4).

In this section, we establish bounds on the error generated by truncation of the series in Equations (5.1)-(5.4). We show that there are two distinct sources of truncation error and we outline methods by which the magnitudes of each of the errors can be estimated. The methods of this section are then used (in sections 5.3, 5.4, and 5.5) to bound the range of frequencies for which the solution to the underlying equations of motion can be approximated by the low order terms of Equations (5.1)-(5.4).

5.2.1 GRAPHICAL REPRESENTATION OF THE SERIES EXPANSIONS

We begin by generating graphical representations of the series expansions of the previous section that are useful for understanding the sources of error incurred by truncation of the series expansions.

Consider the B-component equations of motion (Equations (5.5)-(5.19)). At each order n, those equations are excited by constant terms ($\bar{V}_{B0}(y)$ in Equation (5.7), $U_b\hat{x}$ in Equation (5.8), $\bar{V}_{B1}(y)$ in Equation (5.12), and $\bar{V}_{Bn}(y)$ in Equation (5.17)) and by the solution to Equations (5.5)-(5.19) at lower order ($\bar{U}_{B(n-2)}(\bar{x})$ in Equation (5.15)). These equations for the B-component (5.5)-(5.19), as well as those for the T-component ((5.24)-(5.38)) and those for the R-component ((5.42)-(5.56)) can be expressed as a superposition of linear operators that act on excitatory terms. Define $L_1\{\bar{U}(\bar{x})\}$ so that

$$\bar{U}_2(\bar{x}) = L_1\{\bar{U}_1(\bar{x})\} \tag{5.58}$$

represents the relationships in Equations (5.59)-(5.62).

$$\rho\bar{U}_1(\bar{x}) = -\nabla P_2(\bar{x}) + \mu\nabla^2\bar{U}_2(\bar{x}) \quad ; \ \bar{x} \text{ in the fluid domain} \tag{5.59}$$

$$\nabla \cdot \bar{U}_2(\bar{x}) = 0 \quad ; \ \bar{x} \text{ in the fluid domain} \tag{5.60}$$

$$\bar{U}_2(\bar{x}) = \bar{0} \quad ; \ \{y = 0,G\} \text{ or } \{x,z \to \infty\} \tag{5.61}$$

$$\bar{U}_2(\bar{x}) = \bar{0} \quad ; \ \bar{x} \text{ in } \{R\} \tag{5.62}$$

Define $L_2\{\bar{U}(\bar{x})\}$ so that

$$\bar{U}_4(\bar{x}) = L_2\{\bar{U}_3(\bar{x})\} \tag{5.63}$$

represents the relationships in Equations (5.64)-(5.67)

$$\bar{0} = -\nabla P_4(\bar{x}) + \mu\nabla^2\bar{U}_4(\bar{x}) \quad ; \ \bar{x} \text{ in the fluid domain} \tag{5.64}$$

$$\nabla \cdot \bar{U}_4(\bar{x}) = 0 \quad ; \ \bar{x} \text{ in the fluid domain} \tag{5.65}$$

$$\bar{U}_4(\bar{x}) = \bar{U}_3(\bar{x}) \quad ; \ \{y = 0,G\} \text{ or } \{x,z \to \infty\} \tag{5.66}$$

$$\bar{U}_4(\bar{x}) = \bar{0} \quad ; \ \bar{x} \text{ in } \{R\} \tag{5.67}$$

Define $L_3\{\bar{U}(\bar{x})\}$ so that

$$\bar{U}_6(\bar{x}) = L_3\{\bar{U}_5(\bar{x})\} \tag{5.68}$$

represents the relationships in Equations (5.69)-(5.72).

$$\bar{0} = -\nabla P_6(\bar{x}) + \mu\nabla^2\bar{U}_6(\bar{x}) \quad ; \ \bar{x} \text{ in the fluid domain} \tag{5.69}$$

$$\nabla \cdot \bar{U}_6(\bar{x}) = 0 \quad ; \ \bar{x} \text{ in the fluid domain} \tag{5.70}$$

$$\bar{U}_6(\bar{x}) = \bar{0} \quad ; \ \{y = 0, G\} \text{ or } \{x, z \to \infty\} \tag{5.71}$$

$$\bar{U}_6(\bar{x}) = \bar{U}_5(\bar{x}) \quad ; \ \bar{x} \text{ in } \{R\} \tag{5.72}$$

All three linear operators (L_1, L_2, and L_3) are independent of ω (i.e. time-independent) and characterize the steady motion of fluid that is generated by a single excitatory velocity field.

5.2.1.1 B-COMPONENT

By superposition, Equations (5.5)-(5.19) can be written in terms of L_1, L_2, and L_3.

$$\bar{U}_{B0}(\bar{x}) = L_2\{\bar{V}_{B0}(y)\} + L_3\{U_b\hat{x}\} \tag{5.73}$$

$$\bar{U}_{B1}(\bar{x}) = L_2\{\bar{V}_{B1}(y)\} \tag{5.74}$$

$$\bar{U}_{Bn}(\bar{x}) = L_1\{\bar{U}_{B(n-2)}(\bar{x})\} + L_2\{\bar{V}_{Bn}(y)\} \quad ; \ n > 1 \tag{5.75}$$

Equations (5.73)-(5.75) are depicted graphically in Figure 5.1. Since the linear operators L_1, L_2, and L_3 are indepedent of ω, and the excitation fields $\bar{V}_{Bn}(y)$ and $U_b\hat{x}$ are independent of ω, all of the component velocity fields $\bar{U}_{Bn}(\bar{x})$ are independent of ω. The dependence of $\bar{U}_B(\bar{x},\omega)$ on ω enters through the explicit terms $(j\omega)^{n/2}$ alone.

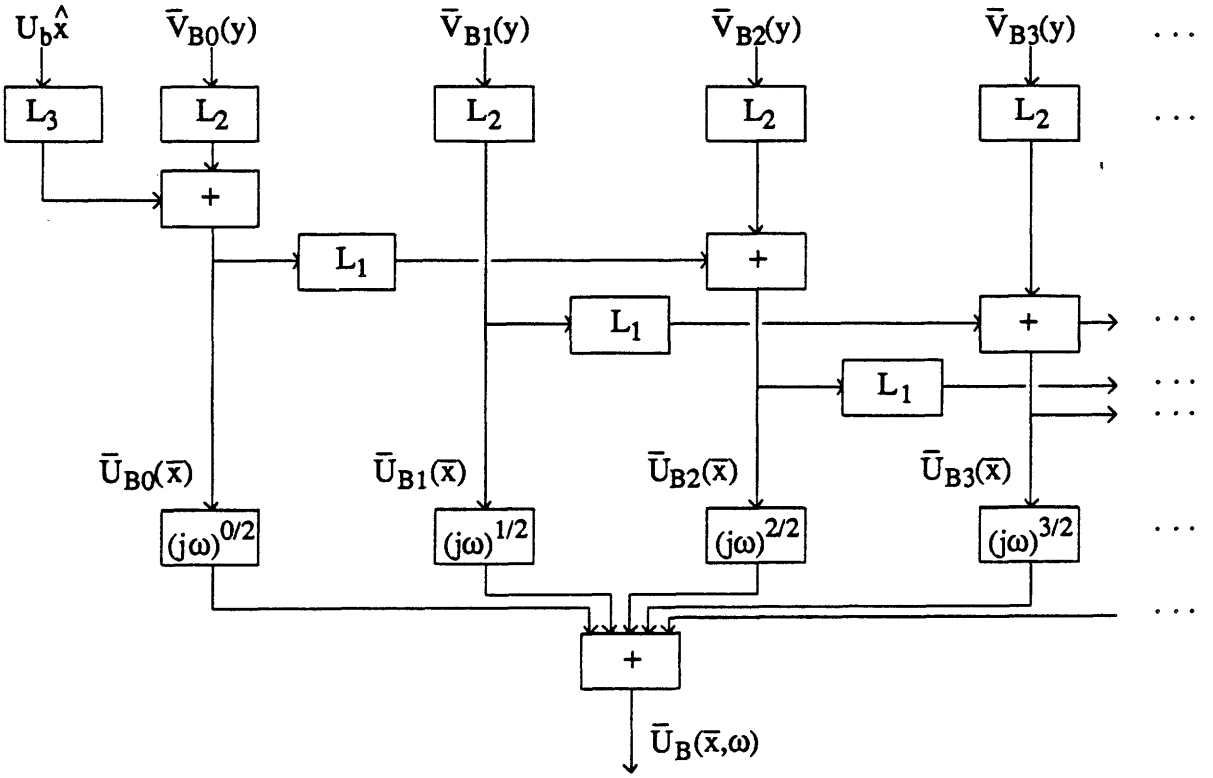

Figure 5.1: Graphical representation of Equations (5.73)-(5.75)

5.2.1.2 T-COMPONENT

By similar reasoning, the equations describing the T-component ((5.24)-(5.38)) can be written in terms of L_1, L_2, and L_3.

$$\bar{U}_{T0}(\bar{x}) = L_2\{\bar{V}_{T0}(y)\} \tag{5.76}$$

$$\bar{U}_{T1}(\bar{x}) = L_2\{\bar{V}_{T1}(y)\} \tag{5.77}$$

$$\bar{U}_{Tn}(\bar{x}) = L_1\{\bar{U}_{T(n-2)}(\bar{x})\} + L_2\{\bar{V}_{Tn}(y)\} \quad ; n > 1 \tag{5.78}$$

Equations (5.76)-(5.78) are depicted graphically in Figure 5.2.

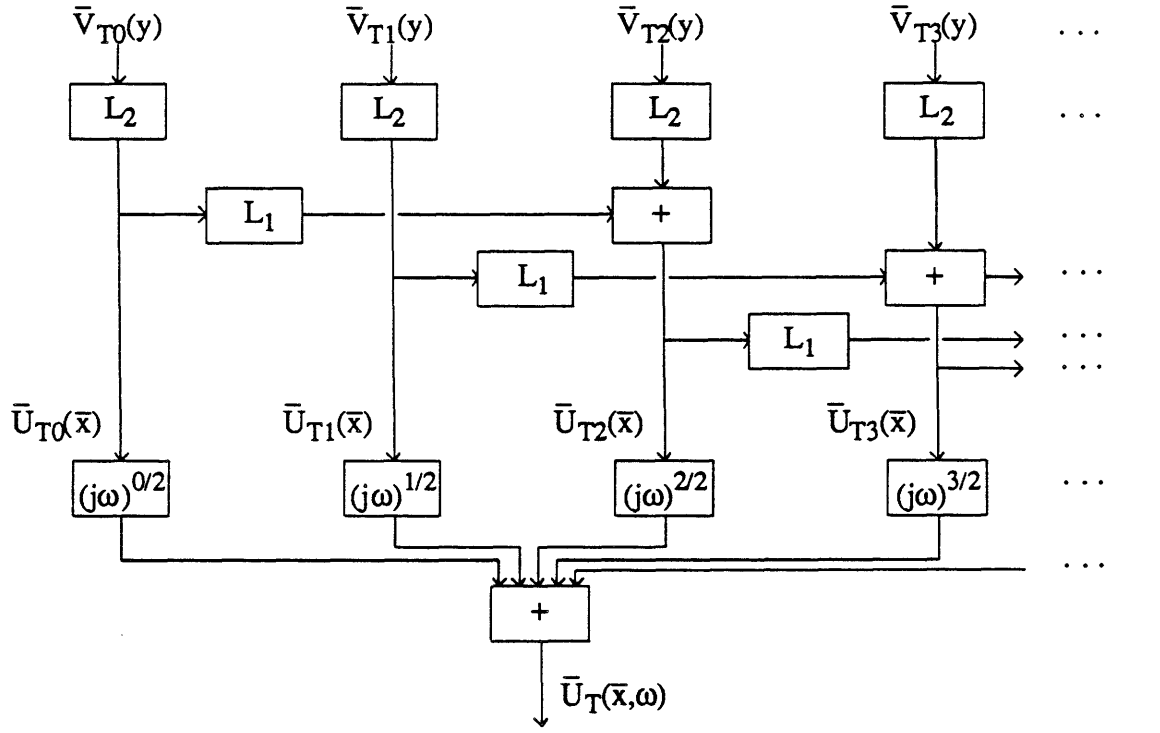

Figure 5.2: Graphical representation of Equations (5.76)-(5.78).

The system illustrated in Figure 5.2 is structurally similar to that in Figure 5.1 -- differing only by the omission of the $L_3\{U_b\hat{x}\}$ term.

5.2.1.3 R-COMPONENT

The equations describing the R-component (Equations (5.42)-(5.56)) can also be written in terms of L_1, L_2, and L_3.

$$\bar{U}_{R2}(\bar{x}) = L_3\{\Theta(\omega)\,\hat{z}\times\bar{r}\} \tag{5.79}$$

$$\bar{U}_{Rn}(\bar{x}) = L_1\{\bar{U}_{R(n-2)}(\bar{x})\} \qquad ;\ n = 4, 6, 8, \ldots \tag{5.80}$$

Equations (5.79)-(5.80) are depicted graphically in Figure 5.3.

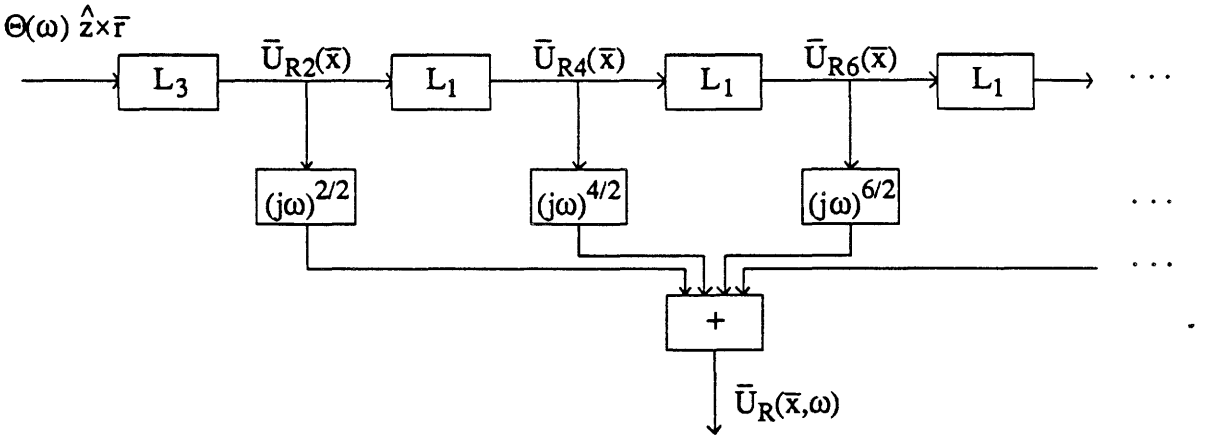

Figure 5.3: Graphical representation of Equations (5.79)-(5.80)

The structures of the systems illustrated in Figure 5.2 and 5.3 are subsets of that illustrated in Figure 5.1.

5.2.2 CONVERGENCE OF THE SERIES

In this section, we establish conditions for the convergence of the series that were generated in section 5.1. Because the structure of the series expansion of the T-component (Figure 5.2) and that of the R-component (Figure 5.3) are subsets of the structure of the series expansion of the B-component (Figure 5.1), we treat only the B-component explicitly in this section. The results for the T- and R-components are analogous to those for the B-component.

Figure 5.4 shows a functionally equivalent reorganization of the elements of Figure 5.1. Since the definitions of each of L_1, L_2, and L_3 are similar in form to equations of steady fluid motion, we take (without proof) that each of these operators produce bounded outputs when applied to an input field that is bounded. With that assumption, the only possibly divergent signal path through Figure 5.4 is through the infinite cascade of transformations $j\omega L_1$. Therefore, if

$$\bar{S}_n(\bar{x}) = \bar{V}_1(\bar{x}) + j\omega L_1 \bar{V}_1(\bar{x}) + (j\omega L_1)^2 \bar{V}_1(\bar{x}) + \cdots + (j\omega L_1)^n \bar{V}_1(\bar{x}) \tag{5.81}$$

converges at all points $\bar{x}$ and for all possible fields $\bar{V}_1(\bar{x})$, it follows that the series expansion for $\bar{U}_B(\bar{x},\omega)$ illustrated in Figure 5.4 must converge. The ratio test for convergence guarantees that $\bar{S}_n(\bar{x})$ converges with increasing n so long as

$$\lim_{n\to\infty} \omega \left| \frac{L_1^{n+1}\bar{V}_1(\bar{x})}{L_1^n \bar{V}_1(\bar{x})} \right| < 1 \tag{5.82}$$

In the next section, we establish a maximum value of the term enclosed in bars in Equation (5.82) and thereby establish that the series expansion of $\bar{U}_B(\bar{x},\omega)$ converges for at least some finite range of low frequencies.

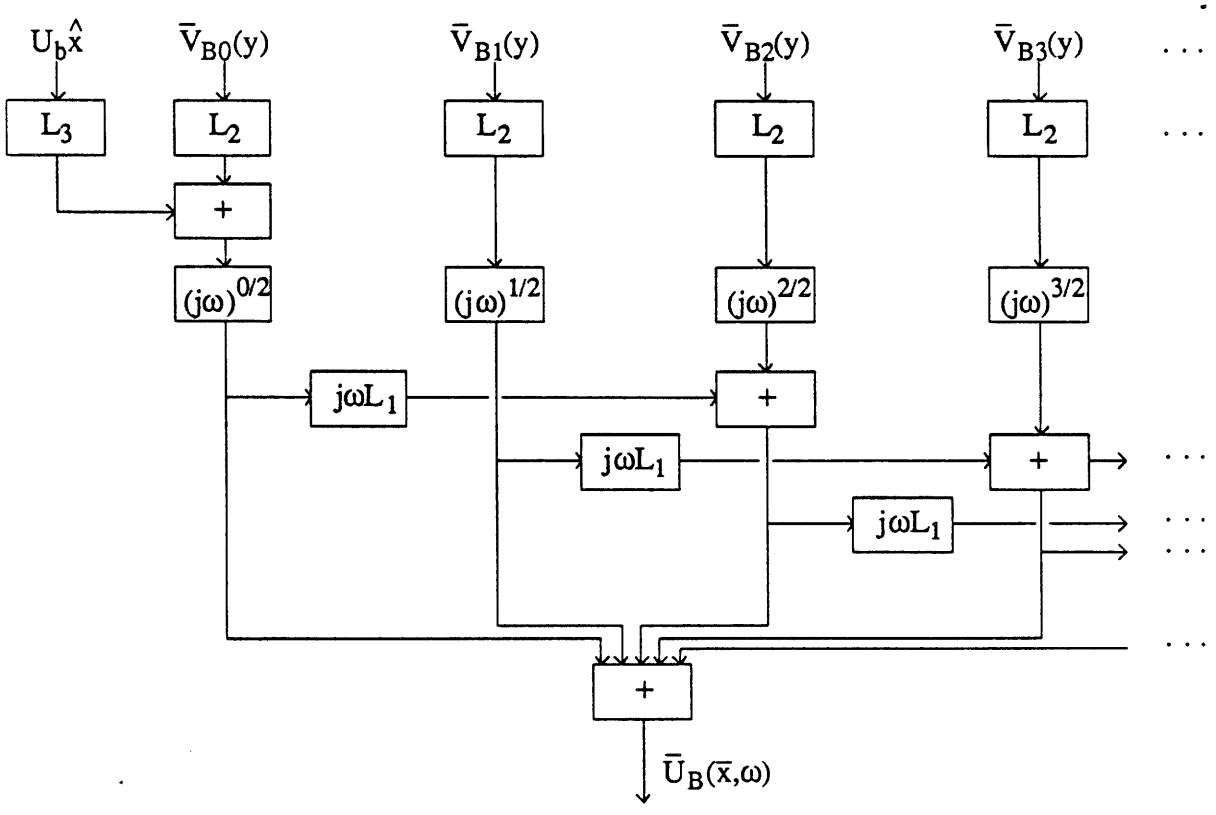

Figure 5.4: Alternative representation for the series expansion of $\bar{U}_B(\bar{x},\omega)$ in Equations (5.73)-(5.75).

5.2.2.1 SPATIAL FOURIER ANALYSIS OF L_1

Consider decomposing $\bar{V}_1(\bar{x})$ in Equation (5.82) into spatial Fourier components. Since the operator L_1 is linear, applying L_1 to a single spatial Fourier component merely multiplies that component by a scalar. After applying L_1 many times, the magnitude of some "fastest growing" spatial component will dominate the magnitudes of all other components at all points in space. The maximum value of the term enclosed by bars in Equation (5.82) will be less than or equal to the magnitude of the factor by which the fastest growing spatial component increases when that component is operated on by L_1.

We begin by decomposing each of $\bar{U}_1(\bar{x})$, $\bar{U}_2(\bar{x})$, and $P_2(\bar{x})$ in the definition of L_1 (Equations (5.59)-(5.62)) into spatial Fourier components.

$$\bar{U}_1(\bar{x}) = \iiint \left[\bar{\bar{U}}_1(\alpha,\beta,\gamma)\hat{x} + \bar{\bar{V}}_1(\alpha,\beta,\gamma)\hat{y} + \bar{\bar{W}}_1(\alpha,\beta,\gamma)\hat{z} \right] e^{j\alpha x} e^{j\beta y} e^{j\gamma z}\, dx\, dy\, dz \qquad (5.83)$$

$$\bar{U}_2(\bar{x}) = \iiint \left[\bar{\bar{U}}_2(\alpha,\beta,\gamma)\hat{x} + \bar{\bar{V}}_2(\alpha,\beta,\gamma)\hat{y} + \bar{\bar{W}}_2(\alpha,\beta,\gamma)\hat{z} \right] e^{j\alpha x} e^{j\beta y} e^{j\gamma z}\, dx\, dy\, dz \qquad (5.84)$$

$$P_2(\bar{x}) = \iiint \bar{\bar{P}}_2(\alpha,\beta,\gamma)\, e^{j\alpha x} e^{j\beta y} e^{j\gamma z}\, dx\, dy\, dz \qquad (5.85)$$

Each of the amplitudes $\bar{\bar{U}}_1(\alpha,\beta,\gamma)$, $\bar{\bar{V}}_1(\alpha,\beta,\gamma)$, $\bar{\bar{W}}_1(\alpha,\beta,\gamma)$, $\bar{\bar{U}}_2(\alpha,\beta,\gamma)$, $\bar{\bar{V}}_2(\alpha,\beta,\gamma)$, $\bar{\bar{W}}_2(\alpha,\beta,\gamma)$, and $\bar{\bar{P}}_2(\alpha,\beta,\gamma)$ are (possibly complex-valued) scalar functions of α, β, and γ. In subsequent references, the explicit functional dependence will be dropped, and these amplitudes will be refered to as $\bar{\bar{U}}_1$, $\bar{\bar{V}}_1$, $\bar{\bar{W}}_1$, $\bar{\bar{U}}_2$, $\bar{\bar{V}}_2$, $\bar{\bar{W}}_2$, and $\bar{\bar{P}}_2$.

The spatial transform of the equations that define L_1((5.59)-(5.60)) can be written in matrix form.

$$\begin{bmatrix} -j\alpha & -\mu(\alpha^2+\beta^2+\gamma^2) & 0 & 0 \\ -j\beta & 0 & -\mu(\alpha^2+\beta^2+\gamma^2) & 0 \\ -j\gamma & 0 & 0 & -\mu(\alpha^2+\beta^2+\gamma^2) \\ 0 & \alpha & \beta & \gamma \end{bmatrix} \begin{bmatrix} \bar{\bar{P}}_2 \\ \bar{\bar{U}}_2 \\ \bar{\bar{V}}_2 \\ \bar{\bar{W}}_2 \end{bmatrix} = \begin{bmatrix} \rho & 0 & 0 \\ 0 & \rho & 0 \\ 0 & 0 & \rho \\ 0 & 0 & 0 \end{bmatrix} \begin{bmatrix} \bar{\bar{U}}_1 \\ \bar{\bar{V}}_1 \\ \bar{\bar{W}}_1 \end{bmatrix} \qquad (5.86)$$

and the solution to Equations (5.86) can be written in closed form.

$$\begin{bmatrix} \bar{\bar{U}}_2 \\ \bar{\bar{V}}_2 \\ \bar{\bar{W}}_2 \end{bmatrix} = \frac{1}{\nu(\alpha^2+\beta^2+\gamma^2)} 2 \begin{bmatrix} (\beta^2+\gamma^2) & -\alpha\beta & -\alpha\gamma \\ -\alpha\beta & (\alpha^2+\gamma^2) & -\beta\gamma \\ -\alpha\gamma & -\beta\gamma & (\alpha^2+\beta^2) \end{bmatrix} \begin{bmatrix} \bar{\bar{U}}_1 \\ \bar{\bar{V}}_1 \\ \bar{\bar{W}}_1 \end{bmatrix} \qquad (5.87)$$

The input vector ($\bar{\bar{U}}_1$, $\bar{\bar{V}}_1$, $\bar{\bar{W}}_1$) and the output vector ($\bar{\bar{U}}_2$,$\bar{\bar{V}}_2$, $\bar{\bar{W}}_2$) can be further decomposed into linear combinations of three eigenvectors defined by the eigenvalue Equation (5.88)

$$s \begin{bmatrix} \bar{\bar{U}} \\ \bar{\bar{V}} \\ \bar{\bar{W}} \end{bmatrix} = \frac{1}{\nu(\alpha^2+\beta^2+\gamma^2)} 2 \begin{bmatrix} (\beta^2+\gamma^2) & -\alpha\beta & -\alpha\gamma \\ -\alpha\beta & (\alpha^2+\gamma^2) & -\beta\gamma \\ -\alpha\gamma & -\beta\gamma & (\alpha^2+\beta^2) \end{bmatrix} \begin{bmatrix} \bar{\bar{U}} \\ \bar{\bar{V}} \\ \bar{\bar{W}} \end{bmatrix} \qquad (5.88)$$

where s is a root of the characteristic equation given in (5.89).

$$s\left[s - \frac{1}{\nu(\alpha^2+\beta^2+\gamma^2)}\right]^2 = 0 \tag{5.89}$$

Each component of the eigenvector decomposition of $(\bar{\bar{U}}_2, \bar{\bar{V}}_2, \bar{\bar{W}}_2)$ is equal to that component of $(\bar{\bar{U}}_1, \bar{\bar{V}}_1, \bar{\bar{W}}_1)$ times the corresponding eigenvalue s. Let s_{max} denote the eigenvalue with the largest magnitude.

$$s_{max} = \frac{1}{\nu(\alpha^2+\beta^2+\gamma^2)} \tag{5.90}$$

The Fourier component corresponding to $\alpha=\beta=\gamma=0$ is excluded by the homogeneous boundary conditions in Equations (5.61)-(5.62). Further, since the domain of the fluid extends over a finite region in y ($0 \leq y \leq G$), β (which is equal to integral multiples of $2\pi/G$) has a magnitude that is greater than or equal to $2\pi/G$. Therefore, s_{max} is less than $G^2/(4\pi^2\nu)$, and we have established a bound on the term enclosed by bars in Equation (5.82) and that the series expansion of $\bar{U}_B(\bar{x},\omega)$ converges at least for all frequencies

$$\omega < \frac{4\pi^2\nu}{G^2} = 2\pi^2\omega_G \qquad ; \omega_G = \frac{2\nu}{G^2} \tag{5.91}$$

where ω_G is the frequency at which the boundary layer thickness is G.

5.2.3 CONCLUSIONS

In section 5.1, we developed a series method for solving the equations of motion for the hinged-body structure (Figure 4.1). In section 5.2, we represented that series method graphically, as a system with multiple inputs (corresponding to the coefficients of the series expansions of the "distant" boundary velocities) that is composed of frequency independent elements (L_1, L_2, and L_3) and frequency dependent elements $((j\omega)^{n/2})$.

By bounding the magnitudes of the velocity fields at critical internal points in the graphical representation, we proved that the series expansions in section 5.1 converge, at least for a finite range of low frequencies (Equation (5.91)). We will use a similar bounding technique in sections 5.3-5.5 to estimate the adequacy with which the solutions to the equations of motion can be approximated by the low order terms of their series expansions.

5.3 LOW-FREQUENCY RELATIONSHIPS FOR FREE-STANDING MODELS

In this section, we apply the method of series expansion that was developed in section 5.1 to determine low frequency asymptotic expressions for the motion of the hinged body in Figure 4.1 when the inter-plate distance G is large. We take the limit as $G\to\infty$ as a model for stereocilia that are free-standing in cochlear fluid and are not in close proximity to other (tectorial) structures.

5.3.1 B-COMPONENT

In the limit as $G\to\infty$, the expression for $\bar{V}_B(\bar{x},\omega)$ in Equation (4.47) can be simplified for bounded values of y.

$$\lim_{G\to\infty} \bar{V}_B(\bar{x},\omega) \equiv \bar{V}_P(\bar{x},\omega) = U_b\, e^{-y\sqrt{j\omega/\nu}}\ \hat{x} \tag{5.92}$$

A power series expansion for Equation (5.92) can be derived from the Taylor expansion of the exponential function.

$$\bar{V}_P(\bar{x},\omega) = \sum_{n=0}^{\infty} (j\omega)^{n/2}\bar{V}_{Pn}(y) = U_b \sum_{n=0}^{\infty} \frac{1}{n!}\left(\frac{j\omega}{\nu}\right)^{n/2}(-y)^n\ \hat{x} \tag{5.93}$$

Substituting $\bar{V}_{Bn}(y)=\bar{V}_{Pn}(y)$ from Equation (5.93) into Equations (5.5)-(5.19) gives rise to a sequence of equations that can be used to approximate the low frequency motion induced by translation of the basal plate in free-standing models.

5.3.1.1 P0-TERM

Let $\bar{U}_{P0}(\bar{x})$ and $P_{P0}(\bar{x})$ denote the solutions $\bar{U}_{B0}(\bar{x})$ and $P_{B0}(\bar{x})$ to Equations (5.5)-(5.9) for free-standing models. Substitute $\bar{V}_{B0}(y) = \bar{V}_{P0}(y) = U_b\hat{x}$ (from Equation (5.93)) into Equations (5.5)-(5.9). The resulting equations are trivially solved.

$$\bar{U}_{P0}(\bar{x}) = U_b\hat{x} \tag{5.94}$$

$$P_{P0}(\bar{x}) = P_{P0} = \text{constant} \tag{5.95}$$

The P0-term of the solution to the equations of motion corresponds to uniform flow in the x direction that is in phase throughout the entire fluid domain.

The hydrodynamic torque associated with the velocity and pressure fields in Equations (5.94)-(5.95) can be computed by substituting those equations into Equation (5.9). Let T_{P0} represent the zeroth order torque for free-standing models. Let V denote the volume enclosed by {R}.

$$\begin{aligned} T_{P0} &= \hat{z}\cdot\int_R \bar{r}\times P_{P0}\,\overline{dR} = P_{P0}\int_R \hat{z}\cdot(\bar{r}\times\overline{dR}) = P_{P0}\int_R \overline{dR}\cdot(\hat{z}\times\bar{r}) \\ &= P_{P0}\int_R \overline{dR}\cdot\left[\hat{z}\times(x\hat{x}+y\hat{y}+z\hat{z})\right] = P_{P0}\int_R \overline{dR}\cdot(-y\hat{x}+x\hat{y}) \\ &= P_{P0}\int_V \nabla\cdot(-y\hat{x}+x\hat{y})\,dV = 0 \end{aligned} \tag{5.96}$$

At the $(j\omega)^{0/2}$ order, the fluid is stationary relative to the basal plate, and no hydrodynamic torque is generated on the rigid body. In order to derive an expression for the asymptotically low frequency torque induced by vibration of the basal plate for free-standing models, we must solve the $(j\omega)^{1/2}$ order equations.

5.3.1.2 P1-TERM

The "distant" boundary velocity that is induced by translation of the basal plate of free-standing models at the $(j\omega)^{1/2}$ order increases with distance from the basal plate (y) (Equation (5.93)).

$$\bar{V}_{P1}(y) = -\frac{U_b}{\sqrt{\nu}}\, y\, \hat{x} \tag{5.97}$$

Let $\bar{U}_{P1}(\bar{x})$, $P_{P1}(\bar{x})$, and T_{P1} denote the solution $\bar{U}_{B1}(\bar{x})$, $P_{B1}(\bar{x})$, and T_{B1} of Equations (5.10)-(5.14) for $\bar{V}_{B1}(y)=\bar{V}_{P1}(y)$. To simplify the comparison of T_{P1} to torques in later sections of this chapter, it is convenient to express T_{P1} in terms of H_Δ, defined to be the torque that is generated on the rigid body per unit of velocity gradient at the "distant" boundary. H_Δ is thus the solution to Equations (5.10)-(5.14) for $\bar{V}_{B1}(y)=-y\hat{x}$. Since the equations that define H_Δ are similar in form to equations that describe the steady motion of fluid, H_Δ is a real-valued number that depends on fluid viscosity μ, on the distance between the plates G, and on the shape of the body. It seems physically plausible that H_Δ will be greater than zero, independent of the shape of the body, but we make no attempt to prove that conjecture. Since the boundary velocity $\bar{V}_{P1}(y)$ is equal to $U_b/\sqrt{\nu}$ times the boundary velocity in the definition of H_Δ,

$$T_{P1} = \frac{U_b}{\sqrt{\nu}} H_\Delta \,. \tag{5.98}$$

So long as H_Δ is non-zero, T_{P1} will dominate the expansion of $T_P(\omega)$ at very low frequencies.

$$T_P(\omega) \approx (j\omega)^{1/2} \frac{U_b}{\sqrt{\nu}} H_\Delta \tag{5.99}$$

Provided that H_Δ is not equal to zero, the magnitude of the torque exerted on the rigid body by very low frequency vibrations of the basal plate (when there is no tectorial plate) will increase with the square root of frequency, and the phase of the torque will lead that of the basal plate velocity by 45^o. At low frequencies, the real and imaginary parts of the transfer impedance

$$H_P(\omega) = \frac{T_P(\omega)}{U_b} \approx (j\omega/\nu)^{1/2} H_\Delta \tag{5.100}$$

are equal and both increase with the square root of frequency.

5.3.2 R-COMPONENT

The equations that govern the R-component (Equations (5.39)-(5.56)) are similar in structure to those for the B-component. However, the lowest order non-zero term in the series expansion of the dependent variables (Equations (5.39)-(5.41)) occurs for n=2. We express the solution to the equations at the $(j\omega)^{2/2}$ order ((5.47)-(5.51)) in terms of R_Θ -- the solution to those equations for $\Theta(\omega)=-1$. Since the equations that define R_Θ are similar in form to equations that describe the steady motion of fluid, R_Θ is a real-valued number that depends on fluid viscosity μ, on the distance between the plates G, and on the shape of the body. Applying linearity, we express T_{R2} in terms of R_Θ.

$$T_{R2} = -\Theta(\omega)R_\Theta \tag{5.101}$$

It is physically reasonable that R_Θ is greater than zero, however we do not prove this conjecture. If R_Θ is non-zero, then at low frequencies, T_{R2} will dominate the expansion of $T_R(\omega)$

$$T_R(\omega) \approx j\omega T_{R2} = -j\omega\Theta(\omega)R_\Theta \tag{5.102}$$

and the impedance of the fluid load on the rigid body

$$Z_R(\omega) = \frac{-T_R(\omega)}{j\omega\Theta(\omega)} \approx R_\Theta \tag{5.103}$$

is purely real-valued, i.e. the impedance represents a resistance. Given that R_Θ is greater than zero, the torque generated on the body by low frequency rotation of the body will be proportional to and in phase with the angular velocity of the body.

5.3.3 SYSTEM FUNCTION -- $\Theta(\omega)/U_b$

For free-standing models ($G\rightarrow\infty$), $H_T(\omega)=0$. Substitute this into the torque balance Equation (4.67).

$$(K+j\omega Z_R(\omega)-I\omega^2)\Theta(\omega) = H_P(\omega)U_b \tag{5.104}$$

The right hand side of Equation (5.104) is equal to the torque that is generated on the rigid body by translation of the basal plate with velocity U_b. The left hand side of Equation (5.104) expresses the angular displacement that is generated by the torque on the right hand side of the equation. Substitute the low frequency approximations to the impedances (Equations (5.100) and (5.103)) into Equation (5.104).

$$(K+j\omega R_\Theta-I\omega^2)\Theta(\omega) \approx (j\omega/\nu)^{1/2}H_\Delta U_b \tag{5.105}$$

Solve Equation (5.105) for the ratio of $\Theta(\omega)/U_b$.

$$\frac{\Theta(\omega)}{U_b} \approx \frac{(j\omega/\nu)^{1/2}H_\Delta}{K+j\omega R_\Theta-\omega^2 I} \tag{5.106}$$

So long as both H_Δ and K are non-zero, the low frequency asymptotic ratio of angular displacement of the body to basal plate velocity

$$\lim_{\omega \to 0} \frac{\Theta(\omega)}{U_b} = (j\omega)^{1/2} \frac{H_\Delta}{K\sqrt{\nu}} \tag{5.107}$$

is proportional to $(j\omega)^{1/2}$. If H_Δ is greater than zero, the magnitude of the angular displacement that is generated by sufficiently low frequency vibration of the basal plate (when there is no tectorial plate) will increases 10 dB per decade of frequency and the phase of the angular displacement of the body will lead that of the imposed velocity of the basal plate by 45^o.

5.3.4 RANGE OF FREQUENCIES FOR WHICH THE APPROXIMATION IS VALID

The left hand side of Equation (5.105), which contains contributions from the stiffness of the spring, from the moment of inertia of the body, and from the fluid load on the body, is dominated by the stiffness term for frequencies that are small relative to both the mechanical resonance frequency $\omega_0=\sqrt{K/I}$, and the frequency at which the viscous fluid load is comparable to the stiffness of the spring, $\omega_1=K/R_\Theta$.

The low frequency approximation of the B-component of torque that is used in Equation (5.105), results from just the first two terms of the series expansion of the "distant" boundary velocity $\bar{V}_P(\bar{x},\omega)$. We compare $\bar{V}_P(\bar{x},\omega)$ to the first two terms of its series expansion

$$\bar{V}'_{P1}(\bar{x},\omega) = \bar{V}_{P0}(y) + (j\omega)^{1/2}\bar{V}_{P1}(y) \tag{5.108}$$

as a first step toward understanding how well $T_P(\omega)$ is approximated by the first two terms of its expansion.

The uniform velocity field, $\bar{V}_{P0}(y)=U_b\hat{x}$, both dominates the low frequency magnitude of $\bar{V}'_{P1}(\bar{x},\omega)$ and produces no torque on the body (Equation (5.96)). Therefore comparison of

$$\tilde{V}_P(y,\omega) = \frac{V_P(\bar{x},\omega) - U_b}{U_b} = e^{-y/L\sqrt{j\omega/\omega_L}} - 1 \tag{5.109}$$

with

$$\tilde{V}'_{P1}(y,\omega) = \frac{V'_{P1}(\bar{x},\omega) - U_b}{U_b} = -y/L\sqrt{j\omega/\omega_L} \tag{5.110}$$

gives a better indication of the adequacy with which $\bar{V}'_{P1}(\bar{x},\omega)$ can be substituted for $\bar{V}_P(\bar{x},\omega)$ for the purpose of calculating torque on the rigid body. Figure 5.5 shows that the magnitude and angle of $\tilde{V}_P(y,\omega)$ are closely approximated by those of $\tilde{V}'_{P1}(y,\omega)$ at sufficiently low frequencies. At a given frequency, the approximation improves as the distance to the plate (y) decreases. For points y less than L, the dimension of the body, and for frequencies smaller than the frequency for which the boundary layer thickness is equal to the body dimension L,

$$\omega < \omega_L \qquad ; \ \omega_L = 2\nu/L^2 \tag{5.111}$$

the magnitude of $\tilde{V}'_{P1}(y,\omega)$ is within 4.4 dB of $\tilde{V}_P(y,\omega)$ and the angle of $\tilde{V}'_{P1}(y,\omega)$ is within 24^o of the angle of $\tilde{V}_P(y,\omega)$. Equation (5.111) does not indicate that $T(\omega)$ is well approximated by the first two terms in its power series for $\omega<\omega_L$, however it does cast doubt on the validity of approximating $T(\omega)$ by just the first two terms for $\omega>\omega_L$.

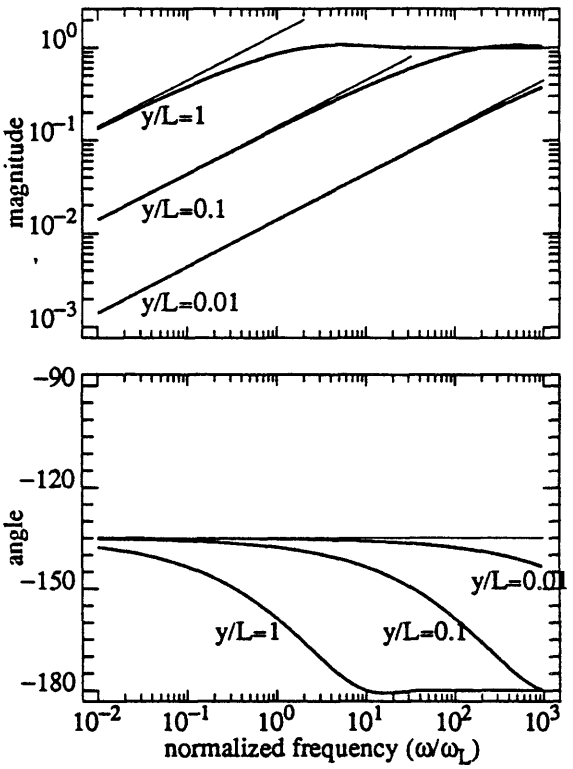

Figure 5.5: Determining the range of frequencies for which $\bar{V}_P(\bar{x},\omega)\approx\bar{V}'_{P1}(\bar{x},\omega)$. The thick curves in the upper and lower panels of this figure show the magnitude and angle of $\tilde{V}_P(y,\omega)$ (Equation (5.109)) as a function of normalized frequency. The three different curves are for three different values of y/L (indicated near each curve). The thin straight lines show the magnitude and angle of $\tilde{V}'_{P1}(y,\omega)$ (Equation (5.110)) for the same three values of y/L. The angle of $\tilde{V}'_{P1}(y,\omega)$ is -135^o for all values of y and ω.

5.3.4 SUMMARY

In section 5.3 we have demonstrated how to use the power series method of section 5.1 to estimate the torque that is generated on the rigid body by low frequency vibrations of the basal plate. We approximated the distant boundary velocity (which depends exponentially on the distance from the basal plate) by the first two terms of a power series expansion (a uniform velocity field and a velocity that increases linearly with distance from the basal plate). We showed that the torque generated by each of these first two terms can be evaluated by solving problems of steady hydrodynamics. We then showed that a number of factors limit the range of frequencies for which the two-term approximation is valid. The range of frequencies for which the approximation is valid is limited to frequencies that are small relative to (1) the mechanical resonance frequency, $\omega_0=\sqrt{K/I}$, (2) the frequency at which the impedance of the spring is equal to the real part of the rotational impedance R_Θ, $\omega_1=K/R_\Theta$, and (3) the maximum frequency at which the distant boundary condition can be approximated (for values of y comparable to the dimension of the body) by two terms of its series expansion, $\omega_2=\omega_L=2\nu/L^2$.

5.4 LOW FREQUENCY RELATIONSHIPS FOR TECTORIAL MODELS

In this section we apply the method of series expansion that was developed in section 5.1 to determine low frequency asymptotic expressions for the motion of the hinged body in Figure 4.1 for finite inter-plate distances G. The development in this section closely parallels that in section 5.3 for free-standing models. It will be shown however that the asymptotic relationships for finite G are very different from those for infinite G from section 5.3.

5.4.1 B-COMPONENT

A power series expansion for $\bar{V}_B(\bar{x},\omega)$ of the form given by Equation (5.1) can be derived from the Taylor expansion of Equation (4.47) about $\omega=0$.

$$\bar{V}_B(\bar{x},\omega) = U_b\left[\frac{G-y}{G}\right]\left[1-\frac{(j\omega)\, y\,(2G-y)}{6\nu}+\frac{(j\omega)^2\, y\,(2G-y)(4G^2+6yG-3y^2)}{360\nu^2}-+\right]\hat{x} \quad (5.112)$$

The zero order term of $\bar{V}_B(\bar{x},\omega)$

$$\bar{V}_{B0}(y) = U_b\,\hat{x} - U_b\,\frac{y}{G}\,\hat{x} \quad (5.113)$$

contains a uniform velocity component ($U_b\hat{x}$) in addition to a component whose magnitude increases with distance from the plate ($-U_b(y/G)\hat{x}$). The torque produced by the uniform component is zero (as in Equations (5.94)-(5.96)). However the torque produced by the linearly increasing velocity is generally not equal to zero and can be expressed in terms of H_G, defined to be the torque that is generated on the rigid body per unit of velocity gradient at the "distant" boundary. H_G is thus the solution to Equations (5.10)-(5.14) for $\bar{V}_{B1}(y)=-y\hat{x}$. H_Δ, defined in section 5.3.1.2, is the special case of H_G for $G\to\infty$. Since the equations that define H_G are similar in form to equations that describe the steady motion of fluid, H_G is a real-valued number that depends on the fluid viscosity μ, on the distance between the plates G, and on the shape of the body. It seems physically plausible that H_G will be greater than zero for all body shapes, but we make no attempt to prove that conjecture. Since the "distant" velocity gradient of the linear componentof $\bar{V}_{B0}(y)$ is equal U_b/G times the distant velocity gradient in the definition of H_G,

$$T_{B0} = \frac{U_b}{G} H_G \ . \quad (5.114)$$

If H_G is non-zero, T_{B0} will dominate the expansion of $T_B(\omega)$ at very low frequencies.

$$T_B(\omega) \approx T_{B0} = \frac{U_b}{G} H_G \quad (5.115)$$

Provided that H_G is not equal to zero, the magnitude of the torque exerted on a rigid body by translation of the basal plate in tectorial models will approach a constant as $\omega\to 0$ and the low frequency asymptotic torque will be in phase with the basal plate velocity. The presence of the tectorial plate thus has a first order effect on the asymptotic torque induced by translation of the basal plate. In the absence of the tectorial plate, the low

frequency asymptotic torque was zero and the asymptotic phase relationship between torque and basal plate velocity was 45^{o}. In the presence of the tectorial plate, the asymptotic torque is finite and is in phase with basal plate velocity. At low frequencies, the imaginary part of the transfer impedance is zero.

$$H_B(\omega) = \frac{T_B(\omega)}{U_b} \approx \frac{H_G}{G} \tag{5.116}$$

5.4.2 T-COMPONENT

A power series expansion of $\bar{V}_T(\bar{x},\omega)$ of the form given by Equation (5.20) can be derived from the Taylor expansion of Equation (4.52).

$$\bar{V}_T(\bar{x},\omega) = U_t\left[\frac{y}{G}\right]\left[1 + \frac{(j\omega)(y-G)(y+G)}{6\nu} + \frac{(j\omega)^2(y-G)(y+G)(3y^2-7G^2)}{360\nu^2} + \cdots\right]\hat{x} \tag{5.117}$$

The magnitude of the zero order term of $\bar{V}_T(\bar{x},\omega)$

$$\bar{V}_{T0}(y) = U_t \frac{y}{G}\,\hat{x} \tag{5.118}$$

increases linearly with distance from the basal plate. T_{T0} can be expressed in terms of H_G, defined in the previous section.

$$T_{T0} = -\frac{U_t}{G} H_G \tag{5.119}$$

It is physically plausible (but unproved) that H_G is greater than zero. If this is true, then T_{T0} will dominate the expansion of $T_T(\omega)$ at low frequencies.

$$T_T(\omega) \approx T_{T0} = -\frac{U_t}{G} H_G \tag{5.120}$$

The form of T_{T0} differs from that of T_{B0} only by its algebraic sign. If H_G is greater than zero, at low frequencies, the real part of the transfer impedance

$$H_T(\omega) = \frac{T_T(\omega)}{U_t} \approx -\frac{H_G}{G} \tag{5.121}$$

will be equal to -1 times the transfer impedance $H_B(\omega)$.

5.4.3 R-COMPONENT

The equations that govern the R-component for tectorial models are similar those for free-standing models. We express the solution to the equations at the $(j\omega)^{2/2}$ order ((5.47)-(5.51)) in terms of R_G -- the solution to those equations for $\Theta(\omega)=-1$. Since the equations that define R_G are similar in form to equations that describe the steady motion of fluid, R_G is a real-valued number that depends on the fluid viscosity μ, on the distance between the plates G, and on the shape of the body. Applying linearity, we express T_{R2} in terms of R_G.

$$T_{R2} = -\Theta(\omega) R_G \tag{5.122}$$

If the physically reasonable conjecture that R_G is greater than zero is true, then at low frequencies, T_{R2} will dominate the expansion of $T_R(\omega)$

$$T_R(\omega) \approx j\omega T_{R2} = -j\omega\Theta(\omega)R_G \tag{5.123}$$

and the impedance of the fluid load on the rigid body

$$Z_R(\omega) = \frac{-T_R(\omega)}{j\omega\Theta(\omega)} \approx R_G \tag{5.124}$$

is purely real-valued.

5.4.4 SYSTEM FUNCTION

The low frequency asymptotic relationships between the imposed velocities of the basal and tectorial plates (U_b and U_t) and the resulting angular displacement $\Theta(\omega)$ can be derived by substituting the low frequency expressions for the impedances (Equations (5.116), (5.121), and (5.124)) into the torque balance equation (4.67).

$$(K+j\omega R_G-\omega^2 I)\Theta(\omega) \approx (U_b-U_t)\frac{H_G}{G} \tag{5.125}$$

If both H_G and K are greater than zero, and U_b is not equal to U_t, then the low frequency asymptotic angular displacement of the body

$$\lim_{\omega\to 0} \Theta(\omega) = (U_b-U_t)\frac{H_G}{G} \tag{5.126}$$

is proportional to and in phase with the difference between the basal and tectorial plate velocities.

5.4.5 RANGE OF FREQUENCIES FOR WHICH THE APPROXIMATION IS VALID

The left hand side of Equation (5.125), which contains contributions from the stiffness of the spring, from the moment of inertia of the body, and from the fluid load on the body, is dominated by the stiffness term for frequencies that are small relative to both the mechanical resonance frequency $\omega_0=\sqrt{K/I}$, and the frequency at which the viscous fluid load is comparable to the stiffness of the spring, $\omega_1=K/R_G$.

The low frequency approximation of the B- and T-components of the torque that are used in Equation (5.125) result from only the first term of each of their series expansions. Since the constant term $U_b\hat{x}$ both dominates the magnitude of the B-component of the "distant" boundary velocity at low frequencies and produces no torque on the body (Equation (5.96)), comparison of

$$\tilde{V}_B(y,\omega) = \frac{V_B(\bar{x},\omega)-U_b}{U_b} = \frac{\sinh((1-y/G)\sqrt{j\omega G^2/\nu})}{\sinh(\sqrt{j\omega G^2/\nu})} - 1 \tag{5.127}$$

with

$$\tilde{V}'_{B0}(y,\omega) = \frac{V_{B0}(\bar{x},\omega)-U_b}{U_b} = -\frac{y}{G} \tag{5.128}$$

gives a better indication of the adequacy with which $\bar{V}_{B0}(y)$ can be substituted for $\bar{V}_B(\bar{x},\omega)$ for the purpose of calculating torque on the rigid body. Figure 5.6 shows that the magnitude and angle of $\tilde{V}_B(y,\omega)$ are closely approximated by those of $\tilde{V}'_{B0}(y,\omega)$ at very low frequencies. Notice that the maximum difference between $\tilde{V}'_{B0}(y,\omega)$ and $\tilde{V}_B(y,\omega)$ is not very sensitive to the value of y (unlike the difference between $\tilde{V}'_{P1}(y,\omega)$ and $\tilde{V}_P(y,\omega)$ in Figure 5.5). $\tilde{V}'_{B0}(y,\omega)$ is a close approximation of $\tilde{V}_B(y,\omega)$ throughout the fluid domain so long as the excitation frequency is such that the boundary layer thickness is large relative to the interplate distance G. For the three values of y/G shown in Figure 5.6, so long as

$$\omega < \omega_G \qquad ; \ \omega_G = 2\nu/G^2 \tag{5.129}$$

the ratio of $\tilde{V}'_{B0}(y,\omega)/\tilde{V}_B(y,\omega)$ is less than 2 dB and the angle of $\tilde{V}'_{B0}(y,\omega)/\tilde{V}_B(y,\omega)$ is smaller than 31^o.

Define normalized functions analogous to $\tilde{V}'_{B0}(y,\omega)$ and $\tilde{V}_{B0}(y,\omega)$ for the T-component of the "distant" boundary condition.

$$\tilde{V}_T(y,\omega) = \frac{V_T(\bar{x},\omega)}{U_t} = \frac{\sinh((y/G)\sqrt{j\omega G^2/\nu})}{\sinh(\sqrt{j\omega G^2/\nu})} \tag{5.130}$$

$$\tilde{V}'_{T0}(y,\omega) = \frac{V_{T0}(\bar{x},\omega)}{U_t} = \frac{y}{G} \tag{5.131}$$

Figure 5.7 shows that the magnitude and angle of $\tilde{V}_T(y,\omega)$ are closely approximated by those of $\tilde{V}'_{T0}(y,\omega)$ at very low frequencies. As with the B-component, the maximum difference between $\tilde{V}'_{T0}(y,\omega)$ and $\tilde{V}_T(y,\omega)$ is not a sensitive function of y. $\tilde{V}_{T0}(y,\omega)$ is a close approximation of $\tilde{V}_T(y,\omega)$ for all values of y, so long as the frequency is such that the boundary layer thickness is large relative to the interplate distance G. For the values of y/G in Figure 5.7, so long as

$$\omega < \omega_G \tag{5.132}$$

the ratio of $\tilde{V}_T(y,\omega)/\tilde{V}'_{T0}(y,\omega)$ is less than 0.2 dB and the angle of $\tilde{V}_T(y,\omega)/\tilde{V}_{T0}(y,\omega)$ is smaller than 19^o.

5.4.6 SUMMARY

In section 5.4, we found that, if K and H_G are not equal to zero, and if the low frequency velocities that is imposed on the basal and tectorial plates differ, then the angular displacement of the rigid body is proportional to and in phase with the difference between the basal and tectorial plate velocities. We showed that a number of factors limit the range of frequencies for which this approximation is valid. The range of frequencies is limited to frequencies that are small relative to (1) the mechanical resonance frequency, $\omega_0=\sqrt{K/I}$, (2) the frequency at which the impedance of the spring is equal to the real part of the rotational impedance R_G, $\omega_1=K/R_G$, and 3) the maximum frequency at which the distant boundary condition can be approximated by the first term in its series expansion, $\omega_2=\omega_G=2\nu/G^2$.

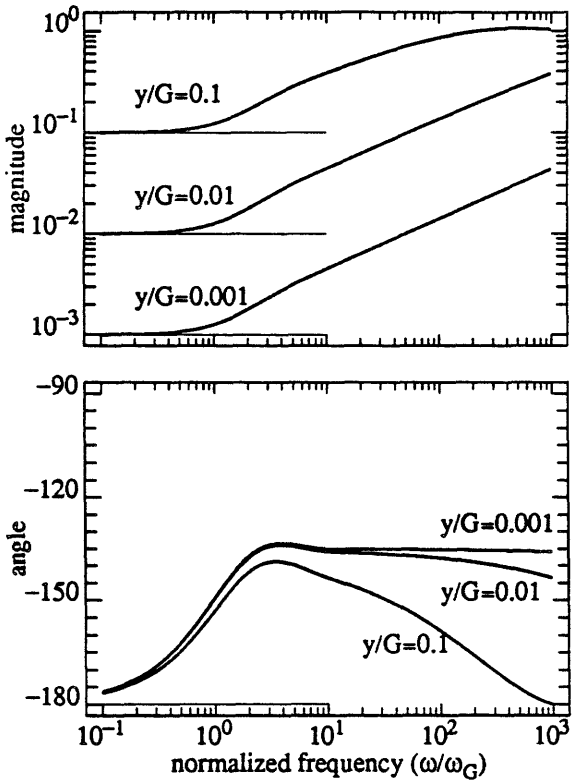

Figure 5.6: Determining the range of frequencies for which $\bar{V}_B(\bar{x},\omega) \approx \bar{V}'_{B0}(\bar{x},\omega)$. The thick curves in the upper and lower panels of this figure show the magnitude and angle of $\tilde{V}_B(y,\omega)$ (Equation 5.127)) as a function of normalized frequency. The three different curves are for three different values of y (indicated near each curve). The thin lines show the magnitude and angle of $\tilde{V}'_{B0}(y,\omega)$ (Equation (5.128)) for the same three values of y. The angle of $\tilde{V}'_{B0}(y,\omega)$ is -180^0 for all values of y and ω.

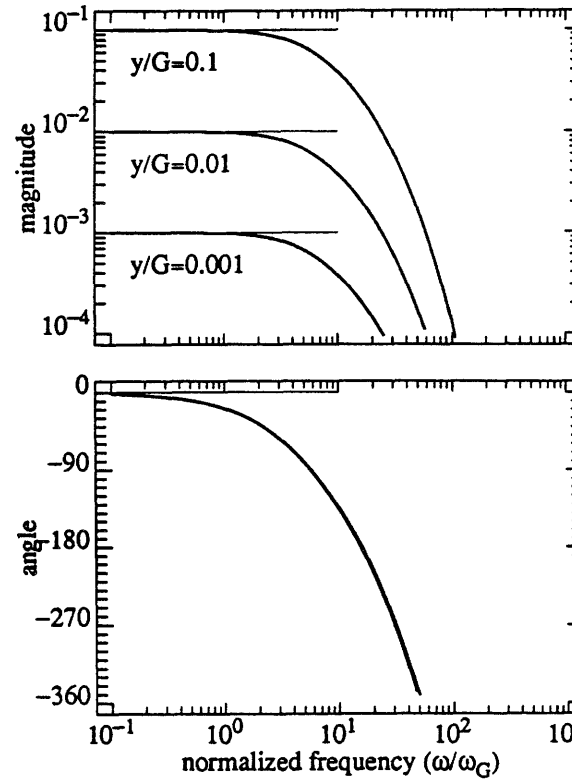

Figure 5.7: Determining the range of frequencies for which $\bar{V}_T(\bar{x},\omega) \approx \bar{V}'_{T0}(\bar{x},\omega)$. The thick curves in the upper and lower panels of this figure show the magnitude and angle of $\tilde{V}_T(y,\omega)$ (Equation 5.130)) as a function of normalized frequency. The three different curves are for three different values of y (indicated near each curve). The thin lines show the magnitude and angle of $\tilde{V}'_{T0}(y,\omega)$ (Equation (5.131)) for the same three values of y. The magnitudes and angles in this figure are only shown for normalized frequencies less than about 100. At higher frequencies the magnitudes and angles continue to fall.

5.5 LOW FREQUENCY RELATIONSHIPS FOR TECTORIAL MODELS WHEN G>>L

The low frequency asymptotic ratio of angular displacement to basal plate velocity is proportional to $(j\omega)^{1/2}$ (Equation (5.107)) for free-standing models and to $(j\omega)^{0/2}$ (Equation (5.126)) for tectorial models (with U_t=0). Intuitively however, one expects that the tectorial results should be similar to the free-standing results for some sufficiently large value of G. In this section, we examine the asymptotic relationships for tectorial models with large values of G (relative to L) and show that this intuition is correct.

The range of frequencies for which these two low frequency relationships can be applied is limited by a number of factors (sections 5.3.4 and 5.4.5). For free-standing models, this range is limited to frequencies less that ω_L -- the frequency at which the boundary layer thickness is equal to the dimension of the body L. For $\omega<\omega_L$, the boundary layer of fluid that is entrained to move with the plate has a roughly constant velocity gradient for y<L (Figure 5.5). For tectorial models, the range is limited to frequencies less than ω_G -- the frequency at which the boundary layer thickness is equal to the inter-plate distance G. For $\omega<\omega_G$, fluid that is distant from the body is uniformly sheared by relative motion of the plates, independent of frequency (Figures 5.6 and 5.7). When the inter-plate distance G is large relative to L, ω_G is much smaller than ω_L.

$$\frac{\omega_G}{\omega_L} = \frac{2\nu}{G^2}\,\frac{L^2}{2\nu} = \frac{L^2}{G^2} \tag{5.133}$$

For tectorial models with G>>L, there is a very low range of frequencies, $\omega<\omega_G$, in which the boundary layer thickness is so large that motion of the tectorial plate induces fluid motion near the body even though the distance from the body to the tectorial plate is large. As frequency increases beyond ω_G however, fluid motion for y<L is decreasingly dependent on the motion of the tectorial plate, and, as we show in Figure 5.8, increasingly similar to the motion that is induced in the absence of the tectorial plate.

Thus for models with G>>L, there are two distinct low frequency regions. For $\omega<\omega_G$, relative motion of the basal and tectorial plates induces the fluid between the plates to move with a velocity that is in phase with the difference between the tectorial plate velocity and the basal plate velocity. The resulting angular displacement of the body at very low frequencies is proportional to the difference between the tectorial and basal plate velocities. For $\omega_G<\omega<\omega_L$, the motion of the tectorial plate has little effect on the motion of fluid near the body. For this range of frequencies, the fluid velocity near the body is similar to that which results when there is no tectorial plate, and the ratio of angular displacement of the body to basal plate velocity is proportional to $(j\omega)^{1/2}$.

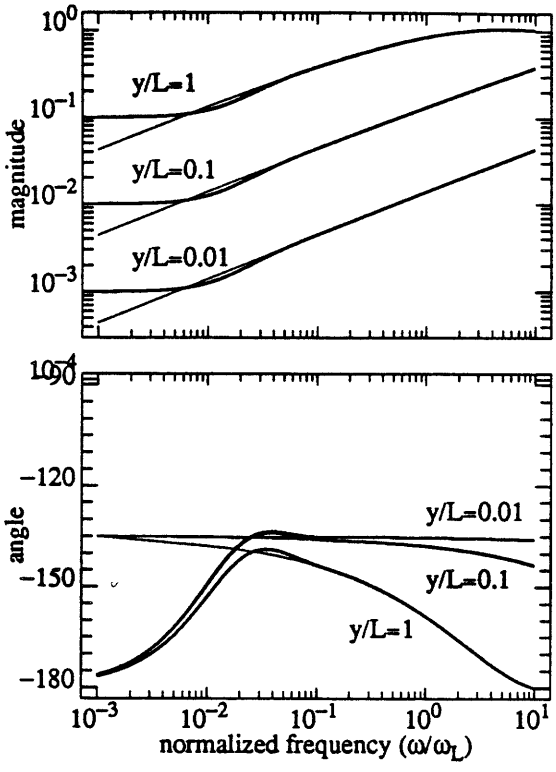

Figure 5.8: Distant fluid velocity induced by motion of the basal plate with and without an overlying tectorial plate. The thin lines show the magnitude and angle of $\tilde{V}_P(y,\omega)$ (Equation (5.109)), the normalized velocity of the fluid relative to the basal plate velocity that is induced by vibration of the basal plate in the absence of an overlying tectorial plate (as in Figure 5.5). The thick lines in this figure show the magnitude and angle of $\tilde{V}_B(y,\omega)$ (Equation (5.127)), the normalized velocity of the fluid relative to the basal plate velocity that is induced by vibration of the basal plate in the presence of an overlying tectorial plate at y=G=10L (similar to Figure 5.6). The (stationary) tectorial plate greatly effects fluid velocities at low frequencies, $\omega<\omega_G=\omega_L/100$, but has little effect on fluid velocities at higher frequencies.

5.6 CONCLUSIONS

The motion of the structure illustrated in Figure 4.1 has been analyzed for asymptotically low frequencies of excitation and several characteristics of that motion have been identified that do not depend on the detailed shape of the rigid body.

First, at very low frequencies of excitation, the impedance of the lumped parameter model for motion (Figure 4.3) is dominated by that of the spring. Thus, the angular displacement of the body that results from low frequency vibration of the plates is proportional to the hydrodynamic torque on the body.

In the presence of a nearby tectorial plate, the hydrodynamic torque on the body is proportional to, and in phase with, the difference between the velocities of the two plates (provided these differ), and therefore the angular displacement of the body is proportional to the difference between the velocities of the two plates.

If however there is no tectorial plate, then for low frequencies, the body is completely engulfed in the boundary layer of fluid near the plate. The velocity of the fluid within the boundary layer, $\bar{V}_\delta(\bar{x},\omega)$,

$$\bar{V}_\delta(\bar{x},\omega) = U_b e^{-y\sqrt{j\omega/\nu}}\,\hat{x} \tag{5.134}$$

depends exponentially on distance from the plate (y). The velocity near the plate, relative to that of the plate is proportional to the derivative of Equation (5.134) with respect to y,

$$\frac{\partial \bar{V}(\bar{x},\omega)}{\partial y} = -\sqrt{j\omega/\nu}\, U_b\, e^{-y\sqrt{j\omega/\nu}}\,\hat{x} \tag{5.135}$$

and for small values of y, the exponential in Equation (5.135) is nearly equal to one.

$$\frac{\partial \bar{V}(\bar{x},\omega)}{\partial y} \approx -\sqrt{j\omega/\nu}\, U_b\,\hat{x} \tag{5.136}$$

Thus, at low frequencies, the difference between the fluid velocity and the velocity of the basal plate is proportional to $(j\omega)^{1/2}$ times the velocity of the basal plate. For these low frequencies, the hydrodynamic torque exerted on the body is proportional to $(j\omega)^{1/2}$ times the velocity of the basal plate, as is the angular displacement of the body.

For models with a "distant" tectorial plate, there are two distinct low frequency regimes. At very low frequencies, the boundary layer thickness is large relative to the distance between the plates, and the fluid motion near the plate is in phase with the difference between the tectorial and basal plate velocities (if those velocities differ), and independent of frequency. The hydrodynamic torque on the body and the resulting angular displacement of the body for these very low frequencies of excitation are proportional to the difference between the tectorial and basal plate velocities. At higher frequencies, for which the boundary layer thickness is large relative to the body dimensions but small relative to the distance between the plates, the tectorial plate has little effect on the

motion of the fluid near the basal plate, and the fluid motion that deflects the body is generated in the boundary layer of fluid near the basal plate. At frequencies for which the boundary layer thickness is large relative to the dimensions of the body but small relative to the distance between the plates, the hydrodynamic torque on the body, and the resulting angular displacement of the body are proportional to $(j\omega)^{1/2}$ times is velocity of the basal plate.

The results of this chapter suggests that the low frequency motion of stereociliary tufts depends critically on the distance to the "nearest" rigid boundary. For frequencies of excitation that are small relative to the frequency for which the boundary layer thickness is equal to the distance to the nearest rigid boundary, the "velocity sensor" model that was discussed in the opening paragraph of this chapter adequately describes the motion of the body. For frequencies of excitation that are large relative to this distance however, the motion of the body is neither proportional to the velocity nor to the displacement of the plates.

CHAPTER 6
HIGH FREQUENCY ANALYSIS OF A RIGID BODY THAT IS ATTACHED TO A VIBRATING PLATE WITH A SPRING LOADED HINGE

In chapter 5 we showed that the motion of the hinged body illustrated in Figure 4.1 could be characterized for very low frequency excitations without detailed specification of the shape of the body. Such a result is very powerful since it is robust across all parameters of a wide class of models. In this chapter, we analyse the hinged body structure for very high frequency excitations. We will show that the motion of the hinged body that is induced by very high frequency excitations is also insensitive to the detailed shape of the body.

We approximate the high frequency asymptotic motion of the hinged body by setting the viscosity of the fluid to zero. We motivate the basis of this approximation in section 6.1. Then, using general properties of the motion of inviscid fluids (developed in section 6.2), we determine the motion of the hinged body structure when immersed in an inviscid fluid (section 6.3). We take the expressions in section 6.3 to also describe the motion of the hinged body structure when immersed in a viscous fluid and excited at very high frequencies.

6.1 INVISCID APPROXIMATION TO THE EQUATIONS OF MOTION FOR HIGH FREQUENCY EXCITATION

6.1.1 MOTIVATION: THE EFFECT OF FLUID ON ISOLATED BODIES OF REGULAR GEOMETRY THAT OSCILLATE AT HIGH FREQUENCIES

Stokes (1855) investigated the motion that is induced in a viscous fluid by sinusoidal vibration of bodies of regular geometry that are isolated in a fluid of infinite spatial extent (chapter 2). Stokes' solution shows that the fluid near the body is entrained to move with the body, while the remaining fluid is pushed out of the path of the body and entrained fluid. The motion of the fluid outside the boundary layer of fluid that surrounds the body is in fact similar to the motion that is induced in an inviscid fluid by the vibration of a larger body whose spatial extent encompasses that of both the original body and the viscously entrained fluid.

The thickness of the boundary layer decreases as the frequency at which the body is vibrated increases. Thus as frequency increases, less fluid is entrained to move with the body and more fluid moves as though the fluid had no viscosity. As the body vibrates, its motion is resisted by a force of fluid origin. As frequency increases, Stokes found that the hydrodynamic force exerted by a viscous fluid on the vibrating body approaches the force exerted by an inviscid fluid.

For sufficiently high frequencies of vibration, both the fluid motion around and the hydrodynamic force on the isolated bodies of regular geometry can be approximated by setting the viscosity of the fluid to zero.

6.1.2 HEURISTIC DESCRIPTION OF BOUNDARY LAYERS AT HIGH FREQUENCIES

Based on Stokes' solution to viscous equations of motion, we expect that the high frequency motion of the hinged body structure (Figure 4.1) can be approximated by setting the viscosity of the fluid to zero. A rigorous proof that the high frequency limit of the solution to viscous equations of motion generally approaches the solution to inviscid equations is not available. We briefly describe the issues that underlie such an approximation here. A more thorough treatment can be found in a number of texts on elementary fluid dynamics (Batchelor, 1967; p. 302).

Motion of the hinged body structure in Figure 4.1 (translation of the basal or tectorial plate or rotation of the rigid body about the hinge) sets the viscous incompressible fluid that surrounds the structure into motion and generates a hydrodynamical torque on the rigid body. So long as the imposed structure velocities are small, the equations of motion can be approximated by linear equations of motion (section 4.2),

$$j\omega\rho\bar{U}(\bar{x},\omega) = -\nabla P(\bar{x},\omega) + \mu\nabla^2\bar{U}(\bar{x},\omega) \qquad ; \ \bar{x} \text{ in } \{V\} \qquad (6.1)$$

$$\nabla \cdot \bar{U}(\bar{x},\omega) = 0 \qquad ; \ \bar{x} \text{ in } \{V\} \qquad (6.2)$$

$$\bar{U}(\bar{x},\omega) = \bar{U}_{bc}(\bar{x},\omega) \qquad ; \ \bar{x} \text{ in } \{S\} \qquad (6.3)$$

$$T(\omega) = \hat{z} \cdot \left[\int_R \bar{r} \times \left[-P(\bar{x},\omega)\overline{dR} + \mu \overline{dR} \cdot \nabla\bar{U}(\bar{x},\omega) \right] \right] \qquad (6.4)$$

where $\{V\}$ denotes the set of points in the fluid domain, $\{S\}$ denotes the set of points on the surface of $\{V\}$, and $\{R\}$ denotes the set of points on the surface of the rigid body. By altering $\bar{U}_{bc}(\bar{x},\omega)$, Equations (6.1)-(6.4) can be specialized to describe the motion of the B-component (Equations (4.45)-(4.49)), the T-component (Equations (4.50)-(4.54)), or the R-component (Equations (4.55)-(4.59)) of the equations of motion for the hinged body.

Consider the hypothesis that as frequency increases, the fluid velocity field $\bar{U}(\bar{x},\omega)$ approaches some limiting distribution.

$$\lim_{\omega\to\infty} \bar{U}(\bar{x},\omega) = \bar{U}_\infty(\bar{x}) \qquad (6.5)$$

If Equation (6.5) were true, then as the frequency of excitation increases, the inertial term in Equation (6.1), $j\omega\rho\bar{U}(\bar{x},\omega)$, would approach $j\omega\rho\bar{U}_\infty(\bar{x})$ and therefore the magnitude of the inertial term would increase in proportion to ω. As frequency is increased, the viscous term, $\mu\nabla^2\bar{U}(\bar{x},\omega)$, will approach $\mu\nabla^2\bar{U}_\infty(\bar{x})$ however and the magnitude of the viscous term will not increase with further increases in frequency. Thus if Equation (6.5) were true, it would follow that the magnitude of the pressure field must increase with frequency and, for asymptotically high frequencies, Equations (6.1) and (6.2) could be replaced by equations that do not involve the viscosity of the fluid.

$$j\omega\rho\bar{U}_\infty(\bar{x}) = -\nabla P_\infty(\bar{x}) \qquad (6.6)$$

$$\nabla \cdot \bar{U}_\infty(\bar{x}) = 0 \qquad (6.7)$$

Equations (6.6) and (6.7) involve only first order derivatives of pressure and fluid velocity while Equations (6.1) and (6.2) involve second order derivatives of the fluid velocity field. The solution to Equations (6.6) and (6.7) requires fewer boundary conditions than are given in Equation (6.3). One can in fact always find the unique solution to Equations (6.6) and (6.7) given only the normal components of the fluid velocity near rigid boundaries. It is generally impossible to satisfy both the normal and tangential components of Equation (6.3) since the solution to Equations (6.6), (6.7), and the normal component of Equation (6.3) generally requires some "slip" along the rigid surfaces.

The apparent contradiction that results from Equation (6.5) can be resolved by considering the structure of the boundary layers that occur for very high frequency vibrations. Although the thickness of the boundary layer decreases as the frequency of vibration increases, it is in this vanishingly small boundary layer that the viscous "no-slip" boundary conditions with the rigid body are made compatible with the "slippery" boundary conditions of the nearly inviscid fluid motion outside of the boundary layer.

As a specific example, consider the motion induced in a fluid by high frequency translation of an infinite plate. Translation of the plate in its plane induces no motion in an inviscid fluid and the no-slip condition that the tangential velocity of the fluid equal that of the plate is not satisfied. The velocity profile for a viscous fluid depends exponentially on distance from the plate with a space constant equal to the thickness of the boundary layer. At distances from the plate that are large relative to the boundary layer thickness, the fluid velocity is small and is thus similar to the fluid velocity of an inviscid fluid. The fluid velocity adjacent to the plate is however equal to that of the plate. In the boundary layer, the gradient of the component of velocity that is parallel to the plate is very large, and the no-slip condition along the plate is made compatible with the slippery condition that is consistent with the nearly inviscid fluid motion outside of the boundary layer.

The torque on the rigid body (Equation (6.4)) depends both on the hydrodynamic pressure at the surface of the body and on the normal component of the gradient of the fluid velocity at the surface of the body. Since even at very high frequencies, the rigid body is surrounded by a boundary layer of fluid, it is not clear at the outset that the torque on the rigid body can be approximated by the pressure generated by an inviscid fluid.

Consider first the component of torque due to hydrodynamic pressure. From the momentum equation (6.1), it follows that the variation in hydrodynamic pressure through the boundary layer is a function of the variation of the component of velocity that is perpendicular to the body surface. Since the normal component of fluid velocity changes little in the boundary layer, the hydrodynamic pressure at the surface of the body is little different from the pressure one boundary layer thickness away from the body. Thus the component of torque that is generated on the rigid body by variations in hydrodynamical pressure within the boundary layer is small.

The viscous contribution to torque through the boundary layer is more complicated to evaluate. At points near the rigid body, the fluid velocity is equal to the velocity of the body. At very high frequencies, the tangential components of the velocity of the fluid that is just one boundary layer thickness away from the body approach those given by the solution of the equations of motion for an inviscid fluid. Thus in the boundary layer, the components of velocity in the plane that is tangent to the body surface change rapidly as a function of distance in the direction normal to that plane. From Equation (6.4), such velocity gradients will exert a viscous torque on the rigid body. Since the magnitude of the velocity gradient in the boundary layer is inversely related to the thickness of the boundary layer, the magnitude of the velocity gradient in fact increases roughly with the square root of frequency. Therefore, the torque that is generated on the rigid body by fluid motion within the boundary layer increases as frequency increases.

If however there is an inviscid contribution to the torque generated on the body, that inviscid component of torque will increase linearly with frequency at high frequencies. Therefore, so long as the cross sectional area of the rigid body in the y-z plane (the plane perpendicular to the direction in which the basal plate is vibrated) is greater than zero, the inviscid component of torque will asymptotically dominate the viscous component that is generated in the boundary layer and the total torque at high frequencies will be well approximated by the torque that is produced by an inviscid fluid.

6.1.3 SUMMARY

In this section we have argued that the fluid motion that results for very high frequencies of excitation of the hinged body structure in Figure 4.1 can be approximated by analyzing the motion that results when the viscosity of the fluid is set to zero. We have also argued that the hydrodynamic torque on the rigid body can be approximated by that generated by an inviscid fluid so long as the cross sectional area of the rigid body in the y-z plane is not zero.

When the viscosity of the fluid is zero, the equations of motion for the rigid body are

$$j\omega\rho\bar{U}_i(\bar{x},\omega) = -\nabla P_i(\bar{x},\omega) \qquad ; \bar{x} \text{ in } \{V\} \qquad (6.8)$$

$$\nabla \cdot \bar{U}_i(\bar{x},\omega) = 0 \qquad ; \bar{x} \text{ in } \{V\} \qquad (6.9)$$

$$\hat{n} \cdot \bar{U}_i(\bar{x},\omega) = \hat{n} \cdot \bar{U}_{bc}(\bar{x},\omega) \qquad ; \bar{x} \text{ in } \{S\} \qquad (6.10)$$

$$T_i(\omega) = \hat{z} \cdot \left[\int_R \bar{r} \times [\, -P_i(\bar{x},\omega)\overline{dR}\,] \right] . \qquad (6.11)$$

In this chapter, we solve Equations (6.8)-(6.11) for each of the three component excitations defined in section 4.3 (B-, T-, and R-components). We then combine these results in the superposition Equations (4.60)-(4.63) and thereby generate the solution of the inviscid equations of motion for the hinged body. This solution is an approximation of the solution of the viscous equations that is valid for asymptotically high frequencies of excitation.

6.2 PROPERTIES OF INVISCID FLUIDS

In this section, we establish that the complex amplitude of the sinusoidal velocity that is induced in an inviscid fluid by sinusoidal boundary velocities whose amplitudes are real-valued over the entire surface of the fluid domain is real-valued throughout the fluid domain. We use this property of inviscid fluids in section 6.3 to establish the form of each of the B-, T-, and R-components of the solution to the inviscid equations of motion for the hinged body.

6.2.1 REPRESENTING THE SOLUTION BY A VELOCITY POTENTIAL

The dependent variables in Equations (6.8)-(6.11) include both a scalar field $P_i(\bar{x},\omega)$ and a vector field $\bar{U}_i(\bar{x},\omega)$, however these equations can be expressed in terms of a single scalar velocity potential field.

Since the curl of the gradient of a scalar function of position is zero, the curl of Equation (6.8) shows that the curl of the velocity field $\bar{U}_i(\bar{x},\omega)$ is zero throughout the fluid domain.

$$j\omega\rho\,(\nabla\times\bar{U}_i(\bar{x},\omega)) = \nabla\times j\omega\rho\bar{U}_i(\bar{x},\omega) = -\nabla\times\nabla P_i(\bar{x},\omega) = \bar{0} \tag{6.12}$$

Since the curl of the velocity field $\bar{U}_i(\bar{x},\omega)$ is zero throughout the fluid domain, the velocity field can be represented by a velocity potential field (Batchelor, 1967; p. 100).

$$\bar{U}_i(\bar{x},\omega) = \nabla\Phi_i(\bar{x},\omega) \tag{6.13}$$

Substituting Equation (6.13) into the velocity continuity equation (6.9) shows that the velocity potential $\Phi_i(\bar{x},\omega)$ for an incompressible fluid satisfies Laplace's Equation,

$$\nabla^2\Phi_i(\bar{x},\omega) = 0 \qquad ;\ \bar{x}\ \text{in}\ \{V\} \tag{6.14}$$

where $\{V\}$ represents the set of points in the fluid domain.

Boundary conditions for $\Phi_i(\bar{x},\omega)$ can be found from the boundary conditions for $\bar{U}_i(\bar{x},\omega)$. Since the component of velocity in any particular direction is equal to the spatial derivative of the velocity potential in that direction, the normal component of the velocity on the boundaries of the fluid domain specifies the derivative of the velocity potential in the direction normal to the boundary,

$$\frac{\partial\Phi_i(\bar{x},\omega)}{\partial n} = \hat{n}\cdot\bar{U}_{bc}(\bar{x},\omega) \qquad ;\ \bar{x}\ \text{in}\ \{S\} \tag{6.15}$$

where $\hat{n}$ is a unit vector in the direction that is perpendicular to the surface of the boundary, $\partial/\partial n$ represents differentiation in the $\hat{n}$ direction, and $\{S\}$ represents the set of points on the surface of $\{V\}$. Equations (6.14) and (6.15) completely define a boundary value problem whose solution then completely determines the solution to Equations (6.8)-(6.11). Substituting Equation (6.13) into Equations (6.8) and (6.11) generates expressions for the pressure in the fluid and the torque on the rigid body in terms of the velocity potential.

$$P(\bar{x},\omega) = -j\omega\rho\Phi_i(\bar{x},\omega) \qquad ;\ \bar{x}\ \text{in}\ \{V\} \tag{6.16}$$

$$T(\omega) = j\omega\rho\,\hat{z}\cdot\int_R\left(\Phi_i(\bar{x},\omega)\,\bar{r}\times\overline{dR}\right) \tag{6.17}$$

6.2.2 UNIQUENESS OF SOLUTIONS TO LAPLACE'S EQUATION

Specification of the normal derivative of $\Phi_i(\bar{x},\omega)$ over the entire surface of the fluid domain uniquely determines the value of $\Phi_i(\bar{x},\omega)$ at every point in the fluid domain (Yih, 1977; Batchelor, 1967). Thus, because of the special form of the boundary conditions in Equation (6.15), Equations (6.14) and (6.15) have a unique solution.

6.2.3 THE VELOCITY POTENTIAL FOR PURELY REAL BOUNDARY CONDITIONS IS A PURELY REAL FUNCTION OF SPACE

Consider the real and imaginary components of a velocity potential as defined in Equation (6.18).

$$\Phi_i(\bar{x},\omega) = \Phi_r(\bar{x},\omega) + j\,\Phi_j(\bar{x},\omega) \tag{6.18}$$

Since the Laplacian operator is linear, if $\Phi_i(\bar{x},\omega)$ satisfies Laplace's equation (6.14),

$$\nabla^2\Phi_i(\bar{x},\omega) = \nabla^2\Phi_r + j\,\nabla^2\Phi_j = 0 \tag{6.19}$$

it follows that both $\Phi_r(\bar{x},\omega)$ and $\Phi_j(\bar{x},\omega)$ individually satisfy Laplace's equation.

$$\nabla^2\Phi_r(\bar{x},\omega) = 0 \tag{6.20}$$

$$\nabla^2\Phi_j(\bar{x},\omega) = 0 \tag{6.21}$$

Similarly separate the components of the boundary conditions for $\Phi_i(\bar{x},\omega)$ in Equation (6.15).

$$\frac{\partial\Phi_r(\bar{x},\omega)}{\partial n} = \hat{n}\cdot \mathrm{Re}\{\bar{U}_{bc}(\bar{x},\omega)\} \tag{6.22}$$

$$\frac{\partial\Phi_j(\bar{x},\omega)}{\partial n} = \hat{n}\cdot \mathrm{Im}\{\bar{U}_{bc}(\bar{x},\omega)\} \tag{6.23}$$

Consider the case when the boundary conditions for $\Phi_j(\bar{x},\omega)$ in Equation (6.23) are homogeneous (i.e. $\mathrm{Im}\{\bar{U}_{bc}(\bar{x},\omega)\}=0$). One solution to Equation (6.21) is trivial

$$\Phi_j(\bar{x},\omega) = 0 \tag{6.24}$$

and the fluid velocity field associated with the solution in Equation (6.24) is $\bar{U}_j(\bar{x},\omega)=\bar{0}$. The uniqueness theorem of the previous section however requires that the solution in Equation (6.24) is the only solution to Equation (6.21) that is compatible with homogeneous boundary conditions of the form given in Equation (6.23).

We have therefore established that if the normal component of the velocity on boundaries that fully enclose the fluid domain are purely real-valued, then the resulting fluid velocity field is purely real-valued at every point in the fluid domain.

6.3 HIGH FREQUENCY EXPRESSIONS FOR THE MOTION OF A HINGED BODY

In this section we derive expressions for the motion of the hinged body in an inviscid fluid. The expressions in this section follow from very general properties of inviscid fluid motion (section 6.2) and do not depend on the shape of the rigid body.

6.3.1 B-COMPONENT OF HIGH FREQUENCY TORQUE

Since the basal plate is translated in its plane, the normal component of velocity at the boundary between the fluid and the basal plate (y=0) is zero. Since, for the B-component, the tectorial plate is stationary, the normal component of velocity at y=G is also zero.

$$\hat{y} \cdot \bar{U}_{Bi}(\bar{x},\omega) = 0 \qquad ; \{y = 0,G\} \tag{6.25}$$

If the rigid body were not present in Figure 4.1, then translation of the basal plate would generate no motion of inviscid fluid. Therefore, Equation (4.47), which specifies that the fluid velocity at the "distant boundary" should equal the fluid velocity in the absence of the body ($\bar{V}_B(\bar{x},\omega)$), specifies a homogeneous boundary condition for inviscid fluid.

$$\bar{U}_{Bi}(\bar{x},\omega) = \left[\lim_{\omega\to\infty} \bar{V}_B(\bar{x},\omega)\right] = 0 \qquad ; \{0 < y < G\} \text{ and } \{x,z \to \pm\infty\} \tag{6.26}$$

When the basal plate is translated however, the rigid body is also translated (Equation (4.48)), and the component of that motion that is normal to the rigid boundary is non-zero if the projection of the body onto the y-z plane of Figure 4.1 has non-zero area.

$$\hat{n} \cdot \bar{U}_{Bi}(\bar{x},\omega) = U_b\, \hat{n} \cdot \hat{x} \qquad ; \bar{x} \text{ in } \{R\} \tag{6.27}$$

Let $\Phi_{Bi}(\bar{x},\omega)$ represent the velocity potential of the B-component of the solution to the inviscid equations of motion for the hinged body. Equations (6.28)-(6.31) completely determine $\Phi_{Bi}(\bar{x},\omega)$.

$$\nabla^2 \Phi_{Bi}(\bar{x},\omega) = 0 \qquad ; \bar{x} \text{ in the fluid domain} \tag{6.28}$$

$$\frac{\partial \Phi_{Bi}(\bar{x},\omega)}{\partial n} = U_b\, \hat{n} \cdot \hat{x} \qquad ; \bar{x} \text{ in } \{R\} \tag{6.29}$$

$$\frac{\partial \Phi_{Bi}(\bar{x},\omega)}{\partial y} = 0 \qquad ; \{y=0,G\} \tag{6.30}$$

$$\Phi_{Bi}(\bar{x},\omega) = 0 \qquad ; \{0 < y < G\} \text{ and } \{x,z \to \infty\} \tag{6.31}$$

Dividing each of Equations (6.28)-(6.31) by U_b results in a set of equations for $\Phi_{Bi}(\bar{x},\omega)/U_b$ whose boundary conditions are purely real-valued. Thus, by the results of section 6.2, $\Phi_{Bi}(\bar{x},\omega)/U_b$ is purely real-valued throughoutthe fluid domain. Furthermore, dividing each of Equations (6.28)-(6.31) by U_b results in a set of equations that are independent of ω. Thus $\Phi_{Bi}(\bar{x},\omega)/U_b$ is independent of ω. Substituting $F_{Bi}(\bar{x}) = \Phi_{Bi}(\bar{x},\omega)/U_b$ into Equation (6.17) results in an expression for the B-component of

the torque that is generated by an inviscid fluid,

$$T_B(\omega) = j\omega M_B U_b \qquad ; \; M_B = \rho \hat{z} \cdot \int_R [F_{Bi}(\bar{x}) \, \bar{r} \times d\bar{R}] \tag{6.32}$$

where M_B is a real-valued constant. The high frequency limit of $H_B(\omega)$ (Equation (4.64))

$$\lim_{\omega \to \infty} H_B(\omega) = H_{Bi}(\omega) = \frac{T_{Bi}(\omega)}{U_b} = j\omega M_B \tag{6.33}$$

is therefore inertial.

6.3.2 T-COMPONENT OF HIGH FREQUENCY TORQUE

We now show that vibration of the tectoral plate in an inviscid fluid does not affect the rigid body. Since the tectorial plate is translated in its plane, the normal component of the velocity at the boundary between the fluid and the basal plate is zero. For reasons that are directly analogous to those given for the B-component, the "distant boundary" condition for asymptotically high frequencies of tectorial plate vibration is homogeneous. Since all of the boundary conditions for the T-component are homogeneous, the T-component of the solution to the equations of motion for the hinged plate for asymptotically high frequencies is given by

$$\bar{U}_{Ti}(\bar{x},\omega) = \bar{0} \tag{6.34}$$

$$P_{Ti}(\bar{x},\omega) = P_{Ti} = \text{constant} \tag{6.35}$$

$$T_{Ti}(\omega) = 0 \tag{6.36}$$

and the high frequency limit of $H_T(\omega)$ (Equation (4.65)) is zero,

$$\lim_{\omega \to \infty} H_T(\omega) = H_{Ti}(\omega) = \frac{T_{Ti}(\omega)}{U_t} = 0 \; . \tag{6.37}$$

6.3.3 R-COMPONENT OF HIGH FREQUENCY TORQUE

Let $\Phi_{Ri}(\bar{x},\omega)$ represent the velocity potential for the R-component of the solution to the inviscid equations of motion. Equations (6.38)-(6.41) completely determine $\Phi_{Ri}(\bar{x},\omega)$.

$$\nabla^2 \Phi_{Ri}(\bar{x},\omega) = 0 \qquad ; \; \bar{x} \text{ in the fluid domain} \tag{6.38}$$

$$\frac{\partial \Phi_{Ri}(\bar{x},\omega)}{\partial n} = j\omega\Theta(\omega) \, \hat{n} \cdot (\hat{z} \times \bar{r}) \qquad ; \; \bar{x} \text{ in } \{R\} \tag{6.39}$$

$$\frac{\partial \Phi_{Ri}(\bar{x},\omega)}{\partial y} = 0 \qquad ; \; \{y=0,G\} \tag{6.40}$$

$$\Phi_{Ri}(\bar{x},\omega) = 0 \qquad ; \; \{0 < y < G\} \text{ and } \{x,z \to \infty\} \tag{6.41}$$

Dividing each of Equations (6.38)-(6.41) by $j\omega\Theta(\omega)$ results in a set of equations for $\Phi_{Ri}(\bar{x},\omega)/(j\omega\Theta(\omega))$ whose boundary conditions are purely real-valued. Thus, by the results of section 6.2, $\Phi_{Ri}(\bar{x},\omega)/(j\omega\Theta(\omega))$ is purely real-valued throughout the fluid domain. Furthermore, dividing each of Equations (6.38)-(6.41) by $j\omega\Theta(\omega)$ results in a set of equations that are independent of ω. Thus $\Phi_{Ri}(\bar{x},\omega)/(j\omega\Theta(\omega))$ is independent of ω.

Substituting $F_{Ri}(\bar{x}) = \Phi_{Ri}(\bar{x},\omega)/(j\omega\Theta(\omega))$ into Equation (6.17) results in an expression for the R-component of the torque that is generated by an inviscid fluid,

$$T_{Ri}(\omega) = \omega^2 I_R \Theta(\omega) \qquad ; \; I_R = -\rho \hat{z} \cdot \int_R [F_{Ri}(\bar{x})\, \bar{r} \times d\bar{R}] \tag{6.42}$$

where I_R is a real-valued constant. The high frequency limit of $Z_R(\omega)$ (Equation (4.66))

$$\lim_{\omega \to \infty} Z_R(\omega) = Z_{Ri}(\omega) = -\frac{T_{Ri}(\omega)}{j\omega\Theta(\omega)} = j\omega I_R \tag{6.43}$$

is therefore inertial.

6.3.4 EQUATIONS OF MOTION FOR THE HINGED BODY FOR ASYMPTOTICALLY HIGH FREQUENCIES OF EXCITATION

The high frequency asymptotic expressions for the hydrodynamic impedances on the hinged body, $H_B(\omega)$, $H_T(\omega)$, and $Z_R(\omega)$, can be used to generate expressions for the motion of the hinged body that results from translation of the basal and tectorial plates at high frequencies. Substitute Equations (6.33), (6.37), and (6.43) into Equation (4.67).

$$[K-(I+I_R)\omega^2]\Theta(\omega) = j\omega M_B U_b + 0\, U_t \tag{6.44}$$

At high frequencies, the angular displacement of the rigid body does not depend on the velocity of the tectorial plate. The high frequency relationship between the angular displacement of the rigid body and the velocity of the basal plate can be found by solving Equation (6.44) for the ratio $\Theta(\omega)/U_b$.

$$\frac{\Theta(\omega)}{U_b} = \frac{j\omega M_B}{K - \omega^2(I+I_R)} \tag{6.45}$$

For high frequencies of excitation, $K << \omega^2(I+I_R)$, so that in the limit of increasing frequency,

$$\lim_{\omega \to \infty} \frac{\Theta(\omega)}{U_b} = \frac{M_B}{j\omega(I+I_R)} \tag{6.46}$$

the ratio of angular displacement of the rigid body to basal plate velocity is inversely proportional to $(j\omega)$, i.e. the angular displacement of the rigid body is proportional to basal plate displacement.

6.3.5 CONCLUSIONS

In this section we have analyzed the motion of the hinged body when the surrounding fluid has no viscosity. Coupled with the linearity of the equations of motion for excitations with infinitesimal amplitude, the inviscid approximation leads to very simple equations of motion whose solution can be characterized without knowing the details of the shape of the rigid body. We found that vibration of the tectorial plate in its plane has no effect on the motion of the rigid body when the fluid viscosity is zero. We found that the angular displacement of the rigid body is proportional to the imposed displacement of the basal plate.

These results are illustrated in Figure 6.1 by a circuit model that is analogous to the one in Figure 4.3.

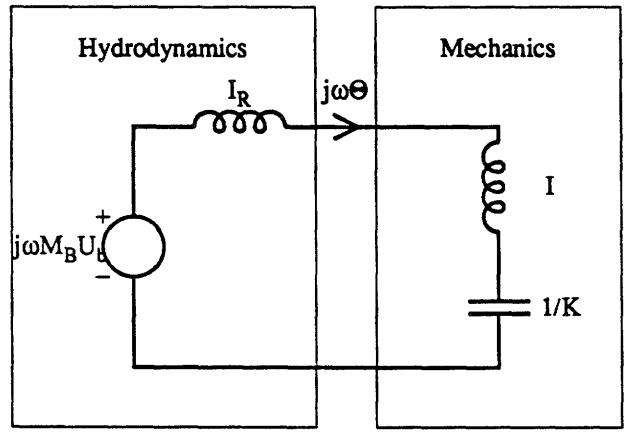

Figure 6.1: Equivalent circuit description of the high frequency asymptotic relationship between U_b and $\Theta(\omega)$. This figure is like Figure 4.3 except that (1) the tectorial term $H_{Ti}U_t$ is zero, (2) $H_{Bi}=j\omega M_B$, (3) $Z_{Ri}=j\omega I_R$ (illustrated as an inductor).

CHAPTER 7
ASYMPTOTIC ANALYSIS OF THE MOTION OF A FREE-STANDING, HINGED FLAP

In chapters 4, 5, and 6, we studied the motion of a rigid body that lies in a fluid filled region that is bounded by two plates, and determined expressions for that motion for both asymptotically high and asymptotically low frequencies of excitation. In this chapter, we develop asymptotic expressions for the motion of a free-standing, rectangular flap that is infinite in extent, has infinitesimal thickness, and is massless (Figure 7.1). There are several reasons for analyzing the asymptotic behavior of the hinged-flap structure, which is a special case of the more general hinged-body structures of chapters 4, 5, and 6. First, this chapter provides an explicit example of the application of the general results of chapters 5 and 6 to a particular body shape. Second, the general results are expressed in terms of constants that depend on the geometry of the body. We evaluate those constants explicitly for the hinged-flap structure. Third, the hinged-flap structure is analyzed numerically in chapter 8. This section provides quantitative asymptotic expressions that can be directly compared to the numerical solutions of chapter 8. To the extent that the asymptotic and numerical results match, the asymptotic methods are corroborated by the numerical analysis and the numerical methods are corroborated by the asymptotic analysis.

In section 7.1, we develop the equations of motion for the hinged-flap structure, and demonstrate several properties of those equations that make analysis of that structure simpler than that of the more general hinged-body structure. In section 7.2, we develop low frequency asymptotic expressions for the motion of the hinged-flap structure, by building on the analysis of chapter 5. In section 7.3, we develop high frequency asymptotic expressions by building on the analysis of chapter 6.

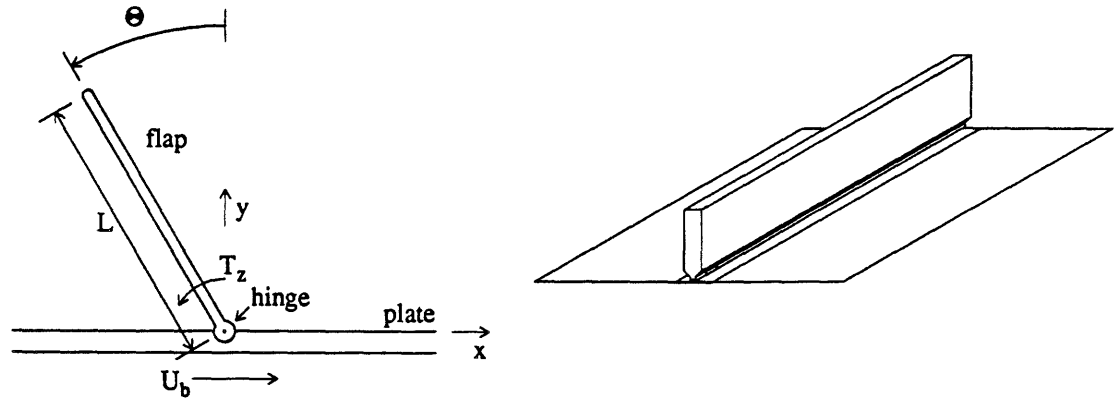

Figure 7.1: The hinged-flap structure. The right panel illustrates a section of the infinitely long flap that is connected by an infinitely long hinge to a flat plate of infinite dimension. All cross sections through planes that are perpendicular to the axis of the hinge are identical, and are illustrated in the left panel of this figure. The flap extends a distance L from the hinge. x and y are rectangular position coordinates in an inertial frame of reference with origin at the (undisplaced) location of the hinge. The z axis is perpendicular to the plane of x and y so that $\hat{z}=\hat{x}\times\hat{y}$, where $\hat{x}$, $\hat{y}$, and $\hat{z}$ are unit vectors pointing in the x, y, and z directions. U_b is the complex amplitude of the sinusoidal velocity of the plate. Θ is the complex amplitude of the angular displacement of the flap from the y-axis. T_z is the complex amplitude of the hydrodynamical torque on the flap about its base per unit length of the flap along the z-axis. U_b, Θ, and T_z are all scalars. The angular displacement of about 30^o shown in this figure was chosen for clarity. All analyses in this chapter are limited to infinitesimally small angular displacements.

7.1 THE EQUATIONS OF MOTION FOR THE HINGED FLAP

In this section, we develop the equations of motion for the hinged-flap structure, and demonstrate a number of properties of those equations that can be used to simplify numerical analysis.

7.1.1 FORMULATION OF THE EQUATIONS OF MOTION

The hinged-flap structure (Figure 7.1) is a special case of the hinged-body structure (Figure 4.1) that is analyzed in chapters 4, 5, and 6. The hinged-flap structure is essentially two dimensional, i.e. all cross sections through planes perpendicular to the z-axis are identical. Furthermore, for excitations of infinitesimal amplitudes, the surfaces of the flap are nearly perpendicular to the plate. For these two reasons, the equations of motion for the flap structure can be expressed in a simpler form than the more general equations of motion for the hinged-body (Equations (4.40)-(4.44)). In this section, we develop the linearized equations of motion of the hinged flap, that are valid for excitations of infinitesimal amplitude.

7.1.1.1 EQUATIONS OF MOTION FOR THE FLUID

Let $\bar{U}(\bar{x},\omega)$ represent the complex amplitude of the sinusoidal steady-state fluid velocity vector. Let $P(\bar{x},\omega)$ denote the complex amplitude of pressure. For sufficiently small velocities, the equations of motion for an incompressible Newtonian fluid are linear, i.e.

$$j\omega\rho\bar{U}(\bar{x},\omega) = -\nabla P(\bar{x},\omega) + \mu\nabla^2\bar{U}(\bar{x},\omega) \tag{7.1}$$

$$\nabla \cdot \bar{U}(\bar{x},\omega) = 0 \tag{7.2}$$

where $j=\sqrt{-1}$, ω is angular frequency, and $\bar{x}$ represents the position vector of a point in the fluid domain with coordinates (x,y,z). Equation (7.1) expresses conservation of momentum at each point in the fluid domain and will be referred to as the momentum equation. Equation (7.2) expresses continuity of fluid velocity at each point in the fluid domain -- a consequence of fluid incompressibility and conservation of mass. Equation (7.2) will be referred to as the continuity equation.

7.1.1.2 BOUNDARY CONDITIONS WITH RIGID SURFACES

The velocity of the fluid that is adjacent to the mechanical boundaries in Figure 7.1 must be equal to the velocity of the boundaries. This technically incorporates two separate constraints. The continuity equation (7.2) requires that the normal component of the velocity of the fluid near a surface equal that of the surface. The viscosity of the fluid requires that a no-slip condition be imposed on the tangential component of velocity near the rigid surfaces. The fluid velocity near the plate is therefore constrained to be $U_b\hat{x}$, where $\hat{x}$ is a unit vector pointing in the x-direction. Points on the flap have velocities with both x and y components. For sufficiently small angular displacements Θ, the

y-component of the velocity of points on the flap is negligible. Thus the no-slip boundary conditions can be summarized as

$$\bar{U}(\bar{x},\omega) = (U_b - j\omega y\Theta(\omega))\,\hat{x} \qquad ; \{y=0\} \text{ or } \{x=0 \;\&\; 0<y<L\} \tag{7.3}$$

where {x=0 & 0<y<L} specifies points near the flap and {y=0} specifies points on the plate.

7.1.1.3 EQUATION OF MOTION FOR THE FLAP

Since the flap can rotate, an equation of motion for the flap is also required. Two mechanisms generate torque on the flap. First, a torque is exerted on the flap as a result of the hydrodynamical pressure on the surfaces of the flap. The hydrodynamical torque exerted per unit length of the infinitely long flap is given by Equation (7.4).

$$T_z(\omega) = \int_0^L y\,\Delta P(y,\omega)\,dy \qquad ; \Delta P(y,\omega) = \left[P(\bar{x},\omega)\Big|_{x=0^+} - P(\bar{x},\omega)\Big|_{x=0^-} \right] \tag{7.4}$$

$\Delta P(y,\omega)$ represents the difference in pressure across the flap and is spatially dependent on y alone. $T_z(\omega)$ has the dimensions of torque per unit distance. A second torque is generated by the spring,

$$T_{Kz} = -K_z\Theta \; . \tag{7.5}$$

T_{Kz} has the dimensions of torque per unit distance. K_z represents the torsional stiffness of the spring and has the units of torque per unit length per unit angular displacement. Since the flap is massless, the total torque on the flap about the hinge must be zero,

$$T_z + T_{Kz} = 0. \tag{7.6}$$

7.1.1.4 DISTANT BOUNDARY CONDITIONS

The spatial extent of the fluid domain in Figure 7.1 is infinite. In this study however, artificial boundary conditions are imposed at the edges of a finite rectangular domain.

$$\bar{U}(\bar{x},\omega) = \bar{U}_\delta(\bar{x},\omega) \qquad ; \{x=\pm X \;\&\; 0<y<Y\} \text{ or } \{-X<x<X \;\&\; y=Y\} \tag{7.7}$$

$\bar{U}_\delta(\bar{x},\omega)$ is equal to the fluid velocity that would result in the absence of the flap, and depends exponentially on distance from the plate.

$$\bar{U}_\delta(\bar{x},\omega) = U_b e^{-y\sqrt{j\omega/\nu}}\,\hat{x} \tag{7.8}$$

7.1.2 SUPERPOSITION

The motion of the hinged flap structure can be completely characterized by two complex-valued scalars -- U_b, the velocity of the plate, and $\Theta(\omega)$, the angular displacement of the flap. Since the equations of motion for the fluid (Equations (7.1)-(7.2)) are linear, we can write the solution to those equations as the sum of the solutions to two component problems (section 4.3). The first component describes the fluid motion that is generated by translation of the plate while the angular displacment of the body is fixed at zero. The second component describes the fluid motion that is generated by angular displacement of the flap while the plate is held fixed.

Let $\bar{U}_P(\bar{x},\omega)$, $P_P(\bar{x},\omega)$, and $T_{Pz}(\omega)$ represent the P-component (plate component) of the solution to the equations of motion of the flap structure (Equations (7.1)-(7.8)), given by:

$$j\omega\rho\bar{U}_P(\bar{x},\omega) = -\nabla P_P(\bar{x},\omega) + \mu\nabla^2\bar{U}_P(\bar{x},\omega) \quad ; \{-X<x<X \ \& \ y>0\} \tag{7.9}$$

$$\nabla\cdot\bar{U}_P(\bar{x},\omega) = 0 \quad ; \{-X<x<X \ \& \ y>0\} \tag{7.10}$$

$$\bar{U}_P(\bar{x},\omega) = U_b\,\hat{x} \quad ; \{y=0\} \text{ or } \{x=0 \ \& \ 0<y<L\} \tag{7.11}$$

$$\bar{U}_P(\bar{x},\omega) = U_b e^{-y\sqrt{j\omega/\nu}}\,\hat{x} \quad ; \{-X<x<X \ \& \ y=Y\} \text{ or } \{x=\pm X \ \& \ 0<y<L\} \tag{7.12}$$

$$T_{Pz}(\omega) = \int_0^L y\,\Delta P_P(y,\omega)\,dy\ . \tag{7.13}$$

Let $\bar{U}_R(\bar{x},\omega)$, $P_R(\bar{x},\omega)$, and $T_R(\omega)$ represent the R-component (rotational component) of the solution to the equations of motion of the flap structure, given by:

$$j\omega\rho\bar{U}_R(\bar{x},\omega) = -\nabla P_R(\bar{x},\omega) + \mu\nabla^2\bar{U}_R(\bar{x},\omega) \quad ; \{-X<x<X \ \& \ y>0\} \tag{7.14}$$

$$\nabla\cdot\bar{U}_R(\bar{x},\omega) = 0 \quad ; \{-X<x<X \ \& \ y>0\} \tag{7.15}$$

$$\bar{U}_R(\bar{x},\omega) = -j\omega\Theta(\omega)y\,\hat{x} \quad ; \{y=0\} \text{ or } \{x=0 \ \& \ 0<y<L\} \tag{7.16}$$

$$\bar{U}_R(\bar{x},\omega) = \bar{0} \quad ; \{-X<x<X \ \& \ y=Y\} \text{ or } \{x=\pm X \ \& \ 0<y<L\} \tag{7.17}$$

$$T_{Rz}(\omega) = \int_0^L y\,\Delta P_R(y,\omega)\,dy\ . \tag{7.18}$$

The solution to Equations (7.1)-(7.8) can be written in terms of the P- and R-components:

$$\bar{U}(\bar{x},\omega) = \bar{U}_P(\bar{x},\omega) + \bar{U}_R(\bar{x},\omega) \tag{7.19}$$

$$P(\bar{x},\omega) = P_P(\bar{x},\omega) + P_R(\bar{x},\omega) \tag{7.20}$$

$$T_z(\omega) = T_{Pz}(\omega) + T_{Rz}(\omega) \tag{7.21}$$

subject also to the constraint that

$$T_z(\omega) = K_z\Theta(\omega)\ . \tag{7.22}$$

7.1.3 LUMPED PARAMETER MODEL OF THE MOTION OF THE HINGED-FLAP

Equations (7.9)-(7.13) define a transformation from U_b to $T_{Pz}(\omega)$ that can be characterized explicitly by $H_{Pz}(\omega)$,

$$H_{Pz}(\omega) = \frac{T_{Pz}(\omega)}{U_b} \tag{7.23}$$

which is a transfer impedance. Equations (7.14)-(7.18) define a transformation from $j\omega\Theta(\omega)$ to $T_{Rz}(\omega)$ that can be characterized explicitly by $Z_{Rz}(\omega)$,

$$Z_{Rz}(\omega) = - \frac{T_{Rz}(\omega)}{j\omega\Theta(\omega)} \tag{7.24}$$

which is a rotational impedance. Substitute Equations (7.23) and (7.24) into Equations (7.21) and (7.22) and eliminate $T_z(\omega)$ to obtain a torque balance equation,

$$(K_z + j\omega Z_{Rz}(\omega))\,\Theta(\omega) = H_{Pz}(\omega)U_b \tag{7.25}$$

which can be represented by the equivalent network shown in Figure 7.2. One can solve Equation (7.25) to obtain an expression for the ratio of angular displacement of the flap divided by the velocity of the plate in terms of K_z and the hydrodynamic impedances.

$$\frac{\Theta(\omega)}{U_b} = \frac{H_{Pz}(\omega)}{K_z + j\omega Z_{Rz}(\omega)} \tag{7.26}$$

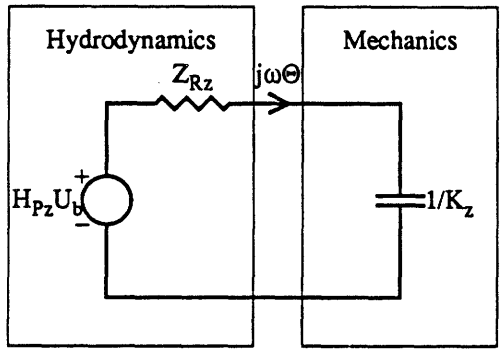

Figure 7.2: Lumped parameter representation of the motion of the hinged flap. This circuit model illustrates the balance of torques that is required at the hinge by Equation (7.25). The hydrodynamic torque on the body is represented as the sum of two components: $H_{Pz}U_b$ is the torque per unit extent along the z-axis that results from translation of the plate with the angular displacement of the flap fixed; and $j\omega\Theta(\omega)Z_{Rz}$ represents the torque per unit extent along the z-axis that is generated by rotation of the flap with the plate fixed. K_z represents the torsional stiffness of the spring per unit length of the hinge.

The results of this section greatly simplify the numerical work required to characterize the solution to the equations of motion. In later sections, we compute $H_{Pz}(\omega)$ by calculating the torque that is generated on a unit length of the flap by translation of the plate with unit velocity when the angular displacement of the flap is held fixed. We also compute $Z_{Rz}(\omega)$ by calculating the torque that is generated on a unit length of the flap by a unit angular velocity of the flap with the plate held fixed. Have done these two hydrodynamic calculations, we then determine the effect of varying K_z by using the lumped parameter representation in Figure 7.2.

7.1.4 NORMALIZED VARIABLES

The motion of the hinged flap depends on the values of five parameters: K_z and L parameterize the rigid structure; ρ and μ characterize the fluid; and ω characterizes the excitation. In this section, we scale the spatial and frequency variables and show that the resulting normalized equations of motion contain a single non-dimensional parameter. We can therefore completely characterize the solution to the equations of motion by computing numerical solutions for all values of a single parameter, rather than for all values of all five physical parameters.

Scale all distances by the height of the flap,

$$x_n = \frac{x}{L} \quad , \; y_n = \frac{y}{L} \; , \tag{7.27}$$

and scale the frequency of excitation ω, by the frequency for which the boundary layer thickness is equal to the height of the flap,

$$\omega_n = \frac{\omega}{\omega_L} \; ; \qquad \omega_L = \frac{2\nu}{L^2} \; . \tag{7.28}$$

Define normalized hydrodynamical and mechanical variables,

$$\bar{U}_n(\bar{x}_n,\omega_n) = \bar{U}(\bar{x},\omega) \; ; \quad \bar{U}_{Pn}(\bar{x}_n,\omega_n) = \bar{U}_P(\bar{x},\omega) \; ; \quad \bar{U}_{Rn}(\bar{x}_n,\omega_n) = \bar{U}_R(\bar{x},\omega) \tag{7.29}$$

$$P_n(\bar{x}_n,\omega_n) = \frac{L}{\mu} P(\bar{x},\omega) \; ; \quad P_{Pn}(\bar{x}_n,\omega_n) = \frac{L}{\mu} P_P(\bar{x},\omega) \; ; \quad P_{Rn}(\bar{x}_n,\omega_n) = \frac{L}{\mu} P_R(\bar{x},\omega) \tag{7.30}$$

$$\Theta_n(\omega_n) = \frac{2\nu}{L} \Theta(\omega) \; ; \quad \Theta_{Pn}(\omega_n) = \frac{2\nu}{L} \Theta_P(\omega) \; ; \quad \Theta_{Rn}(\omega_n) = \frac{2\nu}{L} \Theta_R(\omega) \tag{7.31}$$

$$T_{zn}(\omega_n) = \frac{1}{\mu L} T_z(\omega) \; ; \quad T_{Pzn}(\omega_n) = \frac{1}{\mu L} T_{Pz}(\omega) \; ; \quad T_{Rzn}(\omega_n) = \frac{1}{\mu L} T_{Rz}(\omega) \tag{7.32}$$

and normalized hydrodynamic impedances, $H_{Pzn}(\omega_n)$ and $Z_{Rzn}(\omega_n)$,

$$H_{Pzn}(\omega_n) = \frac{T_{Pzn}(\omega_n)}{U_b} \tag{7.33}$$

$$Z_{Rzn}(\omega_n) = -\frac{T_{Rzn}(\omega_n)}{j\omega_n \Theta_n(\omega_n)} \; . \tag{7.34}$$

Substituting Equations (7.27)-(7.32) into the component equations of motion for the flap (7.9)-(7.18) results in an equivalent set of normalized equations of motion.

$$j2\omega_n \bar{U}_{Pn}(\bar{x}_n,\omega_n) = -\nabla_n P_{Pn}(\bar{x}_n,\omega_n) + \nabla_n^2 \bar{U}_{Pn}(\bar{x}_n,\omega_n) \; ; \; \{-X_n<x_n<X_n \;\&\; y_n>0\} \quad (7.35)$$

$$\nabla \cdot \bar{U}_{Pn}(\bar{x}_n,\omega_n) = 0 \quad ; \; \{-X_n<x_n<X_n \;\&\; y_n>0\} \quad (7.36)$$

$$\bar{U}_{Pn}(\bar{x}_n,\omega_n) = U_b \hat{x}_n \quad ; \; \{y_n=0\} \text{ or } \{x_n=0 \;\&\; 0<y_n<1\} \quad (7.37)$$

$$\bar{U}_{Pn}(\bar{x}_n,\omega_n) = U_b e^{-y_n\sqrt{j2\omega_n}} \hat{x}_n \quad ; \; \{-X_n<x_n<X_n \;\&\; y_n=Y_n\} \text{ or } \{x_n=\pm X_n \;\&\; 0<y_n<1\} \quad (7.38)$$

$$T_{Pzn}(\omega_n) = \int_0^1 y_n \, \Delta P_{Pn}(y_n,\omega_n) \, dy_n \; . \quad (7.39)$$

$$j2\omega_n \bar{U}_{Rn}(\bar{x}_n,\omega_n) = -\nabla_n P_{Rn}(\bar{x}_n,\omega_n) + \nabla_n^2 \bar{U}_{Rn}(\bar{x}_n,\omega_n) \; ; \; \{-X_n<x_n<X_n \;\&\; y_n>0\} \quad (7.40)$$

$$\nabla \cdot \bar{U}_{Rn}(\bar{x}_n,\omega_n) = 0 \quad ; \; \{-X_n<x_n<X_n \;\&\; y_n>0\} \quad (7.41)$$

$$\bar{U}_{Rn}(\bar{x}_n,\omega_n) = -j\omega_n y_n \Theta_n(\omega_n) \hat{x}_n \quad ; \; \{y_n=0\} \text{ or } \{x_n=0 \;\&\; 0<y_n<1\} \quad (7.42)$$

$$\bar{U}_{Rn}(\bar{x}_n,\omega_n) = \bar{0} \quad ; \; \{-X_n<x_n<X_n \;\&\; y_n=Y_n\} \text{ or } \{x_n=\pm X_n \;\&\; 0<y_n<1\} \quad (7.43)$$

$$T_{Rzn}(\omega_n) = \int_0^1 y_n \, \Delta P_{Rn}(y_n,\omega_n) \, dy_n \; . \quad (7.44)$$

A single non-dimensional parameter, ω_n, appears in Equations (7.35)-(7.44). Thus, to compute the solution to the component equations of motion (Equations (7.9)-(7.18)): (1) compute $\omega_n=\omega/\omega_L$; (2) solve the non-dimensional equations of motion (Equations (7.35)-(7.44)); and (3) scale the resulting non-dimensional variables by Equations (7.27)-(7.32).

Substitute Equations (7.27)-(7.32) into Equations (7.33)-(7.34) to compute the relationship between the normalized and unnormalized hydrodynamic impedances.

$$H_{Pzn}(\omega/\omega_L) = \frac{T_{Pzn}(\omega/\omega_L)}{U_b} = \frac{T_{Pz}(\omega)/\mu L}{U_b} = \frac{H_{Pz}(\omega)}{\mu L} \quad (7.45)$$

$$Z_{Rzn}(\omega/\omega_L) = -\frac{T_{Rzn}(\omega/\omega_L)}{j(\omega/\omega_L)\Theta_n(\omega/\omega_L)} = -\frac{T_{Rz}(\omega)/\mu L}{j\frac{\omega L^2}{2\nu}\frac{2\nu}{L}\Theta(\omega)} = \frac{Z_{Rz}(\omega)}{\mu L^2} \quad (7.46)$$

The results of this section greatly simplify the numerical work required to compute $H_{Pz}(\omega)$ and $Z_{Rz}(\omega)$. In later sections, we compute $H_{Pzn}(\omega_n)$ by finding the torque generated on a unit length of the infinitely long flap when $\Theta=0$, $U_b=1$, and $\rho=\mu=\nu=L=1$. We also compute $Z_{Rzn}(\omega_n)$ by finding the torque that is generated on a unit length of the flap when $j\omega_n\Theta=1$, $U_b=0$, and $\rho=\mu=\nu=L=1$. These results can then be generalized by using Equations (7.45) and (7.55) for any set of physical parameters.

7.1.5 STREAM FUNCTION

The geometry of the flap structure is essentially two dimensional, i.e. all cross sections that are perpendicular to the z axis are identical. Furthermore, the imposed velocity of the plate, $U_b\hat{x}$, is independent of z. For these two reasons, the fluid velocity field is not a function of z, and can be represented by a stream function, $\Psi(\bar{x},\omega)$, defined within an additive constant by

$$\hat{x}\cdot\bar{U}(\bar{x},\omega) = \frac{\partial\Psi(\bar{x},\omega)}{\partial y} \quad ; \quad \hat{y}\cdot\bar{U}(\bar{x},\omega) = -\frac{\partial\Psi(\bar{x},\omega)}{\partial x} \quad ; \quad \frac{\partial\Psi(\bar{x},\omega)}{\partial z} = 0 \ . \tag{7.47}$$

Note that the definition of the stream function guarantees that the continuity equation for the fluid (Equation (7.2)) is satisfied provided that $\partial^2\Psi/\partial y\partial x = \partial^2\Psi/\partial x\partial y$. Substitute Equations (7.47) into the linearized momentum equation (Equation (7.1)) and separate the vector components.

$$j\omega\rho\frac{\partial\Psi(\bar{x},\omega)}{\partial y} = -\frac{\partial P(\bar{x},\omega)}{\partial x} + \mu\nabla^2\frac{\partial\Psi(\bar{x},\omega)}{\partial y} \tag{7.48}$$

$$-j\omega\rho\frac{\partial\Psi(\bar{x},\omega)}{\partial x} = -\frac{\partial P(\bar{x},\omega)}{\partial y} - \mu\nabla^2\frac{\partial\Psi(\bar{x},\omega)}{\partial x} \tag{7.49}$$

Subtract the partial differential of Equation (7.49) with respect to x from the partial differential of Equation (7.48) with respect to y. Provided that $\partial P(\bar{x},\omega)/\partial x\partial y = \partial P(\bar{x},\omega)/\partial y\partial x$, the resulting single equation of motion,

$$j\omega\rho\nabla^2\Psi(\bar{x},\omega) = \mu\nabla^4\Psi(\bar{x},\omega) \tag{7.50}$$

is a function of a single scalar variable. Fluid motions that are essentially two dimensional, can thus be completely specified by a single scalar function of space, $\Psi(\bar{x},\omega)$ -- rather than by both a scalar function $P(\bar{x},\omega)$, and a vector function $\bar{U}(\bar{x},\omega)$, as in Equations (7.1) and (7.2). We use the stream function representation in section 8.1.2 to reduce the number of difference equations in the numerical analysis.

Explicit computation of the stream function also simplifies the display of the fluid motion that results from the solution of the equations of motion. Collections of points of equal stream function are called streamlines. Since

$$\nabla\Psi(\bar{x},\omega)\cdot\bar{U}(\bar{x},\omega) = \left(\frac{\partial\Psi}{\partial x}\hat{x}+\frac{\partial\Psi}{\partial y}\hat{y}\right)\cdot\left(\frac{\partial\Psi}{\partial y}\hat{x}+\frac{\partial\Psi}{\partial x}\hat{y}\right) = 0 \ , \tag{7.51}$$

the vector $\nabla\Psi(\bar{x},\omega)$ is everywhere perpendicular to the vector $\bar{U}(\bar{x},\omega)$. Therefore, streamlines, which are perpendicular to $\nabla\Psi(\bar{x},\omega)$, are everywhere parallel to the velocity vector $\bar{U}(\bar{x},\omega)$.

Since the perpendicular distance between uniformly spaced streamlines is inversely proportional to the gradient of $\Psi(\bar{x},\omega)$, and the magnitude of the gradient of $\Psi(\bar{x},\omega)$,

$$|\nabla\Psi(\bar{x},\omega)| = \left[\left(\frac{\partial\Psi}{\partial x}\right)^2+\left(\frac{\partial\Psi}{\partial y}\right)^2\right]^{1/2} = |\bar{U}(\bar{x},\omega)| \tag{7.52}$$

equals the magnitude of the fluid velocity, the fluid velocity at a point is inversely proportional to the distance between uniformly spaced streamlines at that point.

7.1.6 SYMMETRY

Not only is the flap structure essentially two dimensional, but it is also symmetric about the line x=0. We show in this section that, since the equations of motion ((7.1)-(7.8)) are linear, their solution is also symmetric about the line x=0.

Consider the fluid motion that results when the velocity of the plate is $U_b\hat{x}$. Let $\alpha(x,y,\omega)$ denote the x-component of the fluid velocity field $\bar{U}(\bar{x},\omega)$ and $\beta(x,y,\omega)$ denote the y-component, so that

$$\bar{U}(\bar{x},\omega) = \alpha(x,y,\omega)\hat{x} + \beta(x,y,\omega)\hat{y} \ . \tag{7.53}$$

Now (1) rotate the structure about the line x=0 (Figure 7.3 panel 2) and (2) replace x by −x (Figure 7.3 panel 3). This sequence of operations does not change the physics, but merely effects a change in labelling. Fields that had been associated with the point (x,y) are now associated with the point (−x,y). Also, velocities that had pointed in the +x direction now point in the −x direction. Let $\bar{U}_1(\bar{x},\omega)$ represent the relabelled fluid velocity field, which can be expressed in terms of $\alpha(x,y,\omega)$ and $\beta(x,y,\omega)$ as

$$\bar{U}_1(\bar{x},\omega) = -\alpha(-x,y,\omega)\hat{x} + \beta(-x,y,\omega)\hat{y} \ . \tag{7.54}$$

Since the hinged flap structure is symmetric, the rotated and relabelled structure (Figure 7.3 panel 3) differs from the original structure (Figure 7.3 panel 1) by just the sign of the velocity imposed on the plate. Since the equations of motion are linear, the fluid velocity ($\bar{U}_1(\bar{x},\omega)$) that results when the plate velocity is $-U_b\hat{x}$ is the negative of the fluid velocity ($\bar{U}_2(\bar{x},\omega)$) that results when the plate velocity is $U_b\hat{x}$, i.e.

$$\bar{U}_2(\bar{x},\omega) = -\bar{U}_1(\bar{x},\omega) \ . \tag{7.55}$$

Substitute Equation (7.54) into (7.55).

$$\bar{U}_2(\bar{x},\omega) = \alpha(-x,y,\omega)\hat{x} - \beta(x,y,\omega)\hat{y} \tag{7.56}$$

Since the structure and boundary conditions are unchanged by -- (1) rotating the structure about the line x=0; (2) replacing x by −x; and then (3) multiplying all variables by −1 -- it follows that

$$\bar{U}_2(\bar{x},\omega) = \bar{U}(\bar{x},\omega) \ . \tag{7.57}$$

Substituting Equations (7.53) and (7.56) into Equation (7.57) shows that

$$\alpha(x,y,\omega) = \alpha(-x,y,\omega) \tag{7.58}$$

$$\beta(x,y,\omega) = -\beta(-x,y,\omega) \ . \tag{7.59}$$

Thus, the x-component of the fluid velocity field $\bar{U}(\bar{x},\omega)$ is an even function of x and the y-component of the fluid velocity field is an odd function of x.

By similar reasoning, we can show that both the pressure field $P(\bar{x},\omega)$ and the stream function $\Psi(\bar{x},\omega)$ are odd functions of x. These symmetry conditions are summarized in Equations (7.60)-(7.63).

$$\hat{x} \cdot \bar{U}(\bar{x},\omega) = \hat{x} \cdot \bar{U}(\bar{x}_1,\omega) \quad ; \; \bar{x} = (x, y, z) \; ; \; \bar{x}_1 = (-x, y, z) \tag{7.60}$$

$$\hat{y} \cdot \bar{U}(\bar{x},\omega) = -\hat{y} \cdot \bar{U}(\bar{x}_1,\omega) \tag{7.61}$$

$$P(\bar{x},\omega) = -P(\bar{x}_1,\omega) \tag{7.62}$$

$$\Psi(\bar{x},\omega) = -\Psi(\bar{x}_1,\omega) \tag{7.63}$$

The symmetry conditions of Equations (7.60)-(7.63) apply to each of the P- and R-components (Equations (7.9)-(7.18)) as well.

By using the symmetry conditions derived in this section, the spatial field over which numerical solutions must be computed is halved in size.

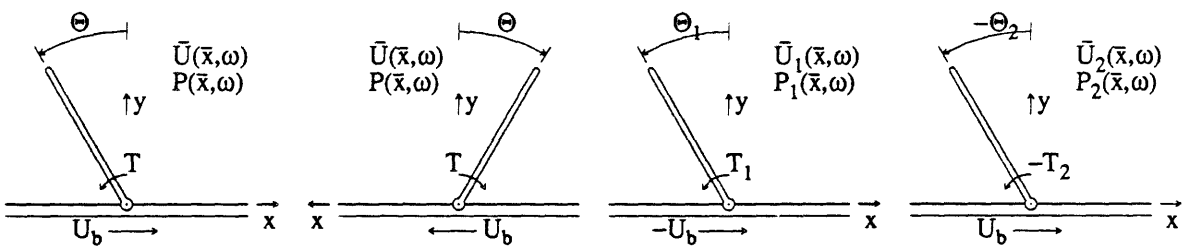

Figure 7.3: Symmetry of the solution to the equations of motion for the flap. This figure motivates the symmetry conditions that apply to the solution to the equations of motion for the hinged flap by a sequence of transformations. The left most panel illustrates key variables of Figure 7.1: x and y are rectangular position coordinates and U_b is the velocity that is imposed on the plate. The solution to Equations (7.1)-(7.8) are denoted by: T, the hydrodynamic torque on the flap; Θ, the angular displacement of the flap; $\bar{U}(\bar{x},\omega)$, the fluid velocity field; and $P(\bar{x},\omega)$, the pressure field. The structure in the first panel is rotated about the line x=0 in the second panel. The variables and equations of motion for this second panel are identical to those of the first panel. In going from the second to the third panel, the reference directions for position, angular displacement, torque, and fluid velocity have been changed. The variables in the third panel are distinquished from those of the first and second panels by the subscript 1. All of the variables in the last panel are equal the the negative of those in the third panel. Since the reference directions in the first and last panels are identical and since the rotated structure in the last panel is identical to the structure in the first panel, it follows that $\bar{U}_2(\bar{x},\omega)=\bar{U}(\bar{x},\omega)$, $P_2(\bar{x},\omega)=P(\bar{x},\omega)$, $T_2=T$, and $\Theta_2=\Theta$.

7.2 LOW FREQUENCY ASYMPTOTIC MOTION OF A FREE-STANDING FLAP

In this section, we determine low frequency asymptotic expressions for the motion of the free-standing flap-structure.

7.2.1 METHOD

As frequency decreases, boundary layer thickness increases, and fluid that is increasingly distant from the basal plate moves in synchrony with the plate. Therefore, as the frequency of vibration decreases, the hydrodynamic torque that is generated on the flap decreases. Since the hinge is spring loaded, the decreasing hydrodynamic torque gives rise to decreasing angular displacements.

Even at very low frequencies of vibration however, the velocity that is induced by translation of the basal plate decreases with distance from the plate. It is the difference between the velocity that is induced near the tip of the flap and the velocity that is induced near the hinge that generates the infinitesimal torques that occur for asymptotically low frequencies. For very low frequencies of excitation, the difference between the velocity at the tip and that at the base of the flap is proportional to $(j\omega)^{1/2}$ times the velocity of the basal plate.

In the low frequency limit, the angular displacement of the flap is zero. Thus the low-frequency fluid motion would be unchanged (to first order) by fixing the hinge so that the flap cannot rotate. Since the fluid motion is unchanged by fixing the hinge, the (infinitesimal) hydrodynamical torque imposed on the flap is also unchanged. Thus the torque on the hinged-flap can be deduced from analysis of a "fixed-flap". The stimulus that is effective at producing torque on the flap at low frequencies is a velocity field with uniform velocity gradient. Thus the torque that is generated on the hinged-flap by low frequency sinusoidal excitation of the basal plate can be derived from the torque that is on a flap with a fixed hinge that interrupts the steady motion of fluid whose velocity very distant from the flap increases with distance from the basal plate.

7.2.2 STEADY EQUATIONS OF MOTION

Dean (1936) generated a series solution to the fluid velocity field that is generated near a fixed-flap that interrupts the steady motion of fluid whose velocity very distant from the flap increases with distance from the basal plate. From Dean's results, we compute low frequency asymptotic expressions for the motion induced in a hinged-flap by sinusoidal translation of the basal plate.

Dean generated a series solution to equations of motion that are identical in form to Equations (5.10)-(5.14). Substituting Equations (7.64) into Equations (5.10)-(5.14) results in equations directly comparable to those of Dean.

$$\bar{x}_D = \frac{1}{L}\bar{x} \; ; \qquad \bar{U}_D(\bar{x}_D) = \frac{1}{L} U_{B1}(\bar{x}) \; ; \qquad P_D(\bar{x}_D) = P_{B1}(\bar{x})$$

$$\bar{V}_{B1}(\bar{x}) = -2y_D \hat{x}_D \; ; \qquad T_D = \frac{1}{L^2} T_{B1} \tag{7.64}$$

7.2.3 LOW FREQUENCY FLUID VELOCITY RELATIVE TO THE BASAL PLATE

The terms in Dean's series individually satisfied all of the constraints in Equations (5.10)-(5.14) except for the no-slip condition along the flap. Dean adjusted the weights of a linear combination of such terms so as to minimize the slip along the flap -- weighting errors near the tip of the flap most heavily. The sum of the first six terms in Dean's solution is shown in Figure 7.4.

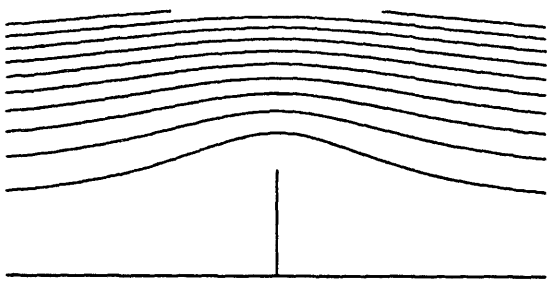

Figure 7.4: Streamlines illustrating the steady motion of fluid past a flap that is fixed so that $\theta=0$. The fluid velocity at points distant from the flap increases linearly with distance from the plate. The streamlines are drawn parallel to the direction of fluid velocity with a density that is proportional to the magnitude of fluid velocity.

The error in Dean's solution can be evaluated by determining the velocity of slip along the flap since all of the other boundary conditions are exactly satisfied. Dean reports that the largest slip velocity resulting from the six term approximation (used in Figure 7.4 and below) is 0.0015 and occurs at $y_D=0.038$. The six term approximation is thus very accurate.

7.2.4 HYDRODYNAMIC PRESSURE ON THE FLAP

Dean did not solve for the pressure field corresponding to the fluid motion illustrated in Figure 7.4 explicitly. It is a simple matter however to derive the pressure from his results by approximating differentials numerically with first order differences. Figure 7.5 shows the hydrodynamic pressure along the line $x=0^+$ that results from such a calculation.

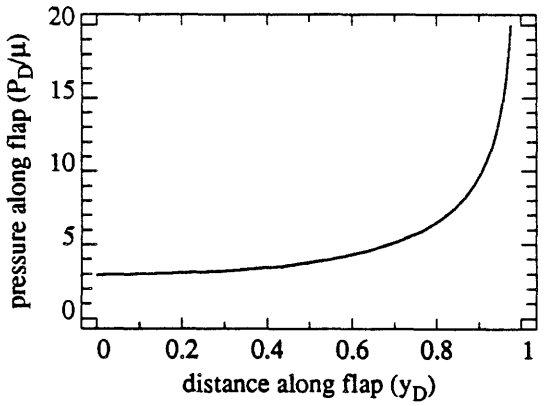

Figure 7.5: Normalized pressure on the flap. This curve plots the normalized pressure $P_D(\bar{x})/\mu$ for $x=0^+$ as a function of y_D. These data are calculated from the six term approximation of Dean (1936).

7.2.5 HYDRODYNAMIC TORQUE ON THE FLAP

The pressure along the flap (Figure 7.5) produces a hydrodynamic torque on the flap. The pressure near the tip of the flap is unbounded. To establish that the hydrodynamic torque, which is equal to the integral of distance from the hinge times the pressure across the flap, is finite, we investigate the behavior of the torque density $2y_D P_D/\mu$ in the neighborhood of the tip of the flap (Figure 7.6).

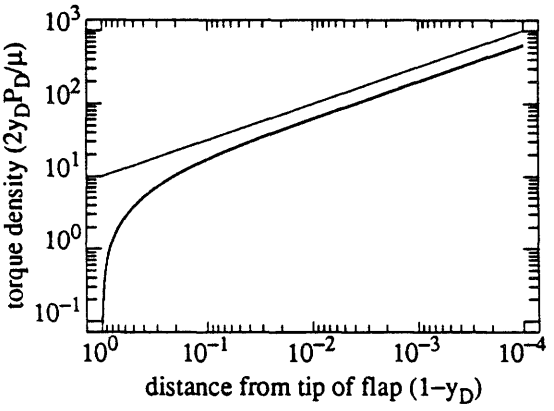

Figure 7.6: Torque density near the tip of the flap. The curved line plots the torque density $2y_D P_D(\bar{x})/\mu$ versus distance from the tip of the flap. The distance scale exaggerates the size of spatial increments that are close to the tip of the flap. The thin straight line has a slope of 1/2.

Close to the tip, the torque density $2y_D P_D(\bar{x})/\mu$ is proportional to $(1-y_D)^{-1/2}$. Thus the integral of $2y_D P_D(\bar{x})/\mu$ along the surface of the flap converges. This integral was evaluated numerically from the series of Dean (1936) and the result is given by

$$T_D = \int_0^1 2y_D P_D(\bar{x})\,dy_D = 7.907\,\mu \ . \qquad (7.65)$$

7.2.6 LOW FREQUENCY ANGULAR DISPLACEMENT OF THE FLAP

Substitute Equation (7.65) into the expression for torque in Equations (7.64).

$$T_{B1} = 7.907 \mu L^2 \tag{7.66}$$

The magnitude of the distant velocity gradient in Equations (7.66) differs from that used to define H_Δ in section 5.3.1.2. Thus H_Δ is equal to $T_{B1}/2$.

$$H_\Delta = 3.954 \mu L^2 \tag{7.67}$$

Substituting Equation (7.67) into Equation (5.100) generates an asymptotic expression for $H_{Pz}(\omega)$.

$$\lim_{\omega \to 0} \frac{H_{Pz}(\omega)}{\mu L} = 3.954 (1+j) \sqrt{\omega/\omega_L} \tag{7.68}$$

Substituting Equation (7.67) into Equation (5.107) generates an asymptotic relationship between $\Theta(\omega)$ and U_b for the free-standing hinged-flap structure.

$$\lim_{\omega \to 0} \frac{\Theta(\omega)}{U_b} = 3.954 (1+j) \sqrt{\omega/\omega_L} \frac{\mu L}{K} \tag{7.69}$$

7.2.7 SUMMARY

From Dean's solution of the steady equations of motion for a fixed-flap, and the low frequency expressions for the motion of free-standing hinged-bodies (section 5.3), we have developed a quantitative expression for the low frequency ratio of angular displacement to basal plate velocity.

We can estimate the fluid velocity and pressure that results for the hinged-flap from Dean's solution to the steady equations. The R-components of the fluid velocity and pressure are zero at the $(j\omega)^{1/2}$ order (Equations (5.57)). Thus the first two terms of the series expansions of $\bar{U}_P(\bar{x},\omega)$ and $P_P(\bar{x},\omega)$ (Equations (5.2) and (5.3))

$$\begin{aligned} \bar{U}_P(\bar{x},\omega) &\approx \bar{U}_{P0}(\bar{x}) + (j\omega)^{1/2}\bar{U}_{P1}(\bar{x}) \\ P_P(\bar{x},\omega) &\approx P_{P0}(\bar{x}) + (j\omega)^{1/2}P_{P1}(\bar{x}) \end{aligned} \tag{7.70}$$

dominate $\bar{U}(\bar{x},\omega)$ and $P(\bar{x},\omega)$ at low frequencies (Equations (4.60) and (4.61)). Substitute Equations (5.94), (5.95), (5.97), and (7.64) into Equations (7.70), (4.60), and (4.61).

$$\bar{U}(\bar{x},\omega) \approx U_b\hat{x} + 1/2\,(j\omega/\nu)^{1/2} L \bar{U}_D(\bar{x}/L) \tag{7.71}$$

$$P(\bar{x},\omega) \approx 1/2\,(j\omega/\nu)^{1/2} P_D(\bar{x}/L) \tag{7.72}$$

The fluid velocity (relative to the plate) that is induced by low frequency vibration of the plate of the hinged-flap structure is linearly related to $\bar{U}_D(\bar{x})$ (Figure 7.4). The hydrodynamic pressure on the flap that is induced by low frequency vibration of the plate is linearly related to $P_D(\bar{x})$ (Figure 7.5). We have thus developed expressions for both the fluid motion and the pressure on the flap that result from low frequency vibration of the plate.

7.3 HIGH FREQUENCY ASYMPTOTIC MOTION OF A FREE-STANDING FLAP

In this section we determine high frequency asymptotic expressions for the motion of a free-standing hinged-flap structure (Figure 7.1).

7.3.1 THE EQUATIONS OF MOTION

The B-component of the equations of motion (section 6.3.1) characterizes the fluid motion that is induced by vibration of the basal plate of the rigid body structure when the hinge is fixed so that $\theta=0$. For an inviscid fluid, the B-component of the equations of motion for the free-standing flap can be written in terms of the velocity potential $\Phi_{Bi}(\bar{x},\omega)$ (Equations (6.28)-(6.31)).

$$\nabla^2\Phi_{Bi}(\bar{x},\omega) = 0 \qquad ; y > 0 \tag{7.73}$$

$$\frac{\partial\Phi_{Bi}(\bar{x},\omega)}{\partial x} = U_b \qquad ; x = 0 \text{ and } 0 < y < L \tag{7.74}$$

$$\frac{\partial\Phi_{Bi}(\bar{x},\omega)}{\partial y} = 0 \qquad ; y = 0 \tag{7.75}$$

The R-component of the equations of motion characterizes the fluid motion that is induced by rotation of the rigid flap in the absence of motion of the basal plate. Let $\Phi_{Ri}(\bar{x},\omega)$ represent the velocity potential for the R-component of the equations of motion for the free-standing flap structure in an inviscid fluid (Equations (6.38)-(6.41)).

$$\nabla^2\Phi_{Ri}(\bar{x},\omega) = 0 \qquad ; y > 0 \tag{7.76}$$

$$\frac{\partial\Phi_{Ri}(\bar{x},\omega)}{\partial x} = -j\omega\Theta(\omega)\, y \qquad ; x = 0 \text{ and } 0 < y < L \tag{7.77}$$

$$\frac{\partial\Phi_{Ri}(\bar{x},\omega)}{\partial y} = 0 \qquad ; y = 0 \tag{7.78}$$

7.3.2 ELLIPTIC COORDINATES

The boundary value problems in Equations (7.73)-(7.78) are considerably simpler to solve in cylindrical elliptic coordinates.

$$y - jx = L\cosh(\xi + j\eta) \tag{7.79}$$

$$y = L\cosh\xi\cos\eta \tag{7.80}$$

$$x = -L\sinh\xi\sin\eta \tag{7.81}$$

The boundaries of the fluid domain of the free-standing flap structure are transformed through Equations (7.79)-(7.81) into the rectangular shape shown in Figure 7.7.

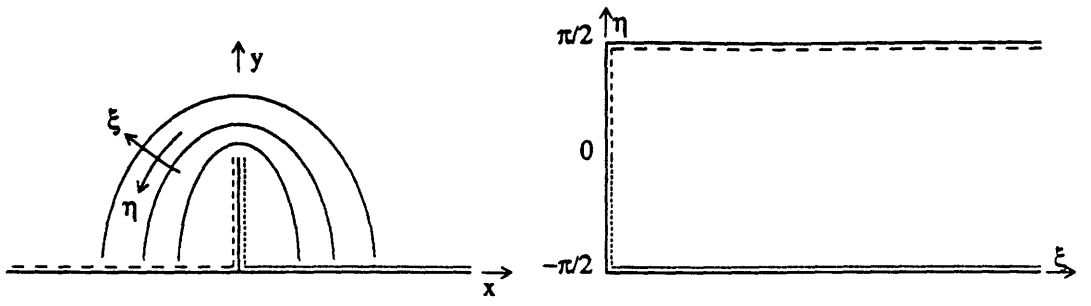

boundary	rectangular coordinates		elliptic coordinates	
left half of plate	$x < 0$	$y = 0$	$\xi > 0$	$\eta = \pi/2$
left side of flap	$x = 0^-$	$0 < y < L$	$\xi = 0$	$0 < \eta < \pi/2$
right side of flap	$x = 0^+$	$0 < y < L$	$\xi = 0$	$-\pi/2 < \eta < 0$
right half of plate	$x > 0$	$y = 0$	$\xi > 0$	$\eta = -\pi/2$

Figure 7.7: Elliptic coordinate transformation. The top left panel illustrates both the rectangular coordinates (x,y) and elliptic coordinates (ξ,η) for the fluid domain of the free-standing flap. The top right panel illustrates the elliptic coordinates of the fluid domain on a rectangular field. The four differently dashed line segments in the top left panel are transformed through Equations (7.79)-(7.81) to the similarly dashed line segments of the right panel. The bottom panel of this figure gives mathematical expressions for each of the dashed lines in the top two panels.

Laplace's Equation is expressed in elliptic coordinates in Equation (7.82).

$$\frac{\partial^2 \Phi}{\partial \xi^2} + \frac{\partial^2 \Phi}{\partial \eta^2} = 0 \tag{7.82}$$

By writing the boundary value problem of Equations (7.73)-(7.78) in terms of elliptic coordinates, the differential equation to be solved (Equation (7.82)) is made no more complicated than it is in rectangular coordinates. The boundaries however are considerably simpler to express in elliptic coordinates than they were in rectangular coordinates.

The boundary conditions in Equations (7.73)-(7.78) can be expressed in elliptic coordinates by applying the chain rule.

$$\frac{\partial \Phi}{\partial \xi} = \frac{\partial \Phi}{\partial x}\frac{\partial x}{\partial \xi} + \frac{\partial \Phi}{\partial y}\frac{\partial y}{\partial \xi} \tag{7.83}$$

$$\frac{\partial \Phi}{\partial \eta} = \frac{\partial \Phi}{\partial x}\frac{\partial x}{\partial \eta} + \frac{\partial \Phi}{\partial y}\frac{\partial y}{\partial \eta} \tag{7.84}$$

Expressions for $\partial\Phi/\partial x$ and $\partial\Phi/\partial y$ are given in the boundary conditions in Equations (7.73)-(7.78). Expressions for $\partial x/\partial \xi$, $\partial x/\partial \eta$, $\partial y/\partial \xi$, and $\partial y/\partial \eta$ can be derived by differentiation of Equations (7.80) and (7.81).

7.3.3 SOLUTION OF THE R-COMPONENT EQUATIONS

The boundary conditions for the R-component of the equations of motion for the free-standing flap in Equations (7.77) and (7.78) can be expressed in elliptic coordinates by using Equations (7.83) and (7.84).

$$\frac{\partial \Phi_{Ri}(\bar{x},\omega)}{\partial \xi} = \frac{1}{2} j\omega\Theta(\omega) L^2 \sin(2\eta) \qquad ; \ \xi = 0 \tag{7.85}$$

$$\frac{\partial \Phi_{Ri}(\bar{x},\omega)}{\partial \eta} = 0 \qquad ; \ \eta = -\pi/2, \pi/2 \tag{7.86}$$

The elliptic formulation of Laplace's equation (7.82) is separable on the boundaries illustrated in Figure 7.7 and the solution can be written as the product of one function that depends only on ξ with another function that depends only on η. Since the boundaries in Figure 7.7 span a rectangular area in the (ξ,η) coordinate space, sinusoidal and exponential basis functions are appropriate. Functions of the form $\sin(k\eta)$ satisfy the boundary condition in Equation (7.86) so long as k is odd. Since the velocity potential must approach zero as ξ approaches infinity, the corresponding function of ξ must have the form $e^{-k\xi}$. Since Laplace's equation is linear, we can form a solution to $\Phi_{Ri}(\bar{x},\omega)$ by a linear combination as in Equation (7.87).

$$\Phi_{Ri}(\bar{x},\omega) = \sum_{\substack{k=0 \\ k \text{ odd}}}^{\infty} A_k \sin(k\eta)\, e^{-k\xi} \tag{7.87}$$

The coefficients A_k can be determined by substituting the series in Equation (7.87) into the remaining boundary condition (Equation (7.85)). The resulting expression for $\Phi_{Ri}(\bar{x},\omega)$ is given in Equation (7.88)

$$\Phi_{Ri}(\bar{x},\omega) = \sum_{\substack{k=0 \\ k \text{ odd}}}^{\infty} \frac{4j\omega\Theta(\omega)L^2}{\pi k(k^2-4)} (-1)^{(k-1)/2} \sin(k\eta)\, e^{-k\xi} \tag{7.88}$$

and the corresponding fluid motion is shown in Figure 7.8.

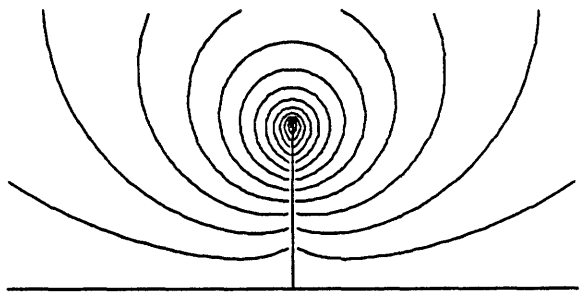

Figure 7.8: Fluid motion generated by rotation of the flap in an inviscid fluid. The streamlines are parallel to the direction of fluid motion and the density of streamlines is proportional to the magnitude of the fluid velocity. The streamlines were determined by numerically summing the first 100 terms of Equation (7.88).

The R-component of torque on the flap can be written in terms of the moment of inertia I_R (Equation (6.42)).

$$I_R = -\rho \hat{z} \cdot \int_R \frac{\Phi_{Ri}(\bar{x},\omega)}{j\omega\Theta(\omega)} (\bar{r} \times d\bar{R}) \tag{7.89}$$

The surface R extends over both sides ($x=0^-$ and $x=0^+$) of the flap, from $0<y<L$, and from $-\infty<z<\infty$.

$$I_R = -\rho \int_{-\infty}^{\infty} \left[\int_0^L \frac{\Phi_{Ri}(\bar{x},\omega)}{j\omega\Theta(\omega)}\bigg|_{x=0^-} y\,dy - \int_0^L \frac{\Phi_{Ri}(\bar{x},\omega)}{j\omega\Theta(\omega)}\bigg|_{x=0^+} y\,dy \right] dz \tag{7.90}$$

Since the flap geometry (Figure 7.1) is uniform in the z-direction, it is convenient to define I_{Rz} equal to the moment of inertia per unit extent along the z axis.

$$I_{Rz} = -\rho \int_0^L \frac{\Phi_{Ri}(\bar{x},\omega)}{j\omega\Theta(\omega)}\bigg|_{x=0^-} y\,dy + \rho \int_0^L \frac{\Phi_{Ri}(\bar{x},\omega)}{j\omega\Theta(\omega)}\bigg|_{x=0^+} y\,dy \tag{7.91}$$

Substitute $\Phi_{Ri}(\bar{x},\omega)$ from Equation (7.88) into (7.91) and convert to elliptic coordinates.

$$I_{Rz} = \sum_{\substack{k=0 \\ k\ odd}}^{\infty} (-1)^{(k-1)/2} \frac{4\rho L^4}{\pi k(k^2-4)} \times \left[\int_0^{\pi/2} \sin(\eta)\cos(\eta)\sin(k\eta)\,d\eta - \int_{-\pi/2}^{0} \sin(\eta)\cos(\eta)\sin(k\eta)\,d\eta \right]$$

$$= \sum_{\substack{k=0 \\ k\ odd}}^{\infty} \frac{8\rho L^4}{\pi k(k^2-4)^2} \approx \frac{\rho L^4}{\pi} \tag{7.92}$$

Even though the flap is infinitesimally thin and massless, angular rotations of the flap are resisted (because of the surrounding inviscid fluid) as though it had mass. I_{Rz} is roughly equivalent to the moment of inertia per unit length of a circular cylinder with density ρ and radius 2L/3 that is rotated through its long axis.

Substitute Equations (7.92) and (7.28) into Equation (6.43) to obtain an asymptotic expression for $Z_{Rz}(\omega)$.

$$\lim_{\omega\to\infty} \frac{Z_{Rz}(\omega)}{\mu L^2} \approx j\,(\omega/\omega_L)\,\frac{2}{\pi} \tag{7.93}$$

7.3.4 SOLUTION OF THE B-COMPONENT EQUATIONS

The boundary conditions for the B-component of the equations of motion for the free-standing flap in Equations (7.74) and (7.75) can be expressed in elliptic coordinates by using Equations (7.83) and (7.84).

$$\frac{\partial \Phi_{Bi}(\bar{x},\omega)}{\partial \xi} = -U_b L \sin\eta \qquad ; \ \xi = 0 \tag{7.94}$$

$$\frac{\partial \Phi_{Bi}(\bar{x},\omega)}{\partial \eta} = 0 \qquad ; \ \eta = -\pi/2, \pi/2 \tag{7.95}$$

The solution to Equations (7.73), (7.94), and (7.95) can be found using the method used for solving the equations for the R-component in the previous section.

$$\Phi_{Bi}(\bar{x},\omega) = U_b L \sin\eta \, e^{-\xi} \tag{7.96}$$

The fluid motion corresponding to Equation (7.96) is shown in Figure 7.9.

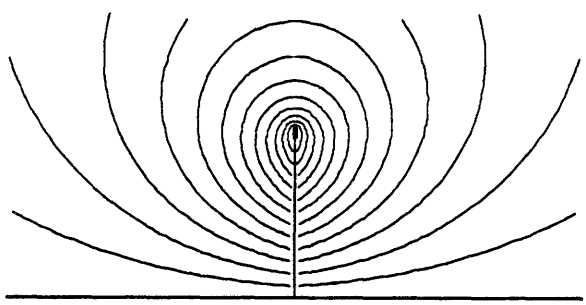

Figure 7.9: Fluid motion generated by vibrating the basal plate of the hinged-flap structure with fixed hinge in an inviscid fluid. The streamlines are parallel to the direction of fluid motion and the density of stremalines is proportional to the magnitude of the fluid velocity. The streamlines were determined from Equation (7.96).

The B-component of torque on the flap can be written in terms of the constant M_B (Equation (6.32)).

$$M_B = \rho \hat{z} \cdot \int_R \frac{\Phi_{Bi}(\bar{x},\omega)}{U_b} (\bar{r} \times d\bar{R}) \tag{7.97}$$

The surface R extends over both sides ($x=0^-$ and $x=0^+$) of the flap, from $0<y<L$, and from $-\infty<z<\infty$.

$$M_B = \rho \int_{-\infty}^{\infty} \left[\int_0^L \frac{\Phi_{Bi}(\bar{x},\omega)}{U_b}\bigg|_{x=0^-} y \, dy - \int_0^L \frac{\Phi_{Bi}(\bar{x},\omega)}{U_b}\bigg|_{x=0^+} y \, dy \right] dz \tag{7.98}$$

Since the flap geometry (Figure 7.1) is uniform in the z-direction, it is convenient to define M_{Bz} equal to the value of M_B per unit extent along the z axis.

$$M_{Bz} = \rho \int_0^L \frac{\Phi_{Bi}(\bar{x},\omega)}{U_b}\bigg|_{x=0^-} y \, dy - \rho \int_0^L \frac{\Phi_{Bi}(\bar{x},\omega)}{U_b}\bigg|_{x=0^+} y \, dy \tag{7.99}$$

Substitute $\Phi_{Bi}(\bar{x},\omega)$ from Equation (7.96) into (7.99) and convert to elliptic coordinates.

$$M_{Bz} = \rho L^3 \left[\int_0^{\pi/2} \sin(\eta)\cos(\eta)\sin(\eta)\,d\eta - \int_{-\pi/2}^{0} \sin(\eta)\cos(\eta)\sin(\eta)\,d\eta \right]$$
$$= \frac{2}{3}\rho L^3 \tag{7.100}$$

Substitute Equations (7.100) and (7.28) into Equation (6.33) to obtain an asymptotic expression for $H_{Pz}(\omega)$.

$$\lim_{\omega\to\infty} \frac{H_{Pz}(\omega)}{\mu L} = j(\omega/\omega_L)\,\frac{4}{3} \tag{7.101}$$

7.3.5 RATIO OF ANGULAR DISPLACEMENT TO PLATE VELOCITY

Translation of the plate in its plane generates a torque on the flap that tends to rotate the flap about its hinged attachment to the plate. Rotation of the flap is however resisted by a moment of inertia of fluid origin. Thus, forces of fluid origin couple motion of the plate to rotation of the flap. Substituting Equations (7.101) and (7.93) into Equation (7.26) results in an expression for the high frequency asymptotic ratio of angular displacement of the flap to basal plate velocity.

$$\lim_{\omega\to\infty} \frac{\Theta(\omega)}{U_b} \approx \frac{2\pi}{j\omega 3L} \tag{7.102}$$

Consider the velocity of the tip of the flap (Equation (7.103)).

$$\bar{U}_{tip} = U_b\hat{x} - j\omega\Theta(\omega)L\,\hat{x} \tag{7.103}$$

At high frequencies, $\Theta(\omega)$ and U_b are related (Equation (7.102)).

$$\bar{U}_{tip} \approx U_b(1-2\pi/3)\,\hat{x} \approx -U_b\hat{x} \tag{7.104}$$

Thus, at high frequencies, the velocity of the tip of the flap and the velocity at the hinge are nearly equal in magnitude but opposite in direction. Thus the velocity at the center of the flap (y=L/2) is nearly zero. At high frequencies, the angular velocity of the flap, the angular velocity of the plate, and the velocity of the fluid at every point in the fluid domain are all in phase.

7.3.6 FLUID VELOCITY GENERATED BY TRANSLATION OF THE PLATE

Just as the fluid velocity for the hinged-flap is the sum of the B- and R-components of the fluid velocity (Equation (4.60)), the velocity potential for the hinged-flap is the sum of the B- and R-components of the velocity potential.

$$\Phi_i(\bar{x},\omega) = \Phi_{Bi}(\bar{x},\omega) + \Phi_{Ri}(\bar{x},\omega) \tag{7.105}$$

Substitute Equations (7.88) and (7.96) into Equation (7.105).

$$\Phi_i(\bar{x},\omega) = U_b L \sin\eta e^{-\xi} + \sum_{\substack{k=0 \\ k\ \text{odd}}}^{\infty} \frac{4j\omega\Theta(\omega)L^2}{\pi k(k^2-4)} (-1)^{(k-1)/2} \sin(k\eta)\, e^{-k\xi} \tag{7.106}$$

Substitute the asymptotic ratio of $\Theta(\omega)/U_b$ from Equation (7.102) into Equation (7.106).

$$\Phi_i(\bar{x},\omega) = U_b L \left[\sin\eta\, e^{-\xi} + \sum_{\substack{k=0 \\ k\ \text{odd}}}^{\infty} \frac{8}{3k(k^2-4)} (-1)^{(k-1)/2} \sin(k\eta)\, e^{-k\xi} \right] \tag{7.107}$$

At sufficiently high frequencies, the velocities induced in the fluid that surrounds the hinged flap are in phase with the velocity of the basal plate. Figure 7.10 illustrates the fluid motion that is induced by high frequency translation of the basal plate.

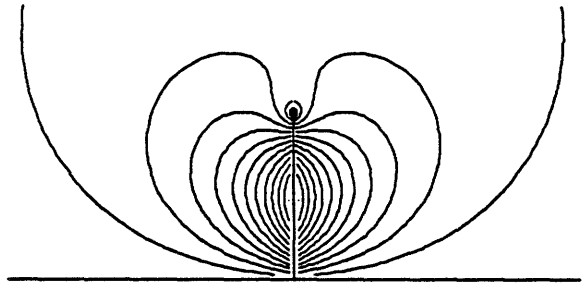

Figure 7.10: Fluid motion generated by translation of the basal plate of the free-standing flap structure in an inviscid fluid. The streamlines were determined from Equation (7.107). Notice that the flap moves in a rocking fashion about a point near its center (as in Equation (7.104)).

7.4 CONCLUSIONS

In this chapter, we have shown that the equations of motion for the essentially two dimensional free-standing flap structure (Figure 7.1) have a number of properties that make analysis of that structure simpler than analysis of the more general hinged body structure that was studied in chapters 4, 5, and 6.

First, using the fact that the shape of the body is completely characterized by a single parameter L, its length, we showed that the solutions to the component equations of motion depend on the value of a single (non-dimensional) parameter ω/ω_L. This considerably simplifies numeric work, since we can completely characterize the motion of the hinged-flap structure by computing solutions for all values of a single parameter, ω/ω_L, rather than for all values of the four physically significant parameters (μ, ρ, ω, and L).

Second, because the hinged-flap structure is essentially two dimensional, the motion of the fluid can be described by a stream function. This simplies both numerical and analytic work, since the equations of motion for the fluid, which we earlier expressed in terms of both a vector fluid velocity field and a scalar pressure field, can be described in terms of a stream function by a single scalar field.

Third, we showed that the symmetry of the hinged-flap structure gives rise to symmetry in the solution to the equations of motion. This simplies numerical work by reducing the number of unknowns in the discrete representation of the hydrodynamic fields by a factor of 2.

Because the equations of motion for the fluid are linear, the effect of fluid on the motion of the hinged-flap structure can be described by a lumped parameter model (Figure 7.2). In this chapter we specialized the results of the asymptotic analyses of chapters 5 and 6 to derive quantitative expressions for the hydrodynamic impedances in that model (Table 7.1).

Asymptotic expressions for the hinged-flap		
parameter	low frequency	high frequency
$H_{P_Z}(\omega)$	$3.954(1+j)\sqrt{\omega/\omega_L}\,\mu L$	$j\,(\omega/\omega_L)\frac{4}{3}\mu L$
$Z_{R_Z}(\omega)$	R_Θ (not evaluated)	$j\,(\omega/\omega_L)\frac{2}{\pi}\mu L^2$
$\Theta(\omega)/U_b$	$3.954\,(1+j)\sqrt{\omega/\omega_L}\,\mu\frac{L}{K}$	$\frac{2\pi}{j\omega 3L}$

Table 7.1: Quantitative values for the hydrodynamic impedances of Figure 7.2 for the hinged-flap structure.

CHAPTER 8
NUMERICAL ANALYSIS OF THE MOTION OF A FREE-STANDING, HINGED FLAP

In this chapter, we use a numerical method to analyze the motion of a rigid rectangular flap that is attached by a spring-loaded hinge to a vibrating plate and is immersed in a viscous fluid (Figure 7.1). This analysis, which characterizes all frequencies of excitation, serves two purposes within the context of this thesis. First, since the hinged-flap is representative of the class of models for which both low and high frequency asymptotic analyses were performed (chapters 4, 5, 6, and 7), the numerical analysis of the hinged-flap and the asymptotic analyses are mutually corroborative. Also however, the results at mid-frequencies characterizes the frequency selectivity of the hinged-flap. The analysis of this chapter therefore addresses whether the motion of a small body that projects from a large surface can exhibit a sharply tuned mechanical resonance.

In section 8.1, we formulate difference equations with which to approximate the equations of motion for the hinged-flap structure. In section 8.2, we outline the algorithm by which we solve those equations on a general purpose computer. In section 8.3, we present numerical solutions to the equations of motion, and compare those solutions to the asymptotic solutions of chapter 7.

8.1 DIFFERENCE APPROXIMATION OF THE EQUATIONS OF MOTION

We seek a numerical solution to the equations of motion for the hinged-flap structure. Because the equations of motion for the fluid are linear, the fluid motion can be expressed as a sum of two components (section 7.1.2). The P-component describes the fluid motion and hydrodynamic pressures generated by translation of the plate when the angular displacement of the flap is fixed with $\Theta=0$. The R-component describes the fluid motion and pressures generated by angular displacement of the flap when the plate is fixed. The ratio of the P-component of torque on the flap to plate velocity defines a transfer impedance $H_{Pz}(\omega)$ and the ratio of the R-component of torque on the flap to angular flap velocity defines a rotational impedance $Z_{Rz}(\omega)$. Neither the components nor the hydrodynamical impedances depend on the mechanical properties of the hinge. The mechanical impedance of the hinge and the hydrodynamic impedances $H_{Pz}(\omega)$ and $Z_{Rz}(\omega)$ determine the angular displacement of the flap through a balance of torques relationship that is illustrated in the equivalent circuit of Figure 7.2.

In this section, we develop difference equations with which to approximate the solution to Equations (8.1)-(8.5).

$$j\omega\rho\bar{U}(\bar{x},\omega) = -\nabla P(\bar{x},\omega) + \mu\nabla^2\bar{U}(\bar{x},\omega) \quad ; \{-X<x<X \ \& \ y>0\} \tag{8.1}$$

$$\nabla\cdot\bar{U}(\bar{x},\omega) = 0 \quad ; \{-X<x<X \ \& \ y>0\} \tag{8.2}$$

$$\bar{U}(\bar{x},\omega) = [U_b - j\omega\Theta(\omega)y]\,\hat{x} \quad ; \{y=0\} \text{ or } \{x=0 \ \& \ 0<y<L\} \tag{8.3}$$

$$\bar{U}(\bar{x},\omega) = U_b e^{-y\sqrt{j\omega/\nu}}\,\hat{x} \quad ; \{-X<x<X \ \& \ y=Y\} \text{ or } \{x=\pm X \ \& \ 0<y<L\} \tag{8.4}$$

$$T_z(\omega) = \int_0^L y\,\Delta P(y,\omega)\,dy \tag{8.5}$$

$H_{Pz}(\omega)$ can be computed from Equations (8.1)-(8.5) by calculating the ratio of $T_z(\omega)$ to U_b when $\Theta(\omega)=0$ (Equations (7.9)-(7.13)). $Z_{Rz}(\omega)$ can be computed from Equations (8.1)-(8.5) by calculating the ratio of $T_z(\omega)$ to $j\omega\Theta(\omega)$ when $U_b=0$ (Equations (7.14)-(7.18)).

8.1.1 DISCRETIZATION OF HYDRODYNAMICAL VARIABLES

In order to "solve" Equations (8.1)-(8.5) numerically, the spatially-continuous functions $\bar{U}(x,y)$ and $P(x,y)$ must be discretized and Equations (8.1)-(8.5) must be approximated by difference equations. There exists considerable latitude in how the discretization is accomplished -- and an acompanying wide range of performances (Peyret & Taylor, 1983). The method used in this study is based on the staggered marker-and-cell (MAC) mesh (Harlow and Welsh, 1965). The fluid domain is broken into a finite grid of rectangular cells. Each cell extends d units in x and d units in y. d is constrained to be a submultiple of L -- so that an integral number of elements (F) face the flap (L=Fd). The artificial boundaries that delimit the computational domain $\{-X<x<X \;\&\; 0<y<Y\}$ are taken so as to enclose an integral number of elements (=2×R×S, where X=Rd and Y=Sd). Each cell is characterized by one pressure (at its center) and four fluid velocities (one velocity associated with each wall of the cell and directed perpendicular to that wall) as illustrated in Figure 8.1.

8.1.1.1 DIFFERENCE APPROXIMATION OF THE FLUID EQUATIONS

The spatial organization of discrete hydrodynamic variables defined by the MAC mesh permits a centered-difference approximation of each of the spatial derivatives in Equations (8.1) and (8.2). Using a first-order centered-difference approximation to the gradient operator, and a second-order centered-difference approximation to the Laplacian operator, the x-component of Equation (8.1) can be approximated by

$$j\omega\rho U_{r,s} = -\frac{1}{d}\left(P_{r,s}-P_{r-1,s}\right)+\frac{\mu}{d^2}\left(U_{r+1,s}+U_{r,s+1}-4U_{r,s}+U_{r-1,s}+U_{r,s-1}\right) \quad ; \; 2\le r\le R \;\&\; 2\le s\le S \tag{8.6}$$

at the point (x=(r−1)d , y=(s−0.5)d). Equation (8.6) will be referred to as the x-momentum equation at the point ((r−1)d,(s−0.5)d). The y-component of Equation (8.1) can be similarly approximated

$$j\omega\rho V_{r,s} = -\frac{1}{d}\left(P_{r,s}-P_{r,s-1}\right)+\frac{\mu}{d^2}\left(V_{r+1,s}+V_{r,s+1}-4V_{r,s}+V_{r-1,s}+V_{r,s-1}\right) \quad ; \; 2\le r\le R \;\&\; 2\le s\le S \tag{8.7}$$

at the point ((r−0.5)d,(s−1)d). Equation (8.7) will be referred to as the y-momentum equation. Using first order centered differences for the divergence operator, Equation (8.2) can be approximated

$$U_{r+1,s} - U_{r,s} + V_{r,s+1} - V_{r,s} = 0 \quad ; \; 1\le r\le R \;\&\; 1\le s\le S \tag{8.8}$$

at the point ((r−0.5)d,(s−0.5)d). Equation (8.8) will be refered to as the discrete continuity equation.

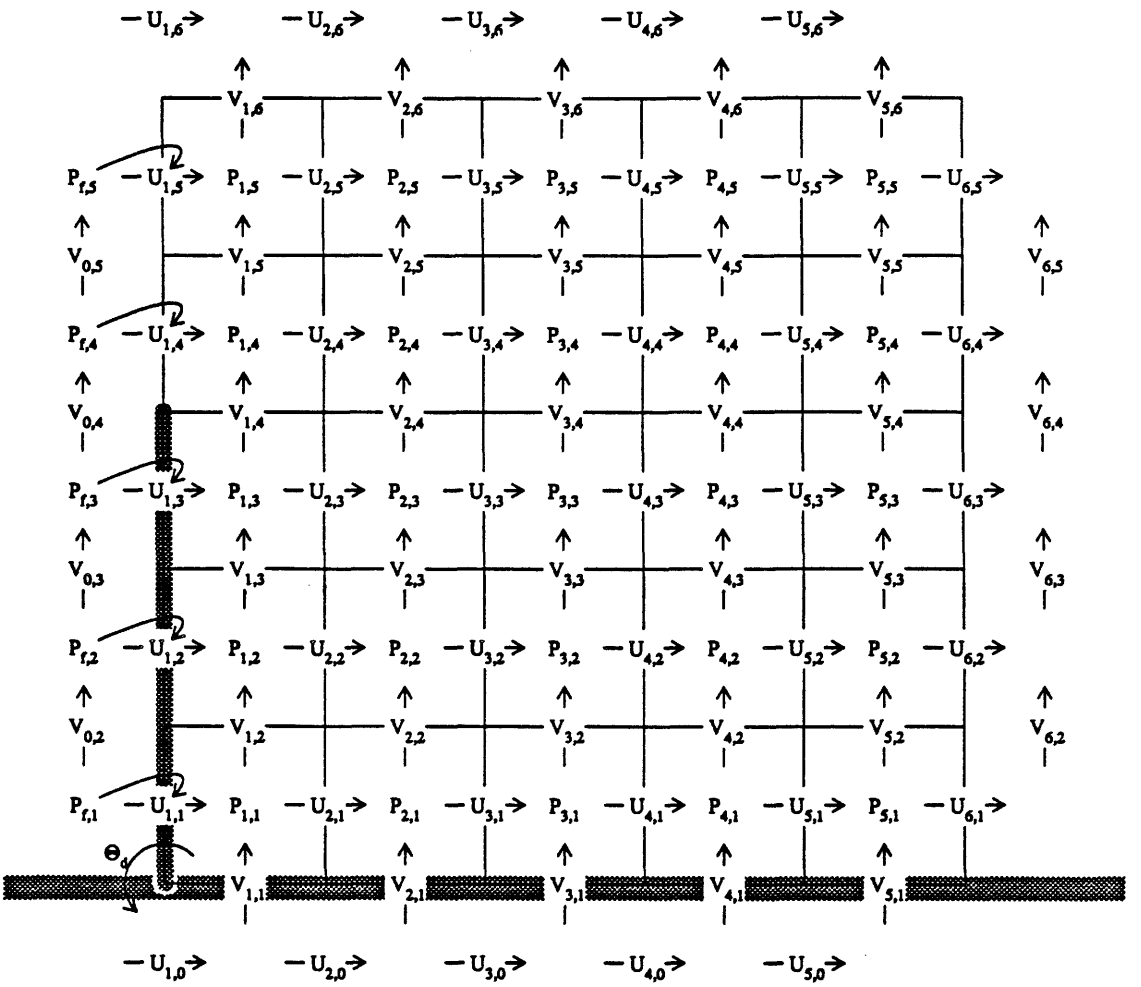

Figure 8.1: Discrete approximation of the hydrodynamic variables in Equations (8.1) and (8.2). The spatial region pictured here is a portion of that shown in Figure 7.1 (the portion for which x>0). The thin lines mark the edges of cells used to define discrete hydrodynamic variables. Cell (r,s) is delimited by the lines x=(r−1)d, x=rd, y=(s−1)d, and y=sd. The shaded regions illustrate the position of the rigid surfaces in Figure 7.1. All of the variables indicated in this figure represent complex-valued sinusoidal steady-state amplitudes. $P_{r,s}$ is the discrete pressure variable associated with cell (r,s). $U_{r,s}$ is the discrete velocity variable that characterizes flow out of cell (r−1,s) and into cell (r,s). $U_{r,s}$ is oriented in the x-direction and is thus a scalar. $V_{r,s}$ is the discrete velocity variable that characterizes flow out of cell (r,s−1) and into cell (r,s). $V_{r,s}$ is oriented in the y-direction. The flap has a length of Fd which is illustrated here for F=3. The computational domain contains R cells in the range 0<x<X and S cells in the range 0<y<Y -- illustrated here for R=S=5. Velocities that lie outside of the computational domain ($V_{0,s}$ and $V_{6,s}$ for $2 \le s \le 5$; $U_{r,0}$ and $U_{r,6}$ for $0 \le r \le 5$) are the "fictitious" velocities described in the text. $P_{f,s}$ for $1 \le s \le F$ are discrete approximations to the pressures on the surface of the flap that faces cells (1,s). $P_{f,s}$ for $F+1 \le s \le S$ are fictitious pressure variables numerically equal to zero. Θ_d is the discrete approximation to angular displacement of the flap.

8.1.1.2 MOMENTUM EQUATIONS NEAR RIGID BOUNDARIES -- TANGENTIAL COMPONENT

Equation (8.6) approximates the x-component of the momentum equation (8.1) for y=1.5d, 2.5d, 3.5d,..., but cannot be applied for locations closer to the plate, e.g. at y=0.5d, since the variable $U_{r,0}$ falls outside of the computational domain (i.e. below the plate). $U_{r,0}$ is part of the centered-difference approximation of the second partial derivative of U with respect to y at y=d/2. Notice also that the discrete variables in Figure 8.1 do not specify an x-component of velocity at y=0 even though that velocity is part of the continuous boundary conditions (Equations (8.3)). Although a second-order centered-difference approximation to that second derivative in Equation (8.1) is not possible at the points along y=d/2, one can derive a non-centered difference approximation from Equation (8.3). Consider that a second-order centered-difference can be generated from the successive application of two first-order centered-differences.

$$\left.\frac{\partial^2 U}{\partial y^2}\right|_{y=d/2} \approx \frac{1}{d}\left(\left.\frac{\partial U}{\partial y}\right|_{y=d} - \left.\frac{\partial U}{\partial y}\right|_{y=0}\right) \approx \frac{1}{d^2}\left(U|_{y=3d/2} - U|_{y=d/2} - U|_{y=d/2} + U|_{y=-d/2}\right)$$

$$\approx \frac{1}{d^2}\left(U_{r,2} - U_{r,1} - U_{r,1} + U_{r,0}\right) \qquad (8.9)$$

In Equation (8.9), $U_{r,0}$ is part of the first-order centered-difference approximation of the first derivative of U with respect to y on the boundary (y=0). The x-component of velocity on the boundary (U_b) can be used to generate an (uncentered) approximation to the first derivative of U on the boundary.

$$\left.\frac{\partial U}{\partial y}\right|_{y=0} \approx \frac{1}{d/2}\left(U|_{y=d/2} - U|_{y=0}\right) \approx \frac{2}{d}\left(U_{r,1} - U_b\right) \qquad (8.10)$$

Substituting Equation (8.10) into (8.9) results in an approximation for the second derivative of U at y=d/2 that does not require $U_{r,0}$

$$\left.\frac{\partial^2 U}{\partial y^2}\right|_{y=d/2} \approx \frac{1}{d^2}\left(U_{r,2} - U_{r,1} - 2U_{r,1} + 2U_b\right). \qquad (8.11)$$

By equating the right hand sides of Equations (8.9) and (8.11), $U_{r,0}$ can be DEFINED to be

$$U_{r,0} = 2U_b - U_{r,1} \qquad ; \ 1 \le r \le R \qquad (8.12)$$

so that the range of s over which Equation (8.6) can be applied can be extended to include s=1. Discrete variables that are not discrete approximations of continuous variables (like $U_{r,0}$) will be referred to as "fictitious".

Similar reasoning is applicable along the rigid boundary of the flap. Equation (8.9) cannot be applied in the case r=1 since $V_{0,s}$ is not part of the fluid domain that contains $V_{1,s}$ and $V_{2,s}$ ($V_{0,s}$ is separated from $V_{1,s}$ by the flap). Furthermore, the y-component of flap velocity is not included in the MAC mesh variables but is part of the continuous boundary specification (Equation (8.3)). Fictitious variables analogous to those defined by

Equation (8.12)

$$V_{0,s} = 0 - V_{1,s} \qquad ; 1 \le s \le F \qquad (8.13)$$

can be defined to extend the range of r for which Equation (8.9) can be applied to include r=1.

8.1.1.3 SYMMETRY

The symmetry conditions of Equation (7.60)-(7.63) can be used to extend the range of r's over which Equations (8.6)-(8.8) can be applied.

$$U_{0,s} = U_{2,s} \qquad ; 1 \le s \le S \qquad (8.14)$$
$$V_{0,s} = -V_{1,s} \qquad ; 2 \le s \le S \qquad (8.15)$$
$$P_{0,s} = -P_{1,s} \qquad ; 1 \le s \le S \qquad (8.16)$$

Notice that Equation (8.15) includes Equation (8.13) as a subset. The non-centered difference treatment of the no-slip boundary condition on the flap is equivalent to the symmetry constraint since both require that the y-component of flap velocity is equal zero.

Equations (8.14) and (8.16) can be used to derive an expression analogous to Equation (8.6) that is valid for cells (1,s) with s>F.

$$j\omega\rho U_{1,s} = -\frac{2}{d}P_{1,s} + \frac{\mu}{d^2}(2U_{2,s}+U_{1,s+1}-4U_{1,s}+U_{1,s-1}) \qquad ; F+1 \le s \le S \qquad (8.17)$$

8.1.1.4 MOMENTUM EQUATIONS NEAR RIGID BOUNDARIES -- NORMAL COMPONENT

The MAC mesh includes discrete velocities that are normal to cell edges. The y-component of velocity near the plate must be zero

$$V_{r,1} = 0 \qquad ; 1 \le r \le R \qquad (8.18)$$

and the x-component of velocity near the flap must equal that of the flap (in Equation (8.3)).

$$U_{1,s} = U_b - j\omega\Theta_d(s-0.5)d \qquad ; 1 \le s \le F \qquad (8.19)$$

$\Theta(\omega)$ is the angular displacement of the flap in the differential equations of motion (Equations (8.1)-(8.5)). Θ_d denotes the angular displacement in the difference equations.

Equations (8.6) approximate the x-component of Equation (8.1) for (x=d, 2d, 3d, ...). Substituting the symmetry Equations (7.60)-(7.63) into Equations (8.6) generates an approximation to the x-component of Equation (8.1) at (x=-d, -2d, -3d, ...). We seek now an approximation for the x-component of Equation (8.1) at $x=0^+$. Let $P_{f,s}$ represent the discrete approximation of the hydrodynamic pressure exerted on the flap at y=(s-0.5)d. Notice that since $P_{f,s}$ approximates a pressure on the edge of cell (1,s) it is not a MAC mesh variable. $P_{f,s}$ is however of considerable consequence to this study since $\{P_{f,s}\}$

couples the equations of motion of the fluid with the equations of motion of the flap. $P_{f,s}$ and $P_{0,s}$ can be used to generate a non-centered approximation to the pressure gradient normal to the flap.

$$\left.\frac{\partial P}{\partial x}\right|_{x=0} \approx \frac{1}{d/2}\,(P_{1,s} - P_{f,s}) \qquad ;\ 1 \le s \le F \tag{8.20}$$

A second-order centered-difference approximation to the second derivative of U with respect to y can be generated at x=0 using the previously defined discrete variables.

$$\left.\frac{\partial^2 U}{\partial y^2}\right|_{\substack{x=0 \\ y=(s-0.5)d}} \approx \frac{1}{d^2}\,(U_{1,s+1} - 2U_{1,s} + U_{1,s-1});\ 1 \le s \le F \tag{8.21}$$

A non-centered approximation of the second derivative of U with respect to x is necessary.

$$\left.\frac{\partial^2 U}{\partial x^2}\right|_{\substack{x=0^+ \\ y=(s-0.5)d}} \approx \frac{2}{d}\left(\left.\frac{\partial U}{\partial x}\right|_{\substack{x=d/2 \\ y=(s-0.5)d}} - \left.\frac{\partial U}{\partial x}\right|_{\substack{x=0^+ \\ y=(s-0.5)d}}\right) \qquad ;\ 1 \le s \le F \tag{8.22}$$

By Equation (8.2),

$$\frac{\partial U}{\partial x} = -\frac{\partial V}{\partial y} \tag{8.23}$$

and from the no-slip condition in Equation (8.3), the partial of V with respect to y must be zero along the flap.

$$\left.\frac{\partial^2 U}{\partial x^2}\right|_{\substack{x=0^+ \\ y=(s-0.5)d}} \approx \frac{2}{d}\left(\left.\frac{\partial U}{\partial x}\right|_{\substack{x=d/2 \\ y=(s-0.5)d}}\right) \approx \frac{2}{d^2}\left(U|_{\substack{x=d \\ y=(s-0.5)d}} - U|_{\substack{x=0 \\ y=(s-0.5)d}}\right)$$

$$\approx \frac{2}{d^2}\,(U_{2,s} - U_{1,s}) \qquad ;\ 1 \le s \le F \tag{8.24}$$

Equations (8.20), (8.21), and (8.24) can be used to approximate the spatial derivatives in the x-component of Equation (8.1) at $x=0^+$.

$$j\omega\rho U_{1,s} = -\frac{2}{d}\,(P_{1,s} - P_{f,s}) + \frac{\mu}{d^2}\,(2U_{2,s} + U_{1,s+1} - 4U_{1,s} + U_{1,s-1}) \qquad ;\ 1 \le s \le F \tag{8.25}$$

Since Equation (8.25) is identical to Equation (8.17) except for the $P_{f,s}$ term, fictitious pressures

$$P_{f,s} = 0 \qquad ;\ F+1 \le s \le S \tag{8.26}$$

can be used to combine Equations (8.25) and (8.17) into a single expression.

$$j\omega\rho U_{1,s} = -\frac{2}{d}\,(P_{1,s} - P_{f,s}) + \frac{\mu}{d^2}\,(2U_{2,s} + U_{1,s+1} - 4U_{1,s} + U_{1,s-1}) \qquad ;\ 1 \le s \le S \tag{8.27}$$

8.1.1.5 HYDRODYNAMIC TORQUE ON THE FLAP

Equation (8.5) can be discretized by approximating the pressure along the flap in terms of $P_{f,s}$. Using a piecewise constant interpolation,

$$P(0^+, y) = P_{f,s} \quad ; (s-1)d < y < sd \tag{8.28}$$

and exploiting the symmetry condition on pressure (7.62), the torque on the flap can be approximated by

$$T_{zd} = 2d^2 \sum_{s=1}^{F} (s-0.5)\, P_{f,s} \ . \tag{8.29}$$

8.1.1.6 ARTIFICIAL BOUNDARIES

The artificial boundaries conditions in Equation (8.4) are imposed by setting boundary velocities equal to $\bar{U}_\delta(\bar{x},\omega)$.

$$U_{R+1,s} = U_b e^{-(s-0.5)d\sqrt{j\omega/\nu}} \quad ; 1 \le s \le S \tag{8.30}$$

$$V_{R+1,s} = 0 \quad ; 2 \le s \le S \tag{8.31}$$

$$U_{r,S+1} = U_b e^{-(S+0.5)d\sqrt{j\omega/\nu}} \quad ; 1 \le r \le R \tag{8.32}$$

$$V_{r,S+1} = 0 \quad ; 1 \le r \le R \tag{8.33}$$

8.1.1.7 DIFFERENCE EQUATIONS OF MOTION FOR THE HINGED-FLAP

boundary variables		
$V_{r,1} = 0$	$; 1 \le r \le R$	(8.18)
$V_{r,S+1} = 0$	$; 1 \le r \le R$	(8.33)
$U_{R+1,s} = U_b e^{-(s-0.5)d\sqrt{j\omega/\nu}}$	$; 1 \le s \le S$	(8.30)
$U_{r,S+1} = U_b e^{-(S+0.5)d\sqrt{j\omega/\nu}}$	$; 1 \le r \le R$	(8.32)
$V_{R+1,s} = 0$	$; 2 \le s \le S$	(8.31)
fictitious variables		
$U_{r,0} = 2U_b - U_{r,1}$	$; 1 \le r \le R$	(8.12)
$V_{0,s} = -V_{1,s}$	$; 2 \le s \le S$	(8.15)
$P_{f,s} = 0$	$; F+1 \le s \le S$	(8.26)
computational molecule		
$j\omega\rho U_{r,s} = -\frac{1}{d}(P_{r,s}-P_{r-1,s}) + \frac{\mu}{d^2}(U_{r+1,s}+U_{r,s+1}-4U_{r,s}+U_{r-1,s}+U_{r,s-1})$	$; 2 \le r \le R \;\&\; 1 \le s \le S$	(8.6, 8.12)
$j\omega\rho V_{r,s} = -\frac{1}{d}(P_{r,s}-P_{r,s-1}) + \frac{\mu}{d^2}(V_{r+1,s}+V_{r,s+1}-4V_{r,s}+V_{r-1,s}+V_{r,s-1})$	$; 1 \le r \le R \;\&\; 2 \le s \le S$	(8.7, 8.13)
$U_{r+1,s} - U_{r,s} + V_{r,s+1} - V_{r,s} = 0$	$; 1 \le r \le R \;\&\; 1 \le s \le S$	(8.8)
additional equations		
$U_{1,s} = U_b - j\omega\Theta_d(s-0.5)d$	$; 1 \le s \le F$	(8.19)
$j\omega\rho U_{1,s} = -\frac{2}{d}(P_{1,s}-P_{f,s}) + \frac{\mu}{d^2}(2U_{2,s}+U_{1,s+1}-4U_{1,s}+U_{1,s-1})$	$; 1 \le s \le S$	(8.27)
$T_{zd} = 2d^2 \sum_{s=1}^{F}(s-0.5)\,P_{f,s}$		(8.29)

Table 8.1: Difference equations describing motion of the flap structure of Figure 7.1. All of the variables listed here (including fictitious variables) appear in Figure 8.1. There are a total of (RS+R+S) $U_{r,s}$'s, (RS+R+2S–2) $V_{r,s}$'s, (RS) $P_{r,s}$'s, (S) $P_{f,s}$'s, and (1) T_{zd} -- and thus (3RS+3R+4S–1) unknowns. Listed above are an equal number of equations.

8.1.2 DISCRETE STREAM FUNCTION FORMULATION

The equations in Table 8.1 specify roughly 3RS equations between the discrete hydrodynamic variables pictured in Figure 8.1. Though these difference equations can be solved directly, both the number of equations and number of unknowns can be reduced by rewriting the equations in terms of a discrete stream function. Let $\Psi_{r,s}$ denote the complex amplitude of a discrete stream function at (x=(r−1)d,y=(s−1)d).

$$U_{r,s} = \frac{1}{d}(\Psi_{r,s+1} - \Psi_{r,s}) \qquad ; \ 1 \le r \le R+1 \ \& \ 0 \le s \le S+1 \tag{8.34}$$

$$V_{r,s} = \frac{1}{d}(\Psi_{r,s} - \Psi_{r+1,s}) \qquad ; \ 0 \le r \le R+1 \ \& \ 1 \le s \le S+1 \tag{8.35}$$

Equations (8.34) and (8.35) determine the (scalar) value of $\Psi_{r,s}$ to within a constant. That constant can be (arbitrarily) specified by setting

$$\Psi_{1,1} = 0. \tag{8.36}$$

Notice that discrete velocities that can be represented by the stream function defined in Equations (8.34)-(8.35) automatically solve the discrete divergence equation (8.8).

$$U_{r+1,s} - U_{r,s} + V_{r,s+1} - V_{r,s} =$$

$$= \frac{1}{d}(\Psi_{r+1,s+1} - \Psi_{r+1,s} - \Psi_{r,s+1} + \Psi_{r,s} + \Psi_{r,s+1} - \Psi_{r+1,s+1} - \Psi_{r,s} + \Psi_{r+1,s}) = 0 \tag{8.37}$$

8.1.2.1 BOUNDARY CONDITIONS

Starting with $\Psi_{1,1}$ as given by Equation (8.36), Equations (8.35) and (8.18) can be solved sequentially for boundary conditions on $\Psi_{r,1}$.

$$\Psi_{r,1} = 0 \qquad ; \ 2 \le r \le R+1 \tag{8.38}$$

Similarly, starting with $\Psi_{R+1,1}$ as given by Equation (8.38), Equations (8.34) and (8.30) can be solved sequentially for boundary conditions $\Psi_{R+1,s}$.

$$\Psi_{R+1,s} = U_b d \sum_{k=1}^{s-1} e^{-(k-0.5)d\sqrt{j\omega/\nu}} \qquad ; \ 2 \le s \le S+1 \tag{8.39}$$

Finally, starting with $\Psi_{R+1,S+1}$ as given in Equation (8.39), Equations (8.35) and (8.33) can be solved sequentially for boundary conditions $\Psi_{r,S+1}$.

$$\Psi_{r,S+1} = U_b d \sum_{k=1}^{S} e^{-(k-0.5)d\sqrt{j\omega/\nu}} \qquad ; \ 1 \le r \le R \tag{8.40}$$

8.1.2.2 FICTITIOUS VARIABLES

Equations (8.12) which express the no-slip boundary condition near the plate can be combined with Equations (8.34) to define fictious variables $\Psi_{r,0}$.

$$\Psi_{r,0} = \Psi_{r,2} - 2U_b d \qquad ; \ 1 \le r \le R \qquad (8.41)$$

Similarly, the symmetry condition in Equations (8.15) can be used with Equations (8.35) to define fictitious variables $\Psi_{0,s}$.

$$\Psi_{0,s} = \Psi_{2,s} \qquad ; \ 2 \le s \le S \qquad (8.42)$$

Combining Equations (8.32) with Equations (8.40) and (8.34) yields $\Psi_{r,S+2}$.

$$\Psi_{r,S+2} = U_b d \sum_{k=1}^{S+1} e^{-(k-0.5)d\sqrt{j\omega/\nu}} \qquad ; \ 1 \le r \le R \qquad (8.43)$$

Combining Equations (8.31) with Equations (8.39) and (8.35) yields $\Psi_{R+2,s}$.

$$\Psi_{R+2,s} = U_b d \sum_{k=1}^{s-1} e^{-(k-0.5)d\sqrt{j\omega/\nu}} \qquad ; \ 2 \le s \le S \qquad (8.44)$$

8.1.2.3 COMPUTATIONAL MOLECULE

By substituting Equations (8.34) and (8.35) into the momentum equations (8.6,8.12) and (8.7,8.13) and combining equations, a computational molecule that depends on values of $\Psi_{r,s}$ but not on $U_{r,s}$, $V_{r,s}$, or $P_{r,s}$ can be derived. Let $M_{r,s}$ denote the x -momentum equation (8.6,8.12) for cell (r,s) and $N_{r,s}$ denote the y momentum equation (8.7,8.13) for cell (r,s). Then the sum $(M_{r,s} - M_{r,s-1} - N_{r,s} + N_{r-1,s})$ is equal to

$$\frac{j\omega\rho}{d}(\Psi_{r-1,s}+\Psi_{r,s+1}-4\Psi_{r,s}+\Psi_{r+1,s}+\Psi_{r,s-1}) = \frac{\mu}{d}3\,(20\Psi_{r,s}-8\Psi_{r-1,s}-8\Psi_{r,s+1}-8\Psi_{r+1,s}$$
$$-8\Psi_{r,s-1}+2\Psi_{r-1,s+1}+2\Psi_{r+1,s+1}+2\Psi_{r+1,s-1}+2\Psi_{r-1,s-1}+\Psi_{r-2,s}+\Psi_{r,s+2}+\Psi_{r+2,s}+\Psi_{r,s-2})$$
$$; \ 2 \le r \le R \ \& \ 2 \le s \le S \qquad (8.45)$$

8.1.2.4 ADDITIONAL EQUATIONS

Let $M'_{1,s}$ denote the x momentum equation (8.27) for cell (1,s). Then (using Equation (8.42) to eliminate $\Psi_{0,s}$ terms), $(M'_{1,s} - M'_{1,s-1} - 2N_{1,s})$ is equal to

$$\frac{j\omega\rho}{d}(2\Psi_{2,s}+\Psi_{1,s+1}-4\Psi_{1,s}+\Psi_{1,s-1}) = +\frac{2}{d}(P_{f,s} - P_{f,s-1}) + \frac{\mu}{d}3\,(20\Psi_{1,s}-16\Psi_{2,s}-8\Psi_{1,s+1}$$
$$-8\Psi_{1,s-1}+4\Psi_{2,s+1}+4\Psi_{2,s-1}+2\Psi_{3,s}+\Psi_{1,s+2}+\Psi_{1,s-2}) \qquad ; \ 2 \le s \le S \qquad (8.46)$$

Combining Equations (8.34) and (8.36) with (8.19)

$$\Psi_{1,s+1} = sU_b d - j\omega s^2 \Theta_d d^2/2 \qquad ; \ 1 \le s \le F \qquad (8.47)$$

8.1.2.5 STREAM FUNCTION FORMULATION OF EQUATIONS OF MOTION

boundary variables

$$\Psi_{r,1} = 0 \qquad ; \ 1 \le r \le R+1 \qquad (8.36,8.38)$$

$$\Psi_{R+1,s} = U_b d \sum_{k=1}^{s-1} e^{-(k-0.5)d\sqrt{j\omega/\nu}} \qquad ; \ 2 \le s \le S+1 \qquad (8.39)$$

$$\Psi_{r,S+1} = U_b d \sum_{k=1}^{S} e^{-(k-0.5)d\sqrt{j\omega/\nu}} \qquad ; \ 1 \le r \le R \qquad (8.40)$$

fictitious variables

$$\Psi_{r,0} = \Psi_{r,2} - 2U_b d \qquad ; \ 1 \le r \le R \qquad (8.41)$$

$$\Psi_{0,s} = \Psi_{2,s} \qquad ; \ 2 \le s \le S \qquad (8.42)$$

$$\Psi_{r,S+2} = U_b d \sum_{k=1}^{S+1} e^{-(k-0.5)d\sqrt{j\omega/\nu}} \qquad ; \ 1 \le r \le R \qquad (8.43)$$

$$\Psi_{R+2,s} = U_b d \sum_{k=1}^{s-1} e^{-(k-0.5)d\sqrt{j\omega/\nu}} \qquad ; \ 2 \le s \le S \qquad (8.44)$$

$$P_{f,s} = 0 \qquad ; \ F+1 \le s \le S \qquad (8.26)$$

computational molecule

$$\frac{j\omega\rho}{d}(\Psi_{r-1,s}+\Psi_{r,s+1}-4\Psi_{r,s}+\Psi_{r+1,s}+\Psi_{r,s-1}) = \frac{\mu}{d^3}(20\Psi_{r,s}-8\Psi_{r-1,s}-8\Psi_{r,s+1}-8\Psi_{r+1,s}$$
$$-8\Psi_{r,s-1}+2\Psi_{r-1,s+1}+2\Psi_{r+1,s+1}+2\Psi_{r+1,s-1}+2\Psi_{r-1,s-1}+\Psi_{r-2,s}+\Psi_{r,s+2}+\Psi_{r+2,s}+\Psi_{r,s-2})$$
$$; \ 2 \le r \le R \ \& \ 2 \le s \le S \qquad (8.45)$$

additional equations

$$\frac{j\omega\rho}{d}(2\Psi_{2,s}+\Psi_{1,s+1}-4\Psi_{1,s}+\Psi_{1,s-1}) = +\frac{2}{d}(P_{f,s}-P_{f,s-1}) + \frac{\mu}{d^3}(20\Psi_{1,s}-16\Psi_{2,s}-8\Psi_{1,s+1}$$
$$-8\Psi_{1,s-1}+4\Psi_{2,s+1}+4\Psi_{2,s-1}+2\Psi_{3,s}+\Psi_{1,s+2}+\Psi_{1,s-2}) \qquad ; \ 2 \le s \le S \qquad (8.46)$$

$$\Psi_{1,s+1} = sU_b d - j\omega s^2 \Theta_d d^2/2 \qquad ; \ 1 \le s \le F \qquad (8.47)$$

$$T_{zd} = 2d^2 \sum_{s=1}^{F} (s-0.5) P_{f,s} \qquad (8.29)$$

Table 8.2: Summary of difference equations needed to solve the stream function formulation of the equations of motion of the structure in Figure 7.1. There are a total of (RS+3R+3S–3) $\Psi_{r,s}$'s, (S) $P_{f,s}$'s, and (1) T_{zd} -- a total of (RS+3R+4S–2) unknowns. Listed above are (RS+3R+4S–2) equations.

8.2 COMPUTATIONAL METHOD

8.2.1 COMPLEX BI-CONJUGATE GRADIENT ALGORITHM

The equations in Table 8.2 were solved using the complex bi-conjugate gradient algorithm (Jacobs, 1981). In this algorithm an initial approximate solution is iteratively "improved" -- in a fashion similar to the method of steepest descent (Luenberger, 1965). The conjugate gradient method differs from other gradient methods in that (in the absence of roundoff error), the exact solution is obtained after a finite number of steps (equal to the number of unknowns).

Let the Equations in Table 8.2 be represented in matrix form,

$$A\underline{x} = \underline{b} \ , \tag{8.48}$$

where $\underline{x}$ is the vector of unknowns, $\underline{b}$ is a vector of (constant) driving terms, and A is the matrix of equation coefficients. Each of A, $\underline{x}$, and $\underline{b}$ contain complex-valued entries. Starting from an initial guess of the solution

$$\underline{x}_0 = \underline{0} \tag{8.49}$$

one calculates an initial residual ($\underline{r}_0$), bi-residual ($\bar{\underline{r}}_0$), direction vector ($\underline{p}_0$), and bi-direction vector ($\bar{\underline{p}}_0$).

$$\underline{r}_0 = \underline{b} - A\underline{x}_0 \tag{8.50}$$

$$\bar{\underline{r}}_0 = \underline{r}_0^{\,*} \tag{8.51}$$

$$\underline{p}_0 = \underline{r}_0 \tag{8.52}$$

$$\bar{\underline{p}}_0 = \bar{\underline{r}}_0 \tag{8.53}$$

Then for each step k = 0, 1, 2, ...

$$\alpha_k = \frac{<\bar{\underline{r}}_k \, , \underline{r}_k>}{<\bar{\underline{p}}_k \, , A\underline{p}_k>} \tag{8.54}$$

$$\underline{x}_{k+1} = \underline{x}_k + \alpha_k \underline{p}_k \tag{8.55}$$

$$\underline{r}_{k+1} = \underline{b} - A\underline{x}_{k+1} \tag{8.56}$$

$$\bar{\underline{r}}_{k+1} = \bar{\underline{r}}_k - \alpha_k^{\,*} A^H \bar{\underline{p}}_k \tag{8.57}$$

$$\beta_k = \frac{<\bar{\underline{r}}_{k+1} \, , \underline{r}_{k+1}>}{<\bar{\underline{r}}_k \, , \underline{r}_k>} \tag{8.58}$$

$$\underline{p}_{k+1} = \underline{r}_{k+1} + \beta_k \underline{p}_k \tag{8.59}$$

$$\bar{\underline{p}}_{k+1} = \bar{\underline{r}}_{k+1} + \beta_k^{\,*} \bar{\underline{p}}_k \tag{8.60}$$

where the superscript * denotes complex conjugate, the superscript ^{H} denotes Hermitian (complex conjugate transpose), and $< \underline{a} \, , \underline{b} >$ denotes the inner product $\underline{a}^H\underline{b}$.

8.2.2 FORMULATION OF A, $\underline{x}$, AND $\underline{b}$

In order to solve the equations in Table 8.2 using the bi-conjugate gradient method, the elements of $\underline{x}$ must be identified with the variables that appear in Table 8.2, the elements of $\underline{b}$ must be identified with the constants in Table 8.2, and the elements of A must be identified with the equation coeficients.

Not all of the unknowns that are listed in Table 8.2 need appear in $\underline{x}$. Specifically, the boundary variables and the fictitious variables, a total of (4R+4S–2) variables, are easily eliminated from the set of (RS+3R+4S–3) equations. For R=20, S=30, F=5, 198 equations out of the 777 original equations are eliminated -- a reduction of roughly 25%. Since the computational burden of solving Equations (8.49)-(8.60) grows roughly with the square of the number of equations, a 25% reduction in the number of equations results in roughlya 44% decrease in computation.

Unfortunately, the equations that result after elimination are more tedious to specify; for example, Equations (8.45) can no longer be applied for r=2, r=R, and s=S. However, an algorithm can be generated to automate the process of elimination. Segregate the elements of $\underline{x}$ in two partitions -- one partition $\underline{x}_t$ containing the variables that are to be eliminated and one partition $\underline{x}'$ containing the variables that are to be retained. Then Equation (8.48) can be written as

$$\left[\begin{array}{c|c} A_1 & A_2 \\ \hline A_3 & I \end{array}\right]\left[\begin{array}{c} \underline{x}' \\ \hline \underline{x}_t \end{array}\right] = \left[\begin{array}{c} \underline{b}_1 \\ \hline \underline{b}_2 \end{array}\right] \tag{8.61}$$

where A and $\underline{b}$ have been partitioned so that $\underline{b}_1$ has the same number of elements as $\underline{x}'$ and the number of rows in the square matrix A_1 is equal to the number of elements in $\underline{x}'$. "I" represents the identity matrix. Equation (8.61) can be split into two equations.

$$A_1\underline{x}' + A_2\underline{x}_t = \underline{b}_1 \tag{8.62}$$
$$A_3\underline{x}' + \underline{x}_t = \underline{b}_2 \tag{8.63}$$

SolvingEquation (8.63) for $\underline{x}_t$, and substituting into Equation (8.62)

$$A_1\underline{x}' + A_2(\underline{b}_2 - A_3\underline{x}') = \underline{b}_1$$
$$(A_1 - A_2A_3)\underline{x}' = (\underline{b}_1 - A_2\underline{b}_2) \tag{8.64}$$

Equation (8.64) can be written as

$$A'\underline{x}' = \underline{b}' \tag{8.65}$$

where

$$A' = A_1 - A_2A_3 \tag{8.66}$$
$$\underline{b}' = \underline{b}_1 - A_2\underline{b}_2 \tag{8.67}$$

The system of Equations (8.65) retains only the non-trivial equations from (8.48). Equations (8.66)-(8.67) relate the coeficients of (8.65) to those of (8.48) through the partitioning represented in Equation (8.61).

8.2.3 STRUCTURE OF THE COMPUTER PROGRAM

The correspondence between $\underline{x}$ and the variables in Table 8.2 is obtained by a simple ordering scheme

$$[\, x_1\, x_2\, x_3 \cdots x_{RS+3R+4S-2}\,] = \tag{8.68}$$
$$[\, \Psi_{0,0}\, \Psi_{1,0} \cdots \Psi_{R+2,0}\, \Psi_{0,1}\, \Psi_{1,1} \cdots \Psi_{R+2,1} \cdots \Psi_{R+2,S+2}\, P_{f,0}\, P_{f,1} \cdots P_{f,S}\,]$$

which not only specifies the indexing of $\underline{x}$, but also specifies the indexing of the columns of A. The correspondence between $\underline{b}$ and the constants in Table 8.2 is obtained by a simple ordering of the equations in Table 8.2 (top-to-bottom) which not only specifies the indexing of $\underline{b}$, but also specifies the indexing of the rows of A.

The number of elements in $\underline{x}$ is equal to the number of unknowns in the equations in Table 8.2. The number of elements in A is equal to the square of the number of unknowns. The matrix A is however sparse -- having at most 18 non-zero elements per row (those rows corresponding to Equations (8.46)). The application of Equations (8.49)-(8.60) does not require specifying A explicitly -- but merely the ability to generate the product of A with a vector ($\underline{p}_k$ in Equation (8.54) and $\underline{x}_{k+1}$ in Equation (8.56)) and the product of A^H with a vector ($\overline{\underline{p}}_k$ in Equation (8.57)).

The algorithm for calculating the product of A with an input vector $\underline{y}$ is readily generated directly from Table 8.2. Since the j^{th} element of $A\underline{y}$ is the product of the j^{th} row of A with $\underline{y}$, all of the elements of A that are required to calculate the j^{th} element of $A\underline{y}$ come from the j^{th} equation in Table 8.2. For each non-constant term in the j^{th} equation, identify i, the column number assigned to that term by Equation (8.68). Multiply the coeficient of that i^{th} term by the i^{th} entry in $\underline{y}$ and add the result to the j^{th} entry in $A\underline{y}$ if the term is from the left hand side of the j^{th} equation, or subtract it if the term is from the right hand side of the equation.

The elements of A that are required to calculate the product of A^H with an input vector $\underline{y}$ come from a single column of A but from many rows. To compute the i^{th} entry in $A^H\underline{y}$, find the variable that Equation (8.68) associates with the i^{th} index of $\underline{x}$. Then for each occurance of that variable in the equations of Table 8.2 find j, the index assigned to that equation. Multiply the term's coeficient by the j^{th} entry of $\underline{y}$ and add the result to the i^{th} entry of $A^H\underline{y}$ if the term came from the left hand side equation j or subtract it if it came from the right hand side.

In order to calculate the product of A' with a vector $\underline{y}'$, first compute

$$\underline{y}_t = -A_3\underline{y}' \tag{8.69}$$

(analogous to the homogeneous part of $\underline{x}_t$ in Equation (8.63)) and partition $\underline{y}'$ with $\underline{y}_t$ to form $\underline{y}$. Next employ the algorithm developed above to calculate $A\underline{y}$ which, from Equation (8.61) will be equal to $A_1\underline{y}' + A_2(-A_3\underline{y}_t)$ partitioned with $A_3\underline{y}'-\underline{y}_t$. By Equation (8.66), the first of these partitions is the desired result, and by Equation (8.69), the second of these partitions contains $\underline{0}$.

To compute A'^H times an input vector $\underline{y}'$, first partition $\underline{y}'$ with $\underline{0}$ to form a new vector $\underline{y}$ with a number of elements equal to the number of rows in A. Next employ the algorithm developed above to calculate $A^H\underline{y}$, which from Equation (8.61) can be partitioned into to $(A^H\underline{y})' = A_1{}^H\underline{y}'$ and $(A^H\underline{y})_t = A_2{}^H\underline{y}'$. Multiplying the second of these partitions by $A_3{}^H$ and subtracting this from the first partion gives the desired result $A'^H\underline{y} = (A_1{}^H - A_3{}^H A_2{}^H)\underline{y}'$.

8.3.4 CONVERGENCE

In the absence of roundoff errors, the approximate solution $\underline{x}_k$ in Equations (8.54)-(8.60) approaches $\underline{x}$ (the solution of Equation (8.48)) as k increases. Moreover, in the absence of roundoff errors, $\underline{x}_k == \underline{x}$ when k = the number of elements in $\underline{x}$. Roundoff errors can however interfere with the progress of the bi-conjugate gradient algorithm. It is therefore necessary to establish a criterion by which convergence of the algorithm can be monitored. The most direct measure of error in the k^{th} step is $\underline{e}_k = \underline{x}_k - \underline{x}$, the difference between the k^{th} approximation to $\underline{x}$ and $\underline{x}$. Since the solution vector $\underline{x}$ is unknown however, $\underline{e}_k$ cannot be calculated.

The magnitude of the residual $\underline{r}_k$ (in Equations (8.50) and (8.56)) can be used as a measure of error. The i^{th} element of $\underline{r}_k$ measures the extent to which the i^{th} equation in the set of equations (8.48) is not satisfied. Thus, by iterating Equations (8.54)-(8.60) until $\underline{r}_k == \underline{0}$ assures that $\underline{x}_k = \underline{x}$. The representation of numbers with limited precision complicates the implementation of the termination condition $\underline{r}_k = \underline{0}$. At some step in the iteration, the computed value of $\underline{r}_k$ consists primarily of the roundoff error incured from the addition of the terms that comprise $\underline{r}_k$ -- and further iteration is pointless.

The termination condition used in this study was derived from two scalar functions of $\underline{r}_k$. The first is the mean of the squared magnitudes of the elements in $\underline{r}_k$.

$$e_{ms} = \langle \underline{r}_k{}^H, \underline{r}_k \rangle \tag{8.70}$$

The second is the maximum of the magnitudes in $\underline{r}_k$.

$$e_{max} = \text{maximum element of } \langle \underline{r}_k{}^H, \underline{r}_k \rangle \tag{8.71}$$

Iteration was continued until $e_{ms} < 10^{-20}$ and $e_{max} < 10^{-10}$.

8.3 NUMERICAL RESULTS

In this section, we show the solutions to the difference equations of motion in Table 8.2 for two different kinds of excitation: translational excitation -- defined as translation of the plate when the angular displacement of the flap is fixed at $\Theta=0$; and rotational excitation -- defined as rotation of the flap when the plate is fixed with $U_b=0$.

For both translational and rotational excitations, the solutions for any values of the physically meaningful parameters -- ρ, μ, ν, L, and ω -- can be derived from the solutions to the normalized equations of motion (section 7.1.4) as a function of a single (nondimensional) parameter $\omega/\omega_L=\omega L^2/2\nu$. We therefore: solve the equations of motion in Table 8.2 for a particular set of fluid properties ($\rho=1$ gm/cm^3, $\mu=1$ gm/cm-sec, $\nu=1$ cm^2/sec), for L=1 cm, and for a family of frequencies ω; compute the normalized representation of that solution (Equations (7.27)-(7.34)); and display the normalized results.

In addition to the physical parameters, the difference equations in Table 8.2 include three discretization parameters -- F (the number of finite elements that face the flap), R (the number of finite elements between the flap and the artificial boundary imposed at x=X), and S (the number of finite elements between the plate and the artificial boundary imposed at y=Y). The choice of F, R, and S influences the accuracy with which the discrete equations of motion approximate the continuous equations. Each cell in Figure 8.1 has dimensions L/F by L/F, so spatial resolution improves with increasing F. Solutions to the difference equations are meaningful only if L/F is small enough to resolve variations in the (unknown) solution to the continuous, differential equations of motion. Significant artifacts can also be generated by the artificial boundary conditions imposed at $x=\pm X=\pm LR/F$ and at $y=Y=LS/F$ unless X and Y are sufficiently large relative to L. X and Y are increased by increasing R and S. Notice however that X and Y are decreased by increasing F. Therefore, increases in F designed to improve spatial resolution must be accompanied by increases in R and S so as not to reduce the spatial domain defined by the boundaries. Lastly, computation time for the bi-conjugate gradient algorithm (section 8.2.1) increases with roughly the square of the number of equations to be solved. There are roughly R×S equations in Table 8.2. This section shows results for F=5, R=20, and S=30 -- for which X=4L and Y=6L. The calculations were performed on a VAX 11-750/FPA using a 64-bit floating-point number representation, and the solution for each set of parameters -- U_b, Θ_d, and ω -- using F=5, R=20, and S=30 required roughly 94 minutes of computer time.

8.3.1 FLUID MOTION

In this section, we illustrate the fluid motion that results from solution of the equations of motion in Table 8.2 with streamlines that are computed directly from the discrete stream function $\Psi_{r,s}$. $\Psi_{r,s}$ is complex amplitude of the stream function that results from steady-state sinusoidal excitation. Streamlines can be used to depict a fluid velocity field at only one time instant, so that representation of the velocity field that results from a periodically-varying excitation generally requires a family of streamlines -- one for each phase of the excitation. For each computation, we will therefore show two sets of streamlines. The first depicts the real part of $\Psi_{r,s}$ and corresponds to the fluid motion at the instant that the excitation (U_b or $j\omega\Theta$) has peak amplitude. The second set of streamlines depicts the imaginary part of $\Psi_{r,s}$ and corresponds to the fluid motion at the instant of time 1/4 period earlier than the first set of streamlines. Since the equations of motion are linear, the stream function at any phase can be determined by a linear combination of the two stream functions that are illustrated.

The algorithm used to generate streamlines from the discrete stream function $\Psi_{r,s}$ (that results from solution of the equations of motion in Table 8.2) is pictured in Figure 8.2 Values are assigned to the stream function $\Psi(x,y)$ at points between (x=r/F, y=s/F) and (x=(r+1)/F, y=s/F) by linear interpolation between $\Psi_{r,s}$ and $\Psi_{r+1,s}$. Similarly, values are assigned to the stream function $\Psi(x,y)$ at points between (x=r/F, y=s/F) and (x=r/F, y=(s+1)/F) by linear interpolation between $\Psi_{r,s}$ and $\Psi_{r,s+1}$. A contour map is then produced by connecting points (x,y) for which the real (or imaginary) part of $\Psi(x,y)$ is an integral multiple of a fixed constant $\Delta\Psi$ with straight line segments.

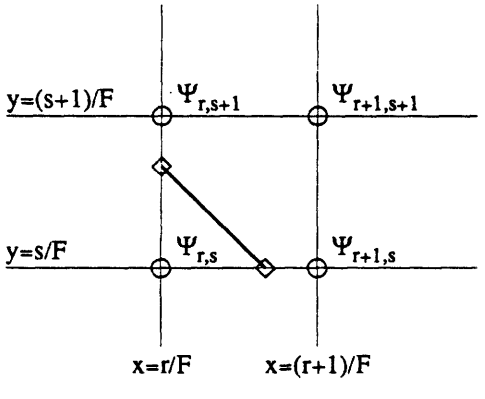

Figure 8.2: Algorithm for generating streamlines from $\Psi_{r,s}$. Values for the discrete streamfunction $\Psi_{r,s}$ are calculated from the equations in Table 8.2 for all points (x=r/F, y=s/F) with $1 \le r \le R+1$ and $1 \le s \le S+1$. Such points are indicated in this figure by circles. Values are assigned to the stream function at all points on the thin lines by linear interpolation of the calculated values. Points on the thin lines for which the real (or imag) part of the (interpolated) stream function is an integral multiple of $\Delta\Psi$ (indicated by $\diamond$'s) are then connected by straight lines (shown as thick).

8.3.1.1 FLUID MOTION -- TRANSLATIONAL EXCITATION

Figures 8.3-8.5 illustrate the fluid motion that results for translational excitation (U_b=1 and Θ_d=0). At low frequencies, the streamlines are very uniformly spaced, indicating that the fluid velocity varies little over the computational field. At low frequencies, the flap is in fact completely engulfed within the boundary layer of fluid that is entrained to move with the plate, and that boundary layer is not affected much by the presence of the flap. Boundary layer thickness decreases with increasing frequency, as evidenced by the decreasing density of streamlines at large distances from the plate at $\omega/\omega_L=10^{-2}$. As the boundary layer thickness decreases, the flap has a greater effect on the motion of nearby fluid. For frequencies for which the boundary layer thickness is comparable to the height of the flap, the disturbance that is caused by the flap has the form of a vortex above the flap. For $\omega/\omega_L=10^{-1}$, the center of the vortex is near y=4L. For ω/ω_L=1, the center of the vortex is near y=3L/2. For ω/ω_L=10, the vortex is so near the tip of the flap that is is not resolved by the spatial resolution of the computation (cell dimension = L/5). For $\omega/\omega_L=10^2$, the thickness of the boundary layer is smaller than the height of the flap by a factor of 10, so vibration of the plate and flap imparts little velocity to points distant from the flap. Streamlines for $\omega/\omega_L=10^3$ differ only slightly from those for $\omega/\omega_L=10^2$. One can detect a slight decrease in boundary layer thickness in going from $\omega/\omega_L=10^2$ to $\omega/\omega_L=10^3$ by the slightly smaller areas enclosed by corresponding streamlines.

Figure 8.4 illustrates the fluid motion that is induced by translational excitation, however, the streamlines correspond to velocities measured relative to the velocity of the plate. This frame of reference for velocity is especially useful for understanding the hydrodynamic torque that is generated on the flap. Notice that in all panels, the fluid is seen (from the reference frame of the plate) to flow over the flap (i.e. no streamlines cut throughthe flap). The fact that the flap is completely engulfed within the boundary layer of fluid entrained to move with the plate at low frequencies is apparant in panel a of Figure 8.4 by the small number of streamlines. Two small vortices with centers near x=L/3 and y=±L/3 are apparant for all frequencies ω/ω_L<1. The curvature of the streamlines generally increases with ω/ω_L.

The streamlines in Figure 8.5 illustrate the imaginary part of complex velocity field that is generated by translational excitation, and thus depict the instantaneous fluid velocity at a time that is 1/4 period earlier than that in Figures 8.3 and 8.4. Since at this earlier time, the instantaneous velocity of the plate is zero, the absolute fluid velocities and the velocities relative to the plate are equal. Notice that at low frequencies, the streamlines that depict the real and imaginary parts of relative fluid velocity (Figures 8.4a and 8.5a respectively) are nearly equal, in keeping with the idea that the phase of the velocity gradient in a boundary layer differs from that of the plate by 45^o. Notice that there is little motion of the fluid at high frequencies (Figure 8.5i), in keeping with the notion that high frequency fluid motion is determined predominately by inertia, and is in phase throughout the fluid domain. In the mid-frequency region however, substantial fluid motions occur near the flap even thoughthe instantaneous velocity of the flap structure is zero.

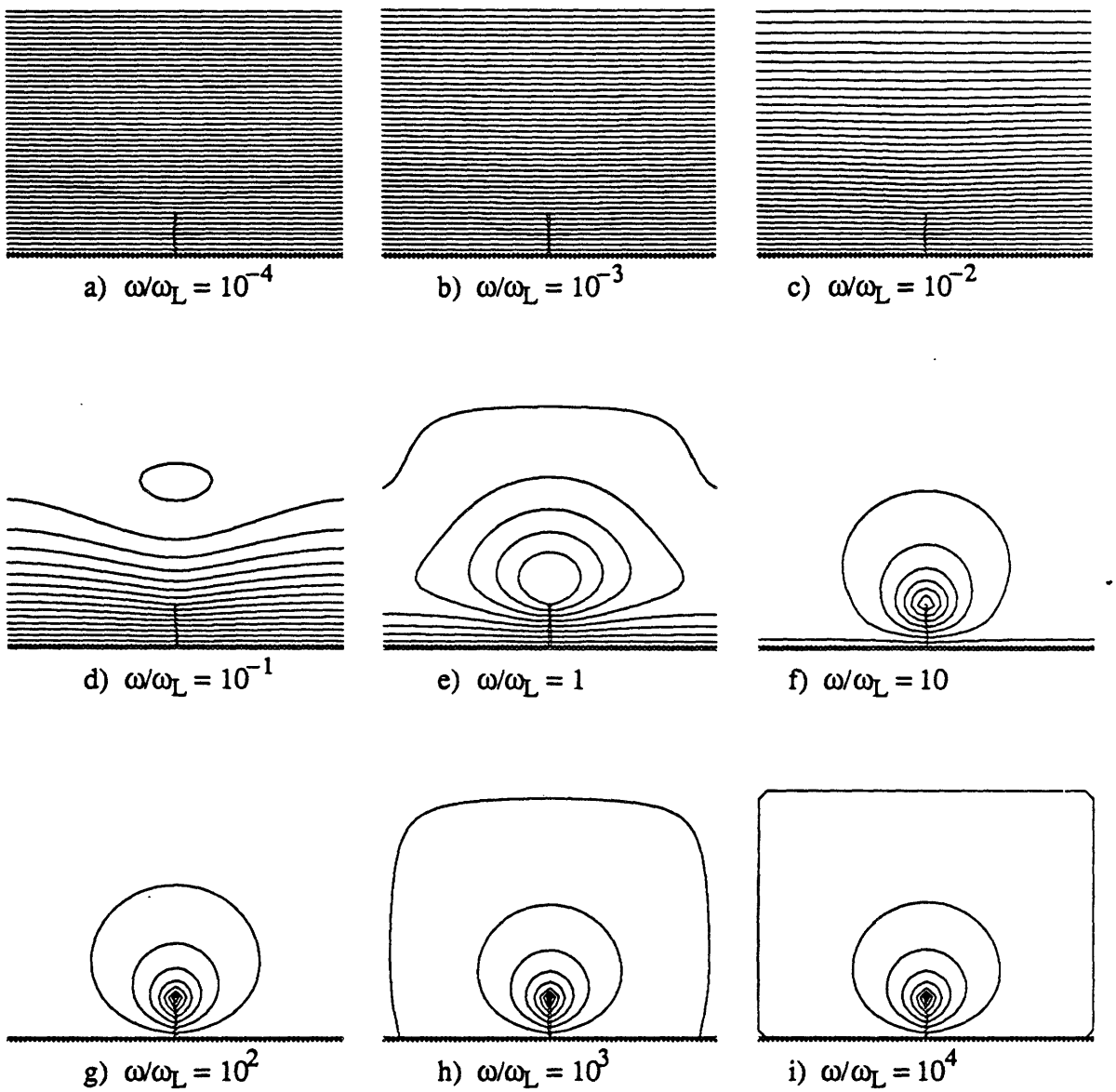

Figure 8.3: Streamlines depicting the real part of the absolute fluid velocity field that results for translational excitation (U_b=1 cm/sec, Θ_d=0). Each panel illustrates the solution of the equations of motion in Table 8.2 for a particular value of ω/ω_L (indicated in each panel) and for discretization parameters: F=5, R=20, and S=30. The thick horizontal line at the bottom of each panel represents the plate and the thick vertical line represents the flap. The streamlines connect points in the fluid field where Real $\Psi_{r,s}$=nL/8 cm^2/sec, for integer values of n. Since the velocities of all points on the flap are equal to 1 cm/sec, exactly 9 streamlines intersect the flap in each panel (one through the plate, one at the tip of the flap and 7 along the interior of the flap).

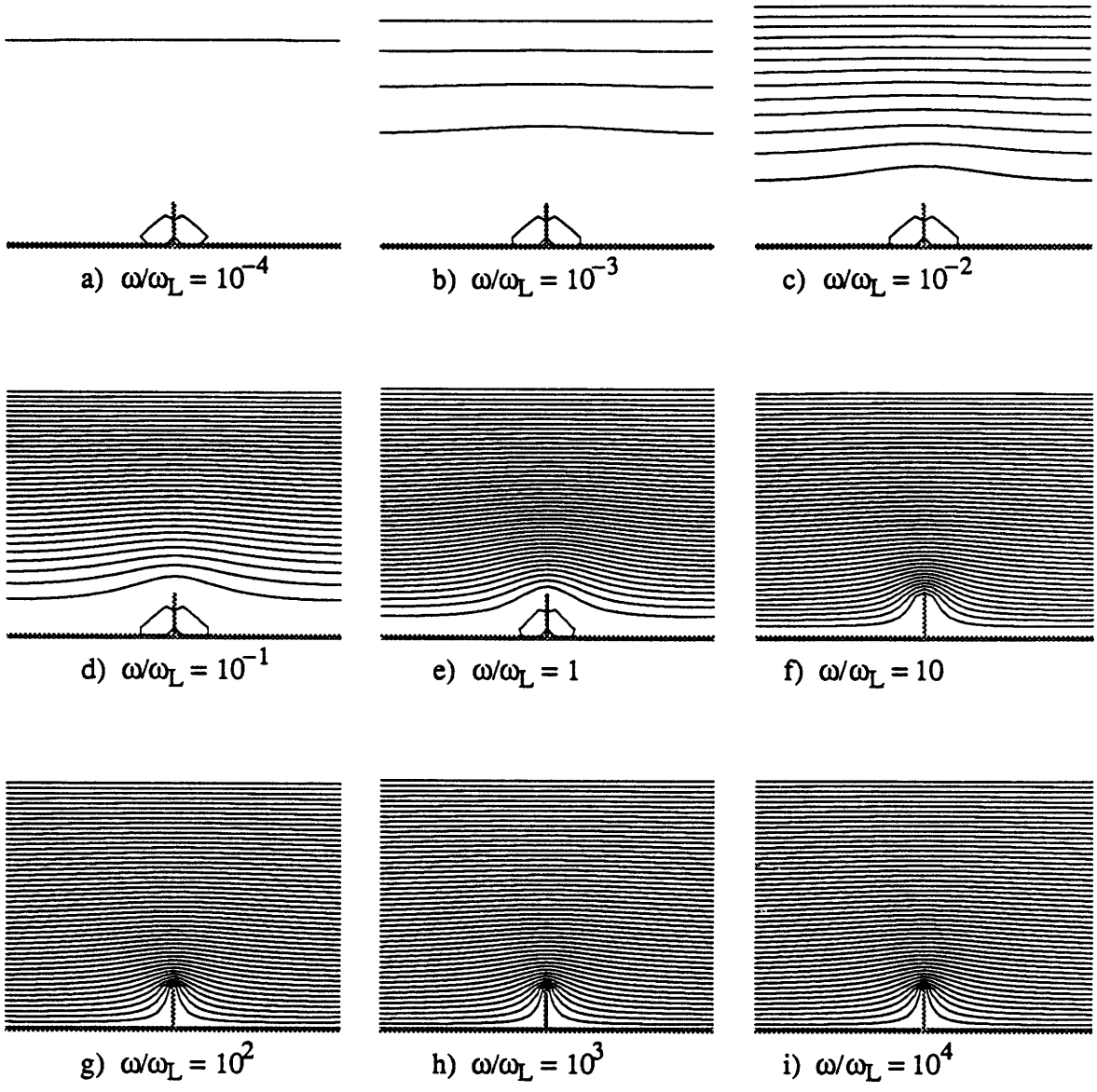

Figure 8.4: Streamlines depicting the real part of the fluid velocities, relative to the velocity of the plate, that results for translational excitation (U_b=1 cm/sec, Θ_d=0). Each panel illustrates the solution of the equations of motion in Table 8.2 for a particular value of ω/ω_L (indicated in each panel) and for discretization parameters: F=5, R=20, and S=30. The thick horizontal line at the bottom of each panel represents the plate and the thick vertical line represents the flap. The streamlines connect points in the fluid field where Real $\{\Psi_{r,s}-yU_b\}$=nL/8 cm^2/sec, for integer values of n. Since the velocities of all points on the flap are equal to the velocity of the plate, no streamlines intersect the flap. Two small vortices can be seen in panels a to e with centers near y=L/3 and x=±L/3.

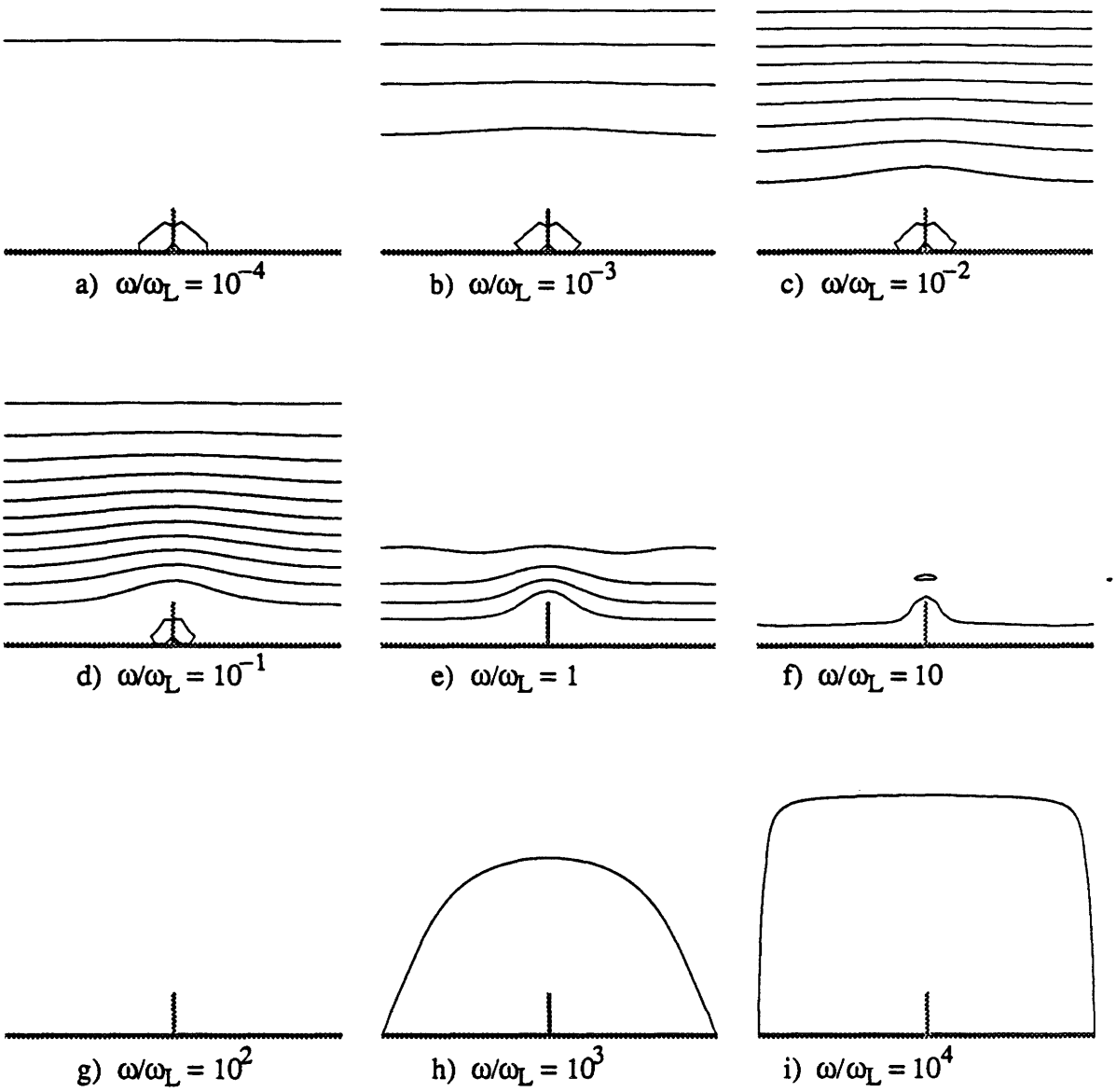

Figure 8.5: Streamlines depicting the imaginary part of the fluid velocity field that results for translational excitation (U_b=1 cm/sec, Θ_d=0). Each panel illustrates the solution of the equations of motion in Table 8.2 for a particular value of ω/ω_L (indicated in each panel) and for discretization parameters: F=5, R=20, and S=30. The thick horizontal line at the bottom of each panel represents the plate and the thick vertical line represents the flap. The streamlines connect points in the fluid field where Imag $\Psi_{r,s}$=nL/8 cm^2/sec, for integer values of n. Since the imaginary part of the velocities of all points on the flap are equal to zero, no streamlines intersect the flap. Since the imaginary part of the velocity of the plate is zero, these streamlines represent both the absolute fluid velocities and the velocities relative to that of the plate. Two vortices can be seen in panels a to d with centers near y=L/3 and x=±L/3.

8.3.1.2 COMPARISON OF NUMERICALLY DETERMINED FLUID MOTION WITH THE LOW FREQUENCY ASYMPTOTIC ANALYSIS

In section 7.2, the motion of the hinged-flap structure was analyzed for asymptotically low frequencies. Equation (7.71) gives an expression for the low frequency P-component of fluid velocity field, which we write here as a function of ω/ω_L,

$$\bar{U}(\bar{x},\omega) = U_b\hat{x} + 1/2\,(1+j)\sqrt{\omega/\omega_L}\,\bar{U}_D(\bar{x}) \tag{8.72}$$

where $\bar{U}_D(\bar{x})$ represents Dean's solution (1936) of the steady equations of fluid motion.

The streamlines in Figures 8.3a, 8.4a, and 8.5a illustrate the complex velocity field that results from solution of the discrete equations of motion for $\omega/\omega_L=10^{-4}$, and are in qualitative agreement with streamlines that would be generated from Equation (8.72). Figure 8.3a shows a nearly uniform flow that is parallel to the plate, consistent with Equation (8.72) since $\sqrt{\omega/\omega_L} = 10^{-2}$. Similarly, Figure 8.4a shows very little relative motion between the fluid and the plate. Furthermore, Figures 8.4a and 8.5a are very similar, showing that the real and imaginary parts of $(\bar{U}(\bar{x})-U_b\hat{x})$ are nearly equal.

Streamlines derived from the low frequency asymptotic analysis of the equations of motion are very similar to those derived from the numerical solution (Figure 8.6), even though the approximations that underlie these two methods are very different. For example, the numerical method imposes an artificial boundary condition at the edges of $-X<x<X$ and $y=Y$, and no such boundary condition is used in the asymptotic method. Therefore, the good match between the numerical and asymptotic solutions suggests that the errors generated by the artificial boundary condition are not excessive. Similarly, the spatial resolution of the numerical method is limited by the size of the cells in the analysis ($d=L/5$ in Figure 8.6 b and c), and no such spatial resolution effects the asymptotic solution. The asymptotic solution is based on just two terms of a series expansion of the solution to the equations of motion. The good match between the numerical and asymptotic solutions thus also suggests that the truncated series representations used in the low frequency analyses of chapters 5 and 7 are reasonable.

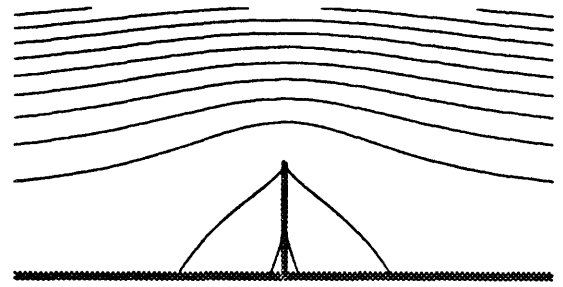

a) $\Psi_D(\bar{x})$

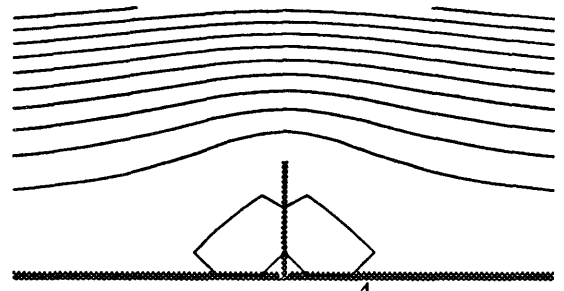

b) real $\Psi_{r,s}$ for $\omega/\omega_L = 10^{-4}$

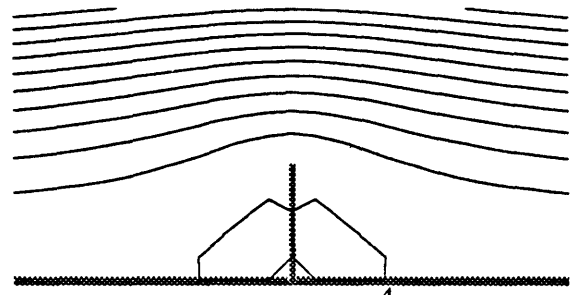

c) imag $\Psi_{r,s}$ for $\omega/\omega_L = 10^{-4}$

Figure 8.6: Comparison of streamlines generated from Dean's solution to the steady equations of fluid motion, and streamlines generated from the numerical solution of the equations of motion for low-frequency translational excitation. Panel a illustrates Dean's solution with streamlines separated by $\Delta\Psi$=0.5. Ψ is equal to zero on all rigid surfaces (shaded). The two curves that intersect the flap also mark points for which Ψ=0 -- and thus reveal the presence of a vortex. Panels b and c illustrate the real and imaginary parts of the fluid velocity (relative to that of the plate) that results from solution of the discrete equations of motion (Table 8.2) for $\omega/\omega_L=10^{-4}$, U_b=1, Θ_d=0, F=5, R=20, and S=30. Panels b and c illustrate the data that was shown in Figures 8.4a and 8.5a with two changes. Though data were computed for $1\leq r\leq 21$ and $1\leq s\leq 31$, panels b and c show data for a smaller range ($1\leq r\leq 13$ and $1\leq s\leq 13$). Secondly, the density of streamlines is greater in panels b and c than it was in Figures 8.4a and 8.5a, i.e. $\Delta\Psi$ is equal to 0.0025 in panels b and c so as to be directly comparable to the streamlines in panel a.

8.3.1.3 COMPARISON OF NUMERICALLY DETERMINED FLUID MOTION WITH THE HIGH FREQUENCY ASYMPTOTIC ANALYSIS

In section 7.3, the equations of motion for the hinged-flap structure were solved analytically for high frequencies of excitation. At high frequencies, the streamlines that represent the real part of the numerically determined fluid velocity vector (Figure 8.3i) are much more dense than are those that represent the imaginary part (Figure 8.5i), consistent with the purely real-valued velocity potential in the analytic study (Equation (7.96)). Streamlines that represent the real parts of the numerical and the asymptotic solutions to the equations of motion for translational excitation are compared in Figure 8.7. Because of the artificial boundary condition at y=Y in the numerical study, the numerical streamlines are slightly compressed in the y direction relative to the asymptotic streamlines. Generally however, the agreement between the streamlines that represent the numerical and asymptotic solutions is good, and attests to the adequacy of both the numerical and asymptotic methods.

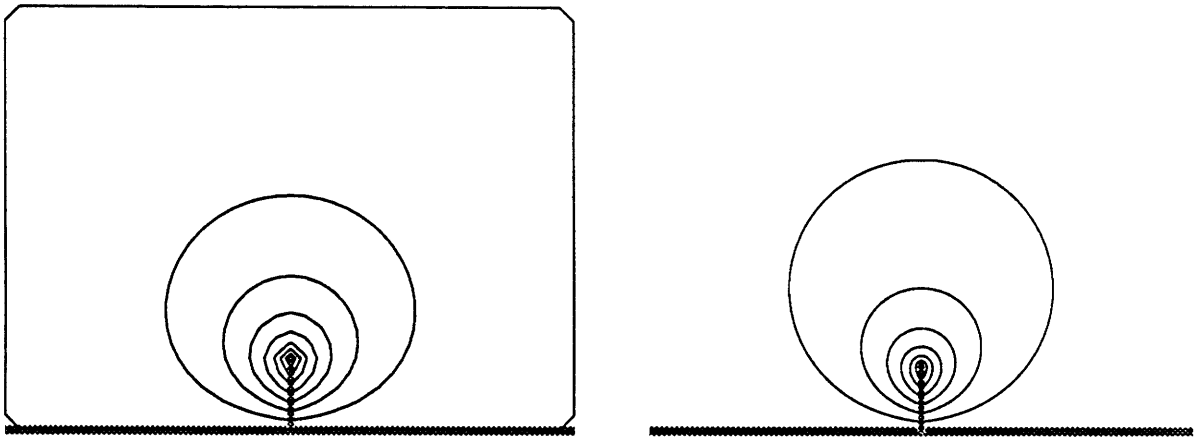

a) solution to discrete equations

b) asymptotic solution of section 7.3.4

Figure 8.7: Comparison of streamlines generated from the numerical solution for high frequency translational excitation with those generated from the analytic solution. Panel a shows streamlines that depict the real part of the numerically determined fluid velocity for U_b=1, Θ_d=0, $\omega/\omega_L=10^4$, F=5, R=20, and S=30. Panel a is identical to Figure 8.3i. Panel b shows streamlines generated from Equation (7.96), and differs from Figure 7.9 by the density of streamlines and by the range of x and y that are displayed. Streamlines in each of panels a and b of this figure connect points in the fluid domain for which Real Ψ=nL/8 cm^2/sec.

8.3.1.4 FLUID MOTION -- ROTATIONAL EXCITATION

Figures 8.8-8.10 illustrate the fluid motion that results for rotational excitation (U_b=0 and $j\omega\Theta_d$=1 rad/sec). Since for rotational excitation, the plate is stationary, only fluid near the flap is set into motion. Rotation of the flap at low frequencies causes motion of fluid at points that are distant from the flap, i.e. at points whose distance from the flap greatly exceeds L, the height of the flap. Fluid near the flap is entrained to move with the flap, while fluid more distant from the flap is pushed out of the path of the flap and entrained fluid. The resulting fluid motion forms a vortex above the tip of the flap. As frequency increases, the distance from the tip of the flap to the center of the vortex decreases, until the vortex is so near the tip that it is no longer resolved by the discretized representation, at frequencies above ω/ω_L≈10. As frequency increases, the curvature of the streamlines increases, and the volume of fluid set into motion by rotation of the flap decreases.

The streamlines in Figures 8.9 and 8.10 illustrate the imaginary part of complex velocity field that is generated by rotational excitation, and thus depict the instantaneous fluid velocity at a time that is 1/4 period earlier than that in Figure 8.8. At low frequencies, the imaginary part of the fluid velocity field that results from rotational excitation is much smaller than the real part. The fluid motion that is generated by low frequency rotation of the flap results primarily from viscous forces of fluid origin, and is in phase with the angular velocity of the flap. At high frequencies, the imaginary part of the fluid velocity field that results from rotational excitation is much smaller than the real part. The fluid motion that is generated by high frequency rotation of the flap results primarily from inerial forces of fluid origin, and is also in phase with the angular velocity of the flap. It is only at mid-frequencies that there is any significant imaginary component of rotational fluid velocity.

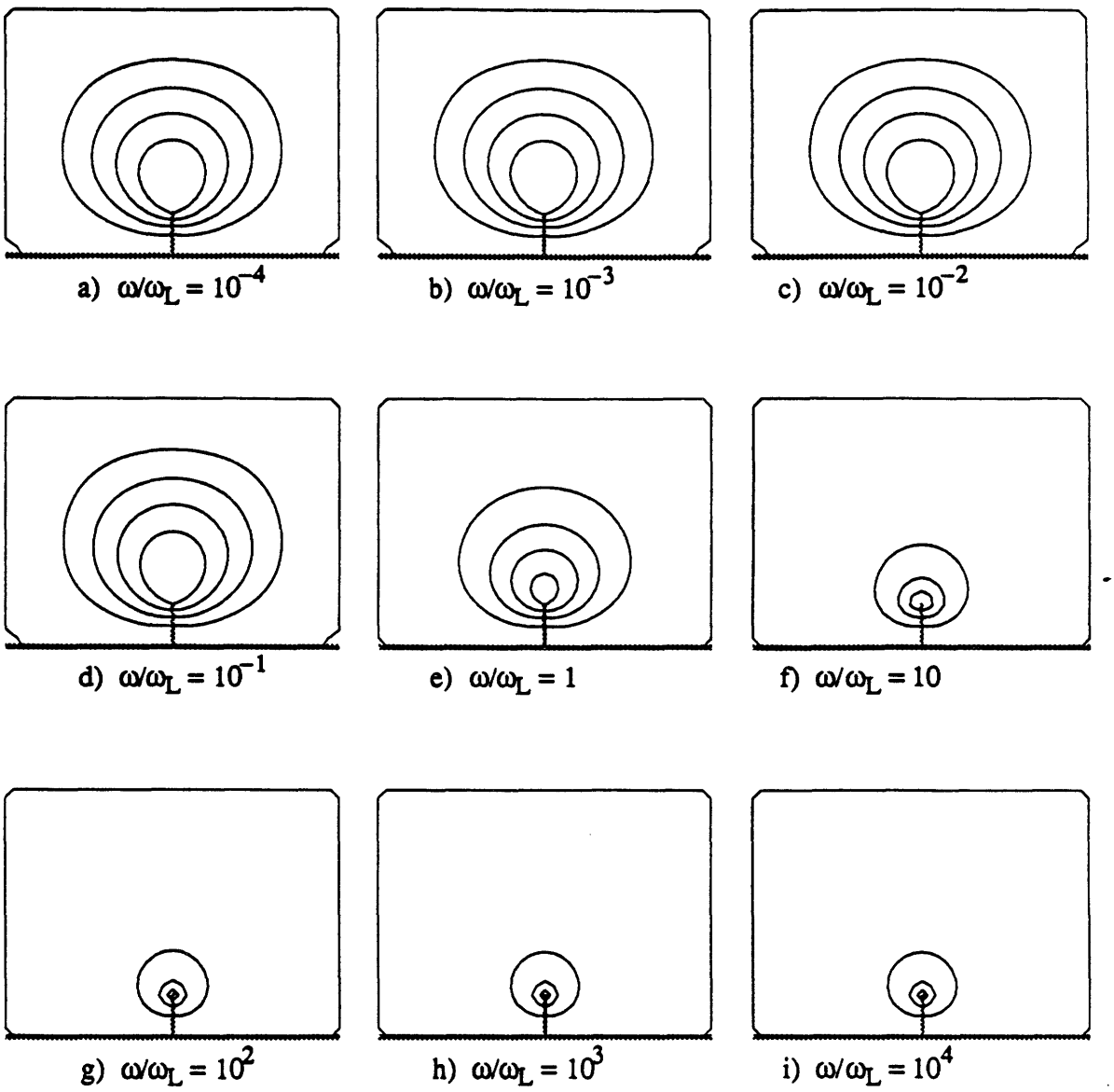

Figure 8.8: Streamlines depicting the real part of the fluid velocity field that results for rotational excitation (U_b=0, $j\omega\Theta_d$=1 rad/sec). Each panel illustrates the solution of the equations of motion in Table 8.2 for a particular value of ω/ω_L (indicated in each panel) and for discretization parameters: F=5, R=20, and S=30. The thick horizontal line at the bottom of each panel represents the plate and the thick vertical line represents the flap. The streamlines connect points in the fluid field where Real $\Psi_{r,s}$=nL/8 cm^2/sec, for integer values of n. Exactly 5 streamlines intersect the flap in each panel, although the contour near the tip of the flap is not distinquishable in panels f through i.

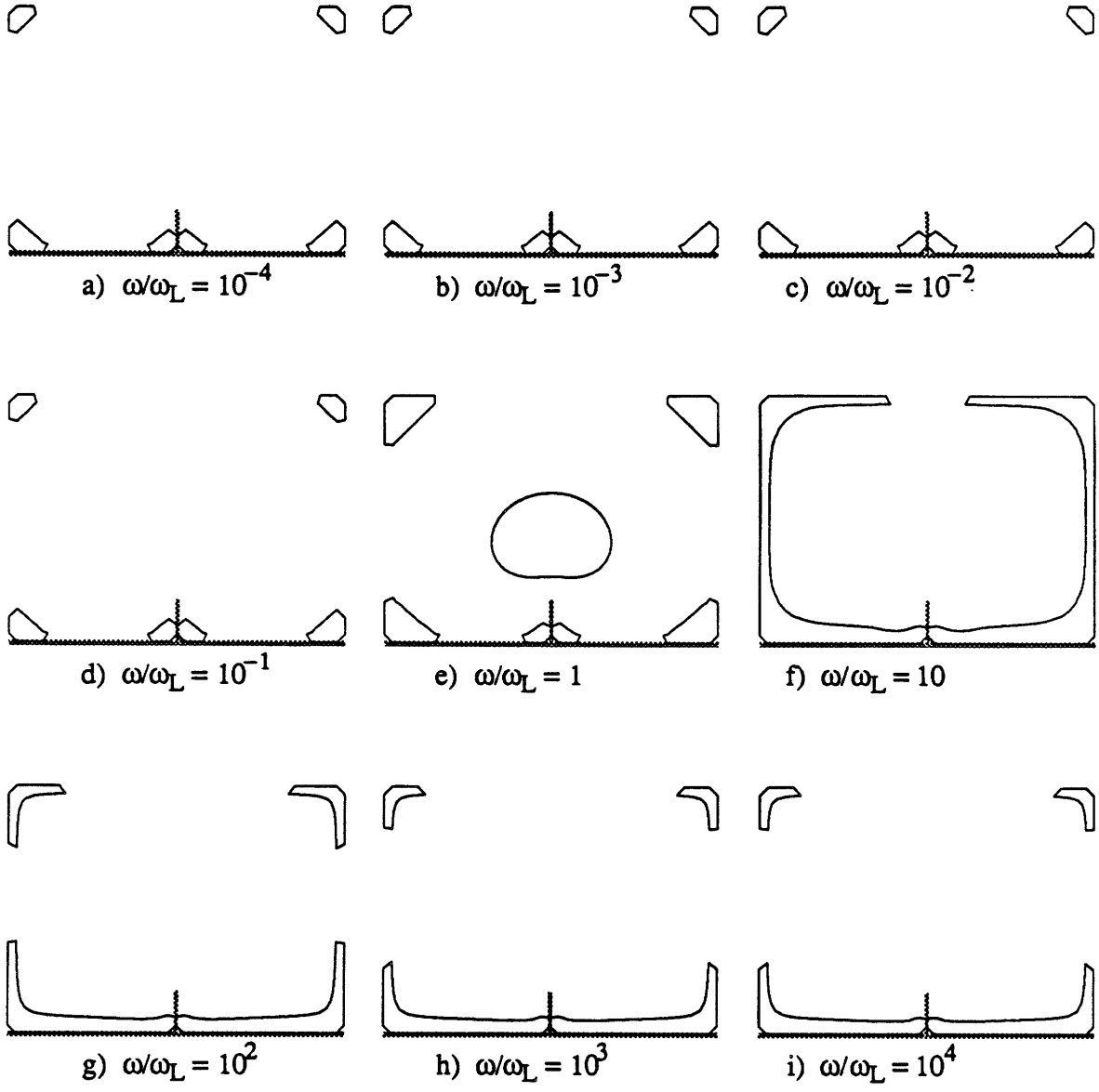

Figure 8.9: Streamlines depicting the imaginary part of the fluid velocity field that results for rotational excitation (U_b=0, $j\omega\Theta_d$=1 rad/sec). Each panel illustrates the solution of the equations of motion in Table 8.2 for a particular value of ω/ω_L (indicated in each panel) and for discretization parameters: F=5, R=20, and S=30. The thick horizontal line at the bottom of each panel represents the plate and the thick vertical line represents the flap. The streamlines connect points in the fluid field where Imag $\Psi_{r,s}$=nL/8 cm^2/sec, for integer values of n.

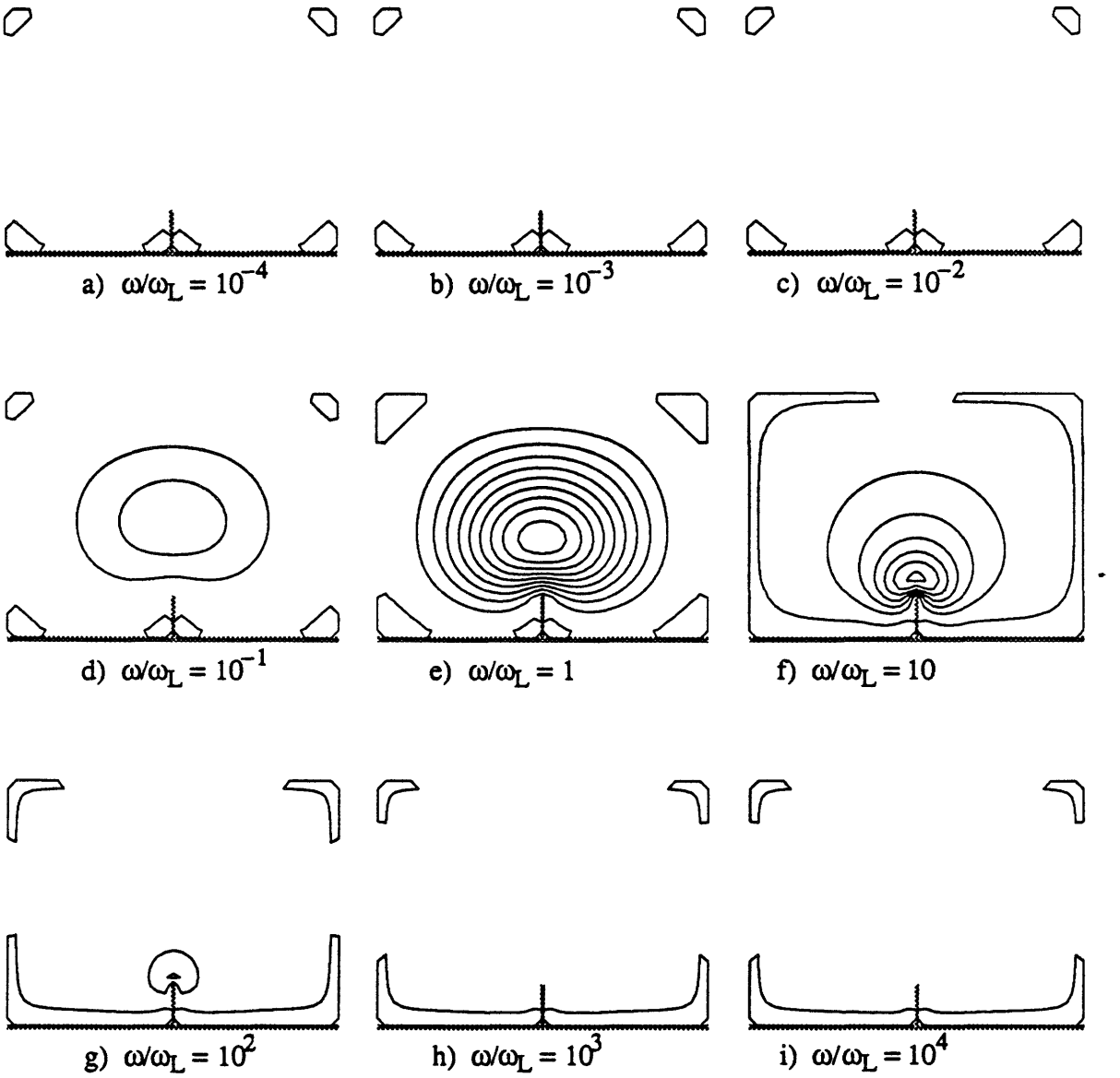

Figure 8.10: Streamlines depicting the imaginary part of the fluid velocity field that results for rotational excitation (U_b=0, $j\omega\Theta_d$=1 rad/sec). Each panel illustrates the solution of the equations of motion in Table 8.2 for a particular value of ω/ω_L (indicated in each panel) and for discretization parameters: F=5, R=20, and S=30. The thick horizontal line at the bottom of each panel represents the plate and the thick vertical line represents the flap. The streamlines connect points in the fluid field where Imag $\Psi_{r,s}$=nL/50 cm^2/sec, for integer values of n, and thus provide a higher resolution view of the same data that were presented in Figure 8.9.

8.3.1.5 COMPARISON OF NUMERICALLY DETERMINED FLUID MOTION WITH THE HIGH FREQUENCY ASYMPTOTIC ANALYSIS

In section 7.3, the equations of motion for the hinged-flap structure were solved analytically for high frequencies of excitation. At high frequencies, the streamlines that represent the real part of the numerically determined fluid velocity vector (Figure 8.8i) are much more dense that are those that represent the imaginary part (Figures 8.9i and 8.10i), consistent with the purely real-valued ratio of velocity potential to $j\omega\Theta(\omega)$ in the analytic study (Equation (7.88)). Streamlines that represent the real parts of the numerical and the asymptotic solutions to the equations of motion for translational excitation are compared in Figure 8.11. Because of the artificial boundary condition at y=Y in the numerical study, the numerical streamlines are slightly compressed in the y direction relative to the asymptotic streamlines. Generally however, the agreement between the streamlines that represent the numerical and asymptotic solutions is good, and attests to the adequacy of the numerical and asymptotic methods.

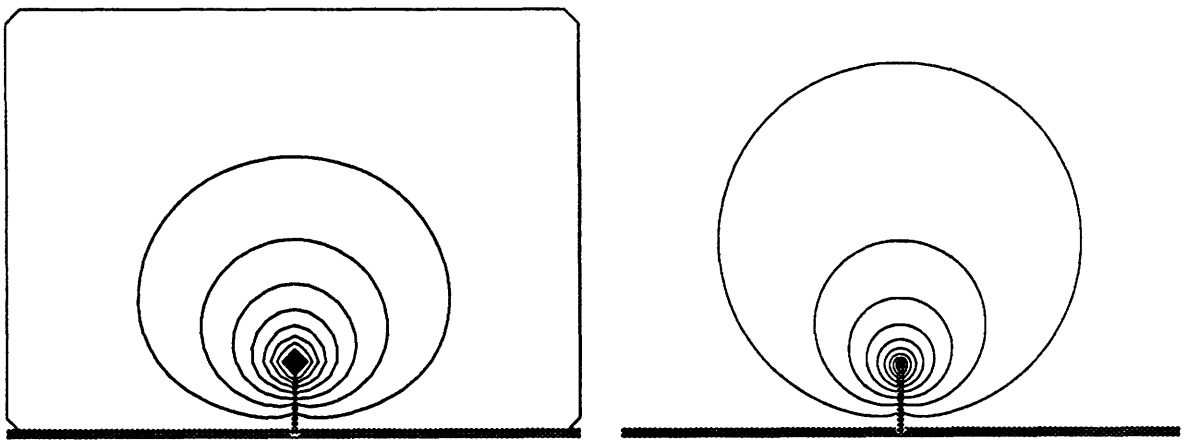

a) solution to discrete equations

b) asymptotic solution of section 7.3.3

Figure 8.11: Comparison of streamlines generated from the numerical solution for high frequency rotational excitation with those generated from the analytic solution. Panel a shows streamlines that depict the real part of the numerically determined fluid velocity for $U_b=0$, $j\omega\Theta_d=1$ rad/sec, $\omega/\omega_L=10^4$, F=5, R=20, and S=30. Panel a is identical to Figure 8.8i. Panel b shows streamlines generated from Equation (7.88) and differs from Figure 7.8 by the density of streamlines and by the range of x and y that are displayed. Streamlines in each of panels a and b of this figure connect points in the fluid domain for which Real $\Psi=nL/8$ cm^2/sec.

8.3.2 PRESSURE ON THE FLAP

Figure 8.12 displays the ratio of pressure on the flap to plate velocity that results for translational excitation of the hinged-flap structure and the ratio of pressure on the flap to angular velocity of the flap for rotational excitation. The pressure on the flap varies over many orders of magnitude as the frequency of the excitation changes, but over less than an order of magnitude as a function of distance along the flap.

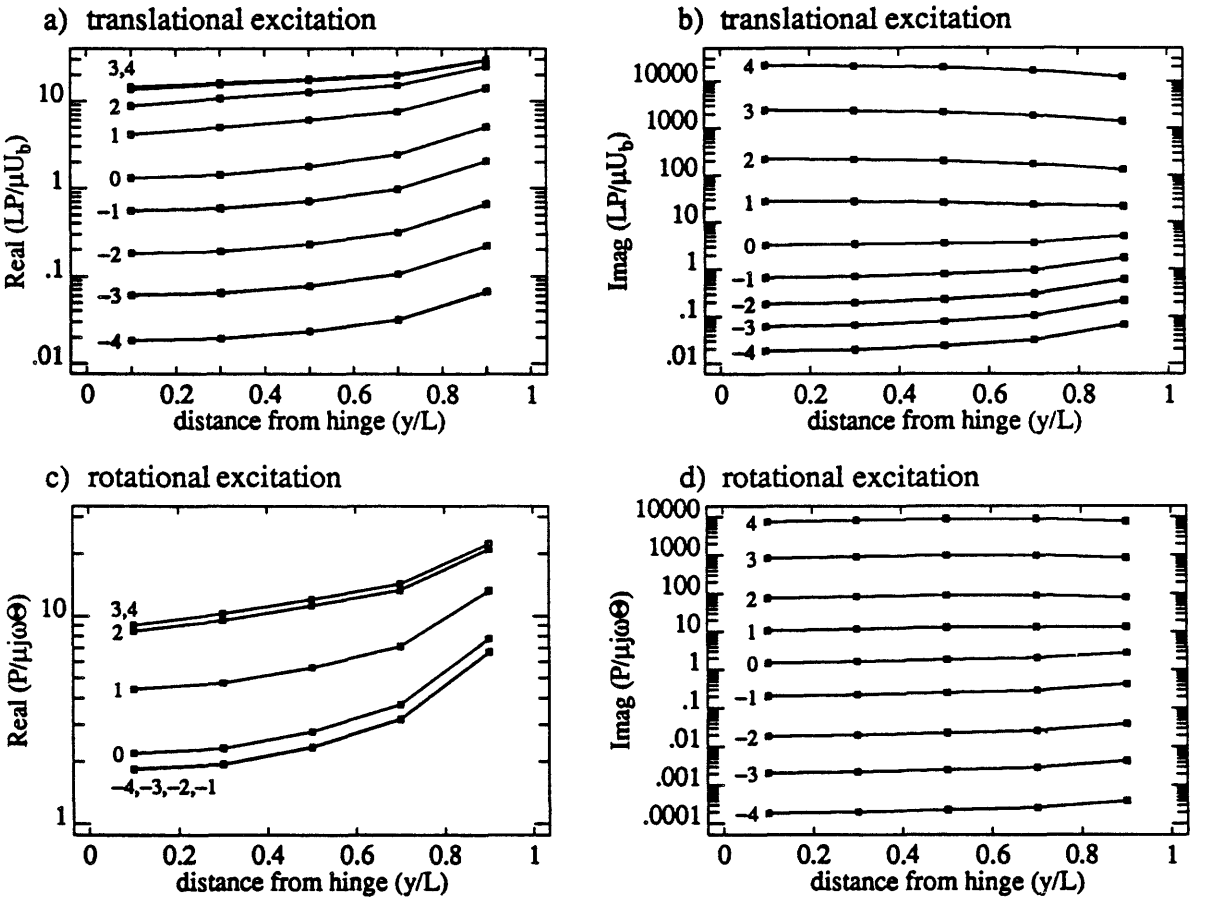

Figure 8.12: Hydrodynamic pressure on the flap. The top panels of this figure show the real and imaginary parts of the ratio of normalized pressure on the flap to plate velocity for translational excitation as a function of normalized distance from the hinge. The bottom panels of this figure show the real and imaginary parts of the ratio of normalized pressure on the flap to angular velocity of the flap for rotational excitation as a function of normalized distance from the hinge. The data plotted in these panels resulted from the same computations that gave rise to the streamlines in Figures 8.3-8.5 and 8.8-8.10, i.e. F=5, R=20, and S=30. Each independent computation generates 5 data points -- in both panels a and b or both panels c and d -- that are connected with a line. The common logarithm of ω/ω_L for each set of 5 points is written near the data points. Notice that the scales for pressure in each panel are different.

8.3.2.1 COMPARISON OF NUMERICALLY DETERMINED PRESSURE WITH THE LOW FREQUENCY ASYMPTOTIC ANALYSIS

The low frequency P-component of hydrodynamic pressure on the flap that results from the series expansion of the equations of motion (Equation (7.72)) has equal real and imaginary parts, and has a magnitude that increases with the square root of frequency. Writing that expression in terms of normalized variables (Equations (7.27)-(7.34),

$$\lim_{\omega \to 0} \frac{LP_P(\bar{x},\omega)}{\mu U_b} = \frac{1}{2}(1+j)\left(\frac{\omega}{\omega_L}\right)^{1/2} \frac{P_D(\bar{x}/L)}{\mu} \tag{8.73}$$

The real and imaginary parts of the numerically determined pressure at low frequencies (Figures 8.12 a and b) are nearly equal and increasing the frequency by a factor of 100 (from $\omega/\omega_L=10^{-4}$ to 10^{-2}) increases the pressure by about a factor of 10. We compare the numerically determined pressure for $\omega/\omega_L=10^{-4}$ with the analytic solution in Figure 8.13.

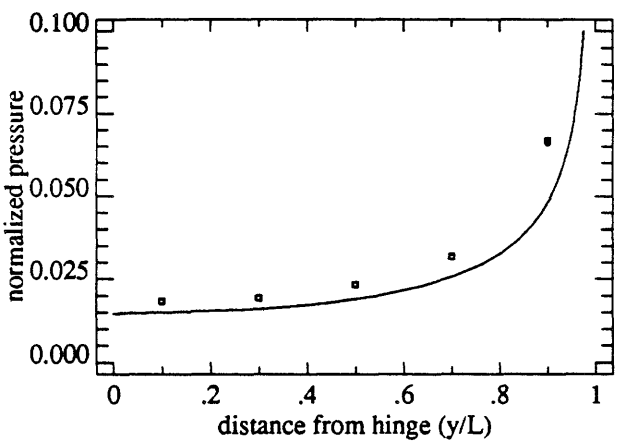

Figure 8.13: Comparison of the numerically-determined pressure on the flap with the low-frequency asymptotic solution of section 7.2. Squares and circles mark the real and imaginary parts of $LP_P(\bar{x},\omega)/\mu U_b$ (from Figures 8.12a and 8.12b) for $\omega/\omega_L=10^{-4}$. In each case, the squares fall directly on top of the circles. The solid line shows $P_D(y/L)/\mu/200$, as evaluated from Dean's solution of the steady equations of motion (see Equation (8.73) and Figure 7.5).

The numerically-determined pressure on the flap and the series solution for the pressure are nearly equal -- even though the methods for determining these two pressures are quite different, and the approximations inherent in the methods are quite different.

8.3.2.2 COMPARISON OF NUMERICALLY DETERMINED PRESSURE WITH THE HIGH FREQUENCY ASYMPTOTIC ANALYSIS

In section 7.3, the equations of motion for the hinged-flap structure where solved analytically for high frequencies of excitation. Substitute the asymptotic expression for velocity potential for translational excitation (Equation (7.96)) into the equation for pressure (Equation (6.16)) and express the result in normalized variables (Equations (7.27)-(7.34)).

$$\lim_{\omega \to \infty} \frac{P_P(y/L)}{U_b} = -j \frac{\omega}{\omega_L} \frac{2\mu}{L} \sin(\cos^{-1}(y/L)) \tag{8.74}$$

Similarly, substitute the asymptotic expression for velocity potential for rotational excitation (Equation (7.88)) into the equation for pressure (Equation (6.16)) and express the result in normalized variables (Equations (7.27)-(7.34)).

$$\lim_{\omega\to\infty} \frac{P_R(y/L)}{j\omega\Theta(\omega)} = -j\,\frac{\omega}{\omega_L}\,\mu \sum_{\substack{k=1 \\ k\ \text{odd}}}^{\infty} (-1)^{(k-1)/2}\,\frac{8}{\pi k(k^2-4)}\,\sin(k\cos^{-1}(y/L)) \qquad (8.75)$$

The ratio of imaginary to real parts of pressure in Figure 8.12 exceeds 500 for $\omega/\omega_L=10^4$, and is thus in good keeping with the purely imaginary-valued analytical solutions in Equations (8.74) and (8.75). The imaginary parts of $P_{f,s}$ are compared to the imaginary parts of Equations (8.74) and (8.75) in Figure 8.13. The general trend of the asymptotic solutions is followed by the numerically computed pressures. There is a consistent bias however. The discrete pressures systematically exceed the asymptotic pressures by between 10% and 25%.

a) translational excitation

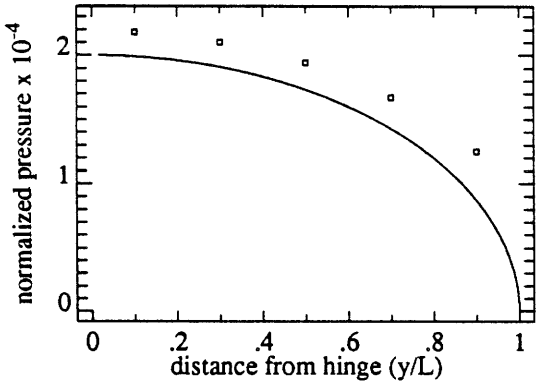

b) rotational excitation

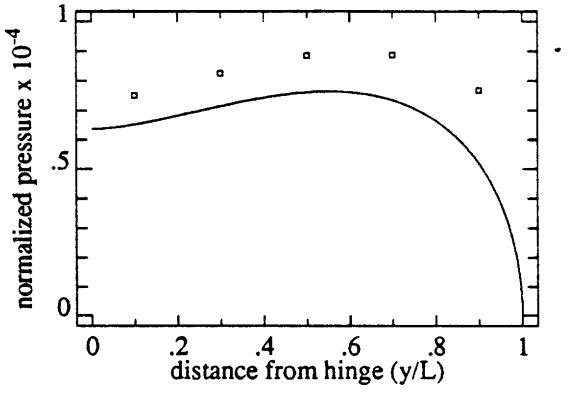

Figure 8.13: Comparison between the numerical and asymptotic pressures on the flap. The solid curve in panel a shows the imaginary part of the normalized ratio of pressure to plate velocity $(LP(\bar{x},\omega/\omega_L)/\mu U_b)$ in Equation (8.74) and the solid curve in panel b shows the imaginary part of normalized ratio of pressure to angular velocity of the flap $(P(\bar{x},\omega)/\mu j\omega\Theta(\omega))$ in Equation (8.75) for $\omega/\omega_L=10^4$. The data points (squares) in panel a show the imaginary parts of $P_{f,s}$ for translational excitation (Figure 8.12b). The data points in panel b show the imaginary parts of $P_{f,s}$ for rotational excitation (Figure 8.12d). In each panel, the normalized ratios are plotted against normalized distance from the hinge along the flap (y/L).

8.3.3 HYDRODYNAMIC TORQUE ON THE FLAP

Computation of the torque on the flap (Equation (8.29)) determines the hydrodynamic impedances in Equations (7.45) and (7.46) (Figure 8.14). The hydrodynamical impedance to rotation of the flap , $Z_{Rz}(\omega)$, approaches a constant at low frequencies and becomes increasingly inertial at high frequencies. The angle of that impedance is 45^{o} at a frequency for which the boundary layer thickness is about half the height of the flap. Thus, the frequency dependence of this rotational impedance is similar to that of the translational impedances on bodies of regular geometry (Figure 2.2).

The ratio of hydrodynamical torque on the flap per unit length to plate velocity, $H_{Bz}(\omega)$, is increasingly inertial at high frequencies. At low frequencies however, the magnitude of $H_{Bz}(\omega)$ increases with the square root of frequency, and the angle of $H_{Bz}(\omega)$ approaches 45^{o}. At low frequencies, the flap is engulfed in the boundary layer of fluid near the plate (Figure 8.3), and torque is exerted on the flap because of shearing motion of the fluid in the boundary layer. The gradient of fluid velocity near the rigid surface in a boundary layer increases with $(j\omega)^{1/2}$ and so the torque also increases with $(j\omega)^{1/2}$.

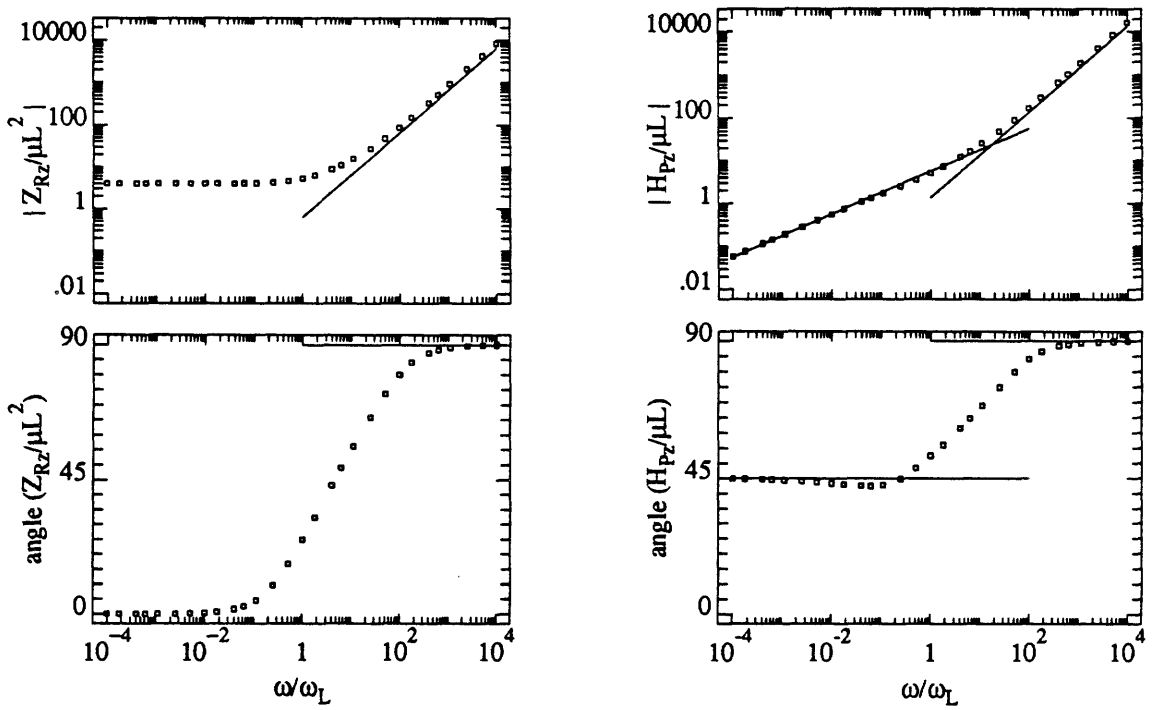

Figure 8.14: Hydrodynamic impedances of Figure 7.2. The left panel of this figure shows the magnitude and angle of the normalized impedance to rotation of the hinged flap, $Z_{Rz}/\mu L^2$, as a function of normalized frequency (ω/ω_L). The right panel shows the magnitude and angle of the normalized ratio of torque generated on a unit length of the flap by translational excitation to plate velocity, $H_{Pz}/\mu L$, as a function of normalized frequency. The symbols show values of the normalized torque T_{zd} computed from Equation (8.29). The high frequency asymptotes are computed from the high frequency analytic analysis (Equation (7.93) for the left panel and Equation (7.101) for the right). The low frequency asymptote in the right panel is computed from the low frequency analytic analysis (Equation (7.68)).

8.3.4 FREQUENCY RESPONSE OF HINGED FLAP

Translation of the plate of the hinged-flap structure (Figure 7.1) induces motion in the fluid, which generates a torque on the flap, and causes the flap to rotate. The ratio of angular displacement of the flap to plate velocity, $\Theta(\omega)/U_b$, can be computed from the impedances illustrated in Figure 8.14 (Equation (7.26)). For a particular set of physical parameters (μ, ρ, L, and K_z), the transfer ratio $\Theta(\omega)/U_b$ depends on frequency (Figure 8.15).

At low frequencies, the magnitude of $\Theta(\omega)/U_b$ increases with the square root of frequency and the angle approaches 45^o, which can be understood as follows. The low frequency impedance of the lumped parameter model for motion (Figure 7.2) is dominated by that of the spring, so that, at low frequencies, the angular displacement of the flap is proportional to the hydrodynamic torque exerted on the flap. The ratio of hydrodynamic torque exerted per unit length of the flap to plate velocity ($H_{P_z}(\omega)$) increases with $(j\omega)^{1/2}$, and so the ratio of $\Theta(\omega)/U_b$ increases with $(j\omega)^{1/2}$.

At high frequencies, the magnitude of $\Theta(\omega)/U_b$ decreases linearly with increasing frequency and the angle approaches -90^o. At high frequencies, the inertial forces of fluid origin dominate the viscous forces of fluid origin and the forces due to the torsional spring in the hinge. The resulting velocities are everywhere in phase, and specifically, the ratio of angular velocity of the flap to velocity of the plate approaches a constant.

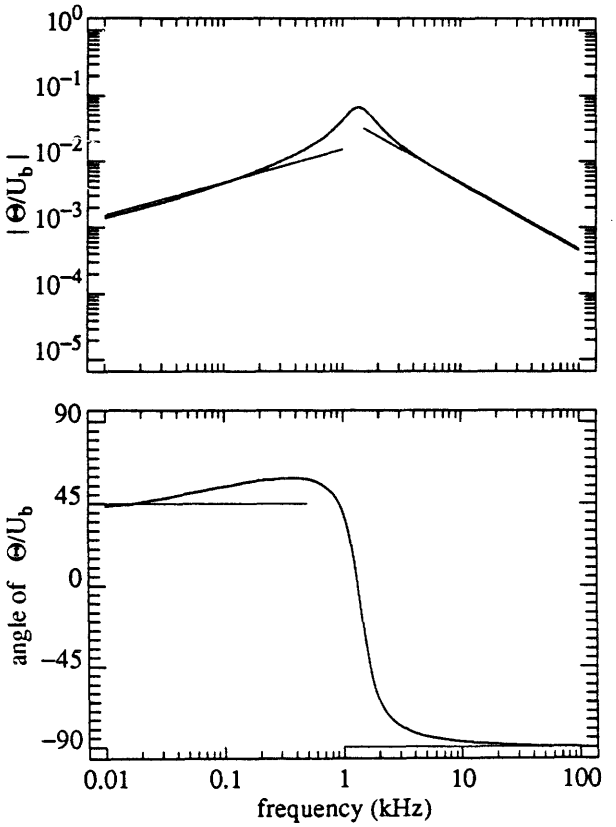

Figure 8.15: Frequency selectivity of the spring-loaded flap. The magnitude and angle of $\Theta(\omega)/U_b$ for a particular set of physical parameters (μ, ρ, L, and K_z) are shown in the top and bottom panels of this figure as a function of frequency. The fluid material properties were chosen to be similar to those of water (μ=0.01 gm/cm-sec and ν=0.01 cm^2/sec), K_z=0.1 dynes/rad, and L=70 μm. The curved line plots the results of the numerical analysis (Equation (7.26) with the impedances taken from Figure 8.14). The straight lines are computed from the asymptotic analysis (Equation (7.69) for the low frequency asymptote and Equation (7.102) for the high frequency asymptote).

The left panels of Figure 8.16 show the effect of varying L by plotting a family of frequency responses -- each for the same value of K_z but for different values of L. Notice that increasing L while holding K_z constant decreases the frequency at which the peak magnitude occurs. Increasing L while holding K_z constant also increases the peak magnitude. The right panels of Figure 8.16 show the effect of varying K_z by plotting a family of frequency responses -- each for the same value of L but for different values of K_z. Notice that increasing K_z while holding L constant increases the frequency at which the peak magnitude occurs and decreases the magnitude of the peak. Increasing K_z while holding L constant also increases the sharpness of tuning.

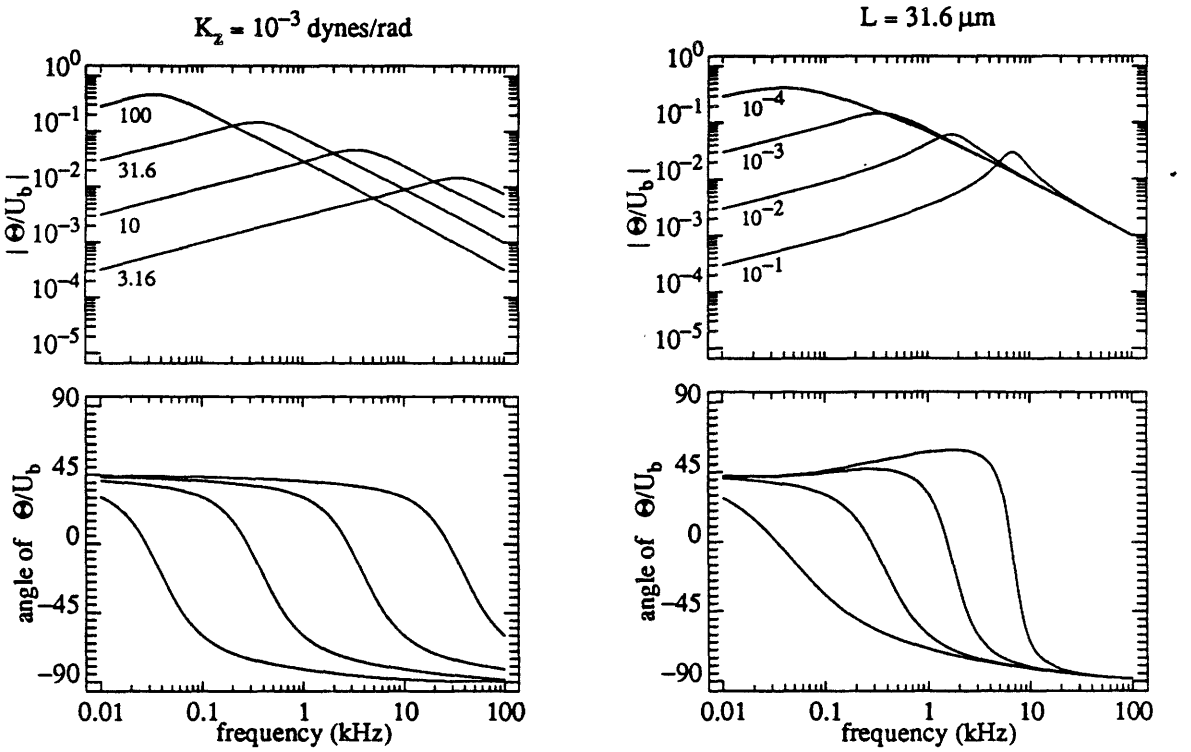

Figure 8.16: The effect of K_z and L on the frequency selectivity of the spring-loaded flap. The magnitude and angle of Θ/U_b are calculated from Equation (7.26) and the data in Figure 8.14 and shown here as a function of excitation frequency (f). The fluid material properties are chosen to be similar to those of water (μ=0.01 gm/cm-sec and ν=0.01 cm^2/sec). Each curve in the left panels results for a different value of L (indicated in μm near each curve) for fixed $K_z=10^{-3}$ dynes/rad. Each curve in the right panels results for a different value of K_z (indicated in dynes/rad near each curve) for fixed L=31.6μm. The phase is near -22^o when the magnitude is maximum.

Two parameters have been extracted from frequency responses such as those in Figure 8.16 in order to characterize the dependence of frequency selectivity on K_z and L. ω_{max} is taken as the frequency at which the magnitude of $\Theta(\omega)/U_b$ is largest. Q_{3dB} (a measure of sharpness of tuning) is taken as the ratio of ω_{max} to the bandwidth of $|\Theta(\omega)/U_b|$ measured 3 dB below its peak value. Write $\Theta(\omega)/U_b$ (Equation (7.26)) in terms of the normalized impedances of Equations (7.45) and (7.46),

$$\frac{\Theta(\omega)}{U_b} = \frac{\mu L H_{Pzn}(\omega/\omega_L)}{K_z + j\omega\mu L^2 Z_{Rzn}(\omega/\omega_L)} = L \frac{\mu H_{Pzn}(\omega/\omega_L)}{K_z + j(\omega/\omega_L)2\nu\mu Z_{Rzn}(\omega/\omega_L)} \tag{8.76}$$

where H_{Pzn} and Z_{Rzn} depend only on the value of ω/ω_L. Since Q_{3dB} is a ratio of frequencies, Q_{3dB} is insensitive to frequency scaling. Q_{3dB} is also insensitive to the multiplying factor L outside the square brackets in Equation (8.76). Therefore Equation (8.76) shows that Q_{3dB} is independent of L. From its definition, ω_{max} is independent of the multiplying factor L outside the square brackets in Equation (8.76). Equation (8.76) shows therefore that ω/ω_{max} is independent of L. Thus both Q_{3dB} and ω/ω_{max} depend only on K_z and the material properties of the fluid. Figure 8.17 plots Q_{3dB} and ω/ω_{max} as a function of K_z for fluid material properties equal to those of water.

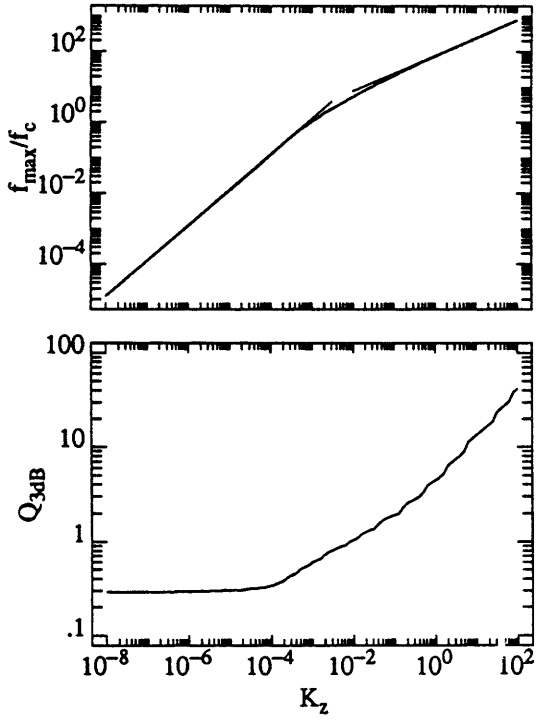

Figure 8.17: Dependence of Q_{3dB} and ω_{max} on K_z and L. Q_{3dB} and ω_{max} are computed from frequency responses $\Theta(\omega)/U_b$ such as those in Figure 8.16 and shown here as a function of K_z. The material properties of the fluid are taken equal to those of water (μ=0.01 gm/cm-sec and ν=0.01 cm^2/sec). Q_{3dB} is independent of L so that the bottom panel illustrates Q_{3dB} for all values of both K_z and L. ω_{max} has been normalized by ω_L ($= 2\nu/L^2$) in the upper panel so that the single curve describes the value of ω_{max} that results for all possible values of K_z and L. The thin straight line passing through low values of K_z has a slope of 1, and the thin straight line passing through high values of K_z has a slope of 1/2.

A flap of arbitrary height, L, can be made to exhibit a peak response ($\Theta(\omega)/U_b$) at any particular frequency ω_0, by adjusting the stiffness of the spring, K_z, appropriately. Generally, larger values of L give rise to more sharply tuned frequency responses (Figures 8.18 and 8.19).

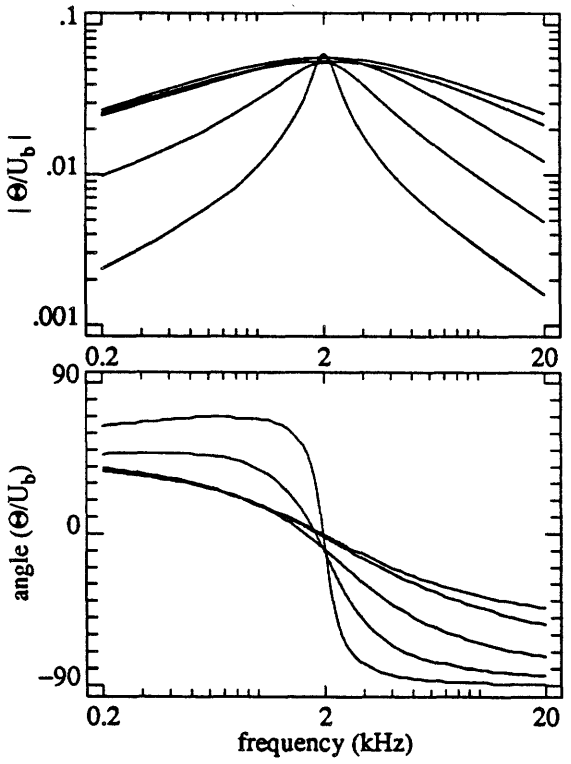

Figure 8.18: Frequency selectivity of the spring-loaded flap. The magnitude and angle of the angular displacement of the flap, $\Theta(\omega)$, that results per unit of plate velocity, U_b, are calculated from Equation 8.76 for the data displayed in Figure 8.14 and shown in this figure as a function of excitation frequency ($f=\omega/2\pi$). The fluid material properties were chosen to be similar to those of water (μ=0.01 gm/cm-sec and ν=0.01 cm^2/sec). The different curves are for different values of the flap dimension L -- 1, 3.16, 10, 31.6, and 100 μm -- with the smaller values corresponding to the more broadly tuned frequency responses. For each value of L, the spring constant K_z was adjusted so that the response magnitudes peaked at 2kHz. The resulting spring constants were (in order of increasing L) -- 5.3×10^{-6}, 5.4×10^{-5}, 5.3×10^{-4}, 1.3×10^{-2}, and 7.2×10^{-1} dynes/rad.

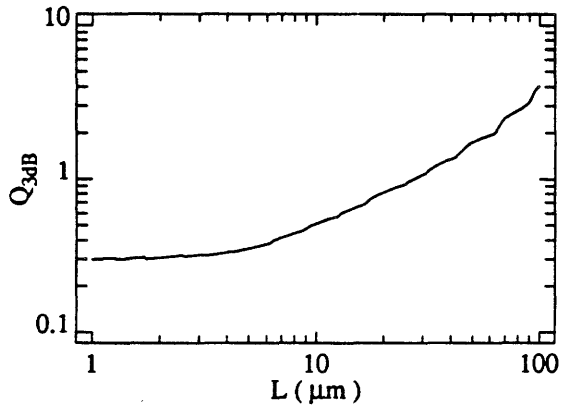

Figure 8.19: Quality of tuning as a function L. Q_{3dB} (defined as the ratio of the frequency at which | Θ/U_b | is maximum to the bandwidth 3 dB below the maximum) is computed for each of the responses in Figure 8.18 and shown here as a function of the flap dimension L -- along with intermediate values computed in exactly the same fashion.

8.4 CONCLUSIONS

In this chapter, we have used a numerical technique to solve the equations of motion for the hinged-flap structure (Figure 7.1). By exploiting: superposition, in order to separately characterize the P- and R-components of the solution to the equations of motion (section 7.1.2); the fact that the hinged-flap geometry is completely characterized by a single parameter L, its height (section 7.1.4); and the essential two-dimensionallity of the structure (section 7.1.5); we were able to characterize the solutions for all possible values of the 6 physically meaningful parameters (μ, ρ, K, L, U_b, and ω) by computing numerical solutions as a function of a single non-dimensional parameter ω/ω_L.

We computed normalized solutions to the P- and R-component equations of motion and illustrated the fluid motion, the hydrodynamic pressure on the flap, and the torque exerted on the flap for each of the computations. We compared the numerically determined fluid motion at low and high frequencies with the motion that was determined by asymptotic methods of sections 7.2 and 7.3. We compared the numerically determined hydrodynamic pressures on the flap at low and high frequencies with those that were determined by asymptotic methods. We compared the numerically determined torques on the flap at low and high frequencies with those that were determined by asymptotic methods. In each case, the numerical and asymptotic solutions were very similar, even though the approximations that underlie these methods are very different. The good match between the numerical and asymptotic results suggests the adequacy of the numerical approximations (the resolution of the spatial grid, the spatial extent of the computational domain, the order of the finite difference scheme), the low frequency asymptotic approximations (the use of a truncated series representation), and the high frequency asymptotic approximations (setting the viscosity of the fluid to zero).

We computed the hydrodynamic impedances, $H_{Pz}(\omega)$ and $Z_{Rz}(\omega)$ that characterize the lumped parameter representation for the motion of the hinged-flap structure (Figure 7.2). We found that the hydrodynamic impedance to rotation of the flap, $Z_{Rz}(\omega)$: approaches a constant resistance at low frequencies, approaches a constant moment of inertia at high frequencies, and has an angle of 45^o at a frequency for which the boundary layer thickness is equal to roughly half the height of the flap. We found that the transfer impedance $H_{Pz}(\omega)$: becomes increasingly inertial as frequency increases, and is proportional to $(j\omega)^{1/2}$ at low frequencies.

We computed the ratio of angular displacement of the flap to plate velocity $(\Theta(\omega)/U_b)$ as a function of frequency and found that it: is proportional to $(j\omega)^{1/2}$ at low frequencies, is proportional to $(j\omega)^{-1}$ at high frequencies, and exhibits a resonance at mid frequencies. We characterized the quality of tuning by ω_{max}, the frequency at which the magnitude of $\Theta(\omega)/U_b$ is greatest and Q_{3dB}, the ratio of ω_{max} to the bandwidth measured 3 dB below the peak magnitude. We computed expressions for bot ı ω_{max} and Q_{3dB} in terms of the physical parameters of the hinged-flap structure.

CHAPTER 9
RESULTS AND CONCLUSIONS

In order to better understand the hydrodynamics of stereociliary tuft motion, we have studied the motions of several canonical micromechanical models (chapter 3). In this chapter, we summarize the results of our analyses and indicate several ways that those results contribute to understanding the motion of stereociliary tufts.

9.1 SUMMARY OF RESULTS

9.1.1 FLUID COMPRESSIBILITY IS NEGLIGIBLE, AND NONLINEAR HYDRODYNAMIC FORCES ARE SMALL.

We assume that cochlear fluids have a uniform density and a viscosity that is both uniform and independent of direction. By considering the velocities of cochlear structures that accompany physiological stimulation, we conclude that fluid compressibility is negligible and that nonlinear forces of fluid origin are negligible except perhaps at very high levels of physiological stimulation.

9.1.2 BOTH VISCOUS AND INERTIAL FORCES OF FLUID ORIGIN RESIST THE MOTIONS OF BODIES THAT ARE SURROUNDED BY FLUID.

The motion of a body that is immersed in fluid is necessarily accompanied by motion of the fluid. Fluid near the body is entrained by viscous forces to move with the body, while fluid that is more distant from the body is pushed out of the path of the body and entrained fluid. The thickness of the boundary layer of fluid (δ) that is entrained to move with the body depends on the material properties of the fluid and on frequency at which the body is vibrated (Figure 9.1).

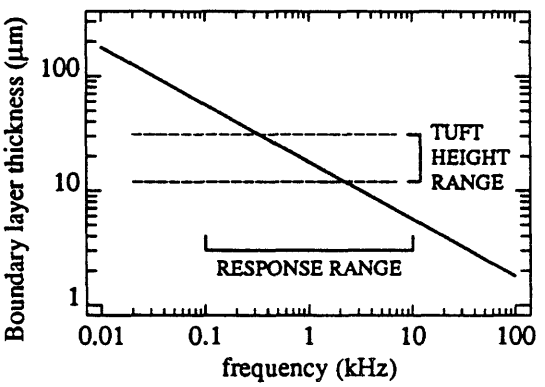

Figure 9.1: Boundary layer thickness (δ) in water as a function of frequency (f). $\delta=\sqrt{\nu/\pi f}$, where ν is the kinematic viscosity of the fluid (taken here to be 0.01 cm^2/sec).

The motion of a body that is immersed in fluid is resisted by a hydrodynamic force with an inertial component that is proportional to the mass of fluid that is set into motion and a viscous component that results from shear that is generated in the surrounding fluid. The forces of fluid origin that act on a vibrating body can be characterized quantitatively by an impedance.

The impedance of the fluid load on each of three different bodies with regular geometries -- a flat plate of infinite dimension, a cylinder of infinite length, and a sphere -- that are isolated in fluid with infinite extent (Figure 9.2) were computed from known solutions to the equations of motion for a viscous fluid (chapter 2). The hydrodynamical impedance depends on the size and shape of the body, and on the frequency of excitation. For frequencies below the frequency for which the thickness of the boundary layer is equal to the radius of the body, the impedances of the cylinder and sphere are predominately resistive. For frequencies above the frequency for which the thickness of the boundary layer is equal to the radius of the body, the impedance is predominately inertial. The resistive and inertial components of the impedance on the plate are equal at all frequencies.

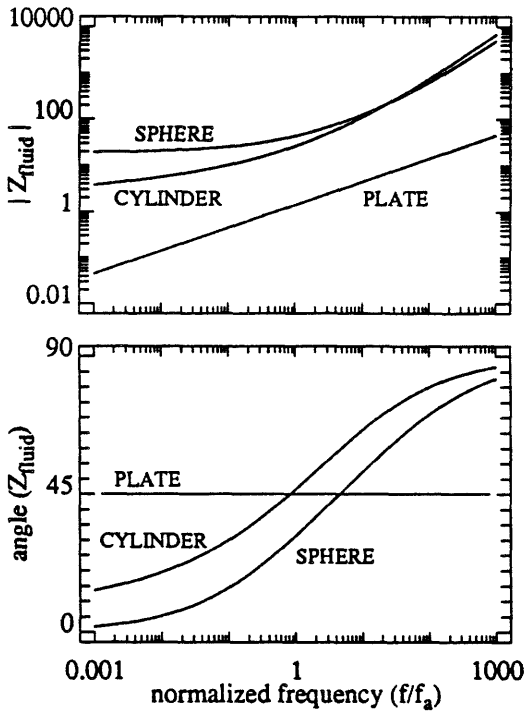

Figure 9.2: Normalized impedance of the fluid load. This figure shows the magnitude and angle of the normalized hydrodynamic impedance to: translation of a flat PLATE in its plane; translation of an infinitely long CYLINDER in a direction that is perpendicular to its axis; and translation of a SPHERE. Frequency (f) is normalized by dividing by the frequency (f_a) for which the boundary layer thickness is equal to the radius (a) of the cylinder or sphere, $f_a=\nu/\pi a^2$. For the plate, the frequency normalization is arbitrary. See the caption of Figure 2.2 for more detailed description of these curves.

9.1.3 THE IMPEDANCE OF THE FLUID LOAD CAN CONTRIBUTE TO A MECHANICAL RESONANCE

The effect of the surrounding fluid on the motion of a mechanical system can be characterized by including the fluid impedance described above in a lumped parameter model of motion, as illustrated in Figure 9.3.

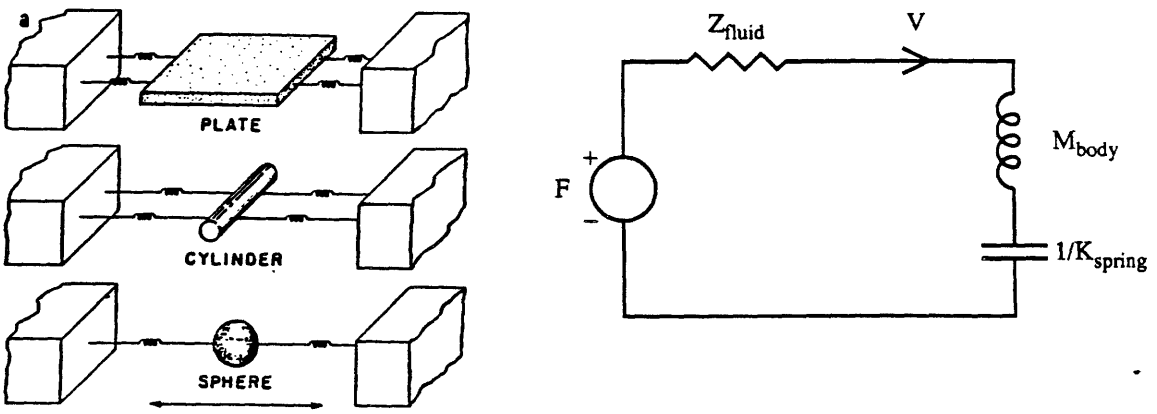

Figure 9.3: Modeling the effect of surrounding fluid on the motion of a mechanical system. The left panel illustrates three different mechanical systems, in which bodies of regular geometry -- a flat plate, a circular cylinder, and a sphere -- are connected by springs to rigid supports. Motion of these bodies in the direction of the arrow is resisted by fluid that surrounds the bodies. The right panel illustrates a lumped parameter model for the motion of each of the bodies on the left. F represents the complex amplitude of the sinusoidally varying external force applied to the body. Z_{fluid} represents the impedance to motion that results from the surrounding fluid (section 9.1.2). K_{spring} represents the stiffness of the spring attachments. M_{body} represents the mass of the body. V represents the complex amplitude of the velocity of the body.

In the absence of fluid, each of the systems illustrated in Figure 9.3 will resonate. Since the impedance of the fluid has both inertial and resistive components, immersing the bodies in fluid tends to both damp the resonance and decrease the frequency of the resonance. The magnitudes of these two effects depends on the magnitudes of the inertial and resistive components of the fluid impedance. Since the fluid impedance depends on both the shape and size of the body, the effect of surrounding fluid on the resonance of mechanical structures depends on the shape and size of the body.

9.1.4 THE HYDRODYNAMIC IMPEDANCE TO ROTATION OF A FLAP THAT IS ATTACHED TO A PLATE IS SIMILAR IN FORM TO Z_{fluid} FOR ISOLATED BODIES

The preceding results characterize the motions of bodies that are isolated in fluid of infinite extent. Stereociliary tufts are not isolated bodies however, but protrude from a receptor surface that is large relative to the dimensions of tufts. The effect of fluid on the rotation of a rectangular flap of infinite length that is attached by a hinge to an infinite plate can be represented by the equivalent network that is illustrated in Figure 9.4 and has a form that is similar to the model in Figure 9.3 (chapter 7).

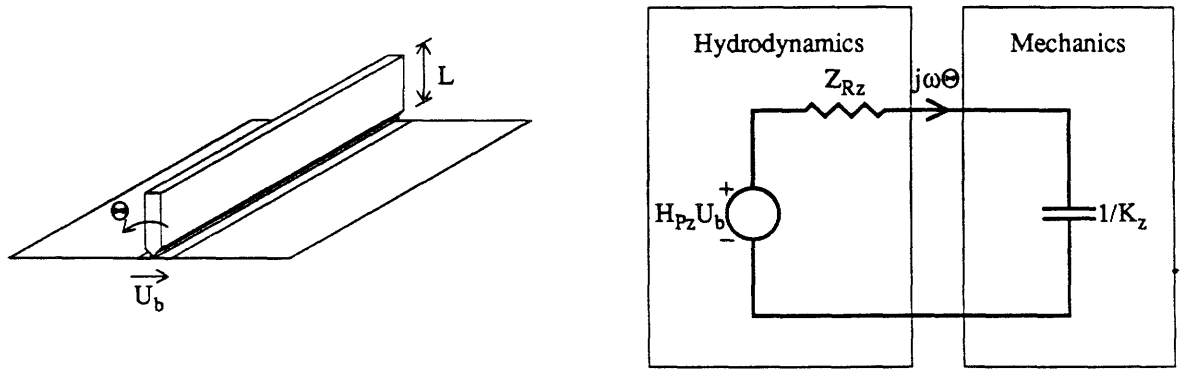

Figure 9.4: Modeling the effect of surrounding fluid on the rotation of a rectangular flap that is attached to an infinite plate by a spring-loaded hinge. The left panel illustrates a section of an infinitely long rectangular flap that is attached to an infinite plate by a hinge of infinite length. The flap extends a distance L into the fluid, has negligible thickness, and has no mass. The right panel illustrates a model for the motion of the structure in the left panel. Motion of the structure is excited by the velocity imposed on the plate (with complex amplitude U_b). The complex amplitude of the angular displacement of the body, Θ, characterizes the output of the model. K_z represents the stiffness of the torsional spring in the hinge per unit of length of the hinge. Z_{Rz} represents the impedance to rotation of the flap that that is exerted by the fluid. H_{Pz} represents the component of torque that is exerted on the flap by translation of the plate.

Despite the presence of the nearby plate, the impedance to rotation of the flap (Z_{Rz}) that results from the surrounding fluid (Figure 9.5) has many properties that are similar to the hydrodynamic impedances on isolated bodies (Figure 9.2). For frequencies below the frequency for which the boundary layer thickness is equal to the height of the flap, Z_{Rz} is predominately resistive. For frequencies above the frequency for which the boundary layer thickness is equal to the height of the flap, Z_{Rz} is predominately inertial.

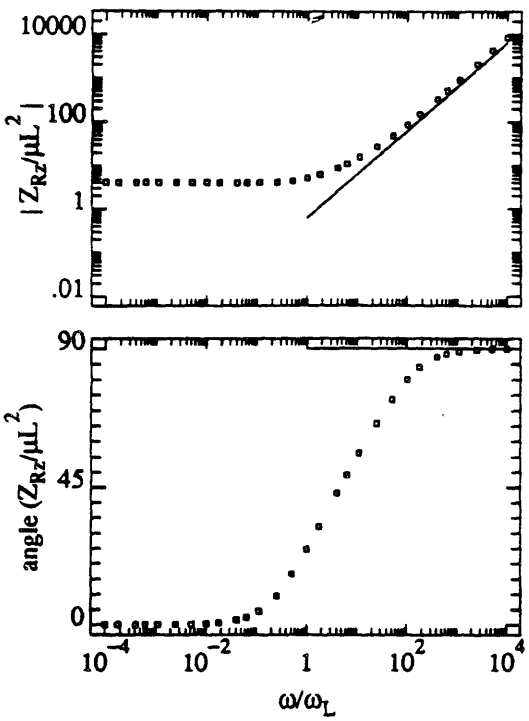

Figure 9.5: Hydrodynamic impedance to rotation of the rectangular flap. The top and bottom panels of this figure illustrate the magnitude and angle of $Z_{Rz}/\mu L^2$ (Figure 9.4) as a function of normalized frequency ω/ω_L, where ω_L is the frequency at which the boundary layer thickness is equal to the height of the flap L ($\omega_L = 2\nu/L^2$). The symbols show the results of the numerical study in chapter 8. The thin straight lines show the high frequency asymptote that was calculated in section 7.3.

9.1.5 THE HYDRODYNAMIC COUPLING BETWEEN TRANSLATION OF THE PLATE AND ROTATION OF THE FLAP IS FREQUENCY DEPENDENT

Motion of the free-standing flap structure is excited by translation of the plate. The source term in the equivalent model (Figure 9.4) shows that this excitation can be represented by a torque that is proportional to U_b, the velocity of the plate. The magnitude of the torque that is exerted on the rigid flap per unit of velocity of the plate, H_{Pz}, depends on frequency (Figure 9.6).

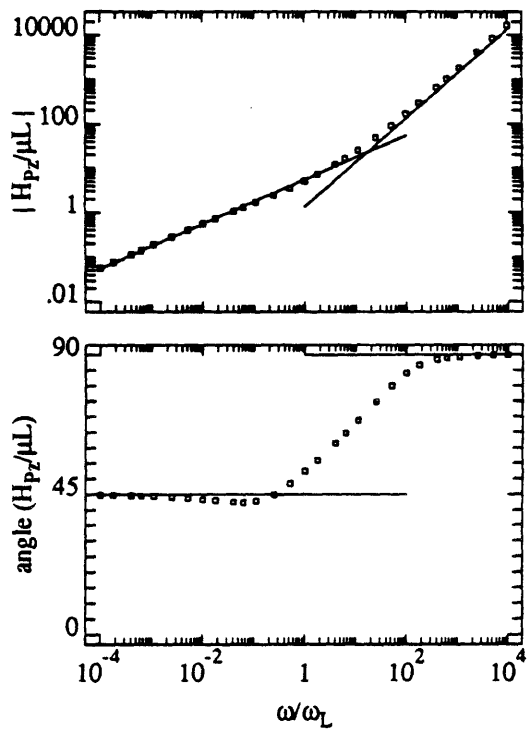

Figure 9.6: Hydrodynamic coupling between translation of the plate and rotation of the flap. The top and bottom panels of this figure illustrate the magnitude and angle of $H_{Pz}/\mu L$ (Figure 9.4) as a function of normalized frequency ω/ω_L, where ω_L is the frequency at which the thickness of the boundary layer is equal to the height of the flap L ($\omega_L = 2\nu/L^2$). The symbols show the results of the numerical study in chapter 8. The thin straight lines show the values computed in the asymptotic studies in sections 7.2 and 7.3.

9.1.6 MOTION OF THE FLAP IS FREQUENCY SELECTIVE EVEN THOUGH THE MASS OF THE FLAP IS ZERO

The ratio of angular displacement of the flap to plate velocity depends on frequency and exhibits a resonance (Figure 9.7). Since the mass of the flap is zero, the resonance results from interaction between the stiffness of the spring in the hinge and the mass of the fluid. The frequency of the maximum response and the sharpness of tuning depend on the material properties of the fluid, on the height of the flap, and on the stiffness of the spring.

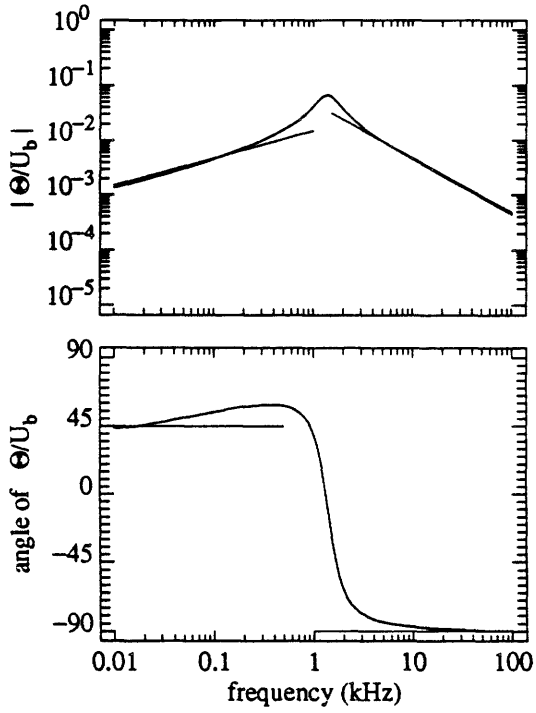

Figure 9.7: Frequency selectivity of the spring-loaded flap. The top and bottom panels of this figure show the magnitude and angle of Θ/U_b as a function of frequency. The material properties of the fluid are similar to those of water (μ=0.01 gm/cm-sec and ν=0.01 cm^2/sec). K_z=0.1 dynes/rad, and L=70 μm. The curved lines show the results from the numerical study in chapter 8. The straight lines show the results of the asymptotic studies of sections 7.2 and 7.3.

9.1.7 RESPONSES OF LARGER BODIES CAN BE MORE SHARPLY TUNED

A flap of arbitrary height can be made to exhibit a peak response (Θ/U_b) at any particular frequency, f_0, by adjusting the stiffness of the spring appropriately. Similarly, a sphere or cylinder of arbitrary radius can be made to exhibit a peak response (V/F) at a particular frequency f_0 by adjusting the stiffness of its attachment appropriately. Generally however, more sharply tuned frequency responses result for larger bodies (Figure 9.8).

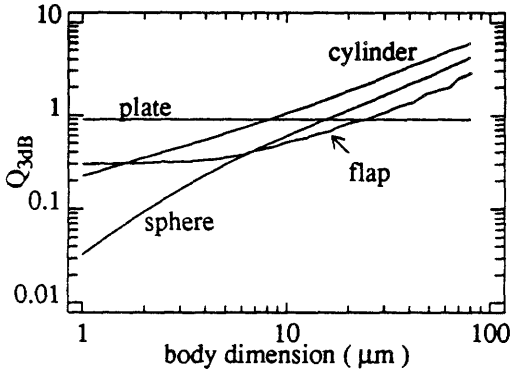

Figure 9.8: Quality of tuning as a function of body dimension. The stiffnesses of the springs in Figures 9.3 were adjusted so that the maximum magnitude of the admittance (V/F) occurs at a frequency of 2 kHz. The stiffness of the torsional spring in Figure 9.4 was adjusted so that the maximum of $|\Theta/U_b|$ occurs at 2 kHz. The resulting frequency selective reponses differed in sharpness of tuning and were characterized by Q_{3dB}, the ratio of the frequency of maximal response divided by the bandwidth 3 dB below the maximum. Q_{3dB} for the cylinder and sphere are plotted versus the radius of the body. Q_{3dB} for the flap is plotted versus the height of the flap L. Q_{3dB} for the plate is a constant.

9.1.8 LOW FREQUENCY ANGULAR DISPLACEMENT OF A FREE-STANDING BODY IS PROPORTIONAL TO $(j\omega)^{1/2}$ TIMES THE VELOCITY OF THE PLATE

At low frequencies of excitation, the magnitude of the ratio of angular displacement of the flap to plate velocity increases with the square root of frequency and the angle of that ratio approaches 45^{o} (Figure 9.6). These relationships can be understood in terms of (1) the motion of fluid within viscous boundary layers and (2) the structure of the model in Figure 9.6 at low frequencies, as follows.

At low frequencies, the flap is completely engulfed by the boundary layer of fluid near the plate. The velocity of the fluid within the boundary layer, $\bar{V}_{\delta}(\bar{x},\omega)$, depends exponentially on distance from the plate (y).

$$\bar{V}_{\delta}(\bar{x},\omega) = U_b\, e^{-y\sqrt{j\omega/\nu}}\, \hat{x} \tag{9.1}$$

The velocity of fluid near the plate, relative to that of the plate is proportional to the derivative of Equation (9.1) with respect to y,

$$\frac{\partial \bar{V}_{\delta}(\bar{x},\omega)}{\partial y} = -\sqrt{j\omega/\nu}\; U_b\; e^{-y\sqrt{j\omega/\nu}}\; \hat{x} \tag{9.2}$$

and for small values of y, the exponential in Equation (9.2) is nearly equal to one.

$$\frac{\partial \bar{V}_{\delta}(\bar{x},\omega)}{\partial y} \approx -\sqrt{j\omega/\nu}\; U_b \hat{x} \tag{9.3}$$

Thus, at low frequencies, the difference between the fluid velocity and the velocity of the plate is proportional to $(j\omega)^{1/2}$ times the velocity of the plate.

Since the relative fluid motion near the plate increases with $(j\omega)^{1/2}$ at low frequencies, the torque that is generated on the flap by this relative motion, which is characterized by H_{Pz}, also increases with $(j\omega)^{1/2}$ at low frequencies (Figure 9.6). In fact, H_{Pz} is proportional to $(j\omega)^{1/2}$ for all frequencies for which the boundary layer thickness is greater than the height of the flap.

At low frequencies, the impedance of the fluid load approaches a constant (Figure 9.5). Therefore, the impedance of the network in Figure 9.4 is stiffness dominated at low frequencies and the angular displacement of the flap, Θ, is proportional to the driving torque $H_{Pz}U_b$. Since at low frequencies, H_{Pz} is proportional to $(j\omega)^{1/2}$, it therefore follows that the ratio of Θ/U_b is proportional to $(j\omega)^{1/2}$ at low frequencies.

The details of this argument do not depend on the shape of the body, and the low frequency ratio of angular displacment to plate velocity is proportional to $(j\omega)^{1/2}$ for a single, free-standing body of arbitrary shape (chapter 5).

9.1.9 THE LOW FREQUENCY ANGULAR DISPLACEMENT OF A BODY THAT IS SURMOUNTED BY, BUT NOT ATTACHED TO, A TECTORIAL PLATE IS PROPORTIONAL TO THE DIFFERENCE BETWEEN THE PLATE VELOCITIES.

If two parallel plates are translated in their planes at very low frequencies but with different velocities, the fluid velocity between the two plates varies linearly with distance between the two plates. In the presence of a tectorial plate, the low frequency fluid velocity gradient is in phase with the difference between the plate velocities and is independent of frequency. Thus, by reasoning similar to that in section 9.1.8, the low frequency angular displacement of an arbitrarily shaped body that is surmounted by a tectorial plate that is moving relative to the basal plate is proportional to the difference velocity. This result is true for all frequencies below the frequency for which the boundary layer thickness is equal to the distance between the plates.

If the distance between the plates is large relative to the size of the body, there is a range of frequencies for which the boundary layer thickness is small relative to the distance between the plates but large relative to the size of the body. For this range of frequencies, the body is again engulfed in a boundary layer of fluid near the basal plate, and the ratio of angular displacement of the body to basal plate velocity is proportional to $(j\omega)^{1/2}$.

9.1.10 THE HIGH FREQUENCY ASYMPTOTIC ANGULAR DISPLACEMENT OF A BODY IS PROPORTIONAL TO BASAL PLATE DISPLACEMENT

At high frequencies, the impedance of the network in Figure 9.4 is dominated by the hydrodynamic impedance to rotation of the flap (Figure 9.5), and is therefore inertial (proportional to $j\omega$). For high frequencies of excitation, the transfer impedance H_{Pz} is inertial (Figure 9.6). Therefore, the high frequency asymptotic angular velocity of the flap is proportional to the velocity of the basal plate. This relationship follows from the high frequency properties of the fluid and does not depend on the shape of the body (chapter 6). The high frequency asymptotic angular velocity of an arbitrarily shaped body is proportional to the velocity of the basal plate.

9.2 CONCLUSIONS

9.2.1 THE LOW FREQUENCY RESPONSE OF MICROMECHANICAL MODELS DEPENDS CRITICALLY ON THE DISTANCE TO THE NEAREST RIGID STRUCTURE

It has been suggested that contact between stereociliary tufts and an overlying tectorial membrane has functional significance (Dallos, Billone, Durrant, Wang, and Raynor, 1972). The response of model hair cells with stereocilia that project from a basal plate and come into contact with an overlying tectorial plate, is proportional to the difference between plate displacements at low frequencies, while the response of model hair cells with stereocilia that do not contact the tectorial plate is proportional to the difference between plate velocities at low frequencies (Billone and Raynor, 1973).

The angular displacement of a model of the free-standing stereociliary tufts in the auditory organ of alligator lizard is proportional to $(j\omega)^{1/2}$ times the velocity of the basal plate, i.e. neither proportional to displacement nor velocity (Weiss and Leong, 1985).

This study suggests that the distance from stereociliary tufts to the nearest rigid structure is the important geometric feature that distinquishes the low frequency behavior of free-standing models from that of models with unattached tectorial membranes. When the distance between two plates that are moving relative to each other is small compared to the boundary layer thickness, the angular displacement of model tufts is proportional to the difference between the plate velocities (similar to the results of Billone and Raynor, 1973). When that distance is large compared to the boundary layer thickness, however, the tectorial plate has little effect on the motion of the body, and the angular displacement of the body is proportional to $(j\omega)^{1/2}$ times the basal plate velocity (similar to the results of Weiss and Leong, 1985).

Table 9.1 summarizes these results, and suggests a quantitative definition of "low frequency". The range of frequencies for which the "unattached" result is valid is limited to those below the frequency at which the boundary layer thickness is equal to the inter-plate distance. The range of frequencies for which the "free-standing" result is valid is limited to those above the frequency at which the boundary layer thickness is equal to the distance to the nearest rigid surface (the walls of scala vestibuli for example).

Low frequency ratio of angular displacement to basal plate velocity				
type of model	asymptotic dependence	slope of magnitude	angle	frequency range
attached (U_t=0)	$\alpha(j\omega)^{-1}$	−20 dB/decade	−90°	
unattached (U_t=0)	$\alpha(j\omega)^{0}$	0 dB/decade	0°	$\omega<\omega_G=2\nu/G^2$
free-standing	$\alpha(j\omega)^{1/2}$	+10 dB/decade	+45°	$\omega>\omega_D=2\nu/D^2$

Table 9.1: Low frequency angular responses of three models of stereociliary tufts to vibration of their basal plates. The first row of this table indicates that the angular displacement of a model tuft that is in contact with an overlying tectorial plate must be proportional to the displacement of the basal plate (when the tectorial plate is stationary). The second row indicates results for the angular displacement of a model tuft that are surmounted by, but not in contact with an overlying (stationary) tectorial plate. The distance between the tectorial and basal plates is G. The third row indicates the response of models tufts that are not in proximity with any tectorial structures. The distance to the nearest rigid structure is taken as D.

9.2.2 BODIES AS SMALL AS STEREOCILIARY TUFTS CAN EXHIBIT PASSIVE MECHANICAL RESONANCE WHEN SURROUNDED BY FLUID

9.2.2.1 BACKGROUND

Studies of the alligator lizard cochlea have shown that free-standing stereociliary tufts show frequency selective mechanical responses to mechanical stimulation (Frishkopf and DeRosier, 1983; Holton and Hudspeth, 1983). One interpretation of these measurements is that a tuft acts as a purely mechanical resonator (Weiss and Leong, 1985). This is not however the only possible interpretation.

We have known for some time that hair cells produce electrical responses to mechanical stimulation. Recent investigations have shown that hair cells can also produce mechanical responses to electrical stimulation (Brownell, Bader, Bertrand, Ribaupierre, 1985; Crawford and Fettiplace, 1985). Since hair cells generate frequency selective electrical responses to electrical stimulation (Crawford and Fettiplace, 1985; Lewis and Hudspeth, 1983; Ashmore, 1983), it is possible that the mechanical frequency selectivity observed in tuft motion results from an electrical resonance mechanism (Weiss, 1982).

The sharpness of mechanical tuning is limited by the viscosity of the surrounding fluid. A number of authors have concluded that no significant passive mechanical resonance is possible in micromechanical systems (Billone and Raynor, 1973; Bialek and Schweitzer, 1985). At least one study indicates that significant mechanical resonance can occur (Weiss and Leong, 1985). Results of this thesis suggest that a passive mechanical resonance is possible and provides an explanation for the theoretical disagreement.

9.2.2.2 RELATIONSHIP BETWEEN TUFTS AND MODELS

The motion of an infinitely long cylinder that is immersed in a viscous fluid and attached by springs to rigid supports is frequency selective (chapter 2), and the sharpness of tuning increases with radius. Q_{3dB}, a measure of sharpness of tuning, is greater than 1 for radii that exceed 8 μm (Figure 9.8). Since the radii of a stereocilia are generally more than an order of magnitude smaller than this critical radius, it follows that isolated stereocilia are not likely to exhibit sharp mechanical resonances.

To the extent that an entire tuft of stereocilia moves as a single rigid body however, the important dimensions are those of tufts, and not those of individual stereocilia. In fact, tufts occur in clusters, and the mechanical resonances of isolated tufts might well differ from those of tufts that are surrounded by other tufts.

Consider the rotation of the hinged-flap as a model for the motion of one row of free-standing tufts in the auditory organ of the alligator lizard (Figure 9.9).

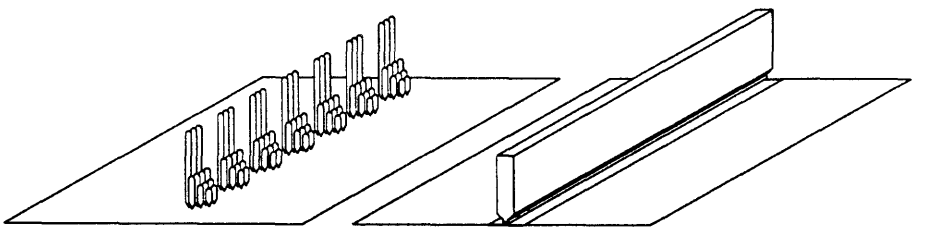

Figure 9.9: Relating the hinged-flap model to the free-standing stereociliary tufts of the auditory organ in the alligator lizard. Free-standing stereociliary tufts in alligator lizard are organized in rows along the long axis of the receptor organ (Figure 1.2). The left panel of this figure illustrates one such row of tufts. In the alligator lizard, the inter-tuft distance is roughly 10 μm, and the heights of the tallest stereocilia in a tuft vary from roughly 12 to 31 μm. The right panel illustrates the hinged-flap model.

9.2.2.3 TUFT COMPLIANCE

The analysis in chapter 8 shows that Q_{3dB} for the hinged-flap structure is determined completely by K_z, the torsional stiffness of the spring per unit length of the hinge (Figure 8.17). Q_{3dB} exceeds 1 for $K_z > 8\times10^{-3}$ dynes/rad. Since the distance between tufts is roughly 10 μm, $K_z=8\times10^{-3}$ dynes/rad would require a tuft stiffness on the order of 8×10^{-6} dyne-cm/rad. The static stiffnesses of tufts have been determined experimentally and range from roughly 10^{-8} to 10^{-5} dyne-cm/rad (Orman and Flock, 1981; Ashmore and Russell, 1983; Strelioff and Flock, 1984). To the extent that these static stiffnesses approximate the dynamical stiffnesses that determine tuft motion, it has been experimentally established that there exists sufficient mechanical stiffness for passive mechanical resonance.

9.2.2.4 PASSIVE MECHANICAL RESONANCE FREQUENCIES

Figure 8.17 specifies the frequency of maximum angular displacement of the flap as a function of K_z, the torsional stiffness of the spring per unit length, and L, the height of the flap. For $K_z=8\times10^{-3}$ dynes/rad (as above), the frequency of maximum response,

$$f_{max} \approx 4.6 \frac{\nu}{\pi L^2} \quad . \tag{9.4}$$

The tallest stereocilia in free-standing tufts of the auditory organ of alligator lizard range from roughly 12 to 31 μm (Mulroy, 1974). Best frequencies for cochlear neurons that project to the free-standing region range from roughly 0.9 to 4 kHz (Weiss, Mulroy, Turner, and Pike, 1976). For $12\ \mu m < L < 31\ \mu m$, f_{max} in Equation (9.4) varies from 1.5 to 10 kHz. The difference between the theoretical estimate of the range of best frequencies for passive mechanical resonance and the range of best frequencies that are experimentally observed is less than a factor of 2.5. Considering how little of the detail of tuft geometry is incorporated in this estimate of best frequency, we consider this result to strongly suggest the possibility of passive mechanical resonance in the motions of the free-standing tufts of alligator lizard.

REFERENCES

Ashmore, J.F. (1983): Frequency tuning in a frog vestibular organ. Nature 304, 536-538.

Ashmore, J.F. and Russell, I.J. (1983): Sensory and effector functions of vertebrate hair cells. J. Submicrosc. Cytol. 15, 163-166.

Batchelor, G.K. (1967): An Introduction to Fluid Dynamics. Cambridge Univ. Press, London.

Bialek, W. and Schweitzer, A. (1985): Quantum noise and the threshold of hearing. Phys. Rev. Letters 54, 725-728.

Billone, M. and Raynor, S. (1973): Transmission of radial shear forces to cochlear hair cells. J. Acous. Soc. Am. 54, 1143-1156.

Brownell, W.E., Bader, C.R., Bertrand D., Ribaupierre, Y. (1985): Evoked mechanical responses of isolated cochlear outer hair cells. Science 227, 194-196.

Crawford, A.C. and Fettiplace, R. (1985): The mechanical properties of ciliary bundles of turtle cochlear hair cells. J. Physiol. (London) 364, 359-379.

Dallos, P., Billone, M.C., Durrant, J.D., Wang, C.-y., and Raynor, S. (1972): Cochlear inner and outer hair cells: Functional differences. Science 177, 356-358.

Dallos, P. and Harris, D. (1978): Properties of auditory nerve responses in the absence of outer hair cells. J. Neuro. Physiol. 41, 365-383.

Davis, H. et.al. (1953): Acoustic trauma in the guinea pig. J. Acoust. Soc. Am. 25, 1180-1189.

Dean, W.R. (1936): Note on the slow motion of fluid. Proc. Camb. Phil. Soc. 32, 598-613.

DeRosier, D.J., Tilney, L.G. and Egelman, E. (1980): Actin in the inner ear: the remarkable structure of the stereocilium. Nature (London) 287, 291-296.

Flock, A. and Cheung, H.C. (1977): Actin filaments in sensory hairs of inner ear receptor cells. J. Cell Biol. 75, 339-343.

Flock, A., Cheung, H.C., Flock, B. and Utter, G. (1981): Three sets of actin filaments in sensory cells of the inner ear. Identification and functional orientation determined by gel electrophoresis, immunofluorescence and electron microscopy. J. Neurocytol. 10, 133-147.

Flock, A., Flock, B., and Murray, M.J. (1977): Studies on the sensory hairs of receptor cells in the inner ear. Acta Otolaryngol. 83, 85-91.

Flock, A. and Orman, S. (1983): Micromechanical properties of sensory hairs on receptor cells of the inner ear. Hearing Res. 11, 249-260.

Flock, A. and Strelioff, D. (1984): Graded and nonlinear mechanical properties of sensory hairs in the mammalian hearing organ. Nature (London) 310, 597-598.

Freeman, D.M. and Weiss, T.F. (1985): On the role of fluid inertia and viscosity in stereociliary tuft motion: analysis of isolated bodies of regular geometry. In: Lecture notes in biomathematics 64: peripheral auditory mechanisms. Springer-Verlag, Berlin.

Frishkopf, L.S. and DeRosier, D.J. (1983): Mechanical tuning of free-standing stereociliary bundles and frequency analysis in the alligator lizard cochlea. Hearing Res. 12, 393-404.

Harlow, F.H. and Welsh, J.E. (1965): Numerical calculation of time-dependent viscous incompressible flow of fluid with free surface. Phys. Fluids 8, 2182-2189.

Holton, T. and Hudspeth, A.J. (1983): A micromechanical contribution to cochlear tuning and tonotopic organization. Science 222, 508-510.

Holton, T. and Weiss, T.F. (1983a): Receptor potentials of lizard cochlear hair cells with free-standing stereocilia in response to tones. J. Physiol. (London) 345, 205-240.

Holton, T. and Weiss, T.F. (1983b): Frequency selectivity of hair cells and nerve fibres in the alligator lizard cochlea. J. Physiol. (London) 345, 241-260.

Hudspeth, A.J. and Jacobs, R. (1979): Stereocilia mediate transduction in vertebrate hair cells. Proc. Natl. Acad. Sci, 76, 1506-1509.

Jacobs, D.A.H. (1981): The exploitation of sparsity by iterative methods. In: Sparse matrices and their uses. Academic Press, London. Edited by Iain S. Duff.

Johnson, R.E. and Brokaw, C.J. (1979): Flagellar hydrodynamics: A comparison between resistive-force theory and slender-body theory. Biophys. J. 25, 113-127.

Johnstone, J.R. and Johnstone, B.M. (1966): Origin of Summating Potential. J. Acoust. Soc. Am. 40, 1405-1413.

Lim, D.J. (1971): Morphological relationship between the tectorial membrane and the organ of Corti -- scanning and transmission electron microscopy. J. Acoust. Soc. Am. 50, 92.

Lim D.J. (1980): Cochlear anatomy related to cochlear micromechanics. A review. J. Acoust. Soc. Am. 67, 1686-1695.

Lewis, R.S. and Hudspeth, A.J. (1983): Voltage- and ion-dependent conductances in solitary vertebrate hair cells. Nature, 304, 538-541.

Luenberger, D.G. (1965): Introduction to linear and nonlinear programming, Addison Wesley, Reading Ma.

Miyagi, T. (1958): Viscous flow at low Reynolds numbers past infinite row of equal circular cylinders. J. Phys. Soc. Jap. 13, 493-496.

Mulroy, M.J. (1974): Cochlear anatomy of the alligator lizard. Brain, Behavior, and Evolution 10, 69-87.

Orman, S. and Flock, A. (1981): Stiffness measurements of stereociliary bundles in frog crista ampularis. Soc. Neurosci. Abstr. 7, 536.

Peake, W.T. and Ling, A.L. (1980): Basilar-membrane motion in the alligator lizard: Its relation to tonotopic organization and frequency selectivity. J. Acoust. Soc. Am. 67, 1736-1745.

Rauch, S. and Rauch, I. (1974): Physico-chemical properties of the inner ear especially ionic transport, in Handbook of Sensory Physiology, Vol V/1: Auditory System, pp. 647-682. Editors: W.D. Keidel and W.D. Neff. Springer, New York.

Rhode, W.S. and Geisler, C.D. (1967): Model of the displacement between opposing points on the tectorial membrane and reticular lamina. J. Acoust. Soc. Am. 42, 185-190.

Rosowski, J.J., Peake, W.T., Lynch, T.J., III, Leong, R., and Weiss, T.F., (1985): A model for signal transmission in an ear having hair cells with free-standing stereocilia: II. Macromechanical stage. Hearing Res. 20, 139-155.

Saunders, J.C. and Garfinkle, T.J. (1985): Morphologic properties of inner hair cell stereocilia in the C57BL/6J mouse. (submitted for publication).

Shotwell, S.L., Jacobs, R., and Hudspeth, A.J. (1981): Directional sensitivity of individual vertebrate hair cells to controlled deflection of their hair bundles. Ann. N.Y. Acad. Sci. 374, 1-10.

Stokes, G.G. (1851): On the effect of the internal friction of fluids on the motion of pendulums. Trans. Camb. Phil. Soc. 9, 6-106.

Strelioff, D. and Flock, A. (1984): Stiffness of sensory-cell hair bundles in the isolated guinea pig cochlea. Hearing Res. 15, 19-28.

Tilney, L.G., DeRosier, D.J. and Mulroy, M.J. (1980): The organization of actin filaments in the stereocilia of cochlear hair cells. J. Cell. Biol. 86, 244-259.

von Bekesy, G. (1960): Experiments in Hearing. New York: McGraw-Hill.

Weiss, T.F. (1982): Bidirectional transduction in vertebrate hair cells: A mechanism for coupling mechanical and electrical processes. Hearing Res. 7, 353-360.

Weiss, T.F. and Leong, R. (1985a): A model for signal transmission in an ear having hair cells with free-standing stereocilia. III. Micromechanical stage. Hearing Res. 20, 157-174.

Weiss, T.F. and Leong, R. (1985b): A model for signal transmission in an ear having hair cells with free-standing stereocilia. IV. Mechanoelectric transduction stage. Hearing Res. 20, 175-195.

Weiss, T.F. and Leong, R. (1986): A model for signal transmission in an ear having hair cells with free-standing stereocilia. VI. Model properties and comparison with measurements. (In preparation).

Weiss, T.F., Mulroy, M.J., Turner, R.G., and Pike, C.L. (1976): Tuning of single fibers in the cochlear nerve of the alligator lizard: relation to receptor morphology. Brain Res. 115, 71-90.

Weiss, T.F., Peake, W.T., Ling, A., and Holton, T. (1978): Which structures determine frequency selectivity and tonotopic organization of vertebrate cochlear nerve fibers? Evidence from the alligator lizard. In: Evoked Electrical Activity in the Auditory Nervous System, pp. 91-112. Editors: R.F. Naunton and C. Fernandez. Academic Press, New York.

Weiss, T.F., Peake, W.T., and Rosowski, J.J. (1985): A model for signal transmission in an ear having hair cells with free-standing stereocilia. I. Empirical basis for model structure. Hearing Res. 20, 131-138.

Yih, C.S. (1979): Fluid mechanics: A concise introduction to the theory. West River Press, Ann Arbor, Michigan.